UNIVERSITÉ DE NANTES
FACULTÉ DES SCIENCES ET TECHNIQUES

ÉCOLE DOCTORALE
MATÉRIAUX MATIÈRE MOLÉCULE EN PAYS DE LOIRE

Année : 2012

N° attribué par la bibliothèque

Analyse des données des calorimètres d'ALICE et étude de la production des hadrons de basse impulsion dans les collisions de grande énergie

THÈSE DE DOCTORAT
Discipline : Physique
Spécialité : Physique Subatomique

Présentée et soutenue publiquement par

Olga DRIGA

Le 21 Septembre 2012, devant le jury ci-dessous

Président	M. MARTINEZ Ginés,	*Directeur de recherche CNRS, Subatech*
Rapporteurs	M. FLEURET Frédéric,	*Directeur de recherche CNRS, Leprince-Ringuet*
	M. KHOZE Valeri,	*Professeur, Institut for Particle Physics Phenomenology, University of Durham*
Examinateurs	M. OESCHLER Helmut,	*Directeur de recherche, Institut für Kernphysik Technische Universität Darmstadt*

Directeur de thèse : M. GOUSSET Thierry, *Professeur, Subatech, Université de Nantes*

N° ED 500

Acknowledgment

Throughout various stages of completion of this thesis and during my graduate education as a whole, I have greatly benefited from discussions with Yuri Kharlov, my ALICE colleague. I am greatly indebted to him for sharing his insight, offering advice, maintaining interest and providing encouragement. Without his support, the experimental part of these studies could not be performed.

I am also greatly indebted to Valeri Khoze and Wolfgang Ochs for suggesting me the phenomenological subject of these studies and for their advices and illuminating discussions. I am also greatly indebted to Frédéric Fleuret for illuminating discussions and for important comments on the manuscript.

Let me also express my deep gratitude to Maxim Konyushikhin. I would not have completed my thesis without his unconditional support.

The studies involved in this thesis were done in an amiable and pleasant collaboration with T. Awes, A. Jacholkowski and J.-P. Revol. I deeply appreciate their participation in my education, their interest, their help and their advices.

I am also indebted to Yu. Dokshitzer, D. Peressounko and B. Polichtchouk, Y. Schutz, A. Smilga for illuminating discussions.

Let me also thank C. Roy for proposing me the PhD position in the SUBATECH laboratory and T. Gousset for suggesting me interesting topic of the current thesis and helping me with the manuscript. I would like to thank J. Martino, P. Latridou and B. Grambow for giving me the ability to complete the thesis in the SUBATECH laboratory.

Finally, I am thankful to all my ALICE colleagues and, in particular, my ALICE colleagues of the SUBATECH laboratory.

Table des matières

Chapitre 1

Résumé

1.1 L'introduction

Prédiction théorique de diverses quantités de la chromodynamique quantique (QCD) est un sujet difficile. En particulier, les spectres des hadrons ne peut être obtenu à partir des premiers principes. Toutefois, certains domaines de la théorie peut admettre description quantitative. Par exemple, dans les processus durs, l'échange d'énergie et de quantité de mouvement entre partons produites en collision des particules hadroniques est si grande que les partons peut être considéré comme les particules libres (non liées). Cela est dû à la liberté asymptotique de la chromodynamique quantique [1] : pour le transfert élevée de quantité de mouvement, la constante d'interaction forte devient petite, et le calcul perturbative basée sur les graphes de Feynman devient possible. Après la collision primaire "perturbative", les partons produites hadronizent, et ce processus est à nouveau n'est pas adressable analytiquement à partir des premiers principes de la QCD.

Un autre domaine de QCD est les spectres des hadrons de bas impulsion et, en particulier, les spectres moux qui sont produits à l'intérieur des jets dans une collision à haute énergie. L'étude de la production dans des collisions relativistes multihadron peuvent apporter l'information précieuse sur les caractéristiques de processus de branchement des partons en QCD. Ces procédés sont originaires de la bremsstrahlung gluon et sont mathématiquement décrit par une somme de nombre infini de graphes de Feynman. Ces dernieres devient singulière (logarithmiquement large) dans la limite d'émission moux. Il s'avère que, grâce à ce q'on appelle le phénomène de *cohérence de couleur*, les grands termes logarithmiques peuvent être additionnées. Ce résultat est bien compri aussi bien qualitativement que quantitativement (voir, par exemple, [2, 3]. Sa confirmation expérimentale a été l'un des plus grands succès qui ont abouti à la révision spectaculaire des attentes théoriques en physique hadronique de bas impulsions.

Calculs analytiques de partoniques processus de branchement de QCD donnent différentes densités partoniques comme une sortie puisque le régime hadronisation, c'est à dire le passage d'partons de couleur pour les hadrons incolores, n'est toujours pas accessible en théorie. Ainsi, l'application des observables multiparton calculées nécessite des hypothèses supplémentaires. L'approche la plus simple est *Local Parton-hadrons dualité* (LPHD) [4]. Il suppose que hadrons et parton spectres sont proportionnelles afin que observables des hadrons sont directement donnée par les observables correspondantes des partons calculées analytiquement. Le LPHD est bien soutenu expérimentalement.

Mesure de la production de hadrons de bas impulsion en collisions *pp* au LHC ouvre nouveau régime cinématique pour tester et valider la capacité prédictive de la chromodynamique quantique. L'expérience ALICE a un excellent detecteur des particules chargées et les capacités d'identification des particules dans un large intervalle des impulsions des particules. En outre, elle est unique parmi les expériences du LHC pour son système de tracking des particules et les capacités d'identification des particules au large gamme d'energies. Ceci est très important dans la vue de scruter la production de rayonnement à l'élan intermédiaire et faible. Bien que ALICE est une expérience dédiée pour ions lourds, son programme de physique dans les collisions *pp* est très riche. Un champ d'investigation est celui de la physique intrajet qui nécessite des outils dédiés pour la sélection et la mesure de jets. Un ingrédient précieux à cette fin est le déclenchement sur “photon-jet” événements qui, avec un jet contenant un photon isolé se déplaçant dans la direction opposée, ce qui donne une bonne estimation de l'énergie des jets. Dans l'expérience ALICE, les photons sont mesurées avec deux calorimètres électromagnétiques, PHOS et EMCAL.

Le but de cette étude était de déterminer et de mesurer les observables adéquats pour l'expérience ALICE afin de vérifier le phénomène de cohérence du couleur. Les écarts entre les prévisions théoriques et les quantités mesurées voudrait dire qu'il ya des contributions inattendues de incohérentes multi-composants des processus. À cette fin, nous examinons les deux sujets suivants ci-dessous : distribution en impulsion inclusive de particules dans un jet et l'universalité de la production de hadrons doux. En conséquence, la présente étude consiste à partie expérimentale consacrée à l'analyse des données recueillies par les calorimètres électromagnétiques ALICE et une partie théorique de l'analyse des spectres des hadrons moux de différentes expériences.

Physique hadronique avec l'expérience ALICE

Les prédictions théoriques de spectres partonic, effectués au sein de ce que l'on appelle *Modified Leading Log Approximation* (MLLA) et complété avec l'idée LPHD, peut être testée expérimentalement en mesurant les spectres de mouvement des particules à l'intérieur d'un jet. Cela peut être fait dans les expériences qui ont une bonne capacité de suivi de particules chargées. Par exemple, considérons la figure 1.1 (à gauche), qui montre le spectre de particules à l'intérieur d'un jet (dans les événements dijet) pour l'expérience CDF dans p$\bar{\mathrm{p}}$ collisions en $\sqrt{s} = 1.8$ TeV [5]. Ici, l'axe X correspond à la coordonnée traditionnelle

$$\xi = \ln \frac{1}{x}, \qquad x = \frac{p}{E_{\mathrm{jet}}}, \tag{1.1.1}$$

où p est l'impulsion de particule, E_{jet} - l'énergie totale d'un jet. La ligne continue représente le résultat du calcul de MLLA. On peut observer sur cette figure un appauvrissement de particules de grande ξ, ce qui correspond à la dynamique de bas impulsion. La forme de la distribution est généralement désigné sous le nom de *Hump-Backed Plateau* (HBP).

Les études de faisabilité de la détection des jets en ALICE avec les évènements des différents topologies [6, 7] montrent que la mesure de la distribution en impulsion des particules compris dans un jet avec ALICE est un projet à long terme car elle nécessite large quantité de statistiques à collecter. Néanmoins, les travaux préparatoires exige

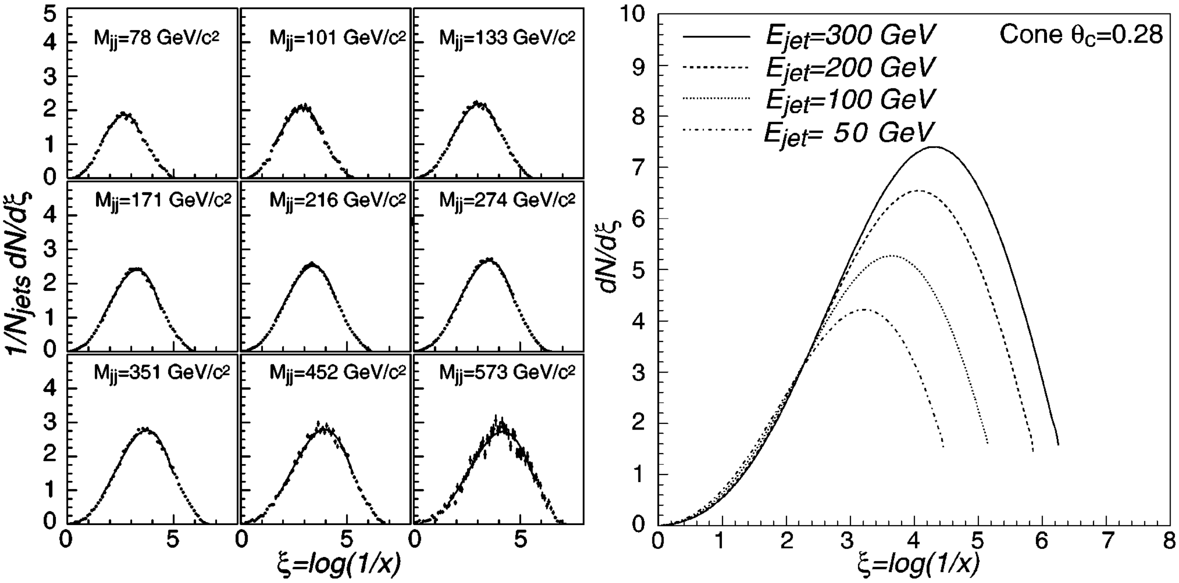

FIGURE 1.1 – Expérience CDF, $p\bar{p}$ collisions à $\sqrt{s} = 1.8$ TeV. A gauche : distribution des impulsions de particules compris dans un jet pour neuf énergies de jet. La ligne continue représente la prédiction MLLA. A droite : l'évolution du spectre des partons prédit par MLLA pour un jet de gluons. Les quatre lignes correspondent aux énergies des jets $E_{\text{jet}} = 50$, 100, 200 and 300 GeV. Jets ont été prises dans un cône restreint de taille $\theta_c = 0.28$ rad. Les plots sont prises de [5].

aussi beaucoup d'efforts. Voici un programme minimal requis qui doit être rempli par les détecteurs ALICE avant toute mesure de jets devient possible :

1. Assurance de la qualité, l'étalonnage et la correction des données recueillies.
2. Les bonnes performances des détecteurs doit être vérifiée en mesurant des quantités relatives aux signaux physiques. Ce faisant, on confirme que chaque sous-système détecteur fonctionne comme prévu.
3. Monte Carlo tuning : un match serré entre la simulation et les données doivent être atteints.
4. Il'inclusion des mesures de spectres hadrons, y compris identifiés hadrons chargés et les mésons neutres détectés par le tracking système d'ALICE et les calorimètres respectivement.
5. Reconstruction des jets.

En tant que membre du groupe EMCal, l'auteur de cette étude a été impliqué dans le travail avec les calorimètres électromagnétiques ALICE, PHOS et EMCal. À la fin de 2009, lorsque prise des données a commencé, il surgi forte nécessité d'effectuer les quatre premières étapes citées ci-dessus.

Les méthodes de vérification de la qualité des données pour les calorimètres ALICE sont décrites dans le chapitre 5. Le cadre d'assurance de la qualité développé [8] donne un moyen rapide et pratique de vérifier la qualité des données à la fois pour PHOS et pour EMCal. Sans il, la fiabilité et la stabilité des données ne peut pas être atteint.

Les étapes 2, 3 et 4 ci-dessus vont discuté dans le chapitre 6 pour le cas du détecteur EMCal. Les performances du calorimètre électromagnétique peut être vérifiée en mesurant le plus léger des mésons neutres spectres (π^0, η, $\omega(782)$, K^0_S). Bien que le détecteur a été installé EMCal parmi les derniers, les données recueillies donne déjà la possibilité de mesurer π^0 et η spectres de production des mésons dans leurs modes de désintégration en deux photons ainsi que η/π^0 ratio. Voir aussi Refs. [9, 10].

L'universalité de la production des hadrons de bas impulsion

Hump-Backed plateau est l'une des distributions de base largement utilisés dans les expériences précédentes pour tester les prédictions MLLA. Comme nous l'avons déjà souligné, une telle mesure implique beaucoup d'efforts car il faut faire la reconstruction jet dans l'expérience ALICE. Il ya encore une autre prédiction qui est remarquablement simple. Ceci est inclus spectres de production hadronique Ed^3n/dk^3 dans la limite de la quantité de mouvement nulle, où E est l'énergie des particules, $\vec{k}$ - son impulsion.

En effet, dans la limite de bas impulsion de parton, le terme de Born domine dans le développement perturbatif d'une cascade partonique. Selon le MLLA, elle est donnée par

$$E\frac{d^3n}{dk^3} \sim C\,\frac{\alpha_S(k_\perp)}{k_\perp^2}, \qquad k_\perp \to 0, \tag{1.1.2}$$

tandis que la prochaine commande de correction disparaître que $\ln 1/k_\perp$. Voici le moment transverse $\vec{k}_\perp$ est prise par rapport à un axe de collision, α_S est running constante de couplage forte, C est un facteur de couleur pertinent pour un processus partonique minime. Celle-ci découle du fait qu'une grande longueur d'onde rayonnée parton ne peut pas résoudre la structure de la collision de sorte que son intensité du rayonnement est sensible uniquement à la charge de couleur totale du processus sous-jacent. En d'autres termes, seuls les premiers temps de la dynamique des processus sous-jacent est important.

La formule (1.1.2) est remarquable. Il montre que dans le limit be dynamique de bas impulsion les spectres inclusives hadroniques sont *indépendante de l'énergie de collision* $\sqrt{s}$ [11]. Cette universalité est l'objet d'études intensives [12, 13].

Une autre conséquence est que la normalisation des spectres par rapport à zéro limit de différents processus de collision est donné par le rapport des facteurs de couleurs correspondantes. En e^+e^- annihilations, dans l'approximation de Born, les gluons mous sont émis à partir d'un quark ou un antiquark, ce qui conduit à un facteur de couleur $C_F = 4/3$ de la représentation fondamentale de SU (3). Au contraire, dans les collisions pp, ce facteur correspond à un octet de couleur (représentation adjointe), $C_A = 3$. De cette façon, on s'attend à ce que le rapport se lit

$$r = \lim_{k\to 0} \frac{d^3n^{pp}/dk^3}{d^3n^{ee}/dk^3} = \frac{C_A}{C_F} = 2.25. \tag{1.1.3}$$

Il ya beaucoup de données expérimentales des spectres des particules chargées non-identifié et identifié dans différentes expériences pour différentes énergies de collision. Dans le chapitre 7 nous procédons à l’extraction des limites zéro d’une manière systématique, conformément à l’esprit des études de Refs [11, 12, 13].

Par ailleurs, dans le chapitre 8, nous mettons en œuvre une approche différente en considérant les ratios de spectres de différentes énergies de collision. Étonnamment, ces rapports semblent être des fonctions linéaires dans une large gamme d’energie.

Structure du manuscrit

The structure of the manuscript is as follows.

In Chapter 3, we give an introduction to color coherence phenomenon in QCD, selecting some of the relevant material from Ref. [2]. In the leading and the simplest order, the calculation of soft parton spectra from Feynman graphs of partonic cascades is performed in the *Double Logarithmic Approximation* (DLA). The DLA incorporates main ingredients of the technique and delivers clear qualitative description of soft parton physics. Still, the incorporation of next-to-leading order terms of the MLLA is necessary to get a good quantitative description. In this chapter, we stay at the level of the DLA, giving just a glimpse of modifications expected within the MLLA.

La structure du manuscrit est la suivante.

Dans le chapitre 3, nous donnons une introduction au phénomène de la cohérence des couleurs dans QCD, la sélection de certains des éléments pertinents de Réf. [2]. Dans le premier et le plus simple pour le calcul des spectres parton doux de graphes de Feynman de cascades partoniques est effectuée dans le *approximation logarithmique double* (DLA). Le DLA incorpore des ingrédients principaux de la technique et offre claire description qualitative de la physique partons mous. Cependant, l’incorporation de termes d’ordre avant-phares de la MLLA est nécessaire pour obtenir une bonne description quantitative. Dans ce chapitre, nous restons au niveau de la DLA, en donnant juste un aperçu des modifications attendues dans le MLLA.

Chapitre 4 est consacrée à un aperçu du LHC ainsi que de l’expérience ALICE.

Le cadre d’assurance qualité des données est abordée dans le chapitre 5. Nous discutons des idées générales de l’assurance de la qualité des données et expliquer les méthodes qui ont été développées et appliquées pour les calorimètres ALICE. Le travail présenté dans ce chapitre est publié une note d’analyse ALICE [8].

Dans le chapitre 7, nous réalisons des études systématiques de la limite impulsion zéro du spectre des hadrons identifié prises de hadrons plusieurs expériences et de leptons dans les énergies de collision du dixième de GeV à l’échelle du TeV du LHC. Pour tester les prédictions de cohérence de couleurs, nous avons ajusté les spectres avec des fonctions différentes et d’extrapoler les crises à zéro dynamique.

Enfin, la conclusion complete le manuscrit.

1.2 L’expérience ALICE

L’expérience ALICE auprès du LHC est dédiée à l’étude des multiples facettes de l’interaction forte. La théorie microscopique de cette dernière, QCD, et sa manifestation dans la production de particules peuvent être explorées en étudiant les observables de jets. La maîtrise de sa calorimétrie est centrale à l’étude de la physique des jets avec ALICE. C’est l’un des sujets abordés dans ce travail. Plus précisément, une des premières tâches est de vérifier la qualité des données disponibles. A cet effet, l’assurance de la qualité (AQ) des données pour les calorimètres électromagnétiques d’ALICE, PHOS et EMCAL, a été développée. Un logiciel dédié a été mis en œuvre qui est implémenté dans le cadre de l’analyse générale de l’expérience ALICE. Le succès dans la compréhension de la dynamique des particules de basse énergie à l’intérieur des jets s’appuie sur des calculs de la QCD perturbative, laquelle a déjà été testée expérimentalement avec un niveau d’accord impressionnant. La théorie prédit que le spectre des particules à l’intérieur des jets est indépendante de l’énergie de la collision dans la limite d’impulsion nulle ($p \to 0$). Afin de tester cette prédiction, une étude systématique des données expérimentales provenant des collisionneurs de hadrons et de leptons aux énergies de collision de quelques dizaines de GeV jusqu’à l’échelle du TeV au LHC a été réalisée.

1.3 Origine de la cohérence

La prédiction théorique pour diverses quantités en chromodynamique quantique (QCD) est un sujet difficile. En particulier, les spectres de hadrons ne peuvent pas être obtenus à partir des premiers principes. Toutefois, certains domaines de la théorie peuvent admettre une description quantitative. Par exemple, dans les processus durs, l'échange d'énergie et de quantité de mouvement entre les partons intervenant lors des collisions de particules hadroniques est si grand que les partons peuvent être considérés comme des particules libres. Cela est dû à la liberté asymptotique de QCD [1] : pour les transferts de grande impulsion la constante d'interaction devient petite et le calcul perturbatif basé sur les graphes de Feynman devient possible. Après la collision primaire perturbative, les partons produits hadronisent, et ce processus n'est pas non plus calculable analytiquement à partir des premiers principes de la QCD.

Ce chapitre est consacré à un autre domaine de la chromodynamique quantique, celui des spectres de hadrons mous et, en particulier, les spectres de hadrons mous à l'intérieur des jets produits dans une collision à haute énergie. Il s'avère que les émissions de particules molles est commandée par ce qu'on appelle la *cohérence de couleur*, un phénomène qui peut être compris aussi bien qualitativement que quantitativement.

A très gros traits, il est possible de déterminer les spectres de particules molles de la manière suivante. Dans une collision à haute énergie, de nombreuses particules sont produites. Leur production dans un jet se présente sous la forme de *gerbes* - (voir Fig. 1.2), c'est-à-dire une succession de branchements de partons. Dans la limite où les particules sont de basse impulsion, la contribution dominante à la section efficace de production de ces particules contient de grands logarithmes. Ces grands logarithmes peuvent être calculés de façon systématique. En ne gardant que les termes dominants (*leading logs*), on peut sommer tout le développement perturbatif des diagrammes de Feynman. Comme résultat, on peut obtenir, par exemple, les *densités de partons* dans une gerbe, c'est-à-dire la distribution en énergie et en angle du nombre de ces partons. Ensuite, les densités de partons calculées peuvent être traduites en spectres de hadrons en utilisant l'hypothèse observée expérimentalement appelée la dualité parton-hadron locale (LPHD). Cette dernière affirme que les spectres des partons de bremsstrahlung coïncident, à un facteur multiplicatif constant près, avec les spectres de hadrons pris à la même quantité de mouvement.

Dans cette première section, nous discutons l'origine physique de la cohérence de couleur dans QCD, en sélectionnant les éléments utiles de la référence [2]. A cet effet, nous considérons l'annihilation e^+e^- (voir Fig. 1.3) comme processus primaire et illustrons la façon dont la ramification partonique se comporte. D'après [2], le quark et l'antiquark émettent les gluons indépendamment, de sorte que, pour fixer les idées, nous allons suivre le processus d'émission de gluons par le seul quark.

L'analyse des diagrammes de $e^+e^- \to q\bar{q} + Ng$ à tous les ordres de la théorie des perturbations montre que la ramification dans une cascade partonique ne se développe que dans la région correspondant à un rétrecissement strict des cônes angulaires successifs. En dehors de cette région cinématique, l'émission des gluons est supprimée à cause d'interférences destructives. Un tel phénomène est analogue au phénomène de cohérence observé en électrodynamique quantique dans l'effet Chudakov bien connu [18].

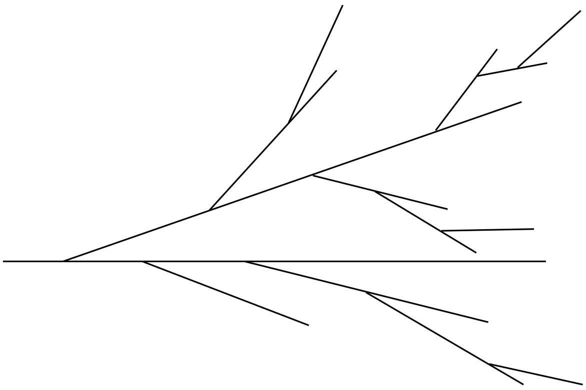

Figure 1.2 – Une image de *gerbe*.

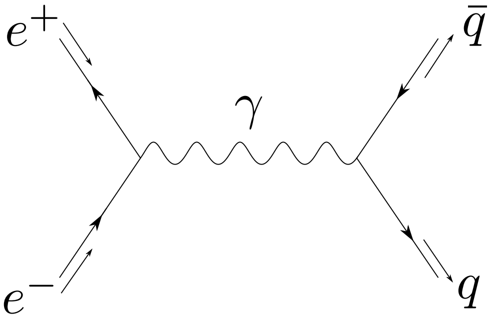

Figure 1.3 – e^+e^- annihilation.

1.3.1 Approximation des doubles logarithmiques

Montrons sur l'exemple du processus $e^+e^- \to q\bar{q} + Ng$ comment la section efficace σ_N se comporte à l'approximation des logarithmiques dominants. La section efficace σ_N est proportionnelle à l'intégrale suivante sur l'espace des phases de l'ensemble des N partons :

$$\sigma_N \sim \int |M_N|^2 \prod_{i=1}^{N} \frac{d^3k_i}{2\omega_i}, \tag{1.3.1}$$

où M_N est l'élément de matrice pour la production de N partons, $\vec{k}_i$ sont les impulsions de ces partons et ω_i leur énergie. Soulignons que la prise en compte de la nature indiscernable des gluons rend possible l'organisation de l'expression de σ_N de telle sorte que les gluons sont énumérés par ordre décroissant de leur énergie : $i = 1$ correspond à la plus grande énergie, tandis que $i = N$ à la plus petite. Nous désignons par E_0 l'énergie du parton parent à partir duquel la cascade des N gluons est engendrée (le quark ou l'anti-quark initial pour notre cas).

Il s'avère que la contribution principale à l'intégrale dans (1.3.1) est accumulée dans la région de l'espace des phases où les énergies des partons sont *fortement* ordonnées :

$$E_0 \gg \omega_1 \gg \omega_2 \gg ... \gg \omega_N \quad \text{[ordonnancement des énergies]}. \tag{1.3.2}$$

La justification de ce fort ordonnancement fort s'explique comme suit. D'abord pour $N = 1$, on peut avoir un grand logarithme si l'intégrale sur ω_1 est de la forme

$$\int_{Q_0}^{E_0} \frac{d\omega_1}{\omega_1} = \ln \frac{E_0}{Q_0} \equiv L,$$

où Q_0 est une énergie seuil nécessaire ici afin de régulariser l'intégrale. Nous verrons plus loin que le formalisme incorpore une échelle de basse impulsion transverse en dessous de laquelle le rayonnement est impossible en raison de l'inexistence des partons de grande longueur d'onde dans QCD. Physiquement Q_0 est alors liée à l'échelle de QCD, Λ, ou, plus de façon plus phénoménologique, à $1/R$, où R est une taille de hadron typique. Le logarithme obtenu ci-dessus est grand si $E_0 \gg Q_0$, soit compte tenu de $Q_0 \sim 200$ MeV, si nous nous intéressons aux énergies E_0 de plusieurs GeV (les jets à haute énergie dans le jargon QCD). Dès lors, limiter le calcul à l'obtention de ces grands logarithmes implique que la hiérarchie forte $E_0 \gg \omega_1 \gg Q_0$ peut être utilisée pour le calcul de l'intégrale puisque les régions $\omega_1 \sim E_0$ et $\omega_1 \sim Q_0$ apportent seulement des contributions finies, négligeables par rapport à la quantité L (considérée incommensurablement plus grande). Pour $N = 2$,

$$\int_{Q_0}^{E_0} \frac{d\omega_a}{\omega_a} \times \int_{Q_0}^{E_0} \frac{d\omega_b}{\omega_b} = L^2,$$

les régions comportant un produit de deux grands logarithmes sont soit $\omega_a \gg \omega_b$ ou $\omega_b \gg \omega_a$, puisque les régions près des frontières sont à nouveau de contribution négligeable, et il est possible, après un ré-étiquetage, d'obtenir

$$\int_{Q_0}^{E_0} \frac{d\omega_a}{\omega_a} \times \int_{Q_0}^{E_0} \frac{d\omega_b}{\omega_b} = 2 \int_{Q_0}^{E_0} \frac{d\omega_1}{\omega_1} \times \int_{Q_0}^{\omega_1} \frac{d\omega_2}{\omega_2},$$

soit la contribution des grands logarithmes avec l'ordonnancment fort des énergies mentionné au début. De la même façon, les angles des émissions consécutives sont fortement ordonnés :

$$1 \gg \theta_1 \gg \theta_2 ... \gg \theta_N \quad \text{[ordonnancement angulaire]}, \tag{1.3.3}$$

où θ_i est l'angle d'émission du i-ème parton par rapport à son parton parent, voir Fig. 1.4. Techniquement, l'apparition de grands logarithmes colinéaires résulte d'intégrales de la même nature que celles qui donnent les logarithmes d'énergie. Cependant, l'ordre angulaire associé est dû à des compensations non triviales entre différents graphes de Feynman, au cœur du phénomène de cohérence déjà mentionné. Par la suite, et de façon plus complète dans le chapitre 3, nous donnons quelques détails sur la façon dont cela se produit pour le cas $N = 2$.

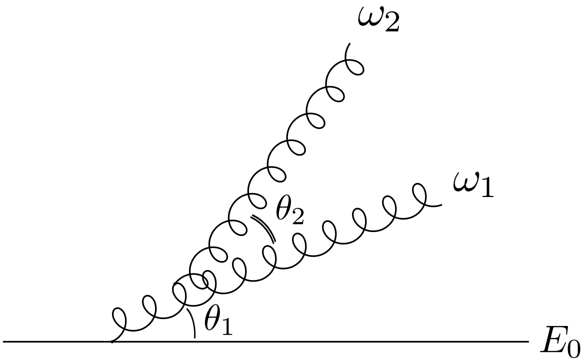

FIGURE 1.4 – Angles et énergies des émissions de partons consécutives. Pour simplifier toutes les émissions de partons sont dessinées dans le même plan.

Ici nous nous contentons d'expliquer la provenance d'une puissance de logarithme d'énergie et de logatithme colinéaire par gluon rayonné au niveau de l'expression de σ_N indiquée à l'équation (1.3.1) dans la région mentionnée ci-dessus pour l'espace de phase. À cette fin, nous utilisons l'expression de la contribution dominante à l'amplitude de M_N, une expression qui sera justifiée pour $N = 2$ dans le chapitre 3. Cette contribution provient de deux types de branchements : $q \to q + g$ et $g \to g + g$, soit à partir d'une émission d'un gluon par un quark ou d'une émission d'un gluon par un gluon. Dans cette approche, l'émission de deux gluons à partir d'un gluon $g \to g + 2g$ est négligeable. Pour les émissions retenues, l'amplitude M_N est donnée par

$$M_N^{\mathrm{DLA}} \sim g_s^N \prod_{i=1}^{N} \frac{e_i \cdot P_i}{k_i \cdot P_i} \times [\text{color factor}] \quad [\text{Approximation double log}], \tag{1.3.4}$$

$e_i = (0, \vec{e_i})$ étant le quadri-vecteur polarisation du i-ème gluon (la composante vectorielle $\vec{e_i}$ étant orthogonale à $\vec{k_i}$, $\vec{e_i} \cdot \vec{k_i} = 0$), $P_i = (E_{P_i}, \vec{P_i})$ étant la quadri-impulsion du parton parent de ce i-ème gluon (voir Fig. 1.5) et g_s étant la constante de couplage de l'interaction QCD. Les produits scalaires $k_i \cdot P_i$ et $e_i \cdot P_i$ dans la région de l'espace des phases d'intérêt (ce qui implique en particulier des petits angles et une situation de partons sans masse) sont donnés par

$$k_i \cdot P_i = \omega_i E_{P_i} - \vec{k_i} \cdot \vec{P_i} \approx \omega_i E_{P_i}(1 - \cos\theta_i) \approx \omega_i E_{P_i} \frac{\theta_i^2}{2} \tag{1.3.5}$$

et

$$e_i \cdot P_i = -\vec{e_i} \cdot \vec{P_i} = |\vec{e}_{i\perp}| E_{P_i} \sin\theta_i \approx |\vec{e}_{i\perp}| E_{P_i} \theta_i, \tag{1.3.6}$$

où $\vec{e}_{i\perp}$ est la projection de $\vec{e_i}$ sur le plan $\{\vec{k_i}, \vec{P_i}\}$. En mettant ensemble tout ce qui précède et en effectuant la somme sur les polarisations physiques des gluons émergeants, on obtient l'expression suivante pour la section efficace (1.3.1)

$$\sigma_N^{\mathrm{DLA}} \sim \prod_{i=1}^{N} \int \sum_{\mathrm{polar.}} \left| g_s \frac{|\vec{e}_{i\perp}| E_{P_i} \theta_i}{\omega_i E_{P_i} \theta_i^2} \right|^2 \frac{\omega_i^2 d\omega_i \theta_i d\theta_i}{2\omega_i} \sim \prod_{i=1}^{N} \left(g_s^2 \int \frac{d\omega_i}{\omega_i} \int \frac{d\theta_i}{\theta_i} \right), \tag{1.3.7}$$

où nous avons substitué $d^3k \sim \omega_i^2 d\omega_i \theta_i d\theta_i$ et utilisé le fait que $\sum_{\mathrm{polar.}} |\vec{e}_{i\perp}|^2 = 1$. Nous observons que pour obtenir ce comportement, le i-ème gluon doit contribuer un facteur $g_s/(\omega_i \theta_i)$ à M_N.

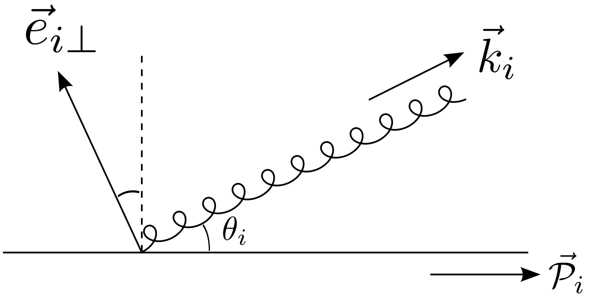

FIGURE 1.5 – Le vecteur de polarisation du gluon $\vec{e}_i$ est dans le plan perpendiculaire à $\vec{k}_i$.

L'expression à droite dans (1.3.7) montre le comportement logarithmique dans la région de l'espace de phase où les angles et les énergies sont fortement ordonnés comme indiqué dans les équations (1.3.2) et (1.3.3). La section efficace résultante section possède donc deux puissances de grand logarithme par gluon dans l'état final, ce qui explique le nom de la contribution discutée que l'on appelle *l'approximation doublement logarithmique* (DLA).

Soulignons que le schéma DLA fournit le moyen d'obtenir des résultats assez simples et physiquement transparents tout en capturant les principales caractéristiques de la physique des cascades de partons. Cependant, il s'avère que DLA n'est pas suffisant pour obtenir une description quantitative, et il s'avère qu'il faut incorporer les termes avec une seule puissance de grand logarithme pour atteindre un bon niveau de précision. La technique correspondante est s'appelle *l'approximation des logarithmes dominants modifiée* (MLLA) [2].

MLLA est une tentative d'aller au-delà du champ d'application de DLA en prenant en compte également une partie des corrections sous dominantes comportant de simples logarithmes. Le changement le plus notable dans MLLA en comparaison avec DLA est que les ordonnancements forts de l'énergie et des angles explicités avec les règles (1.3.2) et (1.3.3) sont remplacés par des ordonnancements simples

$$E_0 \geq \omega_1 \geq \omega_2 \geq \ldots \geq \omega_N \tag{1.3.8}$$

et

$$1 \geq \theta_1 \geq \theta_2 \geq ... \geq \theta_N. \tag{1.3.9}$$

1.3.2 Calcul des amplitudes d'émission de N gluons

Dans cette section, nous indiquons comment la formule de l'équation (1.3.4) découle des règles de Feynman pour l'amplitude de production de N gluons en DLA, pour $N = 1$ et $N = 2$. À cette fin, nous calculons les contributions dominantes de tous les diagrammes de Feynman pertinents, cooprenant les vertex $q \to q + g$ et $g \to g + g$. La recherche des termes avec des grands logarithmes permet de limiter le domaine cinématique à la situation (règle (1.3.2) :

$$E_0 \gg \omega_1 \gg \omega_2. \tag{1.3.10}$$

Ce calcul permettra de montrer aue la règle (1.3.3) est à l'œuvre. Encore une fois, il sera supposé que toutes les particules sont sans masse.

Le cas $N = 1$

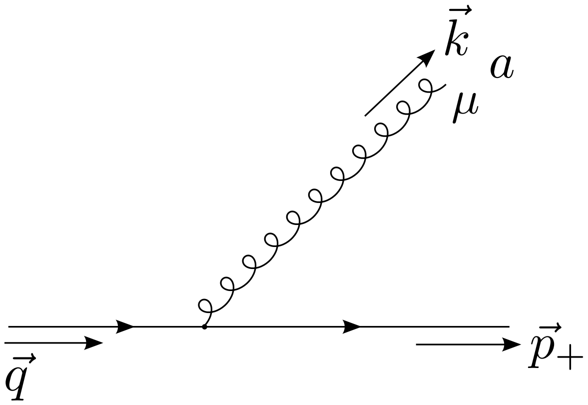

Figure 1.6 – One-gluon emission diagram.

L'amplitude M_N la plus simple possible est pour le cas $N = 1$, à laquelle correspond le seul diagramme de la figure 1.6 qui décrit l'émission du gluon par le quark. On peut facilement écrire son expression mathématique :

$$M_1 = -ig_s \bar{\Psi}_f(p_+)\gamma^\mu t_a e_\mu(k)\frac{i\hat{q}}{q^2}, \tag{1.3.11}$$

où $\bar{\Psi}_f(\vec{p}_+)$ est la fonction d'onde du quark (un spineur comprenant un indice de couleur), t_a sont les générateurs de l'algèbre pour le groupe de jauge SU(N_c) ($N_c = 3$ est le nombre de couleurs), tandis que $e_\mu(k)$ correspond au vecteur polarisation du gluon. Les notations pour les moments sont présentées dans la figure 1.6. En outre, $\hat{q} = \gamma^\mu q_\mu$, $q_\mu = p_{+\mu} + k_\mu$. Remarquons que le propagateur du quark $\frac{i\hat{q}}{q^2}$ est associé à la ligne de quark avant émission. Il est présent ici car le diagramme de la figure 1.6 ne contient qu'une partie du processus de collision, qui devrait, en effet, être attachée au diagramme de la Fig. 1.3.

L'expression (1.3.11) peut être simplifiée dans la limite des gluons mous, $|\vec{k}| \ll |\vec{p}_+|$. En effet,

$$\bar{\Psi}_f(p_+)\gamma^\mu(\hat{p}_+ + \hat{k}) = \bar{\Psi}_f(p_+)\left(2p_+^\mu - \hat{p}_+\gamma^\mu + \gamma^\mu\hat{k}\right) \approx 2p_+^\mu \times \bar{\Psi}_f(p_+), \tag{1.3.12}$$

où nous avons utilisé l'équation de Dirac

$$\bar{\Psi}_f(p_+)\hat{p}_+ = 0 \tag{1.3.13}$$

pour le quark final et négliger le terme $\gamma^\mu\hat{k}$. Ainsi,

$$M_1 \approx g_s \frac{2e \cdot p_+}{q^2}\,\bar{\Psi}_f, \tag{1.3.14}$$

puis en substituant

$$q^2 = (p_+ + k)^2 \approx 2k \cdot p_+, \tag{1.3.15}$$

nous obtenons finalement

$$M_1 \approx g_s \frac{e \cdot p_+}{k \cdot p_+} \times \bar{\Psi}_f t_a. \tag{1.3.16}$$

Cette dernière expression correspond bien à (1.3.4) pour $N = 1$.

Le cas N=2

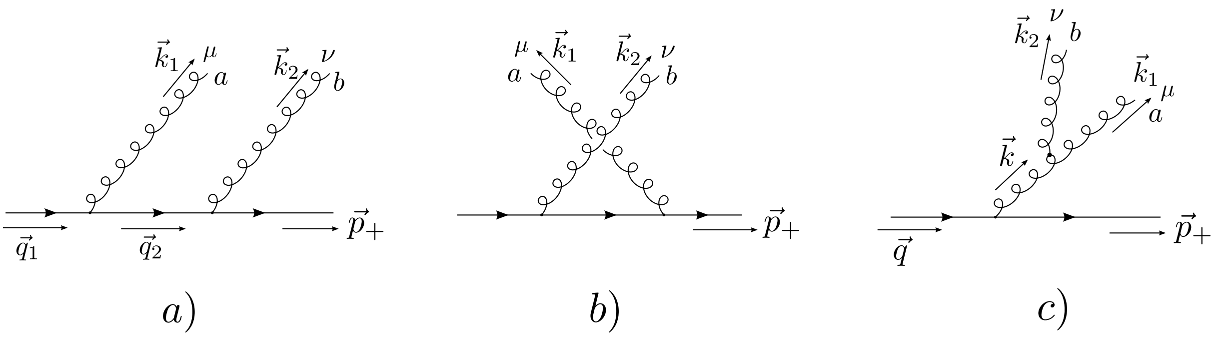

FIGURE 1.7 – Les graphes de Feynman pour l'émission de deux gluons.

L'amplitude de l'émission de deux gluons par un quark dans l'approximation DLA est décrite par la somme des graphes de Feynman dessinés sur la Fig. 1.7. Commençons par la contribution du diagramme de la Fig. 1.7a. L'amplitude correspondante est

$$M_{2a} = \bar{\Psi}_f(p_+)(-ig_s)\gamma^\nu t_b e_{2\nu}(k_2)\frac{i\hat{q}_2}{q_2^2}(-ig_s)\gamma^\mu t_a e_{1\mu}(k_1)\frac{i\hat{q}_1}{q_1^2}, \tag{1.3.17}$$

avec $e_1(k_1)$ et $e_2(k_2)$ étant les polarisations de la première et la seconde lignes de gluons, respectivement, alors que la situation cinématique est précisé dans la Fig. 1.7a. L'élément de matrice (1.3.17) peut être simplifiée de la même manière que cela a été fait pour le cas $N = 1$. Le numérateur est donné par

$$\bar{\Psi}_f(p_+)\gamma^\nu \hat{q}_2\gamma^\mu \hat{q}_1 = \bar{\Psi}_f\gamma^\nu(\hat{p}_+ + \hat{k}_2)\gamma^\mu\hat{q}_1 \approx (2p_+^\nu)(2p_+^\mu) \times \bar{\Psi}_f(p_+), \tag{1.3.18}$$

parce que $\bar{\Psi}_f(p_+)\hat{p}_+ \approx 0$, tandis que pour le dénominateur

$$q_1^2 q_2^2 \approx 2(k_1 + k_2)\cdot p_+ \, 2k_2 \cdot p_+ \tag{1.3.19}$$

Donc

$$M_{2a} \approx g_s^2 \frac{e_1 \cdot p_+}{(k_1 + k_2)\cdot p_+}\frac{e_2\cdot p_+}{k_2\cdot p_+} \times \bar{\Psi}_f t_b t_a. \tag{1.3.20}$$

Cette expression ressemble à celle de l'équation. (1.3.4) mais en diffère par le dénominateur. Cependant, il est possible d'approximer $(k_1 + k_2)\cdot p_+ \approx k_1 \cdot p_+$ dans la région où $\omega_1\theta_1^2 \gg \omega_2\theta_2^2$, qui est la seule région dans laquelle M_{2a} peut contribuer un facteur $1/\theta_1$. Puisque la présence d'un tel facteur est nécessaire pour obtenir le comportement logarithmique double, nous retenons l'expression de l'amplitude avec $(k_1 + k_2)\cdot p_+ \approx k_1 \cdot p_+$ et la région $\omega_1\theta_1^2 \gg \omega_2\theta_2^2$ dans laquelle M_{2a} est pertinente dans DLA.

De toute évidence, la contribution du diagramme de la Fig. 1.7b est similaire à celle du diagramme de la Fig. 1.7a. En échangeant les indices pour le premier et le deuxième des gluons émis, on obtient

$$M_{2b} \approx g_s^2 \frac{e_2 \cdot p_+}{(k_2 + k_1)\cdot p_+}\frac{e_1\cdot p_+}{k_1\cdot p_+} \times \bar{\Psi}_f t_a t_b. \tag{1.3.21}$$

Pour M_{2b} la région DLA est $\omega_2\theta_2^2 \gg \omega_1\theta_1^2$ où l'approximation $(k_2 + k_1)\cdot p_+ \approx k_2 \cdot p_+$ est pertinente.

Le diagramme de la Fig. 1.7c nécessite un calcul séparé. Nous partons de l'expression mathématique correspondante pour celui-ci :

$$\begin{aligned} M_{2c} &= \bar{\Psi}_f(p_+)(-ig_s)\gamma_\sigma t_c \frac{i\hat{q}}{q^2}\, e_1^\mu(k_1)e_2^\nu(k_2)\, g_s\gamma_{\mu\nu\rho}(k_1,k_2,-k) f_{abc}\frac{id^{\rho\sigma}(k)}{k^2} \\ &\approx g_s^2 e_1^\mu(k_1)e_2^\nu(k_2)\gamma_{\mu\nu\rho}(k_1,k_2,-k)\frac{d^{\rho\sigma}(k)}{2k_1\cdot k_2}\frac{p_{+\sigma}}{k\cdot p_+}\, if_{abc}\bar{\Psi}_f t_c, \end{aligned} \quad (1.3.22)$$

où f_{abc} sont les constantes de structure du groupe SU(N_c) et où le coefficient de

$$\gamma_{\mu\nu\rho}(k_1,k_2,k_3) = g_{\mu\nu}(k_1-k_2)_\rho + g_{\nu\rho}(k_2-k_3)_\mu + g_{\rho\mu}(k_3-k_1)_\nu \quad (1.3.23)$$

vient du vertex à trois gluons.

1.4 Prédictions théoriques pour la limite $p \to 0$.

Connaître la production multiparticulaire dans les collisions relativistes peut fournir des renseignements précieux sur les caractéristiques du processus de branchement partonique en QCD. Ce est causé par le bremsstrahlung des gluons qui devient singulier dans la limite d'émission molle ou colinéaire. Les calculs analytiques dans l'approche DLA (voir chapitre 3) permettent de sommer ces contributions singulières. Un des sujets les plus délicats dans la production multiple à haute énergie est la phase d'hadronisation proprement dite, en d'autres termes, la transition des partons coloré pour les hadrons incolores. À l'heure actuelle, il n'y a pas de régle communément acceptée pour prendre en compte cette étape qui est régie par les forces de confinement de la couleur, ce qui maintient le processus d'hadronisation hors du domaine accessible par la théorie des perturbations. Ainsi la considération des observables multiparticulaires exige des hypothèses supplémentaires. La plus simple est l' hypothèse de ressemblance des spectres de hadrons et de partons, dite dualité locale parton-hadron (LPHD), proposée dans [4] et confirmée expérimentalement. L'hypothèse LPHD dit que les observables au niveau hadronique suffisamment inclusives sont directement fournies par les observables correspondantes calculées pour la cascade partonique. L'un des succès impressionnants de toute cette approche est la prédiction de la forme en dos d'âne de la distribution de l'énergie des particules pour la variable $\xi = \ln\frac{E}{E_{jet}}$ pour les particules avec une énergie E dans un jet d'énergie E_{jet}, que l'on appelle le HBP, discuté dans le chapitre 3.

Dans le chapitre 7, nous nous concentrons sur les propriétés du bremsstrahlung des gluons mous. Selon le calcul DLA indiqué au chapitre 3, la densité de particules dans la limite d'impulsion nulle devient indépendante de l'énergie du parton primaire et proportionnelle aux facteurs de couleur, C_A, C_F, selon la nature de ce parton primaire.

La figure 1.17 (à gauche) montre la densité invariante des pion chargés, Ed^3n/dp^3, en fonction de leur quantité de mouvement p à des énergies dans le référentiel de centre de masse différentes allant de 10 GeV à l'énergie du LEP (91.2 GeV). Dans cette figure, nous pouvons deviner le rapprochement des spectres aux petites quantités de mouvement. Sur la figure 1.17 (à droite) les données pour une large gamme d'énergie sont présentées accompagnées des prédictions MLLA tirées de [13]. La caractéristique remarquable est la tendance à la convergence de tous les spectres dans la limite d'impulsion nulle. Cependant, en regardant plus en détail les valeurs obtenues, les données du LEP montre peut-être une valeur limite de 20 % supérieure par rapport aux données à plus basse énergie. Cela peut être dû à un problème de normalisation globale des données expérimentales ou, d'un autre côté, un signal de la présence d'éventuelles contributions incohérentes.

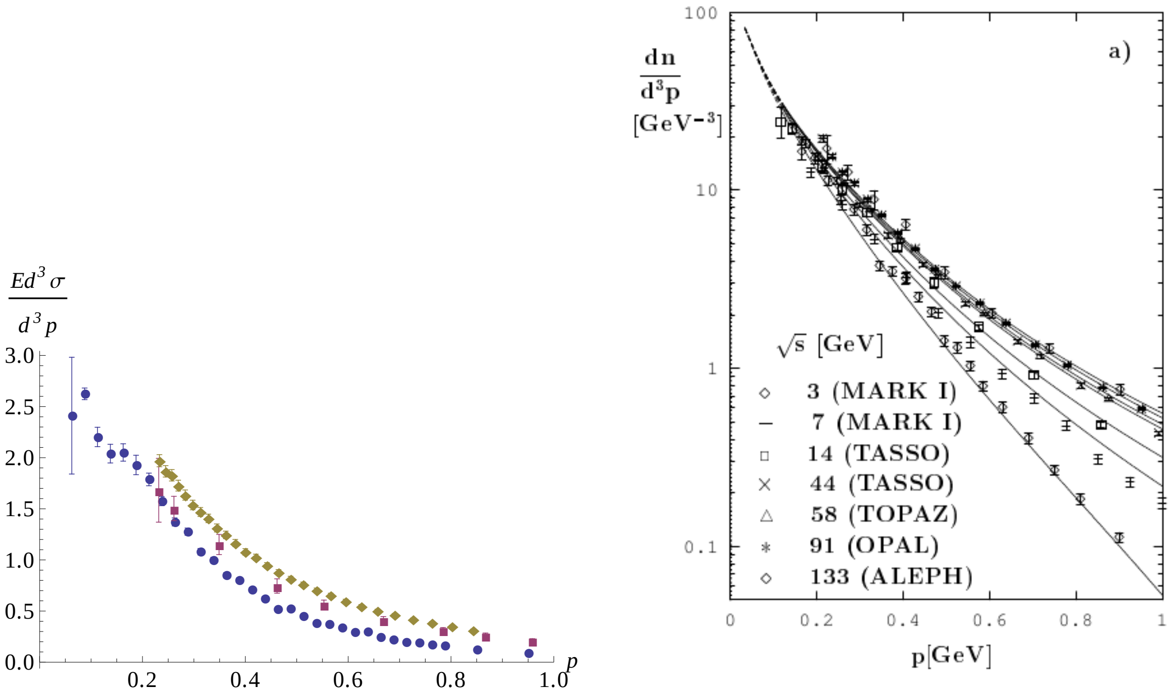

FIGURE 1.8 – La densité de pions chargés $\frac{1}{2}(\pi^+ + \pi^-)$ (à gauche, cercles=ARGUS [10 GeV], carrés=TOPAZ [58 GeV] et carreaux=OPAL [91 GeV]) et la densité des particules chargées $[(h^+ + h^-)/2]$ en collisions e^+e^- avec la comparaison avec les calculs MLLA [13].

De façon analogue à ce qui est obtenu pour les processus e^+e^-, le même calcul peut être effectué pour les collisions de deux protons (voir chapitre 3). Par conséquent, la limite d'impulsion nulle de la densité de particules en collisions pp et e^+e^- devrait différer par un coefficient donné par le rapport des facteurs couleur C_A/C_F.

Les limites des densités de particules ont été étudiées dans [13] et sont présentées dans la figure 1.9. A l'examen de la figure l'impression générale est que les points s'alignent avec l'horizontale avec des écarts par rapport à la valeur moyenne. Toutefois, en regardant les trois premiers points donnés par l'expérience BS auprès de l'ISR, nous remarquons plutôt une tendance à l'augmentation et c'est seulement la considération de toutes les énergies disponibles qui plaide en faveur de l 'indépendance vis-à-vis de l'énergie pour la limite d'impulsion nulle des spectres.

Dans le chapitre 7, nous effectuons les tests des prédictions théoriques associées au

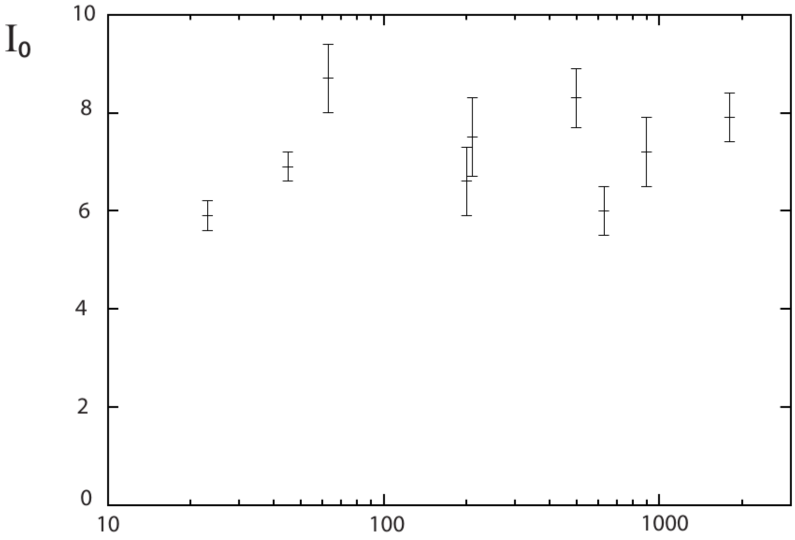

FIGURE 1.9 – Limite d'impulsion nulle I_0 des densités invariantes de particules chargées $[(h^+ + h^-)/2]$ en collision $p\,p$ à différente valeur de l'énergie dans le référentiel du centre de masse.

phénomène de cohérence de couleur discuté auparavant, à savoir :

1. La limite

$$I_0 = \lim_{p \to 0} E \frac{dN}{d^3p} \tag{1.4.1}$$

   est indépendante de l'énergie de collision, $\sqrt{s}$;

2. Le rapport des limites en collisions $p\,p$ et e^+e^- vaut

$$\frac{I_0^{pp}}{I_0^{ee}} = \frac{C_A}{C_F} = \frac{9}{4}. \tag{1.4.2}$$

Nous effectuerons une analyse systématique des données expérimentales disponibles pour les spectres de hadrons identifiés ($\pi^\pm$, $K^\pm$, $p\bar{p}$). La principale difficulté ici est de réaliser des ajustement de spectres et de les extrapoler au point $p = 0$. Par souci de cohérence nous allons effectuer l'étude en utilisant des fonctions d'extrapolation différentes, mais en comparant les résultats pour les différentes expériences avec la même fonction.

1.5 Assurance de la qualité des données

Les calorimètres électromagnétiques de l'expérience ALICE [24], le EMCal [17] et le PHOS [33], sont construits pour mesurer les coordonnées et l'énergie des photons et des électrons. Ces détecteurs ont une structure cellulaire et comprennent des *cellules* arrangées en blocs rectangulaires formant des (super)modules. Le détecteur EMCal est constitué de 10 supermodules de 24 × 48 cellules chacun, tandis que PHOS dispose de 3 modules de 64 × 56 cellules. L'énergie et la position des particules entrantes sont reconstruites à partir des amplitudes des signaux pour chaque cellule mesurées par l'électronique frontale (FEE).

La taille d'une cellule a été choisie de manière que l'énergie totale d'un photon ou d'un électron soit déposée dans un domaine formé par plusieurs cellules adjacentes, qui est appelé un *cluster*. Ainsi, le calorimètre résoud la gerbe électromagnétique. Un cluster avec son énergie et sa position dans le calorimètre représente la plus petite unité qui est intéressante pour une analyse physique.

Dans chaque événement de collision le fonctionnement du calorimètre peut être présenté comme une distribution de l'énergie sur une grille rectangulaire qui couvre une partie de l'angle solide autour du point de collision (voir Fig.1.10). Nous allons utiliser l'analogie d'un calorimètre et sa réponse avec celle d'un écran de télévision ou une caméra avec des pixels noir et blanc, l'énergie correspondant au niveau de gris.

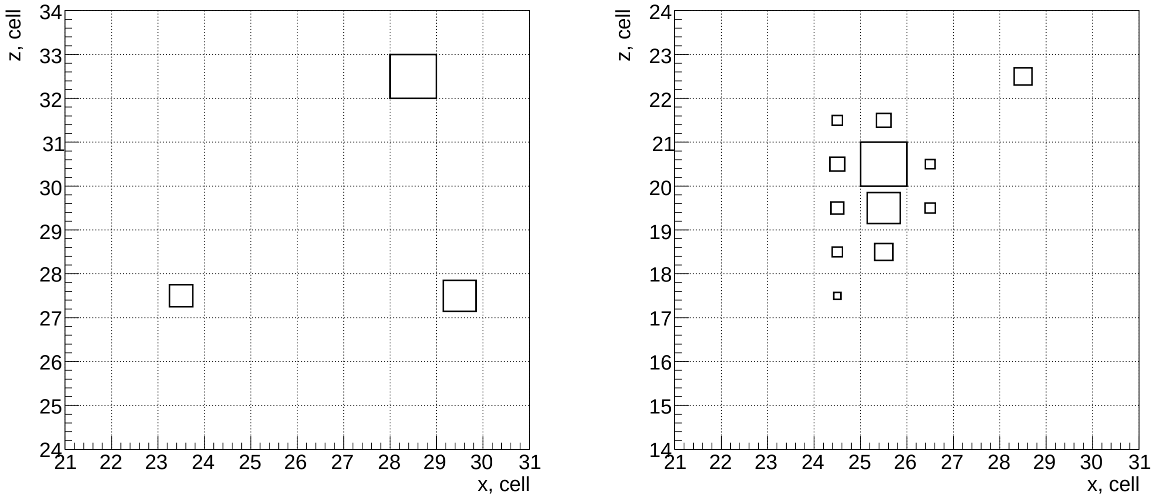

FIGURE 1.10 – Démonstration de cellules isolées avec énergie déposée (à gauche) et un clasteur (à droite).

Idéalement, la distribution en énergie enregistrée doit précisément correspondre à celle déposée par des photons et des électrons dans l'événement. Il est connu que plusieurs problèmes influencent la réponse du détecteur, par exemple, certaines cellules peuvent ne pas fonctionner, d'autres sont mal étalonnées. Ces défauts peuvent être classés en deux catégories :

1. ceux dont la présence est compatible avec une analyse de physique, qui peuvent être corrigés au stade d'analyse ;
2. ceux qui s'opposent à l'analyse physique, qui doivent être identifiés à un stade preliminaire, et dont la reconnaissance et le suivi entre dans un protocole d'assurance-qualité.

Pour PHOS et EMCal, les défauts qui entrent dans la deuxième catégorie comprennent les cellules muettes et bruyantes. Leur existence même dans un détecteur des particules peut s'expliquer par la grande complexité de chaque canal en comparaison avec un pixel d'écran, ainsi que des conditions d'exploitation parfois très exigeantes.

Un autre aspect qui doit être pris en compte est celui de l'évolution au cours du temps. Les données expérimentales recueillies sont accumulées de façon continuelle tout au long de l'année. Ainsi, les conditions sont amenées à changer légèrement. En outre, parfois une partie de l'équipement expérimental peut connaître une défaillance ou être tout simplement débranché si il n'est pas prêt pour la prise de données. Au moment de faire l'analyse physique, on doit être assuré que les données analysées sont “bonnes” dans le sens que le changement dans des conditions lors de la prise de données n'affecte pas les mesures physiques.

Une moyen standard pour s'assurer de la qualité des données est de diviser l'échantillon de données en plusieurs blocs, puis relever pour chaque bloc de données certaines quantités physiques élémentaires (par exemple le signal de référence pour PHOS et EMCal est le pic du méson π^0 reconstruit par masse invariante de deux particules). Les quantités physiques ne devraient pas changer d'un bloc à l'autre, et un bloc avec une trop grande déviation est considéré comme “mauvais” du point de vue de l'analyse physique et doit être enlevé. Les blocs naturels de données sont les *runs* qui constituent chacun un ensemble de données enregistrées dans les mêmes conditions (configuration du détecteur et du trigger, énergie du faisceau et luminosité, etc).

Faute d'une mire, nous utilisons le signal issu des collisions lui-même, le même que nous voulons analyser plus tard, pour vérifier le bon fonctionnement du calorimètre sur une base run par run. Lors d'une collision la probabilité d'illuminer une cellule donnée avec une particule d'une énergie donnée est presque indépendante de l'emplacement de la cellule (il n'y a aucune dépendance avec l'azimut et une légère dépendance avec la pseudorapidité), ainsi à long terme chaque cellule sera exposée à la même distribution d'énergie. Les canaux anormaux peuvent donc être identifiés en comparant les réponses des cellules. Dans la pratique, des quantités de base, telles que l'énergie moyenne ou l'occupation moyenne, fournissent de bons moyens pour l'identification des voies defectueuses, et ont l'avantage de ne nécessiter que peu de statistiques. Le chapitre d'assurance qualité est consacré à la proposition d'une méthode pour faire cette identification des mauvais canaux et sa mise en œuvre dans le contexte de l' assurance-qualité (AQ).

1.5.1 Mauvais canaux dans un calorimètre

Certaines cellules dans un calorimètre montrent une réponse anormalement basse par rapport aux autres. Ces dysfonctionnements des cellules influencent la réponse du détecteur en conduisant à une perte de signal et de ce fait en réduisant l'acceptance du détecteur. Un autre exemple de dysfonctionnement de cellules défectueuses se manifeste par un mauvais spectre d'énergie. L'analyse AQ proposée dans ce travail permet de découvrir ces cellules problématiques. Une comparaison des spectres d'énergie de cluster incluant et excluant les mauvaises cellules est représentée sur la figure 1.11 pour illustration. Le spectre montré à gauche est déformé par les canaux bruyants, et le graphique de droite montre le même spectre sans les mauvais canaux. La présence de canaux bruyants se manifeste clairement dans la forme irrégulière du spectre d'énergie.

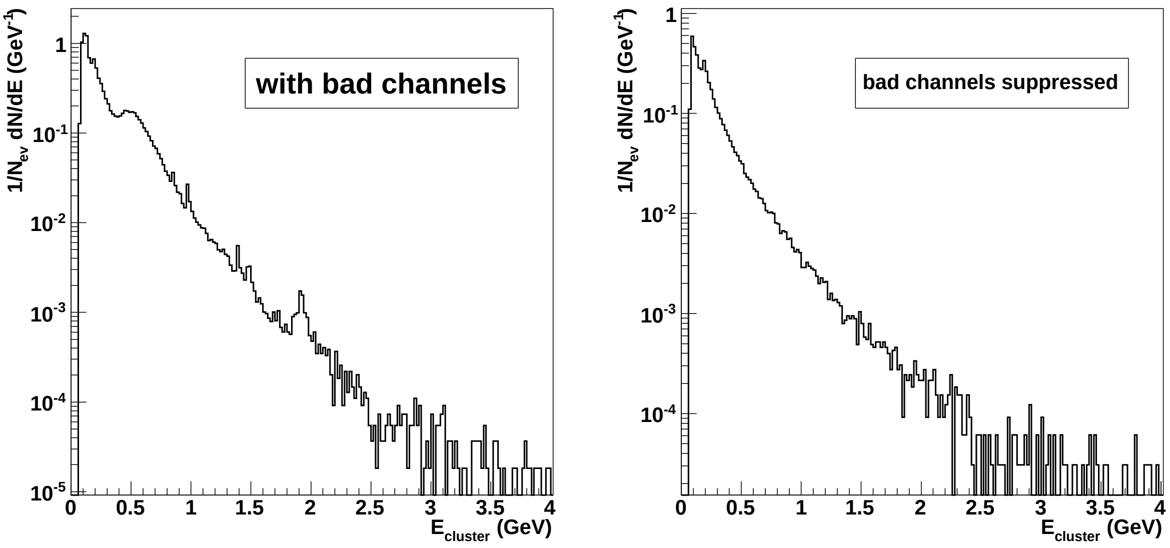

FIGURE 1.11 – Exemple de spectre d'énergie de cluster en présence des canaux bruyants dans un détecteur (à gauche) et avec les canaux bruyants supprimés (à droite).

Il est possible de classer les problèmes rencontrés et qui doivent être repérés par la tâche d'assurance qualité :

- Les canaux muets sont les canaux qui n'ont aucun signal. La raison la plus probable est une rupture de connexion électrique, une mauvaise configuration de la haute tension de polarisation, ou un photodétecteur cassé. Bien sûr, dans les prises de données de courte durée des canaux peuvent ne pas avoir la chance de détecter un signal à cause du manque de statistique. Le traitement AQ doit prendre en compte cette situation.

  L'importance de la prise en compte des canaux muets peut être expliquée de la façon suivante. Si une particule pénètre le calorimètre au voisinage d'une cellule muette, une partie de la gerbe électromagnétique qui tombe dans cette cellule muette n'est pas détectée, et, par conséquent, l'énergie totale déposée par la particule dans le calorimètre va être sous-estimée. Par conséquent, pour réduire l'influence des canaux muets dans le spectre d'énergie détecté, toutes les cellules muettes doivent être marquées et les clusters à proximité de ces canaux muetsnécessiteront un traitement spécial. Les canaux muets, ainsi que la région autour d'eux, conduisent à une réduction de l'acceptance du détecteur qui doit être prise en compte dans les simulations de Monte Carlo effectuées pour calculer l'efficacité de détection et la normalisation des spectres.
- Les canaux bruyants ont en commun avec les bons canaux qu'ils ont des signaux, mais les quantités physique associées à ces signaux révèlent des comportements anormaux par rapport aux autres canaux. Certains canaux peuvent être bruyants à cause d'une mauvaise configuration de cartes FEE, d'un mauvais réglage de la haute tension de polarisation des photodétecteurs qui peut conduire, à son tour, à

l'excitation anormale de la carte FEE ou à une décalibration des canaux.
La présence de canaux bruyants dans l'échantillon de données se révèle généralement par une distorsion des différents spectres d'énergie observés, et, en particulier, dans les distributions de masse invariante. Une des distortions de spectre parmi les plus communes est l'apparition de faux pics qui peuvent imiter les pics associés à la production d'une particule physique, mais avec des paramètres erronés, dont la présence peut aller jusqu'à obscurcir complètement le signal physique, si la fréquence de manifestation du bruit est plus grande que la fréquence des événements physiques. Les canaux bruyants gênent pour cette raison plus particulièrement la recherche des signaux rares avec un très faible rapport du signal sur le bruit de fond. En guise d'illustration, une distorsion sévère peut être observée dans la masse invariante de paires de particules sur la figure 1.12 qui montre le pic du π^0 attendu à la masse invariante de 135 MeV/c^2, mis en évidence par une ligne bleue, avec un faux pic à la masse invariante de 250 MeV /c^2, représenté par une ligne rouge. Cet exemple obtenu à partir des données réelles montre comment les canaux bruyants peuvent affecter les mesures physiques.

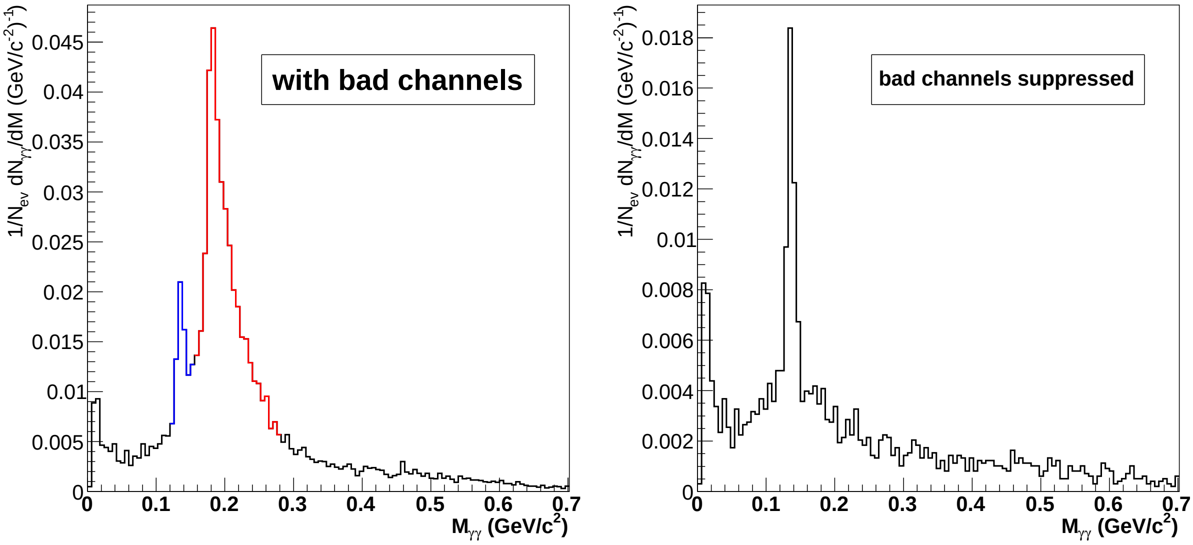

Figure 1.12 – Exemple d'une distribution de masse invariante en présence de canaux bruyants (à gauche) et après leur suppression (à droite).

L'évaluation de la qualité des données comporte plusieurs étapes. À la première étape, nous sélectionnons les candidats de canaux invalides, en d'autres termes, les cellules qui présentent un comportement très anormal. Lors de la deuxième étape, nous traitons chaque candidat pour comprendre précisément la cause du problème. A ce stade, il est possible de révéler les “vrais” canaux défectueux et leur donner un diagnostic précis.

L'analyse proposée est destinée à différents utilisateurs. D'une part, il est important d'avoir un diagnostic précis pour chaque canal afin de lui donner un traitement approprié au niveau du matériel. En conséquence cette analyse doit pouvoir être utile aux électroniciens (étape 2 : sélection des canaux véritablement mauvaiss parmi les candidats). D'autre part, notre objectif principal est de mesurer les observables de physique, et, par conséquent, cette analyse doit servir aux physiciens. Pour eux, il suffit de s'arrêter à l'étape 1 (sélection des candidats) et simplement ignorer les cellules problématiques au niveau de l'analyse. Pour l'analyse, la tendance est d'avoir une seule liste de cellules à ignorer pour un échantillon de données le plus volumineux possible, puisque chaque changement de la liste des mauvais canaux nécessite de recalculer l'acceptance et l'efficacité du détecteur. En outre, diviser l'échantillon de données en plusieurs sous-ensembles limite la gamme accessible en p_T, ce qui est une raison encore plus forte pour garder une liste des mauvaises cellules figée pour l'échantillon de données le grand possible.

On peut se poser une question importante : à quel niveau voulons-nous nettoyer notre signal ? D'une part, nous voulons supprimer les canaux très bruyants, d'autre part, chacun des canaux bruyants recueille également un signal physique, que nous aimerions éviter de perdre. Si nous ne supprimons pas les mauvais canaux, le signal de physique risque de ne pas être visible. Si nous en supprimons trop, l'acceptance du détecteur deviendra trop petite, et nous ne verrons pas le signal physique non-plus. Pour ces raisons, l'exclusion des mauvais canaux est une affaire de compromis.

Energie des cellules et des clusters

La quantité de base dans l'analyse est l'énergie mesurée par une cellule i dans un événement k, notée E_k^i. La conversion en énergie à partir du signal brut requiert plusieurs étapes, en particulier, au niveau de l'électronique frontale (carte FEE).

Dans un événement l'énergie est distribuée sur des groupes de cellules adjacentes. Un groupe de cellules avec des côtés communs s'appelle un cluster (voir Fig. 1.10 à droite.) Un cluster est caractérisé par son énergie, qui est la somme des énergies déposées dans les cellules appartenant au cluster.

L'énergie d'une cellule du calorimètre devient physiquement pertinente quand elle est bien au-dessus du bruit FEE intrinsèque. Le bruit intrinsèque a été estimé au moment de la conception du détecteur et plus tard mesuré dans les mesures de piédestaux pour chaque canal. Un écart-type de la distribution des piédestaux dans les calorimètres ALICE, exprimé en unité d'énergie, est d'environ 15 MeV dans EMCal et 2 MeV dans PHOS. Pour être insensible à des fluctuations de piédestal, un seuil d'amplitude sur la cellule est programmé dans la carte FEE. Cette énergie minimum pour une cellule $E_{\rm min}^{\rm cell}$ a été fixée à 3 écarts-types des distributions de piedestaux, soit 45 MeV et 6 MeV, dans EMCal et PHOS respectivement. Prenant en compte la présence du seuil nous obtenons

$$E^i = \begin{cases} E^i & \text{if } E^i > E_{\rm min}^{\rm cell} \\ 0 & \text{if } E^i \leq E_{\rm min}^{\rm cell} \end{cases} \tag{1.5.1}$$

Les clusters sont formés à partir de cellules lors de la procédure de reconstruction en exigeant qu'un cluster doit comporter au moins une cellule dont l'énergie dépasse un seuil cluster $E_{\rm min}^{\rm clu}$ (voir, par exemple [7]). Ce seuil peut varier d'une phase de reconstruction à une autre, et en 2010 il a été fixé à 100 MeV pour EMCal et 50 MeV pour PHOS. On note que des cellules isolées bruyantes peuvent relever des énergies supérieures au seuil-cellule $E_{\mathrm{min}}^{\mathrm{cell}}$ et rester en dessous du seuil-cluster $E_{\mathrm{min}}^{\mathrm{clu}}$.

1.5.2 Maximum local

La taille des cellules des deux calorimètres a été choisie pour être inférieure au rayon de Molière dans les matériaux du calorimètre. Lorsqu'une gerbe se développe le long de l'axe de la cellule, la plus grande partie, 80-90 %, de l'énergie de la gerbe est déposée dans une cellule. Dans un cluster, il y a toujours une cellule qui transporte plus d'énergie que ses voisines. Cette cellule est appelée un maximum local (ML). Il existe des situations ou plus d'un maximum local peuvent apparaître dans un cluster, par exemple, lorsque deux gerbes se chevauchent. Lorsque deux maxima locaux, ou plus, sont présents dans un cluster, tous les maxima sont conservés dans l'analyse (voir l'équation (1.5.2) et (1.5.3)).

La raison pour se concentrer sur les cellules ML plutôt que sur toutes les cellules dans un cluster est la suivante. Imaginez une cellule bruyante qui donnent régulièrement une réponse à 200 MeV. En conséquence toutes les cellules voisines dès qu'elles dépassent la valeur de $E_{\mathrm{min}}^{\mathrm{cell}}$ seront considérées comme faisant partie d'un cluster, à un taux anormalement plus élevé que celui d'une cellule typique. La considération des cellules correspondant à un maximum local dans l'événement permet de contourner ce problème.

1.5.3 Quantités de base : énergie totale et nombre d'événements

Dans notre analyse, nous allons associer quatre quantités à une cellule. Tout d'abord, nous cumulons sur l'ensemble des données l'énergie recueillie par chaque cellule i lorsque celle-ci est un maximum local dans un cluster

$$E_{\mathrm{tot}}^{i} = \sum_{k|i \quad \text{est ML dans } k} E_{k}^{i}. \tag{1.5.2}$$

La deuxième valeur est le nombre cumulé d'événements où une cellule i est apparue comme un maximum local dans un cluster

$$N_{\mathrm{tot}}^{i} = \sum_{k|i \text{ est ML dans } k} N_{k}^{i}, \tag{1.5.3}$$

où N_k^i vaut 1 si la cellule i est un maximum local dans un cluster pour l'evénement k, et 0 sinon. Enfin, comme la quantité de clusters de basse énergie est exponentiellement plus grande que la quantité de celles de haute énergie, il est utile de séparer la gamme d'énergie en deux régions, une région de basse énergie et une région de haute énergie :

1. $E_k^{i\ (\mathrm{low})} = E_k^i$ si 0.3 GeV $\leq E_k^i <$ 1 GeV, et 0 dans le cas contraire ;

2. $E_k^{i\,(\mathrm{high})} = E_k^i$ si $E_k^i \geq 1$ GeV, et 0 sinon.

Ce fractionnement permet de couvrir une grande gamme d'énergie, de la centaine de MeV à la centaine de GeV, tout en évitant, pour des raisons de consommation de mémoire, un partitionnement serré de l'ensemble de la gamme. Dans la gamme de basse énergie, une étude détaillée du spectre d'énergie pour chaque cellule est possible grâce à une quantité suffisante de données. Dans la région d'énergie élevée une partition comportant de grands intervalles est suffisante pour découvrirles cellules comportant un taux de réponse anormalement élevé de cellules. Une cellule fonctionnement normalement doit montrer un bon spectre dans la gamme de basse énergie et éventuellement des très rares signaux dans la gamme de haute énergie.

Le seuil bas en énergie doit être choisi de telle façon à être le même que celui prévu dans l'analyse de physique. Il peut être fixé à 300 MeV, qui est un choix naturel pour se concentrer sur les gerbes électromagnétiques et ignorer le signal des particules au minimum d'ionisation (PMI), dont l'énergie déposée varie dans la plage de 230 à 270 MeV pour les calorimètres d'ALICE.

1.5.4 Evaluation de la qualité des runs

Comme on l'a déjà indiqué, les conditions physsiques de la prise de données et le fonctionnement du détecteur peuvent évoluer avec le temps. En particulier, la liste des mauvais canaux peut changer si différents modules du détecteur tombent en panne avant d'être par la suite réparés. Pour contrôler cette évolution à long terme il faut étudier la variation de quantités physiques de base au cours du temps, qui sont considérés comme des *trend plots*. Un *run* représentant une unité naturelle pour l'échantillonnage des données, les courbes de tendance peuvent être montrées en fonction de la numérotation des runs, ou *run index*. Elles peuvent également être affichées en fonction du nombre d'événements accumulés.

Dans nos études, nous avons constaté que six observables de base permettent une caractérisation relativement complète de l'évolution à long terme de la propriétés des calorimètres :

1. l'énergie moyenne des clusters ;
2. le nombre moyen de clusters par événement ;
3. le nombre moyen de cellules par cluster reconstruit ;
4. la position du pic du π^0 ;
5. la largeur du pic du π^0 ;
6. le nombre moyen de π^0 reconstruits par événement.

Ces observables partagent la propriété de toutes être formées à partir des objets physiques reconstruits dans les calorimètres : les clusters et les mésons π^0. Par commodité, nous appelons les critères 1 à 3 des moyennes de cluster et les critères de 4 à 6 les moyennes de π^0. Les critères de sélection pour les clusters et les π^0 doivent être de préférence les mêmes que ceux utilisés dans l'analyse physique. Par exemple pour une analyse π^0 avec

PHOS, les seuls clusters retenus pour les courbes de tendance sont ceux constitués de trois cellules et plus avec une énergie du cluster > 0.3 GeV.

Le point clé au cours de l'évaluation de la qualité est la surveillance en vue du repérage des écarts importants dans les courbes de tendance des observables physiques mentionnées ci-dessus. Nous allons montrer que la présence de canaux défectueux est une source de tels écarts dans les courbes de tendance. Nous montrerons aussi que certains écarts ne peuvent pas être attribués à des mauvais canaux. Les conditions globales de fonctionnement du LHC ou d'Alice peuvent également être responsables des écarts dans les courbes de tendance. Par conséquent, dans le paragraphe suivant, nous nous concentrerons d'abord sur l'effet des mauvaises voies, avant de décrire l'effet des conditions globales de fonctionnement. À la suite de l'analyse des tendances, des mauvaises voies sont identifiées et une liste des séries de données exploitables est créée qui peut être utilisée pour l'analyse de physique. Nous montrerons aussi que certaines périodes identifiées comme mauvaises peuvent être récupérées et devenir de bons runs lorsque les écarts peuvent être expliqués.

Dans une première itération de l'analyse AQ, nous partons des données brutes, sans élimination des canaux défectueux. La moyenne de l'énergie des clusters, le nombre moyen de clusters par événement et le nombre moyen de cellules par cluster sont présentés dans la figure 1.13. Les moyennes de cluster sont très sensibles au bruit des cellules du calorimètre. Il peut arriver que la présence d'un seul canal bruité dans un module déplace une valeur moyenne pour ce module particulier. Une telle situation apparaît, par exemple, dans la forte déviation observée entre les index 40 et 60 dans chacun des trois histogrammes. De toute évidence, ce phénomène est apparu en raison de problèmes dans le module numéro 2 (ligne bleue). En effet, les lignes des autres modules montrent des comportements plus réguliers. Une deuxième irrégularité par ordre d'importance se manifeste entre les index 80 et 100 dans le nombre moyen de clusters par événement.

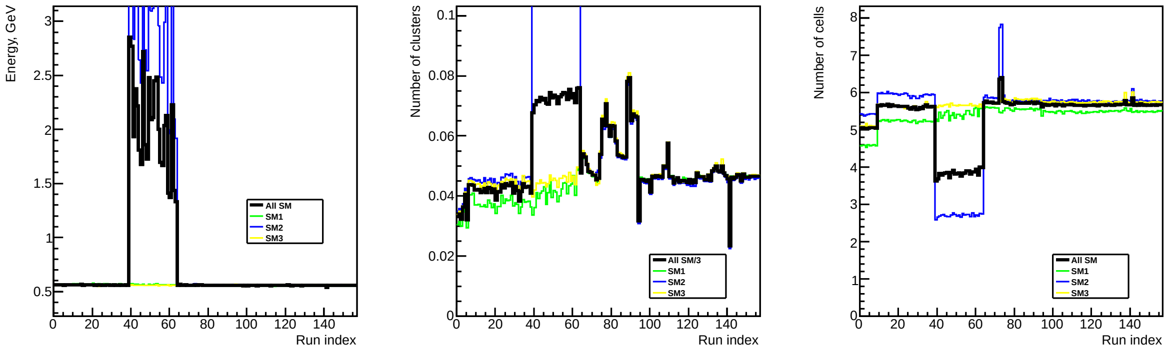

FIGURE 1.13 – Moyenne de cluster.

1.5.5 Moyennes de π^0.

Le méson π^0 est détecté via sa désintégration en deux photons. La distribution de masse invariante est formée à partir de toutes les paires de cluster reconstruites dans le calorimètre. La masse invariante M de la paire de clusters supposés correspondre à des photons avec quadri-impulsions p_1 et p_2 est donnée par l'équation

$$M^2 = (p_1 + p_2)^2. \tag{1.5.4}$$

Le spectre de masse invariante est ajusté par la fonction de Crystal Ball [34] décrivant le pic à laquelle est ajoutée un polynôme du second degré pour décrire le bruit de fond. La fonction de Crystal Ball est définie par

$$f(x, N, m, \sigma, \alpha, n) = N \begin{cases} \exp\left(-\frac{(x-m)^2}{2\sigma^2}\right), & \text{pour } \frac{x-m}{\sigma} > -\alpha \\ A \cdot \left(B - \frac{x-m}{\sigma}\right)^{-n}, & \text{pour } \frac{x-m}{\sigma} \leq -\alpha \end{cases} \tag{1.5.5}$$

où x représente la variable masse invariante et

$$A = \left(\frac{n}{\alpha}\right)^n \cdot \exp\left(-\frac{\alpha^2}{2}\right), \qquad B = \frac{n}{\alpha} - \alpha, \qquad \alpha > 0. \tag{1.5.6}$$

La queue exponentielle à petit x est introduite pour tenir compte de la perte d'énergie par bremshtrahlung des électrons et positrons. Le polynôme du second degré est paramétrisé selon

$$P(x, a_0, a_1, a_2) = a_0 + a_1\,(x - 0.135) + a_2\,(x - 0.135)^2\,. \tag{1.5.7}$$

La figure 1.14 montre un exemple d'extraction du π^0 dans un run. Le méson π^0 se manifeste par un pic très net à la masse $M = 0.135$ GeV/c^2. La fonction polynomiale (ligne bleue) et le polynôme avec la fonction Crystal Ball superposée (ligne rouge) sont indiquées illustrant les capacités de la procédure automatique effectuée dans chaque itération de l'analyse afin d'obtenir les valeurs moyennes de π^0. Pour faciliter la procédure d'ajustement, seules les paires de cluster avec une impulsion transverse $p_T > 0.6$ GeV/c sont prises en compte.

La procédure d'ajustement donne les paramètres de reconstruction des π^0 de la façon indiquée ci-dessus : la position et la largeur du pic des π^0 correspondent aux paramètres M et σ de l'ajustement, et le nombre moyen de π^0 reconstruits par événement est obtenu à partir de l'intégrale de la fonction Crystal Ball. La position du pic des π^0 est une mesure permettant l'étalonnage absolu du calorimètre, tandis que la largeur du pic est une mesure de la dispersion de cet étalonnage de cellule à cellule, largeur qui peut être en partie diminuée par une recalibration des cellules. La figure 1.15 montre la position reconstruite du pic de masse invariante et la largeur pour notre échantillon avec les mauvaises voies exclues. Il n'y a pas de changement notable pour ces observables avant ou après l'exclusion des mauvaises voies, car la présence de ces dernières affecte principalement le bruit. Nous observons que la seconde moitié de la prise de données est plus régulière que la première moitié.

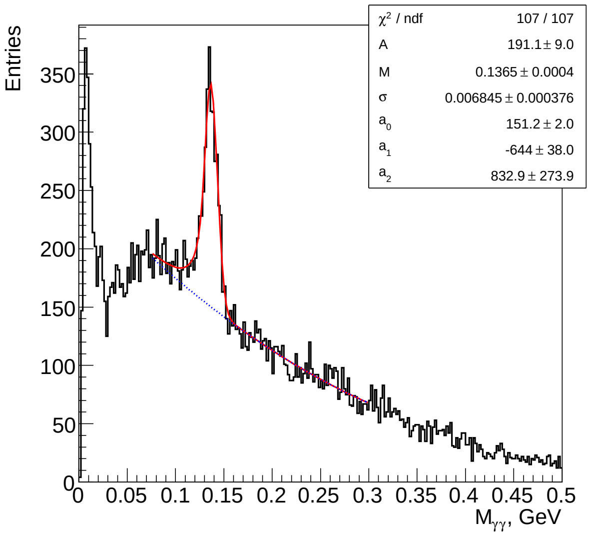

FIGURE 1.14 – Spectre de masse invariante de toutes les paires de $\gamma\gamma$ avec impulsion transverse de la paire supérieure à 0,6 GeV/c. Le pic très net est visible. Il est correctement ajusté par la fonction Crystal Ball ajoutée à un polynôme du second degré (ligne rouge). La ligne bleue représente le fond déterminé par ce polynôme du second degré.

Le nombre moyen des π^0 reconstruits est le dernier mais pas le moins important des critères de l'assurance-qualité des données. La reconstruction des π^0 est une activité standard pour les calorimètres électromagnétiques à cause de sa grande section effice, et, par conséquent, sa facilité de réalisation même avec peu de statistiques dans un run. Un autre avantage de la reconstruction des π^0 dans les collisions *pp* au LHC, par rapport aux autres processsus physiques détectés par les calorimètres, est la qualité du signal dans le spectre de masse invariante avec un fond relativement faible. Enfin, le spectre de π^0, à la différence du spectre inclusif de clusters, est beaucoup moins affecté par des incertitudes dans l'identification des particules, et est donc moins influencé par le changement des conditions de bruit. Avec tous ces avantages, la désintégration $\pi^0 \to \gamma\gamma$ est couramment utilisée comme un signal de référence pour l'étalonnage de l'échelle d'énergie des calorimètres. D'autres signaux de référence sont également pris en considération pour l'étalonnage, comme les électrons célibataires ou les processus $\eta \to \gamma\gamma$ ou $Z^0 \to e^+e^-$. Cependant, ces procédés nécessitent de bien plus grandes statistiques accumulées et une meilleure résolution spatiale. Pour les calorimètres ALICE, EMCal et PHOS, ces procédés ne peuvent pas être utilisés pour l'étalonnage et encore moins pour la démarche assurance-qualité, en raison du manque de statistique.

Le nombre de π^0 reconstruits est extrait de l'analyse de masses invariantes reconstruites pour chaque run (Fig. 1.14). La courbe de tendance pour l'échantillon de données de l'étude est représentée sur la figure 1.16. On peut voir que l'écart entre les index 80 et 100, que nous avons déjà observé dans les moyennes de cluster (Fig. 1.13) est aussi présente sur cette observable.

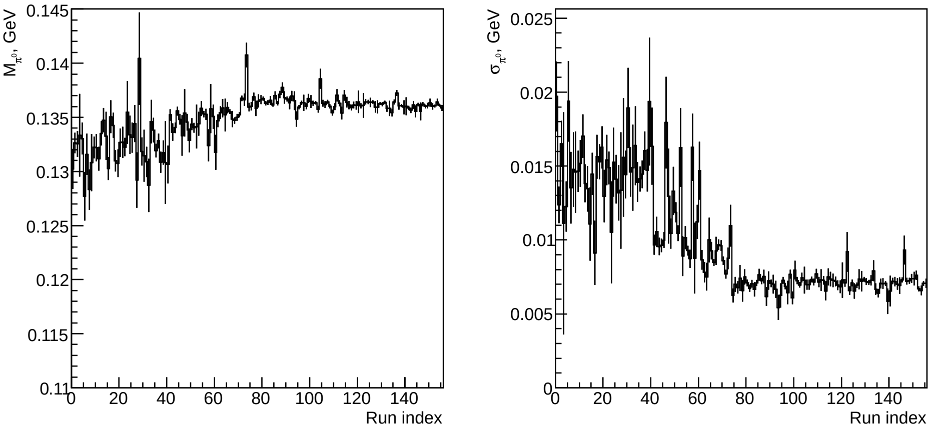

FIGURE 1.15 – Masse et largeur des π^0 en excluant les mauvaises cellules.

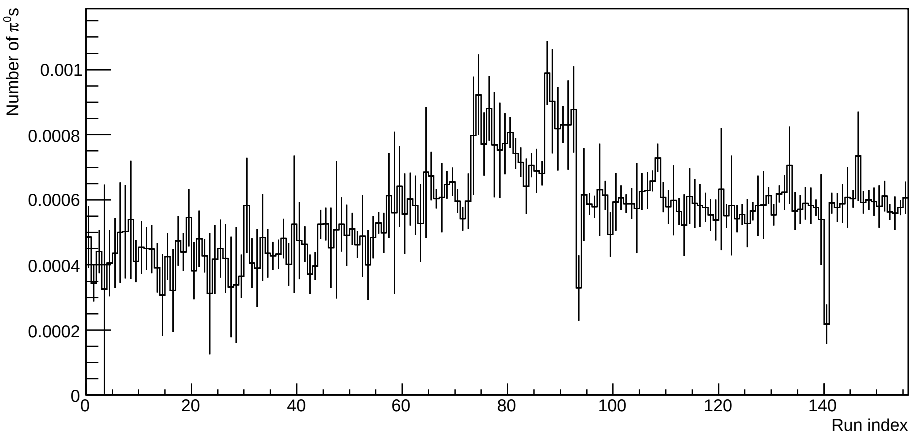

FIGURE 1.16 – Nombre moyen de π^0 par événement en excluant les mauvaises cellules.

1.5.6 Conclusion

Dans ce chapitre, nous avons démontré l'importance de l'assurance-qualité des données en vue de l'analyse physique, et avons donné quelques exemples de l'effet de la présence de mauvaises voies dans un calorimètre sur les observables physiques. Plusieurs paramètres caractéristiques ont été jugés adéquats pour l'identification des mauvaises voies, permettant d'évaluer la qualité des canaux dans chaque lot de données. L'identification des mauvais canaux a fait l'objet d'une analyse quantitative, avec une formulation stricte des critères utiles pour discriminer les bons et des mauvais canaux. D'autres critères peuvent être appliqués pour la recherche de mauvais canaux lorsqu'on peut faire l'analyse sur l'ensemble des données complet. La qualité des canaux et son évolution dans le temps au sein de l'ensemble des données ont un impact direct sur la qualité des observables produites. D'une part, l'identification et la suppression des canaux défectueux permettent un comportement uniforme des observables de physique sur l'ensemble des données. D'un autre côté, les écarts dans les courbes de tendance de certaines observables physiques sont indiquent soit une suppression incomplète des mauvais canaux dans certains lots de données, soit des changements dans les conditions globales de fonctionnement.

Un logiciel a été développé pour l'identification et la visualisation des mauvais canaux permettant de fournir un accès facile à la qualité des données utilisées pour l'analyse physique. Ce logiciel possède une architecture modulaire qui permet de l'appliquer aux deux calorimètres ALICE, EMCal et PHOS, mais il peut aussi être facilement transposé pour d'autres calorimètres électromagnétiques dans d'autres expériences. Ce progiciel a été mis en œuvre dans le cadre de l'analyse standard de l'expérience ALICE, et il constitue maintenant une partie des procédures officielles d'assurance-qualité utilisées à chaque fois que les données sont reconstruites.

L'approche pour l'évaluation de la qualité des données que nous avons développée a été largement utilisée pour l'analyse de EMCal et de PHOS avec les données collectées dans les collisions proton-proton et plomb-plomb prises en 2010 et 2011. Grâce à cette approche, la stabilité et la bonne qualité des résultats obtenus dans l'analyse des données a pu être assurée. Cette approche a fait l'objet d'une note d'analyse interne d'ALICE [].

1.6 La production de particules de bas energie et les prédictions théoriques.

L'étude de la production de particules multiples en collisions à haute énergie peuvent fournir des informations précieuses sur les caractéristiques du processus partonique de branchement et après parton-à-hadron transition en QCD. Le parton processus de branchement en QCD est causée par quarks et de gluons bremstrahlung qui devient singulier dans la limite d'émission de bas energie ou émission colinéaire. Calculs analytiques dans le rapprochement double logarithmique (DLA) (voir le chapitre 3) permettent de faire la somme des contributions de ces singularités. Le sujet le plus délicat dans la production multiparton à haute énergie est le schéma hadronisation soi-disant, en d'autres termes, la transition de couleur partons à hadrons incolores. Actuellement, il n'existe pas de recette communément acceptée pour cette conversion, en particulier parce que le processus hadronisation, est régi par les forces de confinement de la couleur, n'est pas accessible à la théorie des perturbations. En conséquence, toute application d'un cadre donnant des prédictions observables à multiparticulaires nécessite des hypothèses supplémentaires. L'approche la plus simple consiste à s'appuyer sur les ressemblances entre hadrons et parton spectres, la soi-disant locale Parton-dualité de hadrons (LPHD), introduit dans [4] et soutenu expérimentalement []. L'hypothèse suppose que LPHD observables suffisamment inclusives au niveau hadronique sont directement fournies par les observables correspondantes calculées pour la cascade parton. L'un des succès impressionnants de cette approche était la prédiction de la forme en dos d'âne de la distribution de l'énergie des particules exprimée en termes de la variable $\xi = \ln \frac{E_{jet}}{E}$ pour les particules de l'énergie E dans un jet d'énergie E_{jet}, la soi-disant à bosse plateau, discuté dans le chapitre 3.

Dans le présent chapitre, nous nous concentrons sur les propriétés des quarks et de gluons mous bremstrahlung en consultant le comportement dynamique des spectres de faible production inclusive de hadrons. Selon le calcul DLA (voir le chapitre 3), la densité de particules dans la limite impulsion zéro devient indépendante de l'énergie de collision et proportionnels aux facteurs de couleurs C_A ou C_F, en fonction de la couleur de charger primaire recul du point de collision.

Dans le chapitre 3, la figure 1.5 montré les données pour une large gamme d'énergies cms pour les productions de particules chargées présentés ainsi que les prévisions MLLA prises de []. L'élément remarquable est que, avec crises que nous voyons clairement la tendance de convergence pour tous les spectres dans la limite de bas impulsion. L'examen détaillé des valeurs obtenues, les données du LEP peut toutefois tendance à montrer des valeurs limites 20 % de plus de données de plus basses énergies.

La figure 1.8 peut aider à obtenir une vision plus précise de la situation. Elle montre la densité invariante pion chargé, Ed^3N/d^3p, en fonction des quantités de mouvement de la particule p, à des énergies différentes allant de l'énergie de DORIS à 10 GeV à LEP cms énergie à 91 GeV. D'abord la multiplication par E contribue à limiter le range de variation à un ordre de grandeur en amplitude et en secondes de l'échelle linéaire à gauche aide interroger comment la limite est atteint, par exemple, linéaire ou quadratique, et de voir que cela peut ne pas être une tâche simple à effectuer l'extrapolation appropriée pour $p = 0$. Dans la figure de gauche de la jonction entre le LEP et des données énergétiques inférieurs est difficile de décider, même si une diminution du rapport entre le LEP/OPAL (diamants pleins) et ARGUS (cercles pleins) peut être prévu, et confirmé lors de la recherche à la parcelle échelle logarithmique sur la droite. Également en ce qui concerne la question de l' extrapolation à $p = 0$, mentionnons que les spectres identifié peut aider à mieux distinguer les éventuels effets de masse des hadrons.

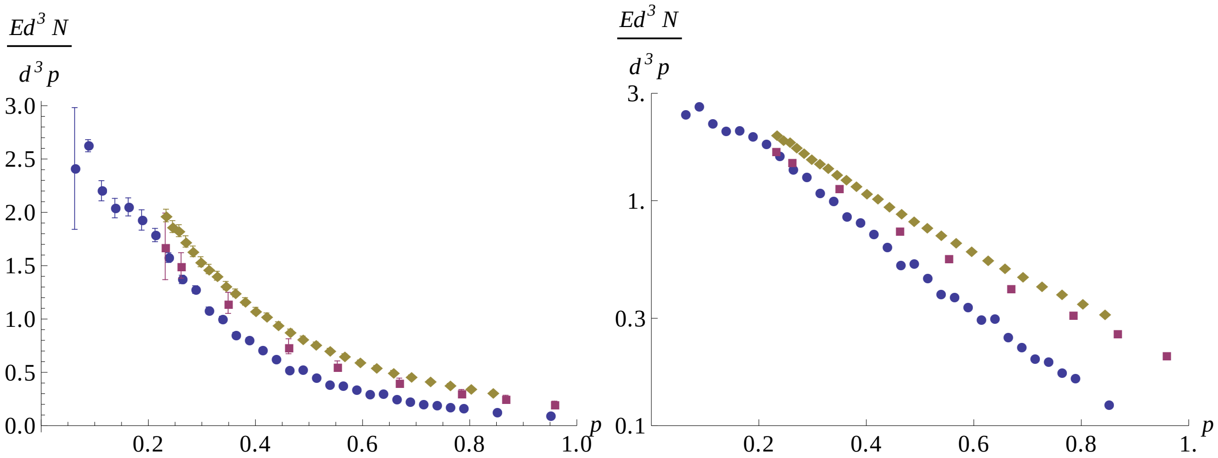

FIGURE 1.17 – La densité inclusive de pions chargés $\frac{1}{2}(\pi^+ + \pi^-)$ en e^+e^- collisions : échelle linéaire (à gauche) et de l'échelle log (droite). Les données sont tirées d'ARGUS (10 GeV), TOPAZ (58 GeV) et OPAL (91 GeV).

En analogie avec processus e^+e^-, la même quantité peut être étudiée [11] pour les collisions de deux protons (voir le chapitre 3). Les résultats de deux mesures sont affichées sur la figure 1.18. En regardant de près la log-terrain, nous prévoyons que le résultat dépend de la façon dont les données seront extrapolées. Dessiner une ligne droite mènerait à la conclusion d'un accroissement du limite $p_T \to 0$, tandis que si certains de nivellement est supposé l'indépendance énergétique de cette limite ne peut être exclue.

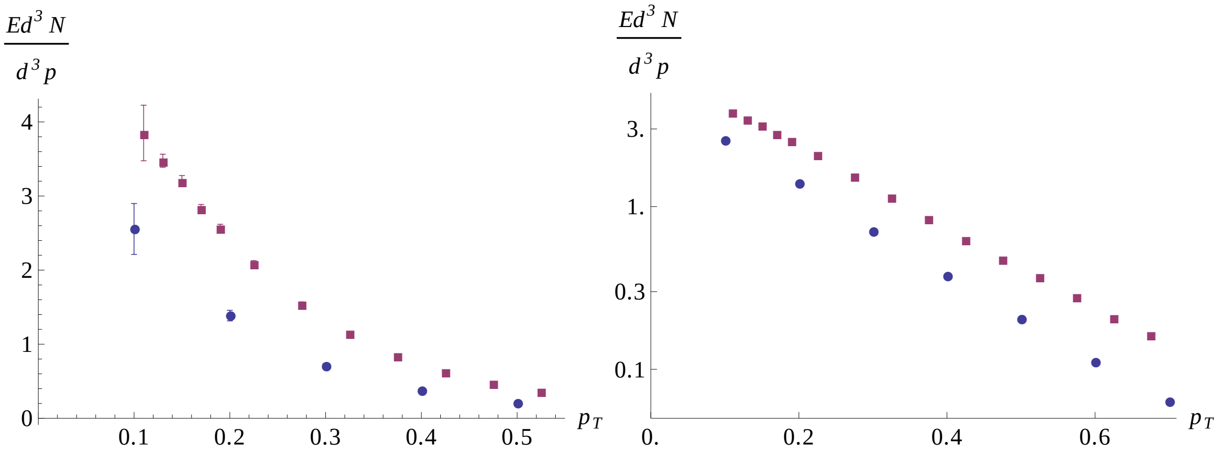

FIGURE 1.18 – La densité des pions chargés $\frac{1}{2}(\pi^+ + \pi^-)$ dans $p\,p$ collisions : échelle linéaire (à gauche) et une échelle logarithmique (à droite). Les données proviennent de BS (23 GeV) et ALICE (900 GeV).

Résultats pour les limites de la densité de particules dans $p\,p$ collisions

$$I_0 = \lim_{p \to 0} E \frac{d^3 N}{d^3 p} \tag{1.6.1}$$

ont été obtenues dans [11] et sont présentés dans la figure 1.19. Aprés l'examen de cette figure nous avons l'impression générale de points aligns avec des écarts au hasard autour de la valeur moyenne. Cependant, en regardant les trois premiers points, donnés par l'expérience ISR, nous avons pu remarquer plutôt tendance à augmenter, et que l'examen de toutes les énergies disponibles parle en faveur de l'indépendance de l'énergie de collision de la limite douce. Les résultats assez impressionnants affichés dans la figure 1.19. Parle en faveur d'une explication de la production à faible dynamique entraînée par couleur cohérence a été le déclencheur à d'autres investigations, en particulier d'étendre l'étude pour englober les énergies du LHC, tel que réalisé dans le présent chapitre.

Plus précisément, nous testons les prédictions théoriques pour la physique hadronique de bas impulsion tel que discuté précédemment, à savoir :

1. La limite
$$I_0 = \lim_{p \to 0} E \frac{dN}{d^3 p} \tag{1.6.2}$$
est indépendant de l'énergie de collision primaire $\sqrt{s}$.
2. Le rapport
$$\frac{I_0^{pp}}{I_0^{ee}} = \frac{C_A}{C_F} = \frac{9}{4}. \tag{1.6.3}$$

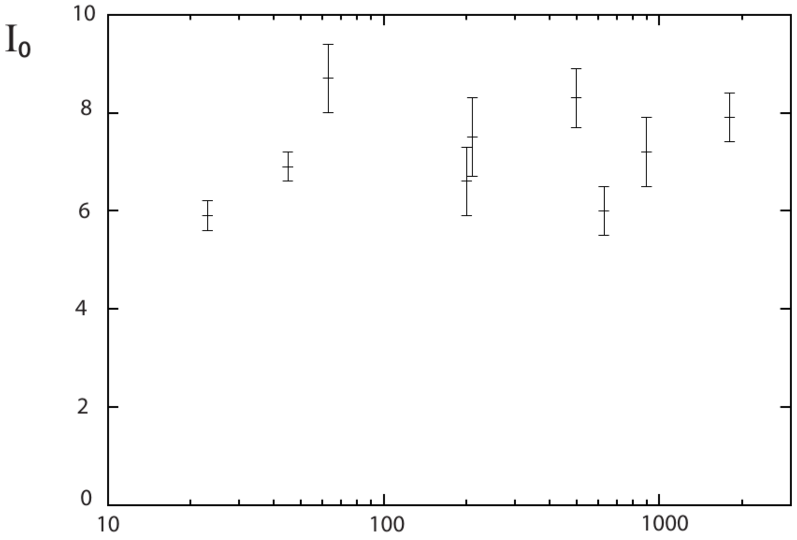

FIGURE 1.19 – Limites de bas impulsion I_0 de densités invariantes de particules chargées $[(h^+ + h^-)/2]$ dans collisions $p\,p$ en fonction de la CMS d'énergie $\sqrt{s}$ [11].

Nous essayons de donner quelques systématique à l'analyse de certaines des données expérimentales disponibles pour les spectres de hadrons identifié ($\pi^{\pm}$, $K^{\pm}$, $p\bar{p}$). Cette phenomenologigy sera discuté dans la section 1.7. La principale difficulté sera d'effectuer des accès de spectres et de les extrapoler à $p = 0$ point. Cette question est abordée dans la section 1.4. Nous avons découvert cela et expliquer que, pour la cohérence de l'extrapolation peut être faite en utilisant les fonctions d'extrapolation différentes, mais les résultats de différentes expériences devraient être donnés et comparés pour une seule et même fonction.

1.7 L'extrapolation des spectres à point de zéro impulsion

1.7.1 Stratégie générale

Dans la présente section, nous examinons différentes façons de montage et l'extrapolation des données expérimentales. L'objectif de l'étude est de mieux cerner les différences entre les différents modèles (fonctions de montage) et les meilleures données expérimentales disponibles, puis, dans la section 1.8, utiliser certains des modèles pertinents pour extraire les quantités d'intérêt.

L'observable de base est de $E\frac{d^3N}{d^3p}$ qui est mesurée en cas de e^+e^- en fonction de la dynamique des particules total p et, dans le cas de $p\,p$ collisions en tant que fonction de la quantité de mouvement des particules transversal p_T et rapidité y, à $y = 0$. Ainsi, selon le cas, soit nous besoin d'une fonction d'ajustement $f(p)$ ou $g(p_T, y = 0)$ simplement notée $g(p_T)$.

Toutefois, la section invariante $E\frac{d^3N}{d^3p}$ n'est pas la valeur qui a été mesurée directement dans l'expérience. Habituellement, la quantité mesurée est soit le spectre de la production $\frac{dN}{dp}$ ou la section efficace différentielle $\frac{d\sigma}{dp}$, ce qui peut être transformé en spectre de production en divisant par le section efficase inélastique. Pour éviter la difficulté d'erreurs recalculer, nous nous situons directement la quantité qui a été mesuré expérimentalement, puis effectuer les opérations mathématiques nécessaires pour obtenir la section invariante souhaitée.

La procédure d'ajustement des spectres peut être effectuée avec le paramétrage de modèle différent. En outre, dans la pratique, des expériences différentes utilisé différentes fonctions d'ajustement de leurs données. Par exemple, les sections invariantes pour les données ISR à $y = 0$ ont été ajusteés de

$$E\frac{d^3\sigma}{d^3p} = g(p_T) = A\, e^{-\frac{p_T}{T} + Bp_T^2}, \tag{1.7.1}$$

tandis que les collaborations PHENIX et ALICE utilisént la paramétrisation (encore une fois de leurs données à $y = 0$)

$$E\frac{d^3\sigma}{d^3p} = g(p_T) = \frac{A}{\left(1 + \frac{m_T}{nT}\right)^n}, \tag{1.7.2}$$

pour leurs spectres identifiés, avec $m_T = \sqrt{m^2 + p_T^2}$. En particulier, l'extrapolation à point $p = 0$ [11] est basée sur différentes crises de différentes expériences.

Dans la présente étude, nous suivons une stratégie différente. Plus précisément, nous ajustons le spectre de chaque expérience avec une seule et même fonction, l'extrapoler au point zéro dynamique et extraire des valeurs pour I_0. Un tel traitement uniforme des spectres est naturel pour nos études que nous voulons tester les dépendances de certains des charactéristiques des spectres des hadrons à l'égard de l'énergie de collision. Plusieurs paramétrisations universels de la combinaison des spectres servent pour notre tâche. Faisons un bref rappel des modèles les plus importants sur le marché, ce qui suggère fonctions d'ajustement pour la production hadronique inclusif invariant section.

1.7.2 Différents modèles d'ajustement

Il a été observé dans les années 1950 que les particules secondaires dans les rayons cosmiques ont limité impulsion transverse ~ 0.5 GeV (plus vaste gamme de particules cosmiques primaires énergies, qui peut atteindre $\sim 10^{11}$ GeV) indépendant de l'énergie de collision primaire [2, 3 de phenix]. Cocconi, Koester et Perkins [4 du phenix] a alors proposé la formule empirique pour le spectre en impulsion transverse de production des mésons :

$$\frac{d\sigma}{dp_T^2} = Ae^{-6p_T}, \tag{1.7.3}$$

où p_T est l'impulsion transverse en GeV/c. Une analyse plus poussée [5, 6, 7 du phenix] conduit à l'interprétation que la production de hadrons douce est "thermique" avec un spectre de Boltzmann statistique (1.7.3) et $T = \frac{1}{6} = 0.167$ GeV/c représentant "la température" à laquelle hadrons moux sont produites. Dans les scénarios thermiques (voir par exemple [8,9 de phenix]) de $p\,p$ collisions, il est plus naturel de représenter l'invariant section transversale en fonction de la rapidité y et transversale de masse $m_T = \sqrt{m^2 + p_T^2}$, où m est la masse des hadrons en considération.

Une extension naturelle dans les approches de modèle thermique est d'intégrer les statistiques de particules identiques de Bose-Einstein ou de Fermi-Dirac fonctions. La fonction de Bose-Einstein a été utilisé dans [11] et sera également examinée ici.

Comme nous l'avons souligné précédemment, la production de hadrons peuvent en général être classés en deux régimes différents selon impulsion de la particule. Le premier est celui de la douce multi-particules production, dominant à faible moment ($p \lesssim 1 - 2$ GeV) et le deuxième régime est celui de la production de particules dures de diffusion, évidente à haute impulsion ($p \gtrsim 2$ GeV), avec, comme une question de fait, pas de frontière nette entre les deux régimes. Ainsi, il est bien connu que les spectres des hadrons dans $p\,p$ collisions peuvent être bien installés dans la région élan ensemble par une seule fonction qui n'a que trois paramètres : A, T, n. C'est la fonction que l'on appelle Tsallis [24 de ph.0], aussi appelée la fonction Levy [7, 25 de ph.0] :

$$g(p_T) = \frac{A}{\left(1 + \frac{m_T}{nT}\right)^n}, \qquad m_T = \sqrt{m^2 + p_T^2}. \tag{1.7.4}$$

Les paramètres T et n caractérisent, respectivement, le basse et haute-p_T région du spectre. Constantino Tsallis dérivée de la formule qui porte son nom, en postulant une forme généralisée de l'entropie d'un système de thermalisation dans lequel les corrélations à longue portée sont présents. Ce faisant, il a présenté, avec la température T, une seconde "non-extensive" paramètre q, ce qui est lié à n comme

$$n = \frac{1}{q-1}. \tag{1.7.5}$$

quand $q \to 1$ ($n \to \infty$), la formule (1.7.4) se réduit à l'expression ordinaire de Boltzmann :

$$\lim_{n\to\infty} \frac{1}{\left(1 + \frac{m_T}{nT}\right)^n} = e^{-\frac{m_T}{T}}. \tag{1.7.6}$$

Pour entrer en contact avec des fonctions utilisées dans [11], on examinera également un "Tsallis_p" modèle obtenu en réglant la masse $m = 0$, c'est à dire le remplacement m_T par p_T en $g(p_T)$, ou E par p si $f(p)$. La forme classique de Tsallis 1.7.4 sera nommé simplement la fonction Tsallis.

Nous avons étudié le dernière modèle

$$f(p) = \frac{I_0}{\left(1 + \frac{p^2}{n\, I_1^2}\right)^n} \tag{1.7.7}$$

inspiré par la dépendance bas impulsion prévu dans le cadre MLLA. Le rationnel de ce modèle est la suivante. Nous partons de la forme limite (2.2)

$$g(p_T, y) = \frac{A}{p_T^2} \tag{1.7.8}$$

(en ignorant le fonctionnement de l'accouplement) et incorporer l'absence de petit-p_T rayonnement sous la forme d'une stabilisation à petits p_T

$$\frac{A}{p_T^2} \to \frac{A}{p_T^2 + Q_0^2}. \tag{1.7.9}$$

Le paramétrage retenu, avec l'exposant de loi de puissance n, est un moyen de restaurer le comportement en loi de puissance à haute p_T inspiré par la fonction Tsallis. Comme pour les autres formes fonctionnelles nous avons simplement étendre le modèle de $g(p_T, y = 0)$ à la même forme fonctionnelle pour la variable p. Notez que les différences avec les fonctions Tsallis sont présents, comme pour le Tsallis_p fonction la limite de basse p est $1 - \frac{p}{T}$, pour la Tsallis il est de 1 $1-\frac{\sqrt{p^2+m_\pi^2}}{T}$, alors que pour la fonction proposée, il est de $1-\frac{p^2}{I_1^2}$.

Pour résumer, nous donnons la liste des différents modèles utilisés par leur nom dans le tableau 1.1.

Table 1.1 – Fonctions d'ajustement. Pour Tsallis_p et Tsallis, il ya aussi une forme limite obtenue lorsque $n \to \infty$, respectivement nommés exponentielle et Boltzmann.

Model	$g(p_T)$	$f(p)$
Tsallis_p	$\frac{A}{(1+p_T/(n\,T))^n}$	$\frac{A}{(1+p/(n\,T))^n}$
Tsallis	$\frac{A}{(1+m_T/(n\,T))^n}$	$\frac{A}{(1+E/(n\,T))^n}$
Coherent	$\frac{I_0}{(1+p_T^2/(n\,I_1))^n}$	$\frac{I_0}{(1+p^2/(n\,I_1^2))^n}$
ISR	$A\ \exp\left(-\frac{p_T}{T}+B\,p_T^2\right)$	$A\ \exp\left(-\frac{p}{T}+B\,p^2\right)$
Bose-Einstein	$\frac{A}{(\exp(m_T/T)-1)}$	$\frac{A}{(\exp(E/T)-1)}$

1.7.3 Résultats

Pour choisir les fonctions d'ajustement qui seront exploitées pour l'extraction de la valeur I_0, nous allons étudier leurs performances sur quelques-uns des ensembles de données et ensuite appliquer les fonctions sélectionnées à une collection de spectres. Pour cela, nous avons choisi de pions et de protons de données pour e^+e^- et $p\,p$ collisions. Les critères pour sélectionner ces échantillons de données étaient d'avoir les données les plus précises du point de vue des barres d'erreur et le nombre de points. De cette façon, nous avons choisi des données OPAL pour e^+e^- collisions avec $\sqrt{s}$ =91.2 GeV et les données ALICE pour $p\,p$ collisions avec sqrt $\sqrt{s}$ =900 GeV. Pour donner une idée de la qualité des données sélectionnées nous citer quelques caractéristiques dans le tableau 1.2.

Table 1.2 – OPAL et ALICE caractéristiques des données. π est synonyme de pions chargés et p pour les deux protons et antiprotons.

experience	processus	nombre de points	stat	syst
OPAL	$e^+e^- \to \pi + X$	27 points $\leq$ 1 GeV	$< 1\%$	$\sim 3\%$
OPAL	$e^+e^- \to p + X$	27 points 0.4-1.4 GeV	$\sim 5\%$	$\sim 5\%$
ALICE	$pp \to \pi + X$	21 points $\leq$ 1 GeV	stat $< 1\%$	$\sim 3\%$
ALICE	$pp \to p + X$	17 points 0.35-1.4 GeV	stat $\sim 3\%$	$\sim 4\%$

Premiere ajustement des données $e^+e^- \to \pi\, X$ et la méthodologie

Pour expliquer les différents tests que nous avons effectués dans le but de décider des formes fonctionnelles sont adéquats pour l'extrapolation, nous allons commencer par la production de pions chargés, telle que mesurée par OPAL équipée avec le fonction Tsallis_p, qui est la fonction Tsallis, mais avec p comme variable pertinente :

$$f(p) = \frac{A}{\left(1 + \frac{p}{nT}\right)^n}. \tag{1.7.10}$$

Notons qu'ici $A = I_0$, soit la quantité extrapolée d'intérêt principal de la présente étude.

Sur la Fig. 1.20 à gauche, les points avec leurs erreurs statistiques sont affichés avec la fonction d'ajustement. On voit que le modèle donne une bonne description des données dans cette gamme de vitesse. La procédure d'ajustement minimisé

$$\chi^2 = \sum_i (y_i - h(p_i))^2, \tag{1.7.11}$$

where y_i stands for the measured quantity at point p_i and $h(p_i)$ stands for the fitting function, in this case où y_i est la quantité mesurée au point p_i et $h(p_i)$ est la fonction d'ajustement, dans ce cas,

$$h(p) = \frac{4\pi p^2}{\sqrt{p^2 + m_\pi^2}} f(p), \tag{1.7.12}$$

depuis OPAL donne $\frac{dN}{dp} = \frac{1}{\sigma}\frac{d\sigma}{dp}$. Dans χ^2 (1.7.11) tous les points entrer avec un poids de 1. Cela se justifie à la condition que les erreurs sont égaux d'un point à un autre. Lorsque ce n'est pas le cas, il faudrait utiliser des poids w_i donnée par l'inverse du carré de l'estimation de l'erreur standard à points p_i. Dans les expériences de taux de comptage cette erreur standard comprend l'erreur statistique associée au comptage, mais doit être complétée par la part des erreurs systématiques qui est statistiquement indépendant d'un point p_i à l'autre. La difficulté est que il n'est pas impossible de calculer l'erreur standard de la table des sections et des erreurs et deuxièmement, que même en supposant que seules les erreurs statistiques sont indépendants, nous sommes coincés pour certaines expériences qui ne donnent pas les erreurs statistiques et systématiques séparément. Dans de telles circonstances, il est possible d'utiliser le χ^2 définition de (1.7.11), qui se rapproche de l'habituel χ^2 procédure d'ajustement si des erreurs sont comparables, une hypothèse qui tourne avéré être considérés comme raisonnables pour les ensembles de données. Nous reviendrons sur ce point pour les données OPAL dans ce qui suit.

Pour étudier plus avant la qualité de l'ajustement, nous formons le rapport $y_i/h(p_i)$, ce qui est montré sur la Fig. 1.20 à droite. Les fluctuations de point-à-point semble être comparable à des erreurs statistiques. Les erreurs systématiques étant trois fois plus larges ne peuvent donc pas être statistiquement indépendants pour ce jeu de données, et seulement une petite partie d'entre eux peut avoir cette propriété. Nous en concluons donc qu'il est préférable d'ignorer les erreurs systématiques lors de la procédure d'ajustement, et les considere plus tard lors du calcul de l'erreur des paramètres ajustés (ou les valeurs extrapolées).

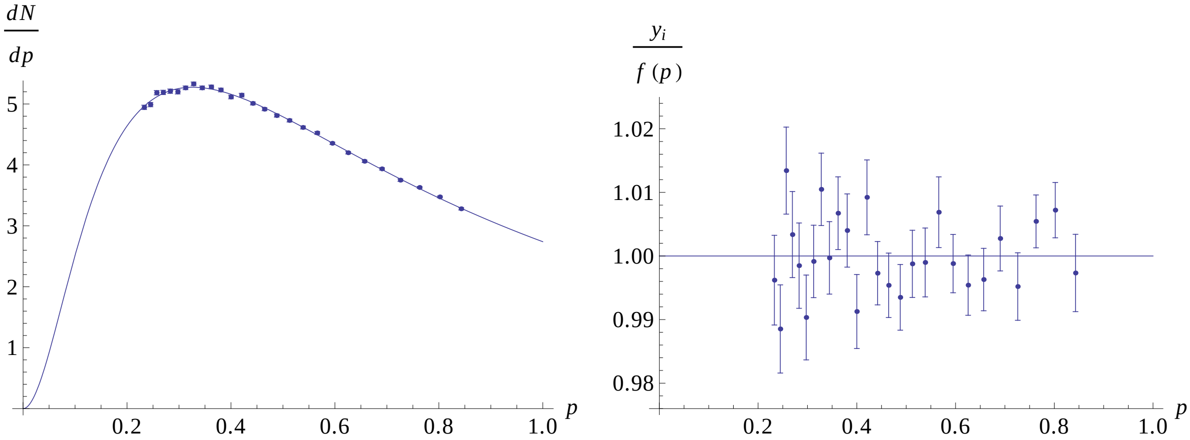

FIGURE 1.20 – Ajustement des données d'OPAL et le rapport des données sur ajustement.

La valeur extrapolée pour la quantité I_0 pour la fonction Tsallis_p est 5.6 GeV^{-2} avec un écart-type (donné par la routine d'ajustement) de $0,1$ GeV^{-2} ou au 95% niveau de confiance à $0,2$ GeV^{-2}.

On peut comparer cette "no-poids" méthode pour l'ajustement en compte des erreurs d'ajustement statistiques, où

$$\chi^2 = \sum_i w_i (y_i - h(p_i))^2 \tag{1.7.13}$$

est réduite au minimum avec les poids $w_i = 1/\sigma_i^2$ où σ_i est l'erreur statistique de l'erreur statistique sur les points y_i qui sont donnés par l'expérience. On peut voir sur la Fig.. 1.21 que les résidus sont très similaires. En fait, les deux procédures d'ajustement conduire à des différences infimes entre les deux fonctions adaptées. Dans la gamme de $p = 0$–1 GeV, cette différence est en effet maximal à $p = 0$, mais ne donne qu'une variation de 1% pour la quantité extrapolée I_0. L'avantage de la méthode avec poids standard est qu'il donne directement un χ^2. Le montant qui en résulte χ^2/ndf value, étant de 1.25, confirme la qualité de l'ajustement déjà observé à l'œil nu. Cette valeur indique également que les erreurs statistiques OPALE sature pratiquement les erreurs de point à point standard, confirmant la nécessité de mettre erreurs systématiques de côté pour le montage. Pour la première méthode de montage (avec $w_i = 1$), nous pouvons comparer l'écart quadratique moyen ($1\,10^{-3}$ GeV^{-}2) à la moyenne des erreurs statistiques carré ($7.5\,10^{-4}$ GeV^{-}2), qui est proche du résultat de χ^2/ndf.

La dernière façon de présenter la façon dont les données et leur impact précisions sur la détermination de l'extrapolation d'ajustement et ultérieure est de montrer des intervalles de confiance de niveau de la fonction ajustée. Voici ci-dessous et 95% est choisie pour le

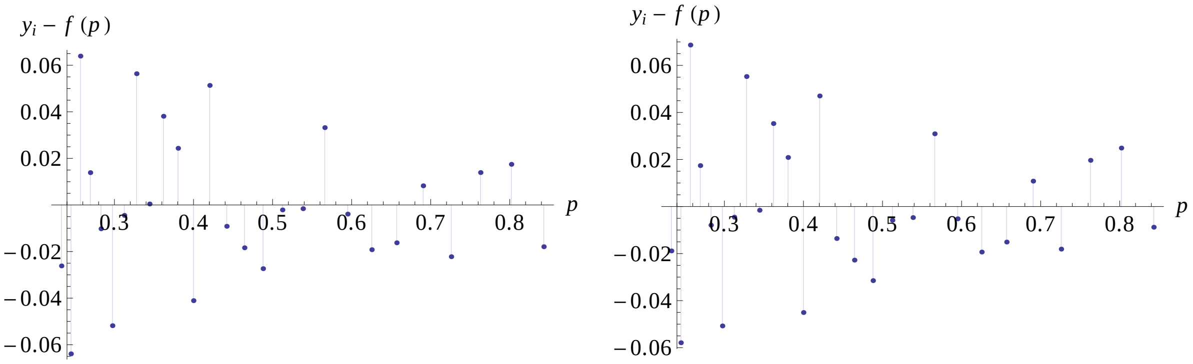

FIGURE 1.21 – Résidus d'OPAL pour la norme χ^2 ajustement (à gauche) et le "no-poids" ajustement (à droite).

niveau de confiance. Pour la quantité dN/dp (montré sur la Fig. 1.22, à gauche), ils sont beaucoup moins visibles que pour la quantité Ed^3N/dp^3 (voir Fig. 1.22, à droite), dans laquelle nous nous intéressons. Cela nous rappelle la difficulté inhérente à la procédure d'extrapolation.

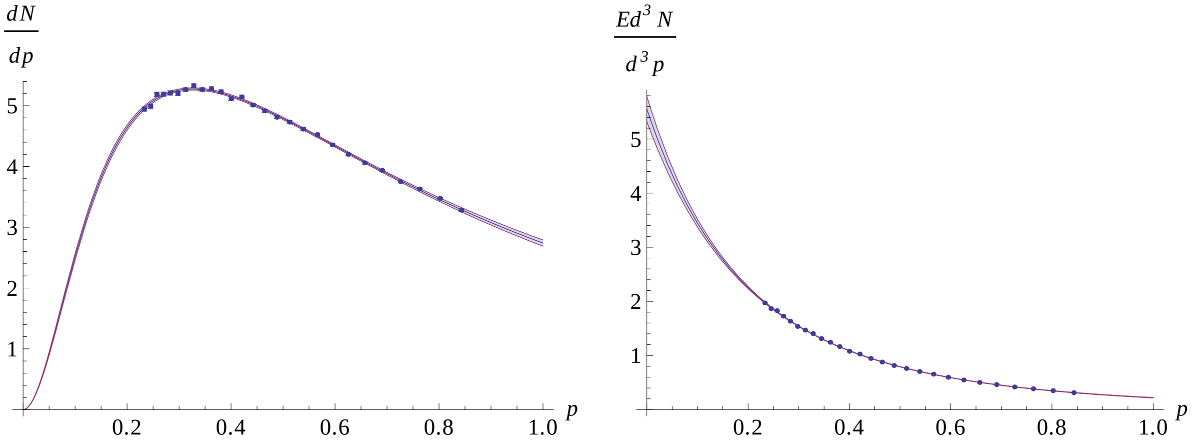

FIGURE 1.22 – Données d'OPAL avec confiance au niveau des bandes.

Divers autres ajustements de $e^+e^- \to \pi X$

Montrons maintenant un exemple moins satisfaisant en utilisant le modèle exponentiel (soit la fonction Tsallis_p (1.7.10) dans le cas particulier où $n \to \infty$). Sur la Fig. 1.23 à gauche, on peut voir que la fonction d'ajustement n'est pas sur les points et la tendance générale n'est pas bien reproduit. On remarque, cependant, que, en mettant en plus les erreurs systématiques de la fonction d'ajustement ne serait pas tout à fait meavauis, même si le fait que la tendance est différente de celle des données est bien sûr toujours observée.

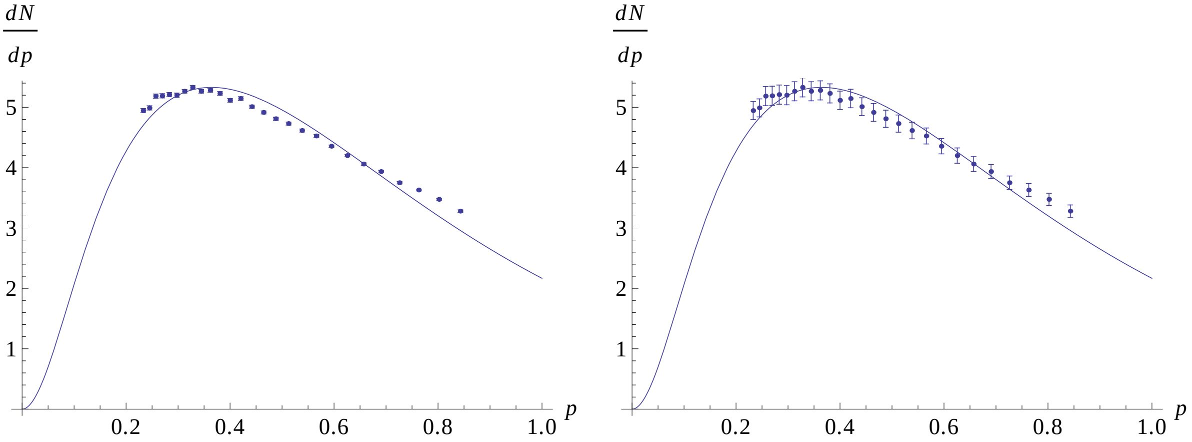

FIGURE 1.23 – OPAL mis en ajusté par la fonction Boltzmann avec (à droite) et sans erreurs statistiques (à droite).

Pour ces données de la Tsallis (classique) modèle

$$f(p) = \frac{A}{\left(1 + \frac{E}{nT}\right)^n}, \tag{1.7.14}$$

et la fonction de Bose-Einstein

$$f(p) = \frac{A}{(e^{E/T} - 1)}, \tag{1.7.15}$$

Les deux a donner une description satisfaisante, la première étant aussi bon que le modèle Tsallis_p, tandis que le second est un peu loin, mais avec un paramètre inférieur. En combinaison avec la fonction exponentielle, sous la forme de Bose-Einstein aide de illustrare un manque de données actuelles concernant la question de l'extrapolation. La comparaison est montré sur la Fig. 1.24. Les deux modèles ont des comportements différents dans le viscinity de $p = 0$, la forme exponentielle est linéaire en p, tandis que la fonction de Bose-Einstein est quadratique en p. Cependant, nous voyons que la fonction ajustée qui ne change pas sa concavité à faible p est une limite à la $p = 0$ qui s'avère être inférieure à celle du modèle dont la courbure change de signe. Cette caractéristique paradoxale est due au fait qu'il n'y a pas de données suffisamment petites p dans la région où l'existence d'un changement de concavité peut se faire sentir, si elle n'est pas observée. Si l'échelle de l'élan de ce changement est en quelque sorte liée à la masse des hadrons on peut s'attendre à quelques indications à protons produits au lieu de pions.

La qualité de l'ajustement du modèle de cohérence est visible sur la Fig. 1.25. Nous notons que l'exposant résultant est proche de 1.

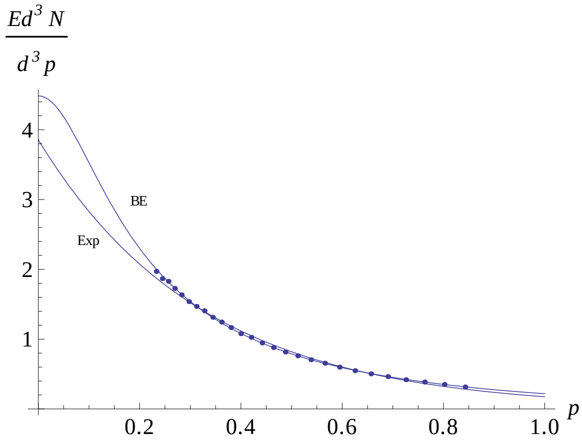

FIGURE 1.24 – Comparaison de deux fonctions d'ajustement et leurs extrapolations à $p = 0$: forme exponentielle et de Bose-Einstein.

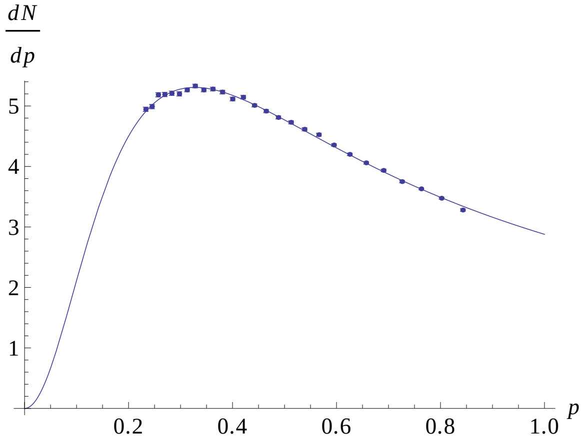

FIGURE 1.25 – OPAL données ajusteés par la fonction cohérente.

Ajustement de $e^+e^- \to p\,X$

Nous allons maintenant examiner les données de production de protons dans les collisions e^+e^- en visant notamment à étudier les effets possibles de masse dans les spectres et les modèles de montage. Le Tsallis_p fonction fait encore un bon travail (voir figure 1.26 (gauche)) avec un écart moyen quadratique $9\,10^{-6}$ GeV^{-2} pour une moyenne des erreurs statistiques carré $10\,10^{-6}$ GeV^{-2}. L'exposant du modèle ($n = 3.4$) est comparable à celle obtenue pour des pions ($n = 3.8$), mais l'échelle dynamique, $T = 0.36$ GeV, est plus grand, car il est de $T = 0.30$ GeV pour les pions.

The precision being worse this affects the confidence level bands as can be seen on Fig. 1.26 (right). La précision est pire cela affecte les bandes du niveau de confiance que l'on peut voir sur la figure 1.26(à droite).

Le modèle de Bose-Einstein est beaucoup moins satisfaisant que c'était pour les pions. Cette conclusion serait moins clair si les barres d'erreur complets devaient être pris en considération. Cependant l'examen des résidus à la fois pour le modèle Tsallis_p et de Bose-Einstein (Fig. 1.27) montrent d'abord que l'ampleur des fluctuations sont moindres

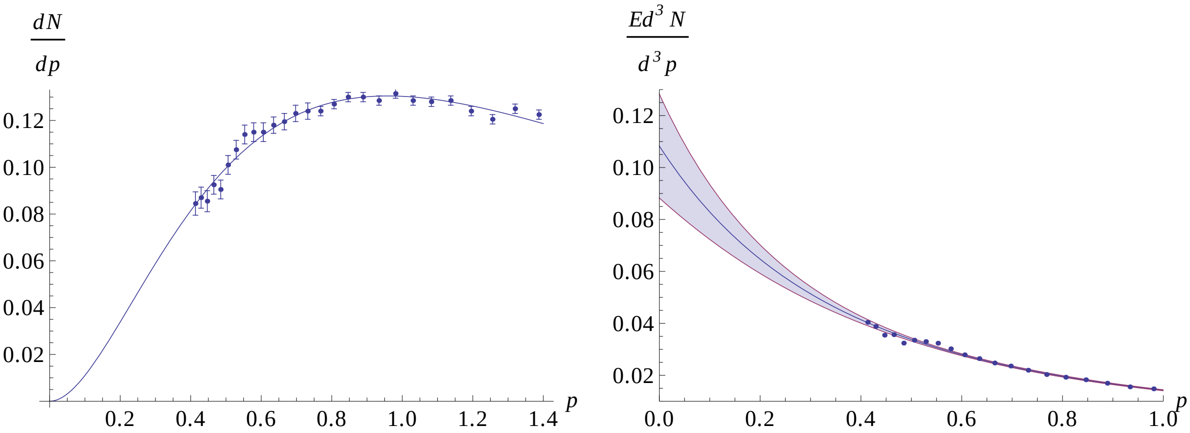

FIGURE 1.26 – OPAL p data fitted with the Tsallis_p model (left). Confidence level bands (right).

pour Tsallis_p et deuxième partie de la tendance est manqué par la fonction de Bose-Einstein. Le modèle Tsallis a également montré des difficultés similaires.

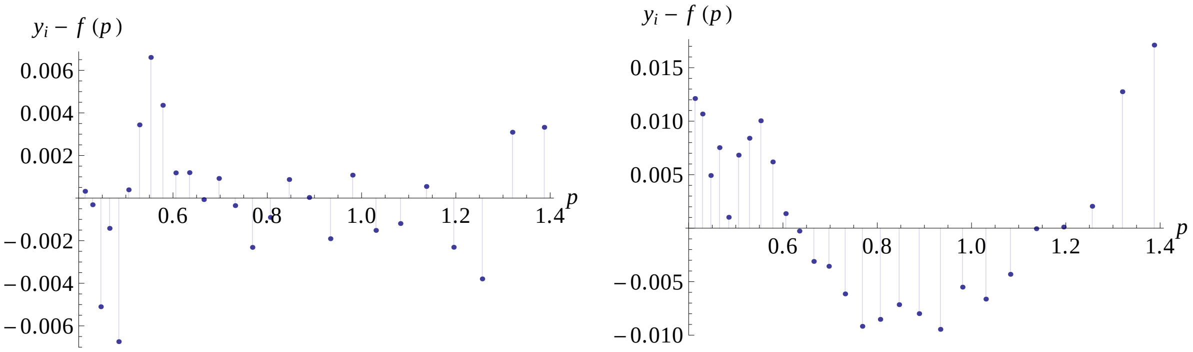

FIGURE 1.27 – OPAL p résiduelles de données avec le modèle Tsallis_p (à gauche) et le modèle de Bose-Einstein (à droite).

Le modèle cohérent fonctionne plutôt bien, comme on peut le voir sur la figure 1.28 à gauche. La puissance n est proche de 1, comme pour les pions. L'échelle dynamique $I_1 = 0.29$ GeV est plus grande qu'elle était pour les pions ($I_1 = 0.53$ GeV). La qualité de l'ajustement est comparable à celle obtenue avec Tsallis_p comme cela a été vérifié en regardant les résidus (non représenté) et à l'écart moyen quadratique de $7\,10^{-6}$ GeV^{-2} (à comparer à $9\,10^{-6}$ GeV^{-2} pour Tsallis_p comme mentionné précédemment). Encore une fois nous constatons en comparant Tsallis_p avec le modèle cohérent que le comportement vs linéaire quadratique à petits p ne peuvent pas être dissociées. Le point d'inflexion pour le modèle cohérent est situé à environ $p = 300$ MeV où il n'existe pas de données. Seuls les emplacements des points d'inflexion autour de 500 MeV, obtenue lors de l'installation soit de Bose-Einstein ou modèles Tsallis, pourrait être rejetée à partir des données et mener à la conclusion que l'échelle de l'élan pour cet endroit fixé par la masse du proton dans ces modèles est trop élevé, tandis que l'échelle inférieure telle que I_1 dans le modèle cohérent ne sont pas exclus.

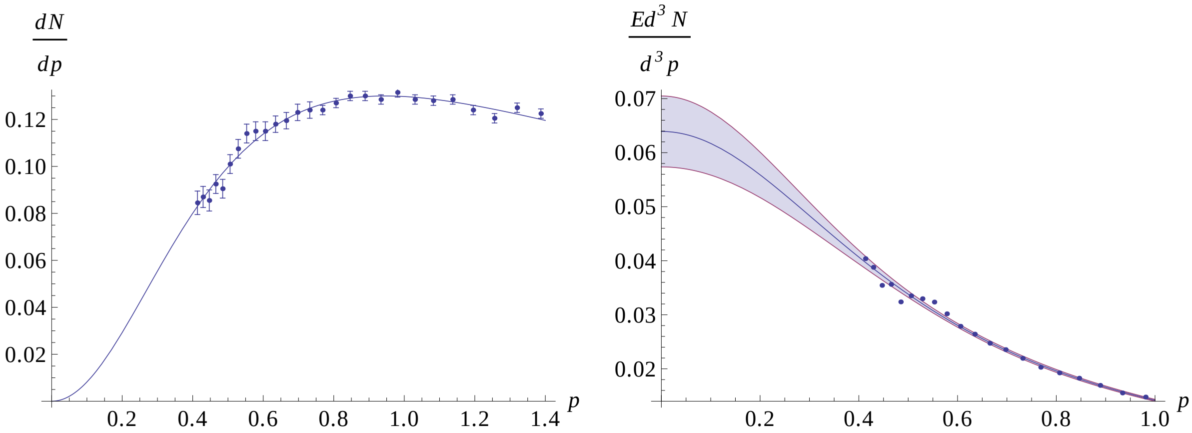

FIGURE 1.28 – Données OPAL p ajusteés par modèle cohérent (à gauche). Bandes de niveau de confiance (à droite).

Ajustement des données des collisions pp

Considérons maintenant les données d'ALICE des pions. Recommençant par le modèle Tsallis_p, nous observons que la première forme et la limite extrapolée I_0 seulement légèrement dépendent des maxima p_T choisis, au moins dans la plage comprise entre 0.5 et 1.0 GeV. Nous avons donc décidé de s'en tenir à 1 GeV pour des pions, même si c'est parfois au prix de grossir χ^2 (voir ci-dessous). La puissance n est grande, en contradiction avec ce qui a été observé avec les collisions e^+e^-, en ligne avec le comportement bien connu exponentielle des spectres p_T à petit p_T. Cependant, comme on peut le voir sur la figure parcelle 1.29 à gauche, la qualité de l'ajustement n'est pas bon quand on y regarde plus en détail sur cet aspect et nous avons observé un bien meilleur comportement de la Tsallis fonction est visible sur la figure 1.29 à droite. Description des données ALICE à la fois avec le rapport de recherche internationale et de Bose-Einstein fonctions n' était pas non plus très satisfaisant.

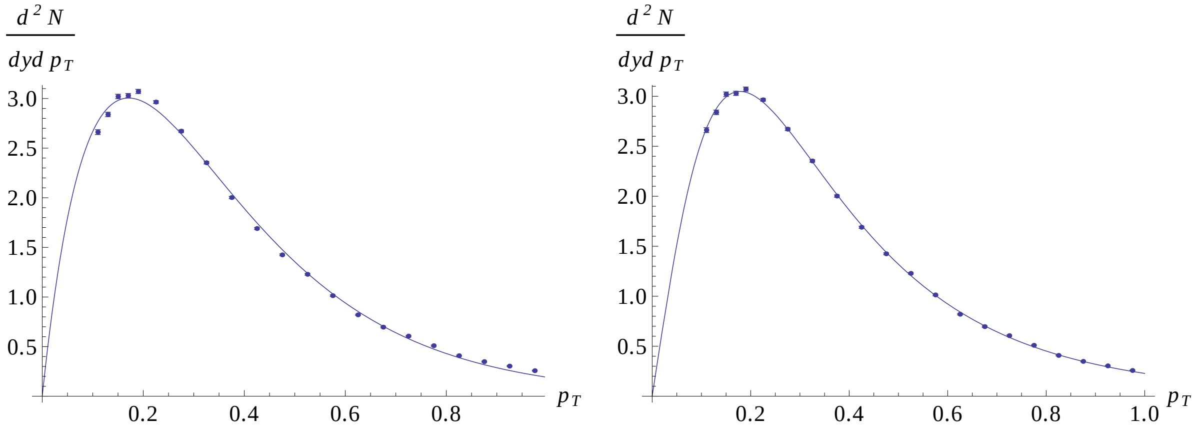

FIGURE 1.29 – ALICE pions données ajustées par le modèle Tsallis_p (à gauche) et la fonction Tsallis (à droite).

Le modèle cohérent pourrait fournir une bonne description quand limitant la gamme des p_T à $p_T \leq 0.5$ GeV. Pour des valeurs plus grandes, une déviation systématique est inévitable, mais depuis cela n'affecte pas le paramètre grossièrement extrait nous avons de nouveau abstenu de l'adaptation de la gamme p_T et a continué à utiliser 1 GeV comme la limite supérieure de la gamme de montage. Le résultat de cet ajustement est montré sur la figure1.30 à gauche. La puissance n est proche de 2 et le paramètre d'échelle $I_1 \approx 0.22$ GeV, un peu plus petit que celui obtenu dans les collisions e^+e^-. Sur la figure 1.30 à droite une comparaison des spectres invariant pour le Tsallis_p et la fonction de cohérence est représenté. On peut voir que contrairement à la situation en e^+e^-, voici le point d'inflexion du modèle cohérent se trouve à un endroit où le premier points de données s'asseoir, avec la conséquence que nous obtenons plus sytematiquement le I_0 pour les modèles où les comportements petites p_T sont linéaires que pour ceux où elle est quadratique.

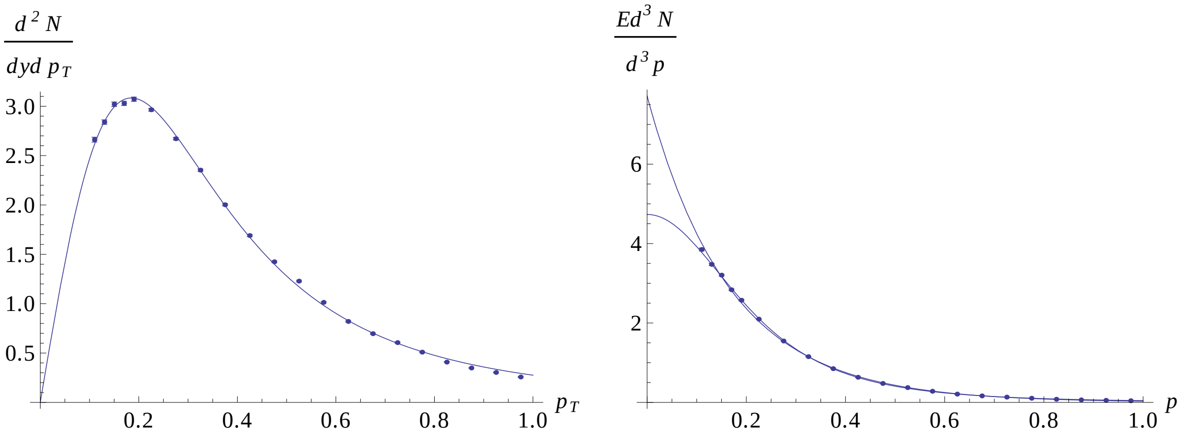

FIGURE 1.30 – ALICE données pion ajusteés par le modèle cohérent (à gauche). Comparaison entre les modèles Tsallis_p et cohérente pour la production de particules invariant (à droite).

1.8 Résultats et discussion

Dans cette section, nous présentons les résultats obtenus pour la limite I_0. Nous le signaler systématiquement pour les deux modèles identifiés précédemment, à savoir la Tsallis et des fonctions cohérentes, parfois citant valeurs obtenues avec un plus grand nombre de modèles. Nous effectuons notre étude pour identifié les pions, kaons chargés et les protons, à la fois dans les collisions e^+e^- et pp.

1.8.1 Les collisions e^+e^-

Les résultats pour les différentes fonctions d'ajustement peut être vu sur 1.31. Les valeurs sont également cités dans le tableau 1.3. La considération des plusieurs fonctions d'extrapolation a l'avantage de donner une vision globale de l'évolution des extraits des valeurs de I_0 et bien que l'ampleur de l'extrapolation varie entre 3 et 6 GeV^{-2} et dépend du modèle, de la tendance générale est plus robuste avec seulement de faibles écarts de fonction pour fonctionner. En regardant la figure 1.31. Nous concluons que la limite souple pour la distribution invariante est presque la même pour toutes les expériences (à l'exception du point TOPAZ qui est d'environ 20 % de moins). Ainsi, l'indépendance énergétique de la limite souple est compatible avec les résultats expérimentaux des collisions e^+e^-.

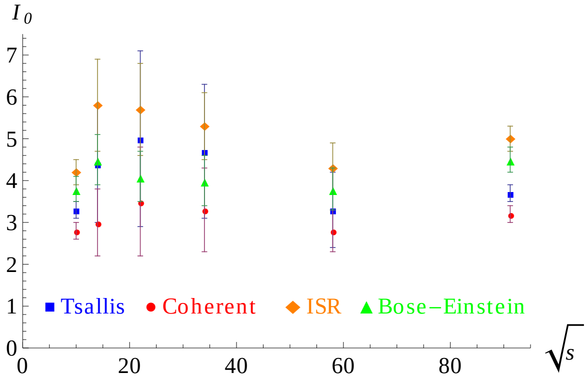

FIGURE 1.31 – Limite de bas impulsion I_0 de la densité invariante extrapolée pour pions chargés $\frac{1}{2}(\pi^+ + \pi^-)$ en collisions e^+e^-.

TABLE 1.3 – Les valeurs de I_0 de la production de pions dans les collisions e^+e^- et les différents modèles d'ajustement.

Experience ($\sqrt{s}$)	modèle	$I^{ee}_{0\pi}$ en GeV^{-2}	ndf	χ^2/ndf	R^2
ARGUS (10 GeV)	Tsallis	3.1 ± 0.2		1.9	98%
	Coherent	2.8 ± 0.1	29	1.4	99%
	ISR	4.2 ± 0.2		3.0	97%
	B-E	3.8 ± 0.2	30	4.4	96%
TOPAZ (58 GeV)	Tsallis	3.3 ± 0.7		-	99.6%
	Coherent	2.8 ± 0.2	6	-	99.6%
	ISR	4.3 ± 0.3		-	99.4%
	B-E	3.8 ± 0.2	7	-	99.4%
OPAL (91 GeV)	Tsallis	3.7 ± 0.1		1.3	99.8%
	Coherent	3.2 ± 0.1	24	1.9	99.7%
	ISR	5.0 ± 0.1		1.4	99.7%
	B-E	4.5 ± 0.1	25	2.4	99.6%

Le tableau 1.3 contient également l'information sur la qualité de l'ajustement. Il est soit fournie par une estimation du χ^2/ndf, lorsque des erreurs statistiques sont connues (ARGUS et OPAL), divisant l'erreur quadratique (1.7.11) par le nombre de degrés de liberté et par l'erreur au carré moyenne statistique, ou proposée par le pourcentage de la variance totale qui est expliqué par la forme, à savoir

$$R^2 = \frac{\sum_i (f(p_i) - \bar{y})^2}{\sum_i (y_i - \bar{y})^2}. \tag{1.8.1}$$

Les deux quantités sont surtout intéressant pour comparer des modèles différents pour le même ensemble de données. Leurs valeurs absolues sont plus difficiles à interpréter. Pour R^2 il manque une référence à la précision des données, mais c'est ce fait même qui permet de le calculer pour toutes les données. Pour χ^2/ndf, nous savons que une valeur d'environ 1 devrait, mais ce n'est pour autant que l'incertitude appropriée non corrélée est utilisée, qui, comme nous l'avons expliqué dans la section 1.7 est difficile avec les données publiée seules.

Nous avons effectué une étude détaillée de toutes les fonctions citées, y compris les quatre modèles qui figurent dans le tableau afin de tester les capacités de chacune des fonctions pour faire face à de telles données. Notre étude a conclu qu'il n'existe pas de modèle qui se démarque comme étant universellement correcte, en conformité avec les conclusions de la section précédente. En e^+e^- collisions, parmi les meilleurs χ^2-valeurs pour les trois types de particules ont été obtenus avec l'ajustement cohérent, comme cela est également indiqué dans le tableau 1.3. Comme on le voit de la fonction Tsallis s'adapte aussi bien les données de production de pions, mais comme on l'a déjà noté dans la section précédente, était en difficulté avec les données de production de protons. Pour ces derniers, la Tsallis_p fonction prévue l'un des meilleurs ajustements. L'ajustement rapport de recherche internationale a plutôt bien χ^2 valeurs de pions et les kaons, mais pour les protons, il n' était pas parmi les meilleurs ajustements.

Pour kaons chargés et les protons nous donnent que des résultats pour les deux types (Tsallis et unique cohérentes) et pour trois ensembles de données couvrant la gamme de e^+e^- énergies cms. Ceci est illustré sur la figure 1.32. Nous avons testé d'autres modèles aussi bien et a observé que la tendance obtenue sur le terrain est également reproduit par d'autres fonctions avec le même écart en magnitude. La valeur I_0 dans le cas des kaons se situe entre 0.1 et 0.3 GeV^{-2}, alors que pour les protons de la valeur est placée entre $0,04$ et 0.08 GeV^{-2}. Il s'avère que dans le cas des kaons et protons, la conclusion à propos de l'indépendance énergétique est plus difficile à établir, car les valeurs montrent des fluctuations assez importantes. Ceci est bien sûr en partie s'expliquer par de plus grandes incertitudes sur les points expérimentaux et le plus petit nombre de points disponibles par jeu de données. Ces données per-soi ne sont que marginalement soumis à la phénoménologie, nous voulons explorer et la seule conclusion que nous pouvons espérer atteindre est qu'il n'y a aucune preuve d'une forte dépendance énergétique des limites I^{ee}_{0K} et I^{ee}_{0p}.

1.8.2 Les collisions $p\,p$

Les résultats obtenus avec les collisions $p\,p$ sont représentés sur les figures1.33 et 1.34. Il est à noter que les points ISR (23, 45, 63 GeV) montrent une légère augmentation, également observée dans [11], qui devient plus doux pour les kaons chargés. Pour les protons,

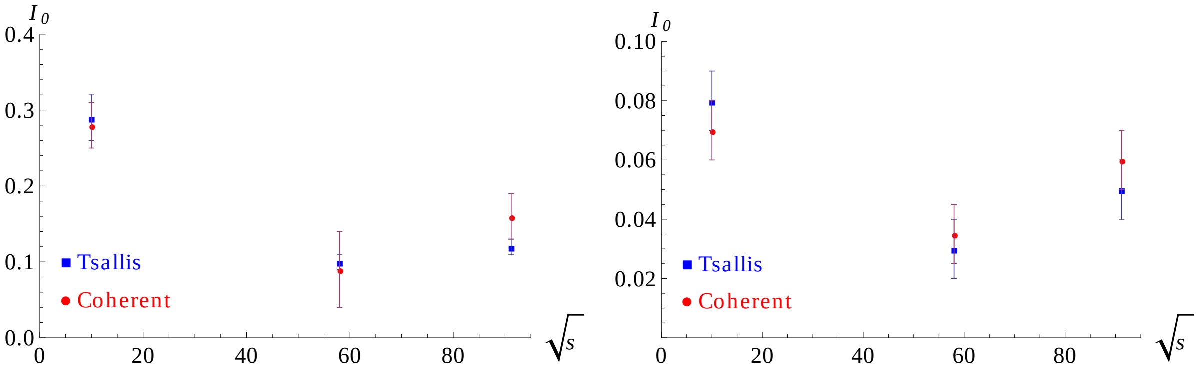

FIGURE 1.32 – Limite souple I_0 de la densité invariante extrapolées à l'aide Tsallis ajustement (jaune) et la fonction cohérente (rouge) pour kaons chargés et les protons en collisions e^+e^-.

TABLE 1.4 – I_0 valeurs GeV^{-2} pour fonction Tsallis pions, kaons pour et de protons dans e^+e^- collisions.

l'expérience	$\sqrt{s}$	$I^{ee}_{0\,\pi}$	$I^{ee}_{0\,K}$	$I^{ee}_{0\,p}$
ARGUS	10	4.334 ± 0.046	0.294 ± 0.010	0.080 ± 0.004
TASSO	14	4.431 ± 1.453	0.225 ± 0.032	0.033 ± 0.006
TASSO	22	5.035 ± 2.082	0.153 ± 0.020	0.035 ± 0.008
TASSO	34	4.690 ± 1.592	0.159 ± 0.019	0.031 ± 0.005
TOPAZ	58	3.086 ± 0.466	0.101 ± 0.013	0.032 ± 0.010
OPAL	91.2	3.670 ± 0.189	0.122 ± 0.004	0.048 ± 0.001

cependant, cette tendance n'est plus visible. Cependant, en regardant le point PHENIX qui a été mesuré à peu près la même énergie que rapport de recherche internationale, 62.4 GeV, on ne voit plus cette augmentation. Ce fait peut s'expliquer par l'incertitude générale de la normalisation des données expérimentales. Le point de l'extrapolation des données ALICE à 900 GeV donne une valeur accrue par rapport à celle de PHENIX données à 200 GeV, qui est reproduit par tous les modèles d'extrapolation. Toutefois, le point ALICE donne la même valeur que point de rapport de recherche internationale à 63 GeV, de sorte qu'il est difficile de demander une augmentation significative, en contradiction avec les attentes de la cohérence des couleurs. Une conclusion plus prudente est que la limite douce ne montrent pas de variation significative dans le domaine d'énergie exploré ensemble.

Pour les données pp, seul l'ajustement Tsallis montré de bons résultats pour les trois types de particules. Nous citons dans le tableau 1.6 les résultats obtenus pour des pions ainsi que des indications sur la qualité de l'ajustement et on voit comment la fonction Tsallis se distingue par rapport aux autres. Pour les pions, l'ajustement cohérent est en difficulté, en particulier parce qu'il ya une tension entre le bas et élevé p_T points de données. Il a été possible d'obtenir un meilleur χ^2/ndf en limitant le range de p_T pour une demi-GeV (dans ce cas, la fonction cohérente pourrait donner un χ^2 aussi petit que

TABLE 1.5 – I_0 valeurs GeV^{-2} pour fonction cohérente de pions, kaons et protons dans e^+e^- collisions.

l'expérience	$\sqrt{s}$	$I^{ee}_{0\,\pi}$	$I^{ee}_{0\,K}$	$I^{ee}_{0\,p}$
ARGUS	10	3.801 ± 0.043	0.282 ± 0.010	0.072 ± 0.005
TASSO	14	2.951 ± 0.801	0.244 ± 0.082	0.029 ± 0.005
TASSO	22	3.470 ± 1.349	0.135 ± 0.027	0.062 ± 0.019
TASSO	34	3.282 ± 0.997	0.149 ± 0.026	0.028 ± 0.004
TOPAZ	58	2.466 ± 0.375	0.087 ± 0.054	0.035 ± 0.012
OPAL	91.2	3.2 ± 0.172	0.162 ± 0.026	0.062 ± 0.007

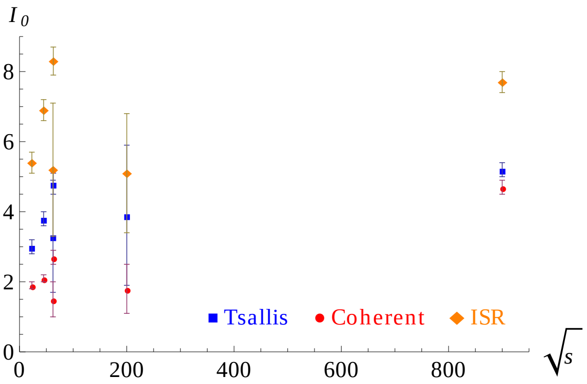

FIGURE 1.33 – Limite souple I_0^{pp} de la densité invariante extrapolées à l'aide Tsallis ajustement (jaune) et la fonction cohérente (rouge) pour pions chargés dans p, p collisions.

celui du modèle Tsallis). Cette tension est la plus efficace dans le χ^2 de valeur, mais a peu d'effet sur le montant extrapolé I_0 et nous n'avons donc pas pousser plus loin ce jeu avec la gamme de p_T et a gardé les valeurs mentionnées ci-dessus. Pour kaons et protons, l'ajustement cohérent fonctionné aussi bien que Tsallis. Enfin, la fonction de Bose- Einstein était assez instable, ce qui donne par hasard une bonne représentation des données et, parfois, une mauvaise description.

Pour les kaons chargés, la limite de bas energies indique la tendance d'être indépendant sur l'énergie de collision, à l'exception du point PHENIX à 62,4 GeV, l'extrapolation de ce qui donne valeur plus petite, ce qui est également le cas pour les protons. Il est également utile de mentionner que les points ISR à 23 et 45 GeV afficher une valeur légèrement supérieure, mais remarquablement, les derniers points qui correspondent à des énergies comprises entre 63 et 900 GeV sont bien alignés les uns avec les autres. En résumé, nous concluons que la limite douce pour la densité d'énergie extraite de protons chargés et kaons se prononcer en faveur de la prédiction MLLA à propos de l'indépendance énergétique.

Table 1.6 – Les valeurs de I_0 pour la production de pions dans e^+e^- collisions et les différents modèles d'ajustement.

l'experience ($\sqrt{s}$)	model	$I^{ee}_{0\,\pi}$ en GeV^{-2}	ndf	χ^2/ndf	R^2
ALICE (900 GeV)	Tsallis	5.2 ± 0.1		2.1	99.97%
	Coherent	4.7 ± 0.1	18	5.3	99.92%
	ISR	7.7 ± 0.2		14.5	99.8%
	B-E	5.7 ± 0.1	19	12.5	99.8%

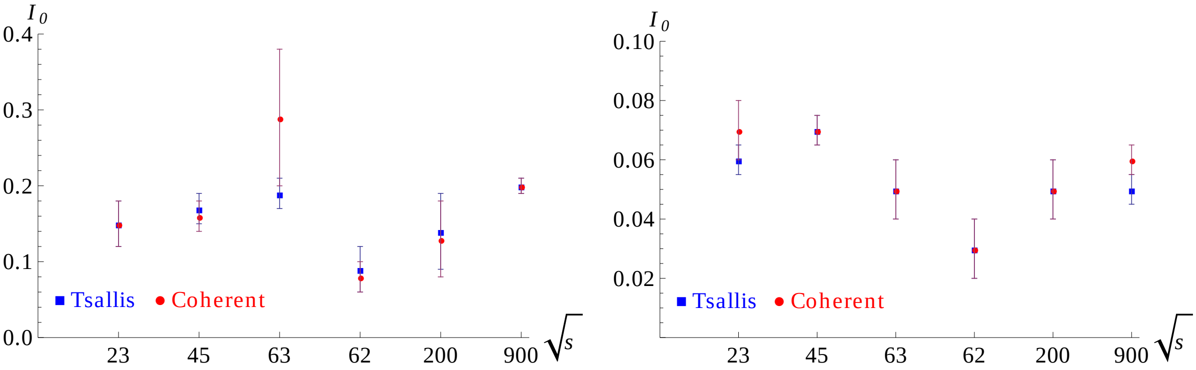

Figure 1.34 – Limite souple I_0 de la densité invariante extrapolées à l'aide Tsallis ajustement (jaune) et la fonction cohérente (rouge) pour kaons chargés et de protons dans des collisions pp.

1.8.3 Comparaison entre e^+e^- et pp

Ayant observé que les limites des différentes distributions invariantes sont conformes à la propriété d'indépendance énergétique, il est utile d'extraire une moyenne de valeur de $I_{0\,\pi}$. Pour les pions, nous obtenons

$$I^{ee}_{0\,\pi} = 4.3 \pm 0.1, \qquad I^{pp}_{0\,\pi} = 4.4 \pm 0.1, \tag{1.8.2}$$

pour l'ajustement Tsallis, et

$$I^{ee}_{0\,\pi} = 3.2 \pm 0.1, \qquad I^{pp}_{0\,\pi} = 3.2 \pm 0.1, \tag{1.8.3}$$

pour la fonction de cohérence. A partir de ces résultats, les ratios de pp/e^+e^- peuvent être estimée

$$\frac{I^{pp}_{0\,\pi}}{I^{ee}_{0\,\pi}} = 1.0 \pm 0.05[\text{Tsallis}] \qquad \frac{I^{pp}_{0\,\pi}}{I^{ee}_{0\,\pi}} = 1.0 \pm 0.05[\text{coherent}]. \tag{1.8.4}$$

Table 1.7 – Les valeurs de I_0 pour la fonction de Tsallis pour les pions, kaons et de protons dans les collisions $p\,p$.

l'experience	$\sqrt{s}$	$I^{pp}_{0\,\pi}$	$I^{pp}_{0\,K}$	$I^{pp}_{0\,p}$
BS	23	3.012 ± 0.174	0.154 ± 0.014	0.065 ± 0.003
BS	45	3.828 ± 0.189	0.170 ± 0.022	0.070 ± 0.003
BS	63	4.837 ± 0.257	0.190 ± 0.024	0.053 ± 0.009
PHENIX	62.4	3.330 ± 1.587	0.094 ± 0.028	0.033 ± 0.010
PHENIX	200	3.858 ± 2.022	0.143 ± 0.049	0.052 ± 0.012
ALICE	900	5.244 ± 0.129	0.205 ± 0.205	0.052 ± 0.004

Table 1.8 – Les valeurs de I_0 de la fonction cohérente pour les pions, kaons et protons dans les collisions $p\,p$.

l'experience	$\sqrt{s}$	$I^{pp}_{0\,\pi}$	$I^{pp}_{0\,K}$	$I^{pp}_{0\,p}$
BS	23	1.864 ± 0.113	0.155 ± 0.032	0.072 ± 0.008
BS	45	2.137 ± 0.114	0.161 ± 0.023	0.073 ± 0.006
BS	63	2.735 ± 0.152	0.286 ± 0.092	0.052 ± 0.009
PHENIX	62.4	1.494 ± 0.521	0.080 ± 0.024	0.031 ± 0.010
PHENIX	200	1.774 ± 0.713	0.128 ± 0.047	0.050 ± 0.013
ALICE	900	4.230 ± 0.117	0.197 ± 0.012	0.057 ± 0.003

Sur la base de l'observation de χ^2/ndf qui a tendance à favoriser le modèle cohérent pour e^+e^- extractions et la fonction Tsallis pour $p\,p$ les le rapport peut-être mieux estimée en utilisant l'estimation de Tsallis pour $I^{pp}_{0\,\pi}$ et le résultat cohérent pour $I^{ee}_{0\,\pi}$ ce qui pousse le rapport un peu plus haut

$$I^{pp}_{0\,\pi}/I^{ee}_{0\,\pi} = 1.4 \pm 0.1, \tag{1.8.5}$$

qui est encore un peu faible en comparaison avec le rapport prévu à partir des facteurs de couleurs.

1.9 Conclusion

Le but de cette étude était de déterminer et de mesurer les observables approprié pour l'expérience ALICE afin de vérifier le phénomène de cohérence du couleur de la chromodynamique quantique. Les deux sujets suivants ont été élaborés : la distribution dynamique inclusive de particules dans un jet et l'universalité de la production de hadrons dans le cas limite d'impulsion nulle.

La mesure de la distribution en impulsion des particules compris dans un jet est un projet de longue haleine qui nécessite plusieurs années de l'exploitation du LHC nécessaires pour collecter les statistiques nécessaires. Pendant ce temps, l'auteur de cette étude a été impliqué dans l'analyse des données recueillies avec les calorimètres électromagnétiques ALICE, EMCAL et PHOS.

La partie expérimentale de cette étude a été principalement consacrée à des mesures neutres mésons à travers leurs désintégrations photons — le sujet le plus possible et adéquat pour le détecteur EMCal au début de l'exploitation du LHC. Les mésons suivants et leurs modes de désintégration ont été envisagées : $\pi^0 \to \gamma\gamma$, $\eta \to \gamma\gamma$, $\omega(782) \to \pi^0\gamma \to 3\gamma$, $K^0_S \to \pi^0\pi^0 \to 4\gamma$. Au cours des études, plusieurs sujets importants liés à EMCal ont été résolus.

Tout d'abord, la correction de non-linéarité d'énergie de la réponse de EMCal a été trouvé à la fois pour les simulations de Monte Carlo (à partir d'une simulation de photon unique), ainsi que pour des données réelles (à partir symétrique $\pi^0 \to \gamma\gamma$ désintégrations). C'est la correction de non-linéarité d'énergie qui nous a permis de voir les sommets de $\omega(792)$ et K^0_S avec les statistiques limitées $L_{\mathrm{int}} = 6.7$ nb^{-1} de l'expérience ALICE en 2010. Les données de simulation/non-linéarité corrections, étant complétées par une décalibration appropriée du détecteur EMCAL dans les simulations, qui nous a permis d'atteindre une bonne coïncidence entre les données et les simulations de Monte Carlo.

Second, the data quality assurance framework was developed for both electromagnetic calorimeters and is now a part of the official ALICE analysis train. This work was published as an ALICE analysis note [8]. Thanks to it, good runs appropriate for the π^0 and η meson measurements were selected, while the EMCAL acceptance was correctly accounted for.

Deuxièmement, le cadre d'assurance qualité des données a été developpé pour les deux calorimètres électromagnétiques et fait maintenant partie du train ALICE analyse officielle. Ce travail a été publié dans une note d'analyse ALICE [8]. Grace à lui, les bons runs appropriées pour les mesures des specters de π^0 et η mésons ont été choisis, alors que l'acceptation EMCal a été correctement comptabilisés.

Bien que le travail préparatoire mentionnée ci-dessus est essentiellement technique, il s'agit d'une condition préalable essentielle pour l'analyse de la physique puisque sans elle, aucun résultat de la physique pourrait être obtenu.

Troisièmement, toutes les mesures nécessaires pour les mesures de π^0, ainsi que pour η mésons ont été effectuées. Cela comprend l'extraction des spectres bruts, le calcul des spectres de production et le calcul des erreurs systématiques pertinentes. Le méson neutre mesuré les spectres, d'être intéressant en soi, donner un point de référence pour les mesures d'ions lourds à laquelle l'expérience ALICE est dédié.

Quatrièmement, le rapport des deux spectres de production d'η/π^0 a été mesurée. Notons que cette mesure est plus simple que mesures distinctes des spectres de π^0 et η depuis plusieurs incertitudes importantes (pour le cas de EMCAL) s'annulent dans le rapport. Il s'agit notamment de : l'incertitude de la position du détecteur intérieur de la machine d'ALICE, l'incertitude du budget de matériau en face de la EMCAL, l'incertitude sur les paramètres de décalibration des simulations de Monte Carlo. Ces trois facteurs s'est avéré être sujets chauds à l'intérieur de la communauté EMCAL. Ainsi, le η/π^0 ratio était, en fait, la première mesure physique qui a été fait avec le détecteur EMCAL.

Enfin, il est à noter que, grâce à ces études pour EMCAL, un haut niveau de compétition amicale a été constamment maintenu entre les deux calorimètres.

En tant que plus proche point de vue, les résultats des mesures de mésons neutres avec le détecteur EMCAL devrait être finalisé et publié. Cela démontrera que toutes les questions liées au détecteur sont résolus ou sous son contrôle, à savoir la réponse du détecteur est bien compris et on sait comment ça marche dans les analyses de physique liés à d'autres photons et des électrons. Plus important encore, ce qui garantira une bonne performance du détecteur à l'avenir.

Séparément des études mentionnées ci-dessus, nous avons effectué une vérification phénoménologique de l'universalité attendu (indépendance de l'énergie de collision $\sqrt{s}$) des spectres des hadrons dans le cas de zéro limite de l'impulsion des hadrons. À cette fin, nous avons appliqué deux méthodes indépendantes à ce sujet.

Dans la première approche, nous avons mesuré les spectres inclusives pour $\pi^{\pm}$, $K^{\pm}$ et (anti)protons pour plusieurs expériences en pp ($p\bar{p}$) et $e^{+}e^{-}$ dans un large gamme d'énergies de collision, a effectué une procédure d'ajustement pour chaque spectre et extrait l'extrapolation des valeurs des spectres invariantes des hadrons à la limite de la quantité de mouvement nulle. Bien que les résultats sont en accord avec les prédictions théoriques, leurs grandes incertitudes systématiques ne permettent pas de faire une déclaration ferme sur l'universalité des spectres.

Cela a été principalement causée par l'absence de données à une dynamique très faible et donc des incertitudes inévitables dans les extrapolations à zéro dynamique.

Comme la seconde approche, nous avons considéré les ratios de spectres inclusive des particules chargées dans les collisions pp. Contrairement aux hadrons spectres eux-mêmes, les ratios des spectres des énergies de collision différentes $\sqrt{s}$ sont des fonctions lentes de l'impulsion. Étonnamment, ils se sont avérés être des fonctions linéaires dans un large gamme d'impulsion $0.6\,\mathrm{GeV/c} < p_T < 2.5\,\mathrm{GeV/c}$. Ce fait nous a permis de faire des extrapolations des rapports à zéro impulsion en toute sécurité et de manière fiable. A la suite, les extrapolations donné l'unité avec une bonne précision qui nous a permis de conclure que, du moins dans les collisions pp, l'universalité a lieu, dans les erreurs systématiques de l'ordre de 10%.

En ce qui concerne le spectre des hadrons eux-mêmes, la linéarité trouvé s'est avéré être lié à ralentir l'évolution de paramètres avec $\sqrt{s}$ des fonctions d'ajustement. En outre, nous avons pu observer des "effets de masse" à l'impulsions $p_T < 0.6$ GeV/c, c'est à dire la rupture de la tendance linéaire en raison de non nulles masses des quarks. Celui-ci suggère que, dans la pratique, au lieu de considérer l'extrapolation des spectres des crises de hadrons à zéro impulsion, il est plus approprié de considérer les rapports de ceux qui s'intègre prises dans une région de l'impulsion de départ d'environ 0.6 GeV/c et linéairement extrapoler les taux à zéro dynamique. Ce travail est cependant un sujet de recherche distinct.

L'approche des rapports de spectres est simple, efficace et prometteur. En ce qui concerne les perspectives, il est très tentant de considérer les prédictions théoriques correspondantes pour les rapports de deux gluons-jets ou deux quarks-jets à différentes énergies $\sqrt{s}$ dans le cadre MLLA.

Chapitre 2

Introduction

Theoretical prediction of various quantities in quantum chromodynamics (QCD) is a challenging subject. In particular, hadron spectra cannot be obtained from first principles. However, certain domains of the theory may admit quantitative description. For instance, in hard processes, energy and momentum exchange between partons produced from colliding hadronic particles is so large that the partons can be considered as free (unbound) particles. This is due to the asymptotic freedom of QCD [1] : for large momentum transfer, the constant of strong interaction becomes small, and the perturbative Feynman graph-based calculation becomes possible. After the primary "perturbative" collision, the produced partons hadronize, and this process is again not addressable analytically from the first principles of QCD.

Another domain of QCD — soft hadronic spectra and, in particular, soft spectra inside jets produced in a high energy collision. Studying multihadron production in relativistic collisions may contribute valuable information about characteristics of partonic branching processes of QCD. These processes originate from the gluon bremsstrahlung and are mathematically described by a sum of infinite number of Feynman graphs. The latter becomes singular (logarithmically large) in the limit of soft emission. It turns out that, driven by the so called *color coherence* phenomenon, large logarithmic terms can be summed up. This result is well understood qualitatively as well as quantitatively (see, for example, [2, 3]). Its experimental confirmation was one of the greatest successes which resulted in dramatic revision of theoretical expectations in soft hadron physics.

Analytical calculations of partonic branching processes of QCD give various partonic densities as an output since the hadronization scheme, i.e. the transition from colored partons to colorless hadrons, is still not accessible theoretically. Thus, the application of calculated multiparton observables requires additional assumptions. The simplest approach is *Local Parton-Hadron Duality* (LPHD) [4]. It assumes that hadron and parton spectra are proportional to each other (with a conversion coefficient determined from data) so that hadron observables are directly given by corresponding parton observables calculated analytically. The LPHD is well supported experimentally.

Soft hadron production measurement in *pp* collisions at LHC opens up a new kinematic regime for testing and validating the predictive power of quantum chromodynamics. The ALICE experiment has excellent charged particle tracking and particle identification capabilities in a wide range of particle momenta. In addition, it is unique among the LHC experiments for its particle tracking and particle identification capabilities at low momentum range (see Chapter 4 for an overview). This is very important in the view of scrutinizing mechanism of particle production at intermediate and low momentum. Although ALICE is a dedicated heavy ion experiment, its physics program in *pp* collisions is very rich. One field of investigation is that of intrajet physics which requires dedicated tools for selecting and measuring jets. A valuable ingredient for this purpose is triggering on "photon-jet" events which along with a jet contain an isolated photon moving in the opposite direction, thereby giving a good estimation of the jet energy (for a brief overview of jet energy resolution, see Appendix I). In the ALICE experiment, photons are measured with two electromagnetic calorimeters, PHOS and EMCAL.

The aim of this study was to find and measure observables adequate for the ALICE experiment in order to verify the color coherence phenomenon. Discrepancies between theoretical predictions and measured quantities would mean that there are some unexpected contributions from incoherent multi-component processes. To this end, we discuss the following two subjects below : inclusive momentum distribution of particles in a jet and universality of soft hadron production. Correspondingly, the present study involves experimental part devoted to analysis of data collected by the ALICE electromagnetic calorimeters and theoretical part of analysis of soft hadron spectra of various experiments.

Hadron physics with the ALICE experiment

Theoretical predictions of parton spectra, performed within the so called *Modified Leading Log Approximation* (MLLA) and supplemented with the LPHD idea, can be tested experimentally by measuring the momentum spectra of particles inside a jet. This can be done in experiments which have good charged particle tracking capability. For instance, consider Fig. 2.1 (left) which shows the spectrum of particles inside a jet (in dijet events) for the CDF experiment in $\mathrm{p\bar{p}}$ collisions at $\sqrt{s} = 1.8$ TeV [5]. Here the X axis corresponds to the traditional coordinate

$$\xi = \ln\frac{1}{x}, \qquad x = \frac{p}{E_{\mathrm{jet}}}, \tag{2.1}$$

where p is a particle momentum, E_{jet} – total energy of a jet. The solid line represents the calculated result of the MLLA. One can observe on this figure a depletion of particles with large ξ which corresponds to low momentum. The shape of the distribution is usually referred to as the *Hump-Backed Plateau* (HBP).

The HBP measurement with the ALICE experiment will allow one to test the predictions of the MLLA at the new energy regime of the LHC.

Feasibility studies of jet detection in ALICE with various event topologies [6, 7] show that the measurement of inclusive momentum distribution of particles in a jet with ALICE is a long-term project since it requires large amount of statistics to be collected (counting rates are quoted in Appendix II). Nevertheless, the preparatory work also demands a lot of efforts. Here is a minimal required program which must be completed by the ALICE detectors before any measurement with jets becomes possible :

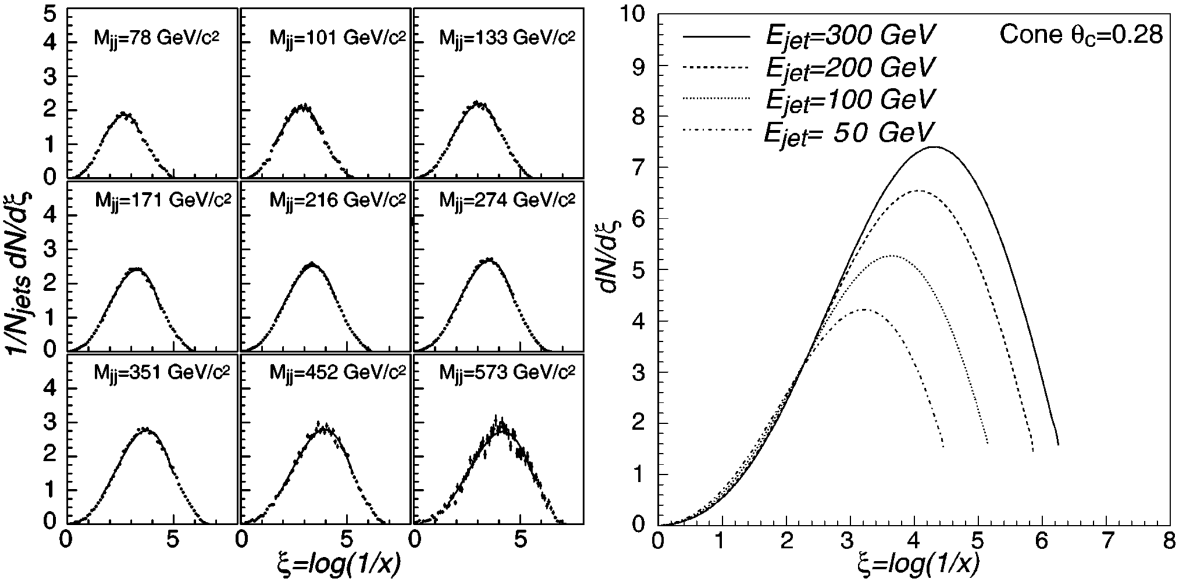

FIGURE 2.1 – CDF experiment, $p\bar{p}$ collisions at $\sqrt{s} = 1.8$ TeV. Left : inclusive momentum distribution of particles in a jet for nine jet energies. Solid line represents the MLLA prediction. Right : the evolution of the MLLA predicted parton spectrum for a gluon jet. The four lines correspond to jet energies $E_{\text{jet}} = 50$, 100, 200 and 300 GeV. Jets were taken in a restricted cone of size $\theta_c = 0.28$ rad. Plots taken from [5].

1. Quality assurance, calibration and correction of collected data.
2. Good detectors performance must be verified by measuring quantities related to physical signals. By doing so, one confirms that each detector subsystem operates as expected.
3. Monte Carlo tuning : a close match between simulation and data must be achieved.
4. Inclusive hadron spectra measurements, including identified charged hadrons and neutral mesons detected by the ALICE tracking system and the ALICE calorimeters respectively.
5. Jet reconstruction.

As a member of the EMCAL group, the author of this study was involved in work with ALICE electromagnetic calorimeters, PHOS and EMCAL. At the end of 2009, when datataking began, there arisen strong necessity to perform the first four steps quoted above.

The methods of data quality verification for the ALICE calorimeters are described in Chapter 5. The developed quality assurance framework [8] gives fast and convenient way to verify data quality both for PHOS and for EMCAL. Without it, the reliability and stability of data cannot be achieved.

The steps 2, 3 and 4 from above are discussed in Chapter 6 for the case of the EMCAL detector. The performance for the electromagnetic calorimeter can be verified by measuring lightest neutral meson spectra (π^0, η, $\omega(782)$, K^0_S). Although the EMCAL detector was installed among the last ones, the collected data already give a possibility to measure the π^0 and η mesons production spectra in their two-photon decay modes as well as η/π^0 ratio. See also Refs. [9, 10].

Universality in soft hadron production

The Hump-Backed Plateau is one of the basic distributions widely used in previous experiments to test the MLLA predictions. As was already pointed out, such a measurement involves much effort as it requires to do jet reconstruction in the ALICE experiment. There is yet another prediction that is remarkably simpler. This is inclusive hadron production spectra Ed^3n/dk^3 in the limit of zero momentum, where E is particle energy, $\vec{k}$ – its momentum.

Indeed, in the limit of low parton momentum, the Born term dominates in the perturbative expansion of a partonic cascade. According to the MLLA, it is given by

$$E\frac{d^3n}{dk^3} \sim C\,\frac{\alpha_S(k_\perp)}{k_\perp^2}, \qquad k_\perp \to 0. \tag{2.2}$$

Here the transverse momentum $\vec{k}_\perp$ is taken with respect to a collision axis, α_S is running strong coupling constant, while C is a color factor relevant for a minimal partonic process. The latter follows from the fact that a radiated long-wavelength parton cannot resolve the structure of the collision so that its radiation intensity is sensitive only to the total color charge of the underlying process. In other words, only early dynamics of the underlying process is important.

The formula (2.2) is remarkable. It shows that at very low momentum inclusive hadron spectra are *independent of the collision energy* $\sqrt{s}$ [11]. This universality is the subject of intensive studies [12, 13].

Another consequence is that relative normalization of spectra at zero momentum in different collision processes is given by the ratio of relevant color factors. In e^+e^- annihilations, in the Born approximation, soft gluons are radiated from a quark or an antiquark, which leads to a color factor $C_F = 4/3$ of fundamental representation of SU(3). On the contrary, in *pp* collisions, this factor corresponds to a color octet (adjoint representation), $C_A = 3$. In this way, one expects that the ratio reads

$$r = \lim_{k\to 0}\frac{d^3n^{pp}/dk^3}{d^3n^{ee}/dk^3} = \frac{C_A}{C_F} = 2.25. \tag{2.3}$$

There are plenty of experimental data for inclusive and identified soft hadron production spectra in different experiments for different collision energies. In Chapter 7, we perform the extraction of the zero-momentum limits in a systematic way, following the spirit of studies of Refs. [11, 12, 13].

Separately, in Chapter 8, we implement a different approach by considering ratios of spectra of different collision energies. Surprisingly, these ratios appear to be linear functions in a wide range of momentum.

Structure of the manuscript

The structure of the manuscript is as follows.

In Chapter 3, we give an introduction to color coherence phenomenon in QCD, selecting some of the relevant material from Ref. [2]. In the leading and the simplest order, the calculation of soft parton spectra from Feynman graphs of partonic cascades is performed in the *Double Logarithmic Approximation* (DLA). The DLA incorporates main ingredients of the technique and delivers clear qualitative description of soft parton physics. Still, the incorporation of next-to-leading order terms of the MLLA is necessary to get a good quantitative description. In this chapter, we stay at the level of the DLA, giving just a glimpse of modifications expected within the MLLA.

Chapter 4 is devoted to an overview of the LHC as well as of the ALICE experiment.

The data quality assurance framework is discussed in Chapter 5. We discuss general ideas of the data quality assurance and explain the methods which were developed and applied for the ALICE calorimeters. The work presented in this chapter is published as an ALICE analysis note [8].

Chapter 6 gives an overview of the performed studies of the neutral mesons with the EMCAL detector [14, 15]. The following processes were considered : $\pi^0 \to \gamma\gamma$, $\eta \to \gamma\gamma$, $\omega(782) \to \pi^0\gamma \to 3\gamma$, $K^0_S \to \pi^0\pi^0 \to 4\gamma$. In particular, the steps for obtaining raw and production spectra as well as final status and results are discussed.

In Chapter 7, we perform systematic studies of the zero momentum limit of identified hadron spectra taken from several hadron and lepton experiments at the collision energies from tenth of GeV up to the TeV scale of the LHC. To test the color coherence predictions, we fit the spectra with different functions and extrapolate the fits to zero momentum.

In Chapter 8, we elaborate a different approach, where we consider ratios of hadron spectra at different energies. With this method, we are able to test the universality of soft hadron production with good precision, as the ratios are linear functions in a wide range of momentum.

Finally, the conclusion completes the manuscript. The original results of this study are collected in Chapters 5, 6, 7 and 8.

Appendix I : jet energy resolution and event topology

Jet energy resolution is affected mainly by two factors :

- *Charge-to-neutral fluctuations.*
  This ambiguity comes from the fact that detector subsystems are able to measure and identify only charged particles and photons. All other neutral particles in jets stay undetected. Neutral particles usually contribute of about 1/3 of a total jet energy. This contribution, however, is not constant and fluctuate from jet to jet.
- *Out-of-cone fluctuations.*
  This uncertainty is related to jet finding algorithms and ambiguity in determination of jet cone radius. Indeed, one usually fixes jet cone radius and counts particles inside the cone around the "jet axis" (e.g. the most energetic particle). By doing so, one also counts particles which do not belong to the jet. The fluctuations of "true" jet particles as well as background particles inside the cone bias the jet energy resolution. Note also that taking smaller cone radius reduces the background but increases a chance to miss particles which, in fact, belong to the jet, and *vice versa.*

The demonstration of the result of fluctuations is shown on Fig. 2.2.

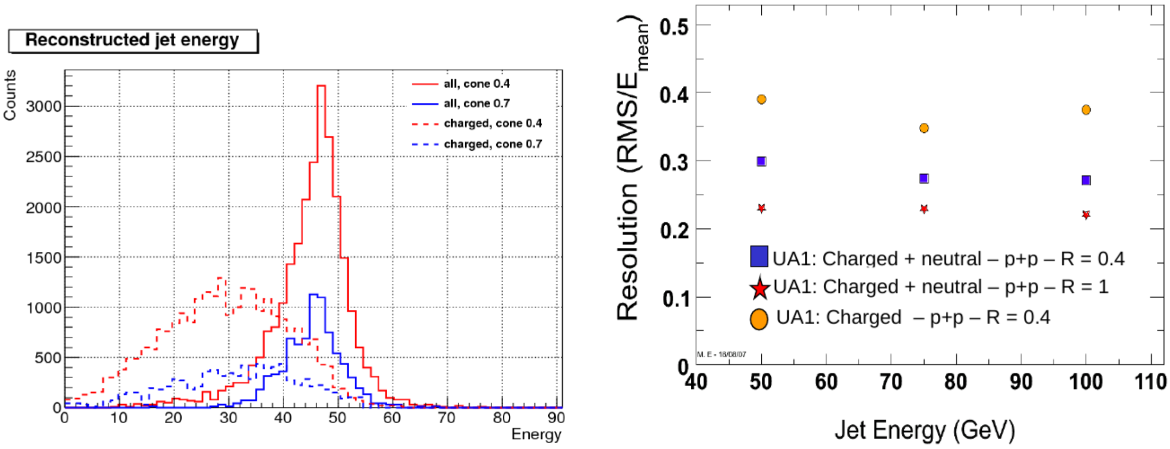

FIGURE 2.2 – Left : jets 48-52 GeV generated with Pythia and reconstructed with Pycell using different cone sizes (0.4 or 0.7) and counting charged+neutral or only charged particles. Right : full Monte Carlo simulation and reconstruction using jet finder UA1 experiment.

The discussed fluctuations make jet reconstruction a challenging procedure. However, jet energy resolution can be improved (in particular, in the case of the measurement of inclusive momentum distribution of particles in a jet) by using different *event topologies.* The following event topologies are usually considered (Fig. 2.3) :

- Inclusive jet events or monojets is just a counting of all jets. It has the worst jet energy resolution.
- Dijet events are whose which contain two jets in opposite directions. Dijet detection improves jet energy resolution as the information comes from two jet reconstructions. On the other hand, by considering dijet events, one clearly reduces the available statistics as compared to monojets.

- γ-jets are whose with a jet and an isolated photon in the opposite direction. Photon tagging of a jet improves jet energy resolution to the level of order of the photon energy resolution. Such events are very rare, however. Photon identification were extensively studied with both ALICE electromagnetic calorimeters [16, 17]. For example, the efficiency of photon identification in EMCAL in *pp* collisions is about unity in 10-50 GeV region, the purity of the signal is more than 70%.
- Finally, we can imagine π^0-jets which is tagging of a jet by an isolated π^0 meson. This worses the jet energy resolution as compared to γ-jets, but may improve the jet counting rates.

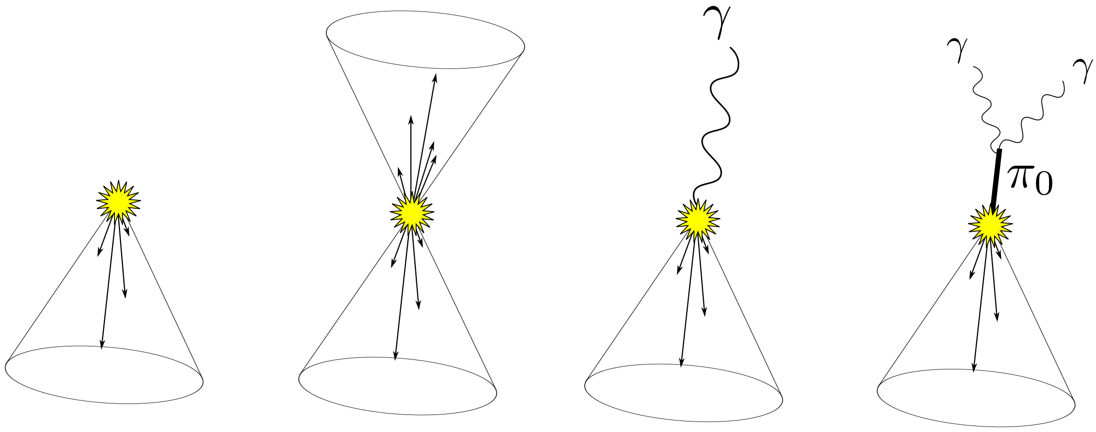

FIGURE 2.3 – Event topologies (from left to right) : inclusive jet events, dijets, γ-jets, π^0-jets.

Generally, in measurements related to the internal structure of a jet, dijet events are considered to be a good compromise between an improvement of energy resolution and a worsening in amount of available statistics. Physics program with the ALICE experiment includes also measurements with γ-jets — a class of events that is very promising for the measurement of inclusive particle spectra inside jets. This requires, however, the mastering of the calorimeters up to the measurement of isolated photons in order to really select the topology of interest. In these studies, the necessary preliminary work with the ALICE electromagnetic calorimeters PHOS and EMCAL was performed. It is described in Chapters 5 and 6.

Appendix II : jet counting rates

The estimations of expected jet counting rates are given in Figs. 2.4, 2.5 and 2.6. The cross-sections were calculated from Monte Carlo simulations using Pythia generator and Pycell reconstruction algorithm, taking the jet cone size $\theta_c = 0.4$. The right plots are drawn for integrated luminosity of $L_{\text{int}} = 1$ pb^{-1}.

In the plots for monojets and dijets, jets are reconstructed in full 2π azimuth angle and $|\eta| \leq 0.5$ pseudorapidity region. In the plot for γ-jets, the photon was taken in PHOS ($260° \leq \varphi \leq 320°$, $|\eta| \leq 0.12$), while the jet was taken in EMCAL ($80° \leq \varphi \leq 120°$, $|\eta| \leq 0.3$).

As of 2012, the integral luminosity of the ALICE experiment was about 5 pb^{-1}. Thus, at this luminosity, one can expect to have of about 10^5 dijet events and of about 20 γ-jet events with jet energy 100 GeV.

Also, as one can see, for 2010 data, where the integrated luminosity is about $L_{\mathrm{int}} = 6\ \mathrm{nb}^{-1}$, the γ-jet sample is negligible for considering the beginning of the HBP measurement program within the present studies.

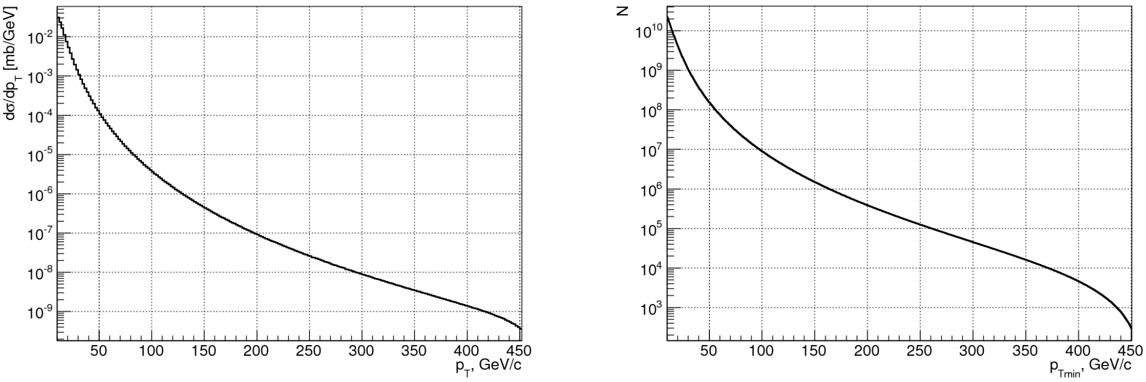

FIGURE 2.4 – Left : jet inclusive cross-section ; right : jet counting rates.

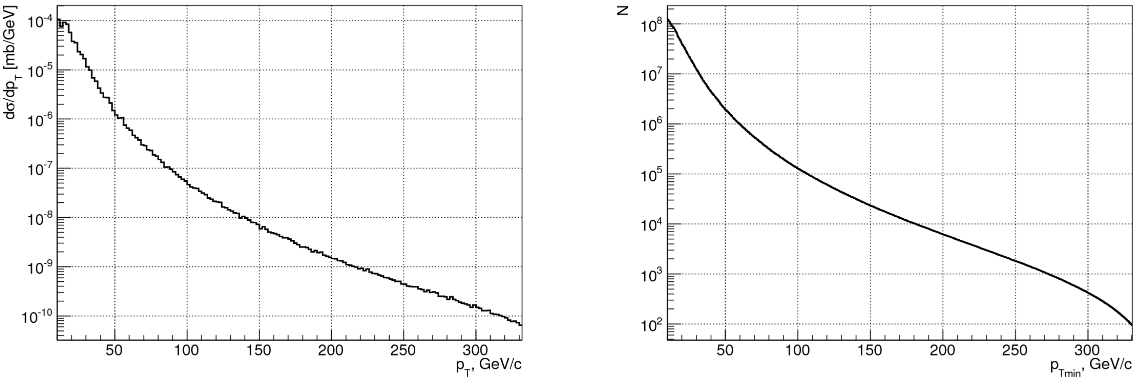

FIGURE 2.5 – Left : dijet inclusive cross-section ; right : dijet counting rates.

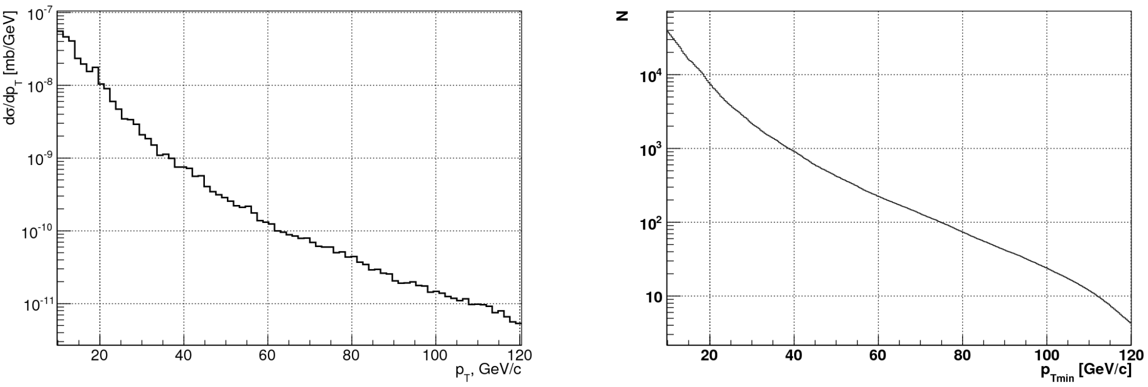

FIGURE 2.6 – Left : γ-jet inclusive cross-section ; right : γ-jet counting rates.

Chapitre 3

Theoretical background : essence of color coherence

In this chapter, the origins of color coherence and angular ordering effects in QCD are explained. We use qualitative (wavelengths and formation time) as well as quantitative (sums of Feynman diagrams) arguments. We show how the discussed double logarithmic approximation formalism allows one to predict qualitatively the Hump-Backed QCD Plateau for distribution of energy of hadrons inside a jet.

3.1 Origin of coherence

Soft hadron spectra and, in particular, soft spectra inside jets produced in a high energy collision can be calculated analytically. To this end, consider a high energy collision, where many soft partons are produced. Their production in a jet can be represented by a *shower picture* – a sequence of parton branchings (see Fig. 3.1). In a soft particle momenta limit, the leading contribution to every cross-section of showering contains large logarithms. These large logarithms can be calculated systematically. By keeping only dominant terms (*leading logs*), one can sum up whole perturbative expansion of Feynman diagrams. As a result, one can obtain, for instance, *parton densities* in a shower cascade, i.e. the distribution of the number of partons in the energy and the angle. Finally, the calculated parton densities can be translated into hadron spectra using the experimentally supported assumption of Local Parton-Hadron duality (LPHD) [4]. The latter states that spectra of the bremsstrahlung partons coincide, up to a constant multiplicative factor, with hadron spectra at the same momenta.

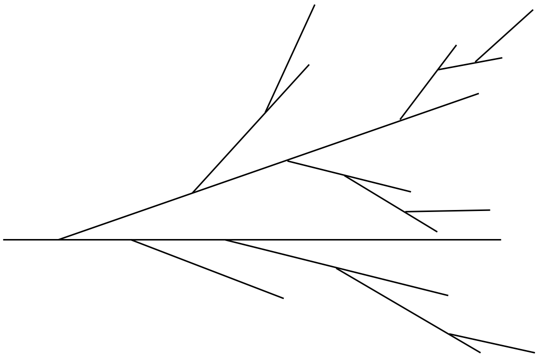

Figure 3.1 – A shower picture.

In the present chapter, we discuss the physical origin of color coherence in QCD, selecting some of the relevant material from Ref. [2]. For this purpose, we consider e^+e^- as a primary collision process (see Fig. 3.2) and illustrate how the parton branching behaves at leading logs. In planar gauge, the quark and the antiquark emit gluons independently, so that, for definiteness, we will follow the process of gluon emission off the quark leg.

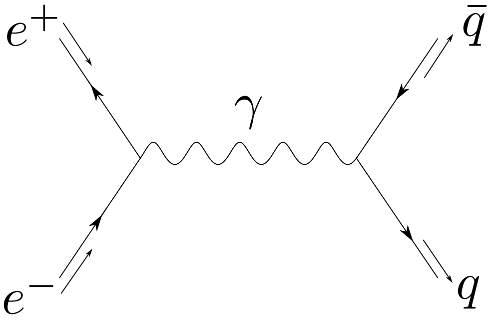

Figure 3.2 – e^+e^- annihilation.

The analysis of diagrams for $e^+e^- \to q\bar{q} + Ng$ in all orders of perturbation theory shows that the branching parton cascade develops only in the region of strictly ordered and sequentially shrinking angular cones. Outside this kinematic region, the emission of soft gluons is suppressed due to destructive interference. Such a coherence phenomenon is analogous to the well known Chudakov effect in quantum electrodynamics [18].

3.1.1 Double logarithmic approximation

Let us show how the leading logarithmic contribution to the cross-section σ_N arises for the process $e^+e^- \to q\bar{q} + Ng$ (N-gluon emission) in the limit of soft gluon momenta.

The cross-section σ_N is proportional to the following integral over the whole phase space of N final gluons :

$$\sigma_N \sim \int |M_N|^2 \prod_{i=1}^{N} \frac{d^3k_i}{2\omega_i}, \tag{3.1.1}$$

where M_N is the matrix element for the production of N gluons, $\vec{k}_i$ – gluon momenta, ω_i – gluon energies. Let us emphasize that, taking into account the indistinguishability of gluons, it is possible to arrange the expression of σ_N in such a way that gluons are enumerated in decreasing order of their energies : $i = 1$ corresponds to the largest energy, while $i = N$ to the smallest. Let us also denote by E_0 the energy of the parent parton from which the shower cascade with N gluons evolved (the primary quark or anti-quark for our case).

It turns out that the leading contribution to the integral in (3.1.1) is accumulated from the region of phase space where the energies of the final gluons are *strongly* ordered :

$$E_0 \gg \omega_1 \gg \omega_2 \gg ... \gg \omega_N \qquad \text{[strong energy ordering]}. \tag{3.1.2}$$

In addition, the angles of the consecutive emissions are small and also strongly ordered *in the same order* :

$$1 \gg \theta_1 \gg \theta_2 \; ... \gg \theta_N \qquad \text{[strong angular ordering]}, \tag{3.1.3}$$

where θ_i is the angle of emission of i-th final gluon *with respect to its parent parton*, see Fig. 3.3.

In the mentioned region of the phase space of N gluons, the amplitude M_N has the most singular behavior with respect to the limit $\omega_i \to 0$, $\theta_i \to 0$. For illustration purposes, we calculate the corresponding amplitudes for $N = 1$ and $N = 2$ cases in Section 3.1.2. Here, let us present the expression for the dominant contribution to the amplitude M_N. To this end, let us note that this contribution comes from two types of branchings : $q \to q + g$ and $g \to g + g$, i.e. from emission of gluon from quark and from emission of gluon from gluon. In this approximation, the emission of two gluons from a gluon $g \to g + 2g$, is

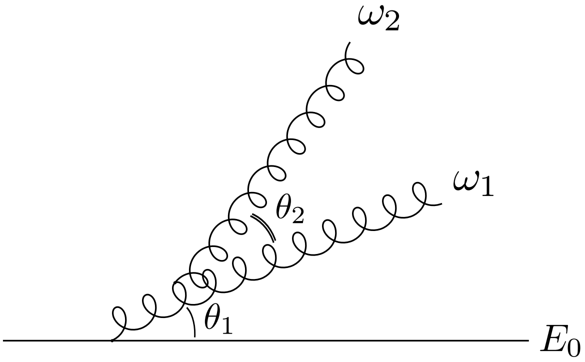

FIGURE 3.3 – Angles and energies of consecutive gluon emissions. For simplicity, all emissions are drawn in one plane.

neglected. In this way, the amplitude M_N is given by

$$M_N^{\mathrm{DLA}} \sim g_s^N \prod_{i=1}^{N} \frac{e_i P_i}{k_i P_i} \times [\text{color factor}] \qquad [\text{Double Log Approximation}] \tag{3.1.4}$$

with $e_i = (0, \vec{e}_i)$ being the polarization 4-vector of the i-th gluon (the 3-vector component $\vec{e}_i$ is orthogonal to $\vec{k}_i$, $\vec{e}_i \vec{k}_i = 0$), $P_i = (E_{P_i}, \vec{P}_i)$ – the 4-momentum of the parent of the i-th gluon (see Fig. 3.4), g_s – the coupling constant of the strong interaction. In the phase space region of interest, assuming that all partons are massless, the scalar products $k_i P_i$ and $e_i P_i$ are given by

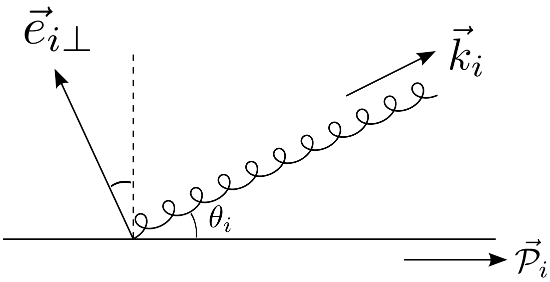

FIGURE 3.4 – The gluon polarization vector $\vec{e}_i$ lies in the plane perpendicular to $\vec{k}_i$.

$$k_i P_i = \omega_i E_{P_i} - \vec{k}_i \vec{P}_i \approx \omega_i E_{P_i} (1 - \cos\theta_i) \approx \omega_i E_{P_i} \frac{\theta_i^2}{2} \tag{3.1.5}$$

and

$$e_i P_i = -\vec{e}_i \vec{P}_i = |\vec{e}_{i\perp}| E_{P_i} \sin\theta_i \approx |\vec{e}_{i\perp}| E_{P_i} \theta_i, \tag{3.1.6}$$

where $\vec{e}_{i\perp}$ is the projection of $\vec{e}_i$ onto the $\{\vec{k}_i, \vec{P}_i\}$ plane.

Combining all the above and performing the sum over the physical polarizations of the final gluons, one obtains the following expression for the cross-section (3.1.1) :[1]

$$\sigma_N^{\mathrm{DLA}} \sim \prod_{i=1}^{N} \int \sum_{\mathrm{polar.}} \left| \frac{|\vec{e}_{i\perp}| E_{P_i} \theta_i}{\omega_i E_{P_i} \theta_i^2} \right|^2 \frac{\omega_i^2 d\omega_i \theta_i d\theta_i}{2\omega_i} \sim \prod_{i=1}^{N} \left(\int \frac{d\omega_i}{\omega_i} \int \frac{d\theta_i}{\theta_i} \right), \tag{3.1.7}$$

where we substituted $d^3k \sim \omega_i^2 d\omega_i \theta_i d\theta_i$ and used the fact that $\sum\limits_{\mathrm{polar.}} |\vec{e}_{i\perp}|^2 \approx 1$.

The very last expression in (3.1.7) shows the leading logarithmic behavior in the region of phase space where the angles and the energies are strongly ordered as in Eqs. (3.1.2) and (3.1.3). Keeping this in mind, one obtains after the integration

$$\sigma_N^{\mathrm{DLA}} \sim \prod_{i=1}^{N} \left(\ln \frac{1}{\omega_i} \ln \frac{1}{\theta_i} \right), \tag{3.1.8}$$

i.e. the resulting cross-section is double-logarithmically divergent in the parameters of each final gluon, and this explains the name of the discussed contribution — *Double Logarithmic Approximation* (DLA).

Let us also illustrate the importance of the strong energy ordering in the DLA. For this purpose, consider, for instance, instead of (3.1.2) the ordering

$$E_0 \gg \omega_1 > \omega_2 \gg \omega_3 \gg ... \gg \omega_N, \tag{3.1.9}$$

i.e. where the energy of the second parton satisfies less strict condition $\omega_2 < \omega_1$. Then, in the last expression of (3.1.7) one would have the following contribution from the second parton :

$$\int_{\omega_2}^{\omega_1} \frac{d\omega_2}{\omega_2} \int_{\theta_2} \frac{d\theta_2}{\theta_2} \approx \ln \frac{\omega_1}{\omega_2} \ln \frac{1}{\theta_2}. \tag{3.1.10}$$

Since $\omega_1 \sim \omega_2$, this gives $\ln \frac{\omega_1}{\omega_2} \sim 1$. Thus, the cross-section σ_N loses one divergent logarithm.

Performing similar reasonings, one can verify the importance of the strong angular ordering. The relative ordering in the energies and the angles cannot be identified, however, on kinematical grounds. It is worth mentioning that the same ordering in the angles as in the energies, which is usually referred to as *angular ordering* (AO), is a non-trivial (quantum mechanical) consequence of the interference between the leading terms in the sum of Feynman graphs. This subject is discussed in more detail in the next section.

Finally, let us remark that the DLA provides means of getting rather simple and physically transparent results and captures main features of physics of parton cascades.

---

[1] We observe that, effectively, the i-th gluon contributes a factor $1/(\omega_i\theta_i)$ to M_N. This fact will be used in Section 3.2, there the toy model of color coherence is considered.

It turns out, however, that the DLA is not enough for quantitative description and, as a consequence, one also needs to incorporate single-log terms to reach a good level of accuracy. The corresponding technique is referred to as *Modified Leading Log Approximation* (MLLA).

Thereby, the MLLA is an attempt to go beyond the scope of the DLA by taking into account also subdominant corrections with single logs. The most notable change in the MLLA as compared to the DLA is that the strong energy and angular ordering rules (3.1.2), (3.1.3) are replaced by less strict

$$E_0 \geq \omega_1 \geq \omega_2 \geq ... \geq \omega_N \tag{3.1.11}$$

and

$$1 \geq \theta_1 \geq \theta_2 \geq ... \geq \theta_N. \tag{3.1.12}$$

In addition, the MLLA accounts for running coupling constant of QCD. A pedagogical approach to the incorporation of the MLLA terms is discussed in the book [2].

3.1.2 Calculation of amplitudes for N-gluon emission

In this section, we explain how the formula of Eq. (3.1.4) for the amplitude of N-gluon production for $N = 1$ and $N = 2$ in the DLA can be obtained. For this purpose, we sum up dominant contributions from relevant tree Feynman diagrams, restricting ourselves to $q \to q+g$ and $g \to g+g$ vertices. In addition, seeking for large logs, we limit ourselves with the requirement that the final gluons are soft with respect to the primary quark, $E_0 \gg \omega_1$, $E_0 \gg \omega_2$. As was discussed above, if $\omega_1 \approx \omega_2$, one logarithm is lost in the cross-section. Consequently, using also the indistinguishability of the gluons, we can order their energies : $\omega_1 \geq \omega_2$. All these arguments lead to the strong energy ordering conditions (3.1.2). We repeat them here :

$$E_0 \gg \omega_1 \gg \omega_2. \tag{3.1.13}$$

Finally, in the $N = 2$ case, seeking for the $1/(\omega_i\theta_i)$ contribution of each gluon to the amplitudes M_N, we demonstrate the emergence of the angular ordering rules (3.1.3).

In what follows, we assume that all partons are massless.

The case N=1

The simplest possible amplitude M_N is for $N = 1$ which corresponds to a single diagram of Fig. 3.5 and describes one-gluon emission off the initial quark. One can easily write a mathematical expression for it :

$$M_1 = -ig_s\bar{\Psi}_f(p_+)\gamma^\mu t_a e_\mu(k)\frac{i\hat{q}}{q^2}, \tag{3.1.14}$$

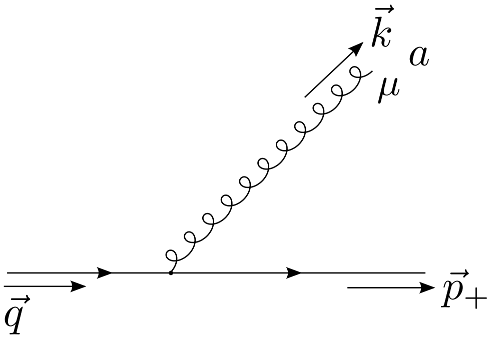

FIGURE 3.5 – One-gluon emission diagram.

where $\bar{\Psi}_f(\vec{p}_+)$ is the final wave function of the quark (which has spinor as well as color indices), t_a are algebra generators for the gauge group SU(N_c) ($N_c = 3$ is the number of colors), while $e_\mu(k)$ stands for the final gluon polarization 4-vector. The notations for the momenta are shown on Fig. 3.5. In addition, $\hat{q} = \gamma^\mu q_\mu$, $q_\mu = p_{+\mu} + k_\mu$. Let us also remark that the quark propagator $\frac{i\hat{q}}{q^2}$ stands for the initial quark leg. It is here since the diagram of Fig. 3.5 presents only a part of the collision process, i.e. it should, in fact, be attached to the diagram of Fig. 3.2.

The expression (3.1.14) can be simplified in the limit of soft gluon momentum, $|\vec{k}| \ll |\vec{p}_+|$. Indeed,

$$\bar{\Psi}_f(p_+)\gamma^\mu(\hat{p}_+ + \hat{k}) = \bar{\Psi}_f(p_+)\left(2p_+^\mu - \hat{p}_+\gamma^\mu + \gamma^\mu\hat{k}\right) \approx 2p_+^\mu \times \bar{\Psi}_f(p_+), \tag{3.1.15}$$

where we used the Dirac equation

$$\bar{\Psi}_f(p_+)\hat{p}_+ = 0 \tag{3.1.16}$$

for the on-shell final quark and neglected the term $\gamma^\mu\hat{k}$. Thus,

$$M_1 \approx g_s \frac{2ep_+}{q^2} \times \bar{\Psi}_f t_a, \tag{3.1.17}$$

substituting

$$q^2 = (p_+ + k)^2 \approx 2kp_+, \tag{3.1.18}$$

we finally get

$$M_1 \approx g_s \frac{ep_+}{kp_+} \times \bar{\Psi}_f t_a. \tag{3.1.19}$$

Clearly, this expression corresponds to (3.1.4) at $N = 1$.

The case N=2

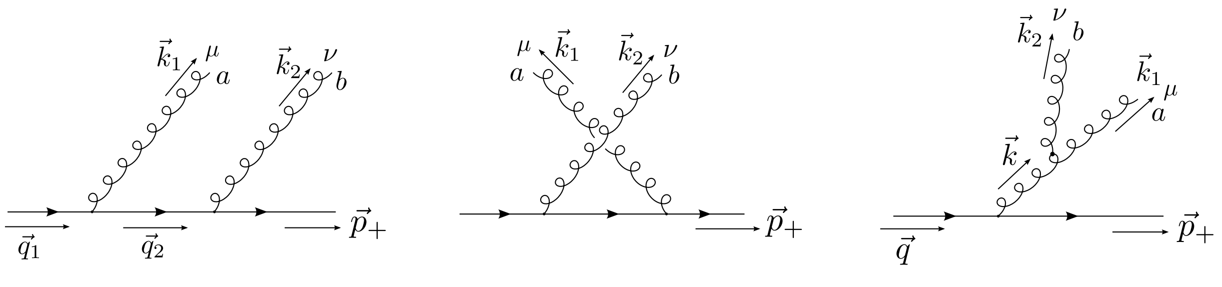

$a)$ $b)$ $c)$

FIGURE 3.6 – Feynman graphs for two-gluon emission.

The amplitude of soft two-gluon emission off a quark is described by the sum of three Feynman graphs shown on Fig. 3.6. Let us begin with the contribution of the diagram on Fig. 3.6a. The corresponding amplitude is

$$M_{2a} = \bar{\Psi}_f(p_+)(-ig_s)\gamma^\nu t_b e_{2\nu}(k_2)\frac{i\hat{q}_2}{q_2^2}(-ig_s)\gamma^\mu t_a e_{1\mu}(k_1)\frac{i\hat{q}_1}{q_1^2}, \tag{3.1.20}$$

with $e_1(k_1)$ and $e_2(k_2)$ being the polarizations of the first and the second gluon respectively, while the kinematic situation is clarified on Fig. 3.6a. The matrix element (3.1.20) can be simplified in the same manner as it was done for the $N = 1$ case, namely, for the numerator,

$$\bar{\Psi}_f(p_+)\gamma^\nu\hat{q}_2\gamma^\mu\hat{q}_1 = \bar{\Psi}_f(p_+)\gamma^\nu(\hat{p}_+ + \hat{k}_2)\gamma^\mu\hat{q}_1 \approx (2p_+^\nu)(2p_+^\mu) \times \bar{\Psi}_f(p_+), \tag{3.1.21}$$

since of Eq. (3.1.16), while for the denominator

$$q_1^2 q_2^2 \approx 2(k_1 + k_2)p_+\, 2k_2 p_+ \tag{3.1.22}$$

Thus,

$$M_{2a} \approx g_s^2 \frac{e_1 p_+}{(k_1 + k_2)p_+}\frac{e_2 p_+}{k_2 p_+} \times \bar{\Psi}_f t_b t_a. \tag{3.1.23}$$

This expression is already quite similar to that of Eq. (3.1.4) but differs in the denominator. However, it is possible to approximate $(k_1 + k_2)p_+ \approx k_1 p_+$ in the region where $\omega_1\theta_1^2 \gg \omega_2\theta_2^2$. This is the only region in which M_{2a} can contribute a factor $1/\theta_1$. The presence of such a factor is required for the double logarithmic behavior of the cross-section.

Obviously, the contribution of the diagram in Fig. 3.6b is similar to the diagram of

Fig. 3.6a. Interchanging the indices for the first and second emitted gluon, one obtains

$$M_{2b} \approx g_s^2 \frac{e_2 p_+}{(k_2 + k_1) p_+} \frac{e_1 p_+}{k_1 p_+} \times \bar{\Psi}_f t_a t_b. \tag{3.1.24}$$

For M_{2b}, the DLA region is $\omega_2 \theta_2^2 \gg \omega_1 \theta_1^2$ where the approximation $(k_2 + k_1)p_+ \approx k_2 p_+$ is relevant.

The diagram on Fig. 3.6c requires a separate calculation. We start from the corresponding mathematical expression for it :

$$\begin{aligned} M_{2c} &= \bar{\Psi}_f(p_+)(-ig_s)\gamma_\sigma t_c \frac{i\hat{q}}{q^2}\, e_1^\mu(k_1) e_2^\nu(k_2)\, (-g_s)\gamma_{\mu\nu\rho}(k_1, k_2, -k) f_{abc} \frac{-id^{\rho\sigma}(k)}{k^2} \\ &\approx g_s^2 e_1^\mu(k_1) e_2^\nu(k_2) \gamma_{\mu\nu\rho}(k_1, k_2, -k) \frac{d^{\rho\sigma}(k)}{2k_1 k_2} \frac{p_{+\sigma}}{k p_+} \times i f_{abc} \bar{\Psi}_f t_c, \end{aligned} \tag{3.1.25}$$

where f_{abc} are the structure constants for the SU(N_c) group and where the coefficient

$$\gamma_{\mu\nu\rho}(k_1, k_2, k_3) = g_{\mu\nu}(k_1 - k_2)_\rho + g_{\nu\rho}(k_2 - k_3)_\mu + g_{\rho\mu}(k_3 - k_1)_\nu \tag{3.1.26}$$

comes from the three-gluon vertex. The second line of Eq. (3.1.25) was obtained in the same way as Eq. (3.1.15). Other notations are shown on Fig. 3.6c. The structure of $d^{\rho\sigma}(k)$ in the gluon propagator $\frac{-id^{\rho\sigma}(k)}{k^2}$ is taken in the convenient planar gauge

$$d^{\mu\nu}(k) = g^{\mu\nu} - \frac{k^\mu c^\nu + c^\mu k^\nu}{kc}, \qquad c^\mu = (1, 0, 0, 0), \tag{3.1.27}$$

where c^μ is a constant 4-vector and with $g_{\mu\nu} = g^{\mu\nu} = \text{diag}(1, -1, -1, -1)$ being the standard metric in Minkowski space-time. The numerator of Eq. (3.1.25) reads :

$$e_1^\mu(k_1) e_2^\nu(k_2) \gamma_{\mu\nu\rho}(k_1, k_2, -k) d^{\rho\sigma}(k) p_{+\sigma} = 2 e_2 k_1 \cdot e_1 p_+ - 2 e_1 k_2 \cdot e_2 p_+ + \ldots, \tag{3.1.28}$$

where we used the identities $e_1 k_1 = e_2 k_2 = 0$, $k_\rho d^{\rho\sigma}(k) = 0$ and $c e_1 = c e_2 = 0$. The ellipsis above stands for terms which are negligible under the conditions (3.1.13). Below, we omit such terms.

In this way, the amplitude of the graph in Fig. 3.6c takes the form

$$M_{2c} \approx g_s^2 \frac{e_2 k_1 \cdot e_1 p_+ - e_1 k_2 \cdot e_2 p_+}{k_2 k_1 \cdot (k_1 + k_2) p_+} \times i f_{abc} \bar{\Psi}_f t_c. \tag{3.1.29}$$

The DLA region for M_{2c} corresponds to the condition $\omega_1\theta_1^2 \gg \omega_2\theta_2^2$. In this case, one can leave only the first term in the numerator, while the denominator would contain $(k_1 + k_2)p_+ \approx k_1p_+$. Thus, in the DLA region, the amplitude M_{2c} coincides with that of Eq. (3.1.4).

The opposite condition $\omega_1\theta_1^2 < \omega_2\theta_2^2$, in combination with (3.1.13), gives $\theta_1 \ll \theta_2$. It is easy to check that this leads to a lack of $1/\theta_1$ factor in the amplitude.

Angular ordering for $N = 2$.

So far, we calculated the three Feynman diagrams of Fig. 3.6 and identified the corresponding DLA regions of the phase space of the two final gluons. The corresponding formulas are given in Eqs. (3.1.23), (3.1.24) and (3.1.29). Let us repeat their expressions in the DLA regions :

$$\begin{array}{lll}
M_{2a} \approx g_s^2 \frac{e_1p_+}{k_1p_+}\frac{e_2p_+}{k_2p_+} \cdot t_b t_a, & \omega_1\theta_1^2 \gg \omega_2\theta_2^2 & \text{with } \theta_1 \gg \theta_2 \text{ or } \theta_1 \ll \theta_2, \\
M_{2b} \approx g_s^2 \frac{e_2p_+}{k_2p_+}\frac{e_1p_+}{k_1p_+} \cdot t_a t_b, & \omega_1\theta_1^2 \ll \omega_2\theta_2^2 & \text{with } \theta_1 \gg \theta_2 \text{ or } \theta_1 \ll \theta_2, \\
M_{2c} \approx g_s^2 \frac{e_2k_1}{k_2k_1}\frac{e_1p_+}{k_1p_+} \cdot i f_{abc} t_c, & \omega_1\theta_1^2 \gg \omega_2\theta_2^2 & \text{with } \theta_{12} \gg \theta_1 \text{ or } \theta_{12} \ll \theta_1
\end{array} \tag{3.1.30}$$

(we also omitted the wave function $\bar{\Psi}_f$ of the final quark). The last column in (3.1.30) appeared due to the strong "disordered" angular ordering requirements, which were discussed at the end of Section 3.1.1.

Thus far, the above amplitudes interfere, since their DLA regions overlap. We chosen the gluon energies to satisfy the conditions (3.1.13). Accordingly, let us examine, in turn, the following angular regions :

I. $\theta_1 \gg \theta_2$.

Here, obviously, the only contribution comes from the amplitude M_{2a}.

II. $\theta_1 \ll \theta_2$.

This region can be split into the following two subregions. In the subregion, $\theta_2^2 \gg \frac{\omega_1}{\omega_2}\theta_1^2$, only the amplitude M_{2b} is relevant. In the second subregion, $\theta_2^2 \ll \frac{\omega_1}{\omega_2}\theta_1^2$, $\theta_2 \gg \theta_1$, both M_{2a} and M_{2c} contribute and thus interfere. Since in this region $\theta_{12} \approx \theta_2$, where θ_{12} is the angle between the gluons (or, equally, the angle between the second gluon and its parent parton), one has $e_2k_1/k_2k_1 \approx e_2p_+/k_2p_+$. Thereby, the amplitude M_{2c} can be rewritten as

$$M_{2c} \approx g_s^2 \frac{e_2p_+}{k_2p_+}\frac{e_1p_+}{k_1p_+} \cdot i f_{abc} t_c \tag{3.1.31}$$

which, when added to M_{2a}, gives exactly M_{2b}.[2]

In this way, the expression for M_{2b} is retained over the whole angular region II.

---

[2] The algebra generators t_a satisfy the following standard commutation relations : $[t_a, t_b] = i f_{abc} t_c$.

III. $\theta_1 \approx \theta_2$, $\theta_{12} \ll \theta_1$.

Here, only the amplitude M_{2c} contributes.

Following the above arguments, one can see how the AO phenomenon (i.e. simultaneous consecutive ordering of the gluon energies as well as the gluon emission angles) emerges from perturbative computations : the corresponding Feynman graph contributions interfere in such a way that only one graph dominates in the DLA in the specific ordering of the gluon angles. For instance, for the $N = 2$ case, the diagram of Fig. 3.6b always represents the answer for the DLA corresponding to the ordering $\theta_2 \gg \theta_1$.

3.1.3 Angular ordering using formation time.

Previously, we discussed dominant contribution to the structure of the amplitude M_N and shown how the answer is obtained for the case $N = 1$ and $N = 2$, using the energy ordering (3.1.2) and thereby deriving the angular ordering (3.1.3). It is instructive to demonstrate how the angular ordering rules necessarily follow from simple qualitative arguments based on the comparison of the softest emitted gluon wavelength and distances in the underlying (previously formed) configuration of partons during the gluon formation time.

For this purpose, consider a process of consecutive emissions of two soft gluons off a quark as shown in Fig. 3.7. The angles θ_1 and θ_2 between the first gluon and the quark and the second gluon and the quark are considered to be small : $\theta_1 \ll 1$, $\theta_2 \ll 1$. In addition, as usual, we neglect the quark mass and assume that it is ultra-relativistic.

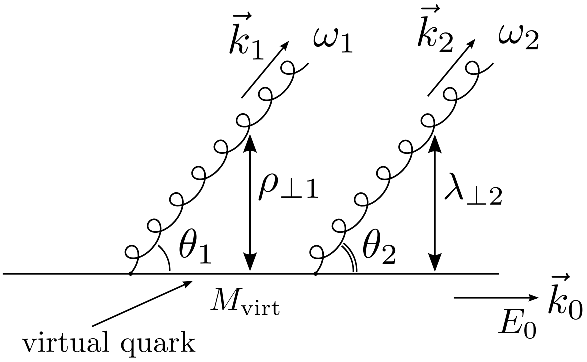

FIGURE 3.7 – Consecutive two-gluon emission.

The second gluon wavelength can be estimated as the inverse of the gluon momentum,[3]

$$\lambda_{\perp 2} = \frac{1}{|\vec{k}_{\perp 2}|} \approx \frac{1}{\omega_2 \theta_2}, \tag{3.1.32}$$

where ω_2 is the second gluon energy. At the same time, the transverse separation between the quark and first gluon is estimated as $\rho_{\perp 1} = \tau\theta_1$, where τ is "formation time" of

---

[3] We put the speed of light and the Plank constant to unity : $c = \hbar = 1$.

the second gluon. The latter, in turn, can be estimated from Heisenberg uncertainty principle, $\tau' E_{\mathrm{virt}} = 1$, where E_{virt} is the energy of the virtual quark (zero component of its 4-momentum) taken in its rest frame, as shown on Fig. 3.7. The formation time τ' is also taken in the rest frame of the virtual quark. It is related to the formation time τ in the laboratory frame with $\tau = \tau' \frac{E_0}{E_{\mathrm{virt}}}$, where E_0 is the energy of the quark in the laboratory frame. Finally, in its rest frame, the energy of the virtual quark coincides with its invariant mass, $E_{\mathrm{virt}} = M_{\mathrm{virt}}$. Consequently,

$$\tau \sim \frac{1}{M_{\mathrm{virt}}} \frac{E_0}{M_{\mathrm{virt}}} = \frac{E_0}{(k_0 + k_2)^2} \approx \frac{1}{\omega_2 \theta_2^2}. \tag{3.1.33}$$

Here k_0 denotes the quark four-momentum. Thus, the transverse separation distance of the quark and the first gluon is

$$\rho_{\perp 1} = \frac{\theta_1}{\omega_2 \theta_2^2} \tag{3.1.34}$$

Two situations are possible here. First, the angles can be ordered as $\theta_1 > \theta_2$. This is equivalent to the condition $\rho_{\perp 1} > \lambda_{\perp 2}$, i.e. the second gluon, due to its small wavelength, resolves the formation of the quark and the first gluon. In the opposite case, when $\theta_1 < \theta_2$, i.e. $\rho_{\perp 1} < \lambda_{\perp 2}$, the second gluon does not resolve the structure of the quark with its first gluon. In other words, the second gluon does not "see" the existence of the first gluon as if it was, in fact, emitted earlier than the first gluon. Consequently, the angular ordering $\theta_1 < \theta_2$ leads to the reverse order of emission of the two gluons off the quark. This reasoning thus roots the results obtained previously from Feynman diagram calculation (the regions I and II for $N = 2$ case) to more general coherence arguments.

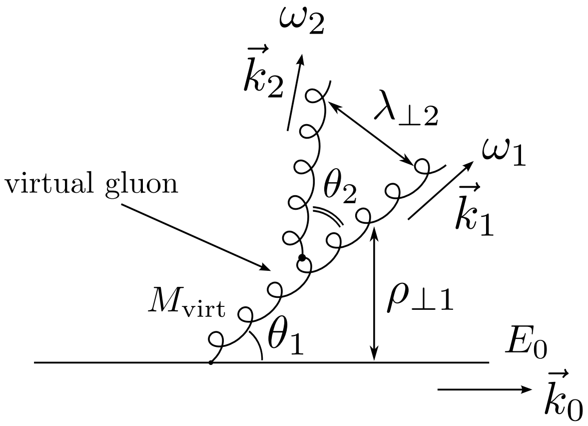

FIGURE 3.8 – Gluon branching process.

There is yet another kind of diagram, in which the second gluon is emitted off the first gluon, see. Fig. 3.8. One can analyze such a diagram in a similar way. Indeed, one has to compare the second gluon transverse wavelength (3.1.32) with $\rho_{\perp 1} = \theta_1 \tau$, where the formation time of the second gluon is

$$\tau = \frac{\omega_1}{M_{\text{virt}}^2} = \frac{\omega_1}{(k_1 + k_2)^2} \approx \frac{1}{\omega_2 \theta_{12}^2}, \tag{3.1.35}$$

where M_{virt} is the virtual gluon mass, while ω_1 is the energy of the first gluon. The case $\theta_1 > \theta_{12}$ corresponds to $\rho_{\perp 1} > \lambda_{\perp 2}$, i.e. the second gluon "knows" from where it was emitted. Since $\rho_{\perp 1} < \lambda_{\perp 2}$ in the opposite case $\theta_1 < \theta_{12}$, the second gluon cannot be emitted from the first gluon (as the former does not resolve the latter), and once again the relevant situation in this case is that the second gluon couples to the initial quark.

3.2 Origin of Hump-Backed Plateau

The depletion of soft particles inside a jet leads to the so called *Hump-Backed Plateau* (HBP) in their inclusive energy and angular spectrums. The HBP is one of the most striking predictions of perturbative QCD [19]. The depletion of soft particles follows from the angular and the energy ordering of a partonic cascade and is a direct manifestation of coherence in QCD. The existence of such a non-flat plateau is a well established experimental fact.

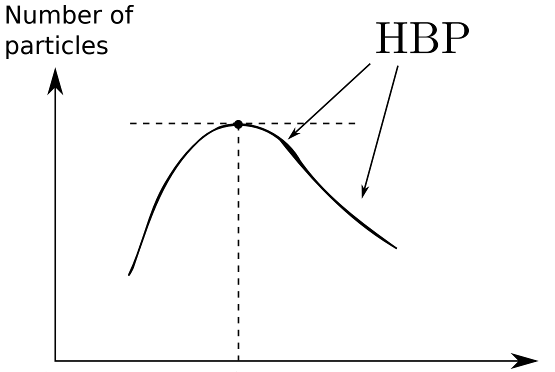

FIGURE 3.9 – Schematic distribution of particles inside a jet.

Schematically, the HBP is shown on Fig. 3.9. Here, the number of particles inside a jet is plotted versus $\xi = \ln \frac{1}{x}$ with $x = \frac{k}{E}$, where k is particles energy, E – total energy of the jet. Equally, one could consider $x = \theta$, where θ is particles angle with respect to the jet axis. As x becomes smaller, the logarithm grows, and the depletion of soft particles inside a jet is signaled on the plot by a fall off (the HBP) after some peak value at ξ_0. The position of the maximum ξ_0 and its height together with the overall shape are measured experimentally and are compared with theoretical predictions.

The purpose of this section is to explain how general features of the HBP originate as the result of two conflicting tendencies. On one hand, a parton wavelength cannot be larger than the *hadronization scale* R (with $R^{-1} \sim 200$ MeV) since the parton must “resolve” the hadronic structure from where it was emitted or, saying differently, the parton formation time $t_{\text{form}} \sim \frac{1}{k\theta}$ must be smaller than its hadronization time $t_{\text{hadr}} \sim \frac{1}{R}$. In this way, soft gluon emission at small angles is suppressed, $\theta \gtrsim \frac{1}{kR}$. On the other hand, the allowed decaying angle is shrunk to small values after a few successive parton branchings due to the angular ordering.

3.2.1 Toy model of color coherence

Consider the following toy model of gluon branchings.

We start with a single primary gluon which finally produces a gluon-jet by fragmenting naturally into multiple gluons, as shown in Fig. 3.10. At zeroth order, this fragmentation can be described with a realistic (at low momenta) gluon density

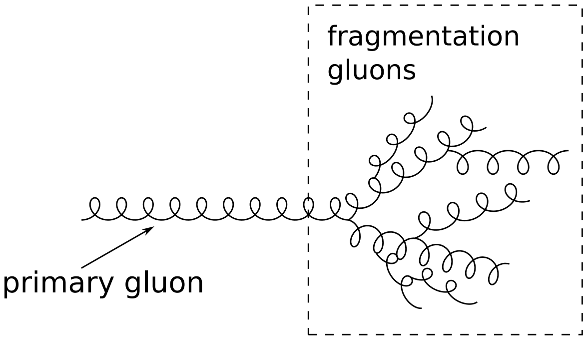

Figure 3.10 – Primary gluon and fragmentation gluons.

$$\frac{dN^{(0)}}{dk} \sim \frac{1}{k} \quad \text{or} \quad \frac{dN^{(0)}}{d\ln\frac{1}{k}} = \text{const} \qquad \text{[gluon fragmentation]}, \qquad (3.2.1)$$

which corresponds to the dashed horizontal line instead of the HBP on Fig. 3.9. The dependence of $N^{(0)}$ on the emission angle θ can be incorporated by combining the preference of bremsstrahlung for small angles with the upper limit on the gluon wavelength leading to $\frac{1}{k\theta} \sim R$. Thereby, at the zeroth order, we will use the following gluon density as a function of k and θ :[4]

$$dN^{(0)}(k,\,\theta) = \frac{1}{R}\frac{dk d\theta}{k\theta}\,\delta(k\theta - R^{-1})\,\Theta(E-k)\,\Theta(1-\theta). \tag{3.2.2}$$

In this formula, fragmentation gluon energies are limited by the energy E of the initial gluon, $k \leq E$, while the condition $\theta \leq 1$ places the lower limit on the gluon energy, $k \geq R^{-1}$. Note also that the angle of radiation θ of a fragmented gluon is not limited by angular ordering to be small.

Lastly, the coefficient in front of the delta-function in Eq. (3.2.2) is chosen in such a way that the integration of (3.2.2) over θ gives (3.2.1). In addition, the total energy of the fragmentation jet is

$$\int k\, dN^{(0)} = \int\limits_{R^{-1}}^{E} k\frac{dk}{k} \approx E. \tag{3.2.3}$$

Thus, it coincides with the energy of the primary gluon. (In this calculation, for the sake of additional simplicity, we neglected $R^{-1} \sim 200$ MeV with respect to E, which is of order of at least of tens of GeV.)

Let us emphasize that the fragmentation of the primary gluon happens late, decoupled from the process from where the primary gluon emerged. This fact is reflected in the delta-function in Eq. (3.2.2) which fixes the fragmentation gluon wavelength $\lambda_{\text{frag}} \sim R$, i.e. at a scale where fragmented gluons do not "see" the structure of a primary process.

Let us now introduce a radiative correction which give a possibility for the primary gluon to make a perturbative splitting. Such secondary emission gluons are radiated after the primary collision and subsequently decay into fragmentation gluons, see Fig. 3.11. Accordingly, the wavelength of the secondary gluons is smaller than the hadronic scale, i.e. $\frac{1}{k\theta} < R$. In its lowest α_S order (with $\alpha_S = \frac{g_s^2}{4\pi}$), taking into account the double logs, the primary gluon branching can be described with the following radiation probability :

$$d\omega(k',\theta') = \alpha_S \frac{dk' d\theta'}{k'\theta'}\Theta(k'\theta' - R^{-1})\Theta(E-k')\Theta(1-\theta'), \tag{3.2.4}$$

where k' – emitted gluon energy, θ' – emitted gluon angle, measured with respect to its parent.

After this branching, gluons fragment in the same fashion as the primary gluon does. This time, however, we account for the energy and angular ordering rules which limit energy and angles of fragmentation gluons.

---

[4] The step-function $\Theta(x)$ is defined as

$$\Theta(x) = \begin{cases} 0, & \text{if} \quad x < 0, \\ 1, & \text{if} \quad x \geq 0. \end{cases}$$

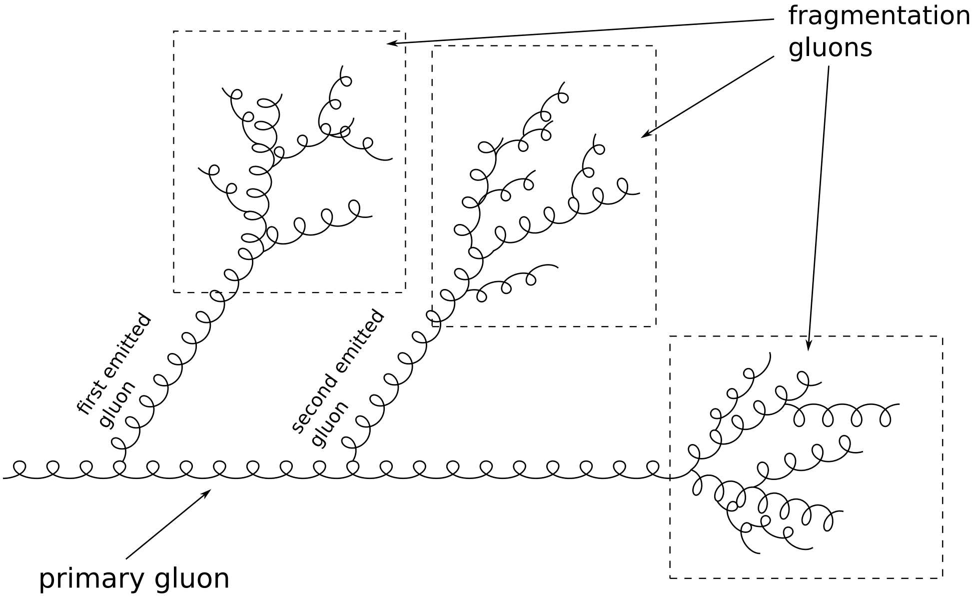

FIGURE 3.11 – Full picture of gluon radiation.

3.2.2 Angular distribution of gluons

Let us discuss angular distribution of gluons inside a gluon-jet in the toy model at hand. Up to order α_S, the gluon multiplicity reads

$$N(\theta) = N^{(0)}(\theta) + N^{(1)}(\theta). \tag{3.2.5}$$

In this expression, the term $N^{(0)}(\theta)$ corresponds to pure fragmentation of the primary gluon. According to Eq. (3.2.2), it is given by

$$\begin{aligned} N^{(0)}(\theta) = \int_0^\theta \frac{d\theta'}{\theta'}\Theta(1-\theta')\Theta(\theta'-(ER)^{-1}) \int_0^E \frac{dk'}{k'R}\delta(k'\theta'-R^{-1}) \\ = \int_0^\theta \frac{d\theta'}{\theta'}\Theta(1-\theta')\Theta(\theta'-(ER)^{-1}) \end{aligned} \tag{3.2.6}$$

or

$$\frac{dN^{(0)}}{d\xi} = 1, \qquad \xi = \ln\frac{1}{\theta}, \tag{3.2.7}$$

while the angles of fragmentation gluons satisfy

$$(ER)^{-1} \leq \theta \leq 1, \qquad 0 \leq \xi \leq \ln(ER). \tag{3.2.8}$$

The term $N^{(1)}$ in Eq. (3.2.5) stands for the first order in α_S gluon radiation and subsequent gluon fragmentation, namely :

$$N^{(1)}(\theta) = \alpha_S \int\limits_0^1 \frac{d\theta'}{\theta'} \int\limits_0^E \frac{dk'}{k'} \Theta(k'\theta' - R^{-1}) \int\limits_0^{k'} \frac{dk''}{k''} \int\limits_0^{\theta_{\max}(\theta')} \frac{d\theta''}{R\theta''} \delta(k''\theta'' - R^{-1})\, \Theta^{3\mathrm{D}}(\theta,\, \theta',\, \theta''), \tag{3.2.9}$$

where we introduced a new parameter $\theta_{\max}(\theta')$. This parameter controls how the angular ordering rules are used for the fragmentation gluons, since the angle θ'', being defined *with respect to the intermediate gluon direction of flight*, is limited with $\theta'' \leq \theta_{\max}(\theta')$. In addition, we accounted for the fact that directions of the primary gluon, the secondary (intermediate) gluons and the fragmentation (final) gluons do not lie in one plane and the final angle cannot be simply written as $\theta' + \theta''$. This is reflected symbolically in the factor $\Theta^{3\mathrm{D}}(\theta,\, \theta',\, \theta'')$, which should be understood as “the resulting angle between the primary gluon and a fragmentation gluon, being dependent on θ' and θ'', must not be greater than θ”.

Let us now compare the impact of the angular ordering rules on the angular distribution of gluons. To this end, take $\theta_{\max}(\theta') = \theta'$. In this case, the leading contribution to Eq. (3.2.9) is gained in the region of angles where $\theta'' \ll \theta'$ (the DLA region), owing to singular factor $1/\theta''$. Consequently, we approximate the symbolical step-function to be $\Theta^{3\mathrm{D}}(\theta,\, \theta',\, \theta'') \approx \Theta(\theta - \theta')$. The integrals in Eq. (3.2.9) can now be taken straightforwardly, leading to

$$N^{(1)}_{\mathrm{coh}}(\theta) \approx \frac{\alpha_S}{2} \int\limits_0^{\theta} \frac{d\theta'}{\theta'} \ln^2 (ER\theta')\, \Theta(ER\theta' - 1) \tag{3.2.10}$$

or, differently,

$$\frac{dN^{(1)}_{\mathrm{coh}}}{d\xi} \approx \frac{\alpha_S}{2} \left[\ln(ER) - \xi\right]^2 \tag{3.2.11}$$

with same allowed regions (3.2.8) for θ and ξ.

Thus, if the angular ordering takes place (coherent gluon emission), the constant zero-order behavior of Eq. (3.2.7) (dashed horizontal line on Fig. 3.9) is enhanced with the parabolic first-order correction (3.2.11). The peak value of the HBP is located at $\xi_0 = 0$ which corresponds to the angle $\theta = 1$.

Finally, consider the situation when the angular ordering is absent. This corresponds to the case of unrestricted maximum angle of fragmentation gluons : $\theta_{\max}(\theta') = 1$. Thanks to factors $1/\theta'$ and $1/\theta''$, the dominant contribution in Eq. (3.2.9) is gained when either $\theta'' \ll \theta'$ or $\theta' \ll \theta''$. The first case was already considered above. In the second case, we approximate the symbolical step-function with $\Theta^{3\mathrm{D}}(\theta,\, \theta',\, \theta'') \approx \Theta(\theta - \theta'')$. Then, the calculation gives exactly the same expression as is written in Eq. (3.2.10) (the simplest way to perform the calculation is to rearrange the integrals in (3.2.10) in such a way that the integral over θ'' is the last one to be taken). Thus, the incoherent first-order correction simply reads twice as large answer in comparison with the coherent case :

$$\frac{dN^{(1)}_{\rm incoh}}{d\xi} \approx \alpha_S \left[\ln(ER) - \xi\right]^2 . \tag{3.2.12}$$

3.2.3 Energy distribution of gluons

For energy distribution of gluons inside a jet, it turns out that the difference between coherent and incoherent gluon emission is more essential. The calculation proceeds similarly to what was already discussed above.

At the zeroth order, the distribution is given in Eq. (3.2.1) under the conditions

$$R^{-1} \leq k \leq E, \tag{3.2.13}$$

while the first-order correction is

$$N^{(1)}(k) = \alpha_S \int\limits_0^k \frac{dk''}{k''} \int\limits_{k''}^E \frac{dk'}{k'} \int\limits_0^1 \frac{d\theta'}{\theta'} \Theta(k'\theta' - R^{-1}) \int\limits_0^{\theta_{\max}(\theta')} \frac{d\theta''}{R\theta''}\, \delta(k''\theta'' - R^{-1}). \tag{3.2.14}$$

Again, in the coherent case $\theta_{\max}(\theta') = \theta'$, while in the incoherent case $\theta_{\max}(\theta') = 1$. The calculation of the integrals in (3.2.14) reads :

$$\begin{aligned} \frac{dN^{(1)}_{\rm coh}}{d\ln\frac{1}{k}} &= \alpha_S \ln\frac{E}{k} \ln(kR) \\ \frac{dN^{(1)}_{\rm incoh}}{d\ln\frac{1}{k}} &= \frac{\alpha_S}{2}\left[\ln^2(ER) - \ln^2(kR)\right]. \end{aligned}$$

Still, the conditions (3.2.13) must be applied. In ξ units,

$$\xi = \ln\frac{E}{k}, \qquad 0 \leq \xi \leq \ln(ER), \tag{3.2.15}$$

one has :

$$\begin{aligned} \frac{dN^{(1)}_{\text{coh}}}{d\xi} &= \alpha_S \; \xi \left[\ln(ER) - \xi\right], \\ \frac{dN^{(1)}_{\text{incoh}}}{d\xi} &= \alpha_S \; \xi \left[\ln(ER) - \frac{1}{2}\xi\right]. \end{aligned}$$

The trend here is clearly different in both situations. In the incoherent version of the model, the first-order correction is maximal at the smallest possible k (largest possible ξ), i.e. $k = R^{-1}$. On the contrary, when angular ordering is incorporated into the model, the maximum is reached in the middle of the range, at $\xi_0 = \frac{1}{2}\ln(ER)$, with a symmetric fall off around this maximum.

Lastly, let us remark that the number of gluons in the coherent case is half that one of the incoherent case : $N^{(1)}_{\text{coh}}(E) = \frac{1}{2}N^{(1)}_{\text{incoh}}(E)$.

3.3 Soft emission and the Born term

The DLA approximation discussed in this chapter is sufficient for derivation of the statement about the universality of soft parton spectra, i.e. their independence of the collision energy $\sqrt{s}$. The necessary mathematical details are given below in the appendix.

In brief, in the limiting case $k_\perp \to Q_0$, the first-order term (the Born term) in the fragmentation function $d(\ell, y)$ of Eq. (3.4.18) dominates since $y \to 0$ in this case, whereas ℓ stays finite. Using Eqs. (3.4.26) and (3.4.12), one obtains

$$D^p(\vec{k}) \sim \frac{\alpha_S}{k_\perp^2}, \tag{3.3.1}$$

which successfully reproduces Eq. (2.2) from the Introduction with the color factor $C = 1$. Accordingly, the MLLA just introduces running of the coupling constant in this formula : $\alpha_S = \alpha_S(k_\perp)$.

A verification of the universality is discussed in Chapter 7, where we study zero-momentum limits of hadron spectra, as well as in Chapter 8, there we elaborate a different approach by considering ratios of hadron spectra of different collision energies.

3.4 Appendix : method of generating functionals

This section is rather technical and is not essential for understanding the material of subsequent chapters. Here we, however, explain mathematical framework for description of parton densities in jets and illustrate how soft parton spectra can be calculated.

A generating function $G(u)$ of a variable u for series a_N, $N = 0, 1, 2, ...$ is defined as

$$a_N = \left.\frac{d^N G(u)}{du^N}\right|_{u=0}. \tag{3.4.1}$$

For instance, series $a_N = N!$ are generated by

$$G(u) = \frac{1}{1-u}. \tag{3.4.2}$$

Indeed,

$$G(u) = 1 + u + u^2 + u^3 + ... \tag{3.4.3}$$

and the derivative of the N^{th} term at $u = 0$ gives $N!$. All the cross-sections

$$\sigma_N(\vec{p}; \vec{k}_1, ..., \vec{k}_N) = C_N \int \sum_{\text{polar.}} |M_N|^2 \prod_{i=1}^{N} \frac{d^3 k_i}{2\omega_i} \tag{3.4.4}$$

($\vec{p}$ is momentum of a primary parton, C_N – normalization factors) as well as their differential counterparts can be generated by a functional

$$Z(\vec{p}; u) = \frac{1}{Z_0} \sum_{N=0}^{\infty} \frac{1}{N!} C_N \int \sum_{\text{polar.}} |M_N|^2 \, u(\vec{k}_1) u(\vec{k}_2) \dots u(\vec{k}_N) \prod_{i=1}^{N} \frac{d^3 k_i}{2\omega_i}, \tag{3.4.5}$$

with Z_0 being a normalization factor. We introduced an arbitrary function $u(\vec{k})$, the functional derivatives of which give the original (differential) cross-sections. Indeed,

$$\left.\frac{\delta}{\delta u(\vec{k}_1)} ... \frac{\delta}{\delta u(\vec{k}_N)} Z(\vec{p}; u)\right|_{u=0} = \frac{1}{Z_0} C_N \sum_{\text{polar.}} |M_N|^2 \prod_{i=1}^{N} \frac{d^3 k_i}{2\omega_i} = \frac{1}{Z_0} d\sigma_N, \tag{3.4.6}$$

where the matrix element M_N is taken for parton momenta $\vec{k}_1$, ... $\vec{k}_N$. Here we used the rule of functional differentiation

$$\frac{\delta}{\delta u(\vec{k}_i)} u(\vec{k}) = \delta^{(3)}(\vec{k}_i - \vec{k}). \tag{3.4.7}$$

We choose the normalization factor Z_0 in such a way that

$$Z(\vec{p};u)\big|_{u=1} = 1. \tag{3.4.8}$$

The generating functional $Z(\vec{p};u)$ is very convenient for obtaining various parton multiplicities (inclusive cross-sections) which, being combined with the LPHD hypothesis, can be measured experimentally. In particular, we are interested in one-parton inclusive differential cross-section (i.e. the cross-section for the emission of one parton with fixed momentum and any number of additional partons) which is expressed through of $Z(\vec{p};u)$ as

$$k\frac{d^3N}{dk^3} = k\frac{\delta Z(\vec{p};u)}{\delta u(\vec{k})}\bigg|_{u=1} \tag{3.4.9}$$

with $k = |\vec{k}|$ being final parton energy, $\vec{k}$ – its momentum. The most striking fact is that the generating functional $Z(\vec{p};\, u)$ satisfies the following integral equation [2] :

$$Z_A(\vec{p};u) = u(\vec{p}) \exp\left(\int\limits_{\Gamma} \frac{dk}{k} \frac{d^2k_\perp}{2\pi \vec{k}_\perp^2} \frac{C_A}{N_c} \gamma_0^2(\vec{k}_\perp) \left[Z_G(\vec{k};u) - 1 \right] \right), \tag{3.4.10}$$

where $\vec{k}_\perp$ is a projection of $\vec{k}$ to a direction perpendicular to $\vec{p}$, $N_c = 3$ – number of colors in QCD. The color factors C_A, where the index A is either $A = F$ or $A = G$, are defined for the fundamental (quarks) and for the adjoint (gluons) representations of the SU(3) group respectively : $C_F = 4/3$, $C_G = 3$.

The equation (3.4.10) is a nonlinear integral equation which involves two generating functionals, Z_F and Z_G. The generating functional Z_G corresponds to the case when the primary parton was a gluon and it provides description for the so-called gluon-jets. On the other hand, the functional Z_F is responsible for the description of a showering process which started from an initial quark (quark-jets). The equation (3.4.10) was derived taking into account only $q \to q + g$ and $g \to g + g$ parton branchings. Due to this, only the gluon functional Z_G stays in the integral on the right hand side. In other words, gluons serve as a source of other gluons with the coefficient $\frac{C_G}{N_c} = 1$. In addition, for quark-jets, gluons are emitted from the quark with the coefficient $\frac{C_F}{N_c} = 4/9$.

The integration region Γ for an emitted gluon with momentum $\vec{k}$ takes into account the angular ordering rules, where the direction of $\vec{k}$ is considered with respect to the direction of its parent parton. Thus,

$$\Gamma(E,\,\theta):\ \{k\le E;\ \theta_k\le\theta;\ k\theta_k\ge Q_0\}\,, \tag{3.4.11}$$

where $E=|\vec{p}|$ is the energy of the parent parton, θ_k is the angle of emission of the gluon with respect to its parent, while θ is the angle of emission of the parent parton with respect to its own parent.

The parameter $Q_0\sim 200$ MeV in (3.4.11) is a low energy cut-off which forbids low transverse momentum radiation, $|\vec{k}_\perp|\ge Q_0$, because of nonexistence of long wavelength partons in QCD. Physically, Q_0 is then related to the QCD scale, $\Lambda_{\rm QCD}$, or, more phenomenologically, to R^{-1}, where R is a typical hadron size which we used in Section 3.2.

The equation (3.4.10) can be proven directly by summing the DLA contributions at all orders. While doing so, one arrives at the following expression for the intensity of emission $\gamma_0^2(\vec{k}_\perp)$:

$$\gamma_0^2=2N_c\frac{\alpha_S(\vec{k}_\perp)}{\pi} \tag{3.4.12}$$

with $\alpha_S=\frac{g_s^2}{4\pi}$ being the running strong coupling constant. For instance, in one-loop approximation of the perturbative QCD

$$\alpha_S(\vec{k}_\perp)=\frac{1}{b\ln\frac{|\vec{k}_\perp|}{\Lambda_{QCD}}},\qquad b=\frac{11}{3}N_c-\frac{2}{3}n_f, \tag{3.4.13}$$

where b is the coefficient staying in the β-function, n_f is the number of quark types (flavors) in the theory.

3.4.1 Gluon-jet fragmentation function in the DLA

In the double logarithmic approximation, using the method of generating functionals, one can calculate the parton fragmentation function

$$D(\vec{k})=k\frac{d^3N}{dk^3}. \tag{3.4.14}$$

With this method, $D(\vec{k})$ can be expressed as a functional derivative of the generating functional $Z(\vec{p};u)$. Below, we limit ourselves to the gluon-jets, so that the factor $\frac{C_G}{N_c}=1$.

According to general considerations at the beginning of Section 3.4, one has :

$$D^p(\vec{k}) = k\frac{\delta Z(\vec{p};u)}{\delta u(\vec{k})}\bigg|_{u=1} . \tag{3.4.15}$$

The upper index "p" here reminds ourselves that the fragmentation function depends of the initial parton with momentum $\vec{p}$ and also on its angle of emission with respect to its own parent.

Applying the derivative (3.4.15) to Eq. (3.4.10) leads to the following linear integral equation on the fragmentation function :

$$D^p(\vec{k}) = k\,\delta(\vec{k}-\vec{p}) + \int\limits_{\Gamma} \frac{dk'}{k'}\frac{d^2k'_\perp}{2\pi\vec{k}'^2_\perp}\gamma_0^2(\vec{k}'_\perp)D^{k'}(\vec{k}). \tag{3.4.16}$$

In deriving this relation, the defining equality (3.4.8) was used. Also, the fragmentation function on the left-hand side is written for the initial gluon (with momentum $\vec{p}$), whereas in the integral on the right-hand side is written with respect to an intermediate gluon with momentum $\vec{k}'$.

The evolution equation (3.4.16) can be solved analytically in the case when the running coupling $\alpha_S(\vec{k})$ is fixed, so that $\gamma_0^2(\vec{k}_\perp)$ is constant. To this end, first notice that the fragmentation function $D^p(\vec{k})$ depends effectively only on the ratios of the energies p/k and on the angle of emission of parent parton with momentum $\vec{p}$. Indeed, in the DLA, one can assume that $\theta_k \ll \theta_p$, where θ_k and θ_p are the emission angles of partons with momenta $\vec{k}$ and $\vec{p}$ respectively, and thus can neglect θ_k. In addition, the jet has axial symmetry around its axis. Thereby, introduce dimensionless variables

$$l = \ln\frac{p}{k}, \quad l' = \ln\frac{k'}{k}, \quad y = \ln\frac{k\theta_k}{Q_0}, \quad y' = \ln\frac{k'\theta_{k'}}{Q_0} \tag{3.4.17}$$

($\theta_{k'}$ is the angle of emission of parton with momentum $\vec{k}'$) and the function

$$d(l,y) = \int \frac{d\varphi_k}{2\pi}\,\vec{k}_\perp^2 D^p(\vec{k}), \tag{3.4.18}$$

where φ_k is the azimuthal angle of $\vec{k}$.

Making the changes of variables in Eq. (3.4.16) and performing the integration on the azimuthal angle, we get

$$d(l,y) = \delta(l)\delta(y) + \int\limits_0^l dl' \int\limits_0^y dy'\, \gamma_0^2\, d(l',y'). \tag{3.4.19}$$

Several comments are relevant here. First, notice that at small angles

$$\frac{dk}{k'}\frac{d^2k'_\perp}{\vec{k}'^2_\perp} \approx dl'dy'd\varphi_{k'}, \tag{3.4.20}$$

which is easy to check by a direct calculation. Of course, the same is also valid for the vector $\vec{k}$. Then, to guess the form of the three-dimensional delta-function in new coordinates, let us use the above formula in the following way :

$$d^3k \approx k\,\vec{k}^2_\perp\, dl\, dy\, d\varphi_k. \tag{3.4.21}$$

Multiplying both sides of this equality with the delta-function, we see that

$$d^3k\,\delta(\vec{k}-\vec{p}) \equiv \delta(l)\delta(y)\delta(\varphi_k)\, dl\, dy\, d\varphi_k, \approx k\,\vec{k}^2_\perp\, \delta(\vec{k}-\vec{p})\, dl\, dy\, d\varphi_k \tag{3.4.22}$$

i.e.

$$\delta(\vec{k}-\vec{p}) \approx \frac{1}{k\vec{k}^2_\perp}\delta(l)\delta(y)\delta(\varphi_k). \tag{3.4.23}$$

It is easy now to find a solution of Eq. (3.4.19). To do so, consider the solution as power series of γ_0^2 with the zero-order approximation $d^{(0)}(l,y) = \delta(l)\delta(y)$. Then

$$d(l,y) = d^{(0)}(l,y) + d^{(1)}(l,y) + \ldots, \tag{3.4.24}$$

where

$$d^{(k+1)}(l,y) = \int\limits_0^l dl' \int\limits_0^y dy'\, \gamma_0^2\, d^{(k)}(l',y'). \tag{3.4.25}$$

For instance,

$$d^{(1)}(l,y) = \gamma_0^2, \qquad d^{(2)}(l,y) = \gamma_0^4\, l\, y \qquad d^{(3)}(l,y) = \gamma_0^6\frac{l^2y^2}{4}. \tag{3.4.26}$$

One can check by induction that the k-th term reads

$$d^{(k)}(l,y) = \gamma_0^{2k}\frac{l^{k-1}y^{k-1}}{((k-1)!)^2}. \tag{3.4.27}$$

The whole series is nothing more than than the standard modified Bessel function :

$$d(l,y) = \delta(l)\delta(y) + \gamma_0^2\, I_0(2\gamma_0\sqrt{ly}). \tag{3.4.28}$$

Let us finally conclude with a remark about the hump-backed plateau for this fragmentation function. At fixed angle θ, $ly = \ln(E/k)\ln(k\theta/Q_0)$ has a maximum in $\ln\frac{1}{k}$ units in the middle of the allowed region. Since I_0 is an increasing function of its argument, the spectrum rises from small $\ln\frac{1}{k}$ where $y = 0$ to this maximum and then decreases again.

Chapitre

4

The LHC and the ALICE experiment

The main aspects of experimental setup of A Large Ion Collider Experiment (ALICE) are given. The chapter starts by introducing the Large Hadron Collider. After that, we pass to the ALICE experiment, focusing on the detectors which are relevant to the analysis presented in subsequent chapters.

4.1 The Large Hadron Collider

The Large Hadron Collider (LHC) [20, 21, 22] is the largest and the most powerful particle accelerator in the world. It is located in the European Organization for Nuclear Research (CERN) near Geneva, at the border between France and Switzerland. The LHC is a synchrotron which is aimed to accelerate two counter-rotating beams in separate beam pipes. Its circular tunnel 27 kilometers in circumference is located 50-175 meters underground. The LHC is designed to accelerate beams of protons (with the proton momentum up to 7 TeV/c) or heavy ions (with the ion momentum up to $7 \times Z/A$ TeV/c, where Z and A are the ion charge and atomic number, respectively), colliding them at four points of the tunnel 40 million times per second and creating up to thousands of secondary particles in each collision.

The system of superconducting magnets of the LHC machine maintains beams of particles in the accelerating ring. It is one of the coldest points in the Universe : its temperature is 1.9 K in comparison with the temperature of the open space 2.7 K. At the same time, the temperature in the collision points in the million of times exceeds the one in the center of the Sun !

At the four intersection points along the tunnel, in large caverns, six detector systems are located. Each detector system is a separate experiment. The ATLAS (A Toroidal LHC Apparatus) experiment and the CMS (Compact Muon Solenoid) experiment are large, general purpose particle detectors devoted to searches of signs of new physics. The ALICE (A Large Ion Collider Experiment) is studying a state of strongly interacting matter called quark-gluon plasma which is supposed to be existed shortly after the Big Bang. The LHCb (Large Hadron Collider beauty) experiment aims to investigations of asymmetry of the matter and the antimatter of the Universe. Finally, the rest two experiments – LHCf and TOTEM – are very much smaller and are designed for very specialized research.

4.1.1 Physics goals of the LHC

During the 20-th century, the Standard Model — a theory of elementary particles and their interactions — was theoretically developed and confirmed experimentally. However, some fundamental questions remain open, and physicists hope that the LHC will help to find the answers.

In particular, there still remains a question why elementary particles have mass and why is it different for different particles ? English physicist Peter Higgs suggested an explanation which is known as the Higgs mechanism. This mechanism predicts the existence of a new particle – the Higgs boson. In simple words, imagine a party, where all guests have uniformly filled several rooms. At once, the Queen (the Higgs boson) enters. Everyone is moving towards her. Passing through the rooms, she attracts guests which are near her. Those who are left behind start again to fill the room uniformly. And the group of people around her has greater mass than in average. For this elegant explanation, the British physicist David Miller has got a bottle of champagne from the British science minister William Waldegrave. *The experimental discovery of the Higgs boson is the primary task of the LHC.*

An outstanding achievement at the LHC — the discovery of the boson with mass of about 125 GeV consistent with the long-sought Higgs boson [23].

The second most important goal of the LHC is *search for signs of supersymmetry.* The supersymmetry is a symmetry which relates particles of one spin to other particles that differ by half a unit of spin and are known as superpartners. There is no experimental evidence for the existence of supersymmetry. It is motivated by possible solutions to several theoretical problems of the Standard Model. In addition, particles-superpartners provide a natural candidate for dark matter in the Universe. The search for superpartners is one of the most exciting research projects at the LHC.

Other goals include : search for extra dimensions, investigation of the properties of the quark-gluon plasma, explaining the difference between the matter and the antimatter, etc.

4.1.2 More about the LHC

In the LHC tunnel, beams of particles are accelerated in opposite directions. More than 1600 superconducting magnets with the weight of 27 tons direct and focus the beams in the four intersection points.

For the proton beams, the speed of each proton differs from speed of light in less than one millionth of percent. According to the nominal parameters of the LHC, each proton will have the energy of 7 TeV which is in 7000 times exceeds its rest mass. This is around 7 times more than the energy of the previous record-holder collider, Tevatron, located in Fermi National Laboratory, USA. LHC is designed to collide beams with the intensity which 40 times exceeds the one of the Tevatron.

For proton collisions, protons move in one of 2808 beams, distributed along the whole LHC tunnel. In the moment of collision, each beam, containing up to 100 billion protons, will not exceed the length of a sewing needle, having the diameter less than the most thin human hair. The beams pass the full ring by 0.0001 seconds, i.e. perform around 10 thousand circles per second.

Particle beams pass quite a long way before reaching their maximum momentum : the acceleration is performed in many steps (or phases). A schematic view of the CERN accelerator complex is shown in Fig. 4.1.

Protons are obtained by removing electrons from hydrogen atoms. In the beginning, they are injected from the linear accelerator (LINAC2) into the PS Booster, then into the Proton Synchrotron (PS), where they accelerate to the momentum of 25 GeV/c. After that, the beams circulate in the Super Proton Synchrotron (SPS), where they reach the momentum of 450 GeV/c, before final injection into the LHC ring takes place. The beams circulate in the LHC for 20 minutes before reaching the maximum momentum.

Lead ion acceleration is supplemented by additional stripping and accumulating phases in the very beginning. Ions start from a source of vaporised lead and enter LINAC3 before being collected and accelerated in the Low Energy Ion Ring (LEIR). After that, they follow the same route to maximum acceleration as the proton beams.

At the nominal parameters of the LHC operation, the total energy of the particles in the accelerator ring can be compared to the total energy of water which falls every second

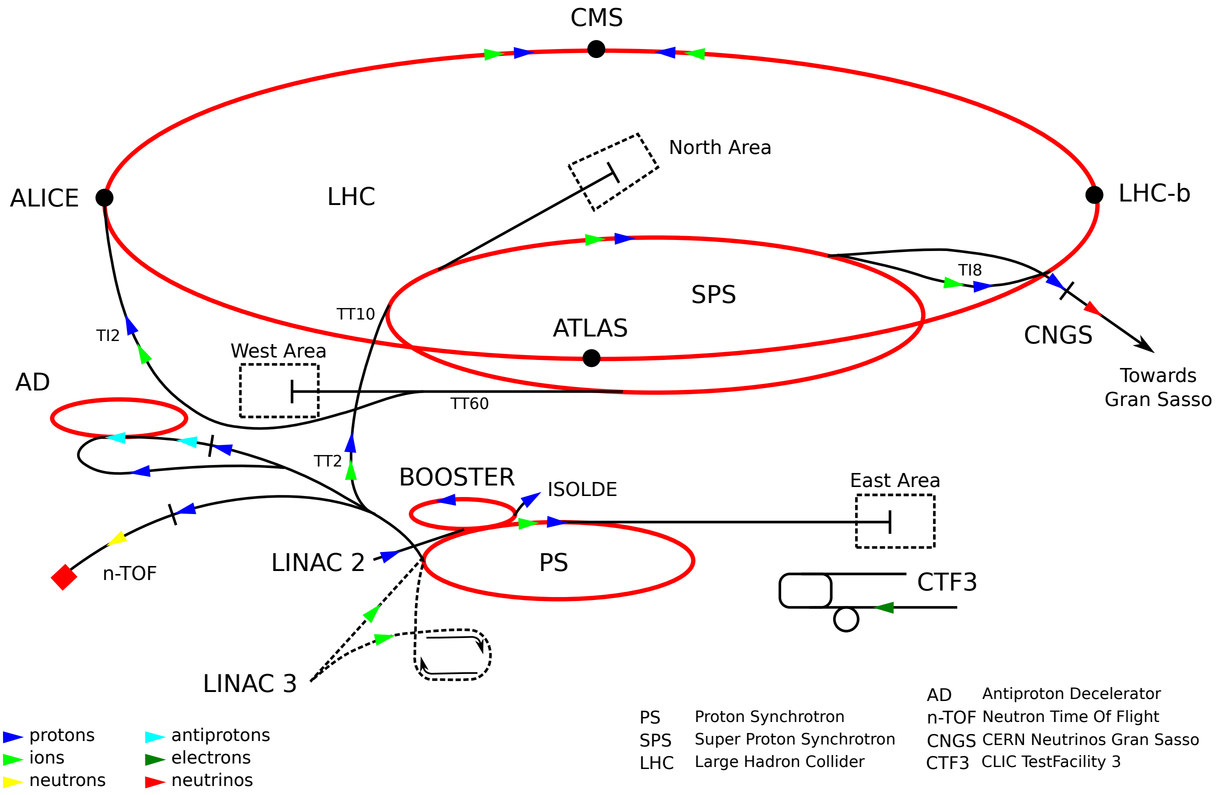

FIGURE 4.1 – Schematic view of the CERN accelerator complex.

from the Niagara Falls, or to the energy of a reactive plain, which is especially striking if one takes into account the fact, that the total mass of all accelerated particles does not exceed a nanogramm, and one can not even see them with bare eye.

The four giant detector systems (ATLAS, CMS, ALICE and LHCb) measure simultaneously parameters of thousands of particles produced in each collision. The biggest experiment, ATLAS, occupy half of the Notre-Dame de Paris, whereas for the construction of the heaviest detector, ALICE, was spent more iron than for the construction of the Eiffel Tower ! Despite the giant size of the detectors, they are in the literal sense a jeweler's work : certain detector subsystems (i.e. Silicon Vertex Detector) require accuracy of assembly up to 50 microns.

There is no single country which would be capable to create a tremendous project, like the LHC. That is why the LHC was established by 20 states-members of CERN organization joining the effort of more than ten thousand scientists from more than hundred countries all over the world. The budget of the LHC as for June 2010 made up 10 billion American dollars, which makes the LHC the most expensive experiment in the human history.

The designed energy consumption of LHC is 1000 gigawatt, 700 gigawatt from which are related to the accelerator. This makes up only 10% of the total energy consumption of Geneva canton.

4.1.3 Design considerations

A beam of particles which is left as is will move linearly and with a constant speed. To be able to hold it inside the LHC accelerating ring, one needs a powerful system of magnets. An ordinary magnet at room temperature is not able to perform this task for particles which are moving at a speed close to the speed of light. For this reason, 1628 superconducting magnets with total length 22 km and weight around 27 tons were used. In a superconducting magnet, currents can circulate infinitely long (without resistance), creating extremely powerful magnetic field. It is the first time in the history that the ring of such a diameter was moved to the superconducting state! This requires, however, very reliable cooling system.

As it was already mentioned, at the nominal luminosity of the LHC, the beams collide 40 million times per second and give birth to up to thousands of particles which then traverse detector subsystems and leave footprints along their paths. To be able to register such "snapshots", the detector subsystems must be very fast in operation and exactly synchronized between each other. Every 25 nanoseconds, the detector subsystems are required to collect all the tracks which were made by the particles, transform them into electrical signals and make necessary clean ups in order to be ready for next portion of particles. Moreover, during these 25 nanoseconds, an average particle have time to fly for 7.5 meters, which is comparable with the size of the whole detector. Thus, while the signal from the passed particles is still collected in the external layers of the detector, a new portion of particles from the next collision already travel through its inner layers!

One more key requirement for the detector subsystems is their radiation resistance. Elementary particles, traveling from a collision point, are nothing more than radiation, moreover, very hard one. The detector must absorb giant dozes of radiation over years and remain functional. This concerns not only materials of the detector, but also electronics with which it is stuffed.

The other requirement to the electronics is low energy consumption. There is no free space inside detectors of several meters in size, each cubic centimeter of volume is filled with useful equipment. The detector cooling system inevitably takes away the working space since particles hitting a cooling pipe are not detected. That is why the energy consumption from the electronics, which may be hundreds of thousands of separate plates and wires reading information from all the components of the detector, should be minimal.

4.1.4 Practical application of results from the LHC

Fundamental research hardly correlates with quick practical applications, it is aimed for the future. Probably, one has to wait for decades before an implementation into different spheres of national economies become possible. The LHC is aimed at extending our knowledge about the laws of Nature and the structure of the Universe. Nevertheless, the complexity of the detectors and computer analyses forces scientists to engineer new materials, new technologies and new computing solutions.

For instance, there was a need for collection, storage and processing of huge amount of experimental data. This way GRID technology was implemented. GRID is a distributed computer network which consists of several thousands of powerful computers physically located in many institutes all over the world, connected to eleven huge centers on three continents, which, in their turn, are connected to CERN by means of dedicated optical channels. The GRID network, which is a by-product of scientific research, is now used, e.g., in medicine.

4.1.5 Risks and safety at the LHC

The most frequently mentioned in press risks caused by the LHC are theoretical miniature black holes. CERN has created special group for the estimation of safety of the LHC. It has performed a detailed study and presented summary about probability of disasters which could be caused by the LHC experiment. Theoretical probability of “risky” processes is extremely low and scientists declared such worries to be ungrounded.

Let us consider creation of a miniature black hole which is indeed not forbidden at the LHC. According to the Hawking principle, it will evaporate immediately after its creation and will have no time to capture the environment. General principles of quantum theory state that such a black hole cannot be stable unless there are rules which forbid its decay. As far as those rules were not discovered, the black hole should be unstable.

A good argument in favor of safety of the experiments at the LHC can be the existence of cosmic rays traversing the atmosphere : the energy of cosmic rays exceed thousand of times the energies reachable at the LHC. The uniqueness of the LHC does not lie in the fact that this energy can not be reached in Nature. On the contrary ! The point is that the frequency of collisions at the LHC exceeds by million of times the one in cosmic rays. This means that the discovery of a new particle is feasible in a year instead of million of years.

4.2 The ALICE experiment

ALICE (A Large Ion Collider Experiment) is a general-purpose, heavy ion detector at the LHC which focuses on QCD – the strong-interaction sector of the Standard Model. It is designed to address the physics of strongly interacting matter and the quark-gluon plasma at extreme values of energy density and temperature in nucleus-nucleus collisions. Besides running with Pb ions, the physics program includes collisions with lighter ions, lower energy running and dedicated proton-nucleus runs. ALICE also takes data with proton beams at the top LHC energy to collect reference data for the heavy ion program and to address several QCD topics for which ALICE is complementary to the other LHC detectors.

In this section, we give an overview of the ALICE experiment and follow, without being original, Ref. [24] – an excellent source of information about ALICE.

4.2.1 Purpose

ALICE experiment is aimed to investigate the primordial state of matter which have existed in the first instances of life of our Universe.

According to modern knowledge, 13.7 billion years ago, our today's Universe was as small as an eye of a needle. It has arisen from a primary highly uniform and highly isotropic bundle with an incredibly high energy density, temperature and pressure, and since that time it is constantly broadening. Phase transitions, analogical to those of liquid condensation and gas evaporation, but for elementary particles, have taken place as a result of broadening and cooling down of the Universe. Those processes have given the beginning of matter from which all structures which we see nowadays were produced, from atoms to far-away galaxies.

During first instances of its life, the Universe has passed through a state which is commonly referred to as quark-gluon plasma (QGP). The QGP is a very hot and dense mixture of unconfined quarks and gluons. In ten microseconds after the Big Bang, the QGP has "frozen" giving birth to protons and neutrons.

At common temperatures, quarks and gluons are firmly bound inside nucleons, and there is absolutely no way to isolate them from each other. At very high temperatures, exceeding thousands of times the one in the center of the Sun, however, ordinary matter passes into the QGP phase. Thus, it is believed that, by colliding heavy ions at very high energies, one can create the QGP for very short instants of time. ALICE experiment is designed to measure properties of such "little Big Bangs".

4.2.2 Main specifications

The ALICE detector has been built by a collaboration including over 1000 physicists and engineers from 105 Institutes in 30 countries. Its overall dimensions are $16 \times 16 \times 26$ m^3 with a total weight of approximately 10000 t. The experiment consists of 18 different detector systems each with its own specific technology choice and design constraints, driven both by the physics requirements and the experimental conditions expected at the LHC. *The most stringent design constraint is to cope with the extreme particle multiplicity anticipated in central Pb-Pb collisions.* The different subsystems were optimized to provide high-momentum resolution as well as excellent particle identification (PID) over a broad range in momentum, up to the highest multiplicities predicted for LHC. This allows for comprehensive studies of hadrons, electrons, muons and photons produced in the collision of heavy nuclei.

ALICE capabilities for momentum measurement span from 0.1 GeV/c (necessary for global event characterization and hadron spectroscopy) to over 250 GeV/c (for perturbative QCD studies). This is achieved with a combination of very low material budget to reduce multiple scattering at low pt (13% of radiation length up to the end of the TPC) and a large tracking lever arm of up to 3.5 m to guarantee a good resolution at high pt.

Particle Identification (PID) over much of this momentum range is essential, as many observables are either mass or flavor dependent. ALICE employs essentially all known PID techniques : specific ionization energy loss dE/dx, time-of-flight, transition and Cherenkov radiation, electromagnetic calorimetry, muon filters, topological decay reconstruction.

The acceptance is chosen to be sufficient to cover particle decays at low momentum as well as to cover jet fragmentation. The interaction rate is up to 200 kHz with pp and 3 kHz with Pb-Pb. Radiation doses are moderate (< 3000 Gy), allowing the use of slow but high-granularity detectors like TPC. Rare signals are enriched with selective triggers operating at several levels wherever possible (jets, high pt electrons, muons, photons). A number of rare signals like heavy flavor decays are, however, very difficult to select at the trigger level in heavy ion reactions. These require a large sample of minimum bias or central collisions to collect the order of a few 10^7 events in few weeks of LHC operation dedicated to ions each year. In 2011, the integrated luminosity was 5 pb^{-1} for pp runs at $\sqrt{s} = 7$ TeV and 100 μb^{-1} for Pb-Pb runs at $\sqrt{s} = 2.76$ TeV.

4.2.3 Detector layout

ALICE consists of a *central barrel part*, which measures hadrons, electrons and photons, and a *forward muon spectrometer*. Figure 4.2 summarizes the location of the various detector systems.

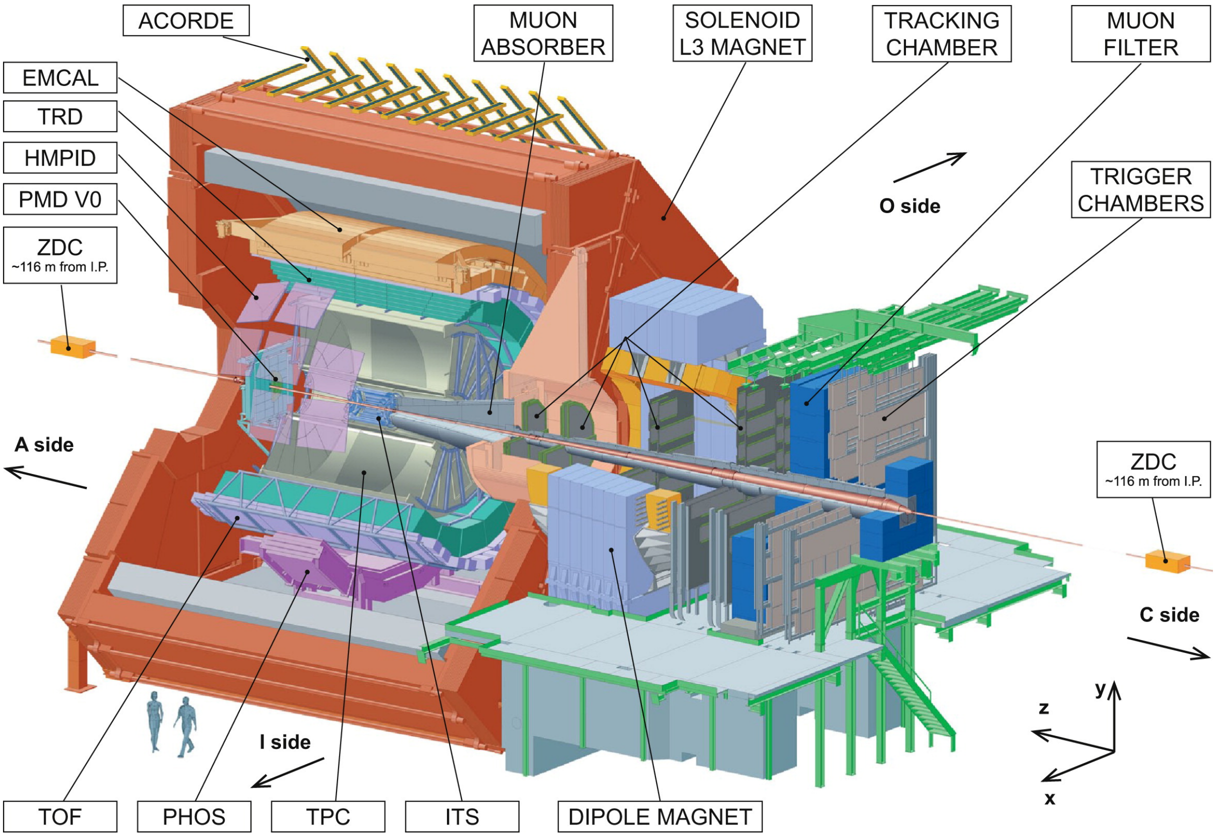

FIGURE 4.2 – Perspective view of the ALICE detector.

The central part covers polar angles from 45° to 135° and is embedded in a large solenoid magnet (which provides moderate magnetic field 0.5 T) reused from the L3

experiment at LEP. From the inside out, the barrel contains :
- an Inner Tracking System (ITS) of six planes of high-resolution silicon pixel (SPD), drift (SDD) and strip (SSD) detectors ;
- a cylindrical Time-Projection Chamber (TPC) ;
- Time-of-Flight (TOF) detector for particle identification ;
- Transition Radiation (TRD) detector ;
- Ring Imaging Cherenkov (HMPID) detector ;
- two electromagnetic calorimeters – PHOS and EMCAL.

All detectors except HMPID, PHOS and EMCAL cover the full azimuth.

The forward muon arm (2° – 9°) consists of a complex arrangement of absorbers, a large dipole magnet and fourteen planes of tracking and triggering chambers.

Several smaller detectors (ZDC, PMD, FMD, T0, V0) for global event characterization and triggering are located at large pseudorapidies. An array of scintillators (ACORDE) on top of the L3 magnet is used to trigger on cosmic rays.

4.2.4 Central tracking detectors

Tracking in the central barrel is divided into the *Inner Tracking System* (ITS), cylindrical six-layer silicon vertex detector, and the *Time-Projection Chamber* (TPC). The Transition Radiation Detector (TRD) is also used for tracking in the central region improving the pt resolution at high momentum. The basic functions of the inner tracker are :
- secondary vertex reconstruction of heavy flavor and strange particle decays ;
- particle identification and tracking of low-momentum particles ;
- improvement of the impact parameter and momentum resolution.

Central tracking system covers the pseudorapidity range $|\eta| < 0.9$.

Inner Tracking System (ITS)

The main tasks of the Inner Tracking System (ITS) are :

1. localize the primary collision vertex with a resolution better than 100 μm ;
2. reconstruct the secondary vertices from decays of hyperons and D and B mesons ;
3. track and identify particles with momentum below 200 MeV/c ;
4. improve momentum and angle resolution for particles reconstructed by the Time-Projection Chamber (TPC) ;
5. reconstruct particles traversing dead regions of the TPC.

The ITS therefore contributes to practically all physics topics addressed by the ALICE experiment, as discussed in detail in [6]. An overview of the ITS detector in shown in Fig. 4.3.

The ITS covers the pseudorapidity range $|\eta| < 2.0$. Its outer radius is about 43.6 cm.

The *Silicon Pixel Detector* (SPD) constitutes the two innermost layers of the ITS. It is a fundamental element for the determination of the position of the primary collision vertex

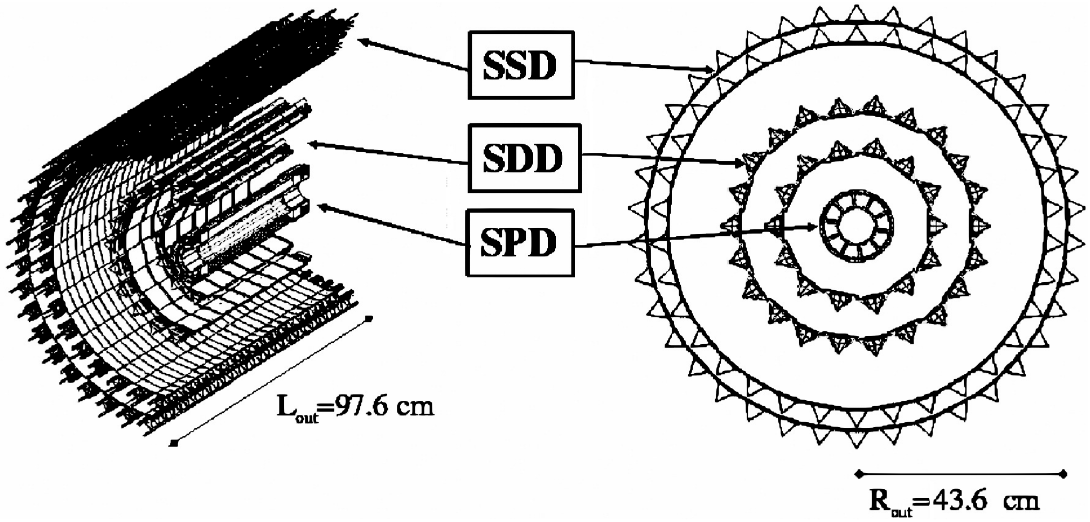

FIGURE 4.3 – ITS detector schematic view.

as well as for measurements of the impact parameter of secondary tracks originating from the weak decays of strange, charm and beauty particles. The SPD is able to achieve the required impact parameter resolution under high particle density expected in heavy ion collisions (as many as 50 particles per cm^2) due to its two-dimensional structure and high granularity.

The *Silicon Drift Detectors* (SDD) equip the two intermediate layers of the ITS, where the charged particle density is expected to reach up to 7 particles per cm^2. SDD have very good multitrack capability and provide two out of the four dE/dx samples needed for the ITS particle identification, see below.

The *Silicon Strip Detectors* (SSD) – the outer two layers of the ITS – are crucial for the matching of tracks from the TPC to the ITS. They provide a two-dimensional measurement of track position. In addition, they provide dE/dx information to assist particle identification for low-momentum particles, see below. The system is optimized for low mass in order to minimize multiple scattering. The track density is expected to be below one particle per cm^2.

The SDD and the SSD (the four outer layers of ITS) have analogue readout and therefore can be used for particle identification via dE/dx measurement in the non-relativistic ($1/\beta^2$) region. The analogue readout has a dynamic range large enough to provide the dE/dx measurement for low-momentum, highly ionizing particles, down to the lowest momentum at which tracks can still be reconstructed. This feature gives the ITS standalone capability as a low-pt particle spectrometer.

The relative momentum resolution $\Delta p/p$ achievable with the ITS is better than 2% for pions with transverse momentum between 100 MeV/c and 3 GeV/c.

The granularity of the detectors was optimized to cope with a track density of 8000 tracks per unit of rapidity at midrapidity – the upper limit of theoretical predictions in Pb-Pb collisions at $\sqrt{s} = 5.5$ TeV. Under these conditions, the ITS would detect simultaneously more than 15000 tracks. Keeping the system occupancy low, at the level of a few percent, requires several million effective cells in each layer of the ITS.

Time-Projection Chamber (TPC)

The Time-Projection Chamber (TPC) [25] is the main tracking detector of the central barrel and is optimized to provide, together with the other central barrel detectors, charged-particle momentum measurements with good two-track separation, particle identification and vertex determination. In addition, data from the central barrel detectors are used to generate a fast online High-Level Trigger (HLT) for the selection of rare signals.

The need for efficient and robust tracking has led to the choice of a TPC as the main tracking detector. In spite of its drawbacks – slow operation speed and huge data volume, only such a conservative and redundant tracking device can guarantee reliable performance at unprecedented charged particle densities of order of 10^4 per unit of rapidity.

The detector is made of a gas-filled ($Ne/CO_2/N_2$: 85.7/9.5/4.8%) cylindrical chamber with multi-wire proportional chambers (MWPC) as endplates. Along its length, the chamber is divided in two halves by means of a central high-voltage electrode disc, which establishes an electric field between the center and the end plates. Charged particles crossing the gas of the TPC ionize the gas atoms along their path, liberating electrons, which are when transported by the electrical field towards the end plates of the detector, where their signals are amplified and read. The active volume of the TPC has the inner radius of 85 cm, the outer radius of about 2.5 m and the total length (along the beam direction) of 5 m, see Fig. 4.4.

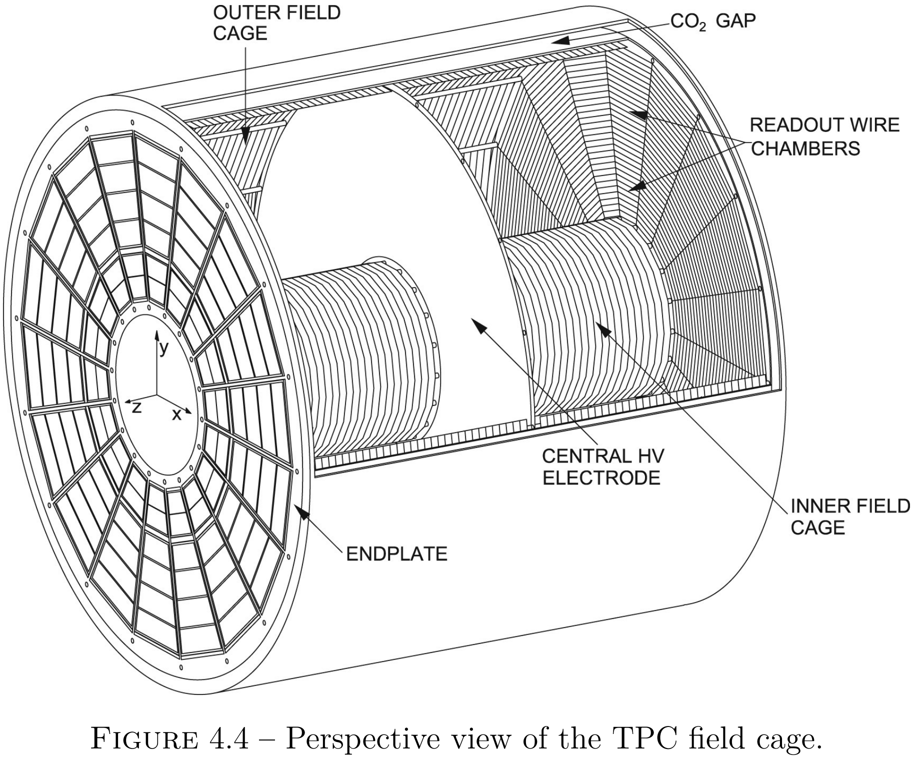

Figure 4.4 – Perspective view of the TPC field cage.

The phase space covered by the TPC in pseudorapidity units is $|\eta| < 0.9$ for tracks with full radial track length (matches in ITS, TRD, and TOF detectors). For reduced track length (and at reduced momentum resolution), an acceptance up to about $|\eta| = 1.5$ is accessible. The TPC covers the full azimuth (with the exception of the dead zones). A large transverse momentum range is covered with good resolution : from about 0.1 GeV/c up to 100 GeV/c.

The achievable dE/dx resolution is designed to be better than 5–7%. With this resolution, the TPC can serve, in addition to tracking, as a detector for particle identification in the region of the relativistic rise.

4.2.5 Particle identification detectors

Particle identification over a large part of the phase space and for many different particles is an important design feature of ALICE with several detector systems dedicated to PID.

Transition Radiation Detector (TRD)

The main purpose of the ALICE Transition Radiation Detector (TRD) [26] is to provide electron identification in the central barrel for momenta above 1 GeV/c. Below this momentum, electrons can be identified via dE/dx energy loss measurement in the TPC.

In conjunction with data from the ITS and the TPC, it is possible to study the production of light and heavy vector meson resonances and the dilepton continuum both in pp and in Pb-Pb collisions. Exploiting the excellent impact parameter resolution of the ITS, it is furthermore possible to reconstruct open charm and open beauty in semileptonic decays.

The TRD was designed to derive a fast trigger for charged particles with high momentum. It is part of the Level 1 trigger and can significantly enhance the recorded Υ-yields, high-pt J/Ψ, the higher-mass part of the dilepton continuum as well as jets.

The necessary pion (and other hadron) rejection capability is achieved by exploiting together the transition radiation (TR) from electrons passing a radiator and the specific energy loss in a suitable gas mixture. The TRD consists of six layers of Xe/CO_2-filled time expansion wire chambers following a composite foam and fibre radiator.

The TRD is designed to provide hadron rejection (signal-to-background ratio) of the order of 100 for momenta above 1 GeV in central Pb-Pb collisions. Only this level of rejection makes feasible the measurement of J/Ψ and lighter vector mesons as well as the determination of the continuum between the J/Ψ and the Υ by bringing the background from misidentified hadrons below the level of real electrons [27].

Time-Of-Flight (TOF) detector

The Time-Of-Flight (TOF) detector [28] is a large cylindrical area array of a radius close to 4 m that covers the central pseudorapidity region, $|\eta| < 0.9$. Its main purpose is particle identification in the intermediate momentum range : below about 2.5 GeV/c for pions and kaons and up to 4 GeV/c for protons, with a proton/kaon and kaon/proton separation better than 3σ. The TOF, combined with the ITS and TPC for track and vertex reconstruction and for dE/dx measurements in the low-momentum range (< 1 GeV/c), provides event-by-event identification of large samples of pions, kaons and protons. In addition, at the inclusive level, identified kaons allow invariant mass studies, e.g., the detection of open heavy-flavored states and vector meson resonances such as the ϕ meson.

The TOF array consists of 160000 individual cells, each put in an electric field. The requirement for an affordable system with a large number of channels, needed to keep the occupancy at or below 10% at the highest predicted charged-particle density, as well as state-of-the-art time resolution of better than 100 ps, was solved with the development of a novel type of gas detector – the Multigap Resistive Plate Chamber (MRPC).

The key aspect of these chambers is that the electric field is high and uniform over the full sensitive gaseous volume of the detector. Any ionization produced by a traversing charged particle immediately starts a gas avalanche process which generates the observed signals on the pickup electrodes. Unlike other types of gaseous detectors, there is no drift time associated with the movement of the electrons to a region of high electric field. In addition, the signal in such a detector is the analogue sum of signals from many gaps ; the construction technique is, in general, rather simple and makes use of commercially available materials.

High-Momentum Particle Identification Detector (HMPID)

The High-Momentum Particle Identification Detector (HMPID) [29] is dedicated to inclusive measurements of identified hadrons at momenta greater than 1 GeV/c. The aim is to enhance the PID capability of ALICE by enabling identification of charged hadrons beyond the momentum interval attainable through energy loss (in ITS and TPC) and time-of-flight measurements (in TOF). The detector was optimized to extend the useful range for proton/kaon and kaon/proton discrimination, on a track-by-track basis, up to 3 GeV/c and 5 GeV/c, respectively. In addition, the identification of light nuclei and antinuclei (D, T, ^{3}He, α) at high transverse momenta in the central rapidity region can also be performed.

The HMPID detector is a single-arm array of proximity focusing ring imaging Cherenkov counters with liquid radiator and solid CsI photocathode evaporated on the segmented cathode of multiwire proportional chambers. It extends in about 5° of the central barrel acceptance.

4.2.6 Electromagnetic calorimeters

Photons, spanning the range from thermal emission to hard QCD processes, as well as neutral mesons are measured in the small single-arm, high-resolution and high-granularity PHOS electromagnetic calorimeter. It is located far from the vertex (4.6 m) and made of dense scintillating crystals ($PbWO_4$) in order to cope with the large particle density. $PbWO_4$ has both a small Moliere radius and sufficient light output to measure the lowest energies of interest with good resolution. A set of multiwire chambers in front of PHOS acts as a charged particle veto (CPV).

The interaction and energy loss of high-energy partons in dense matter play an essential role in the study of nuclear collisions at the LHC. In order to enhance the capabilities for measuring jet properties, a second electromagnetic calorimeter (EMCAL) is installed in ALICE. The EMCAL is a Pb-scintillator sampling calorimeter with longitudinal wavelength-shifting fibres, read out via avalanche photo diodes. Much larger than PHOS, but with lower granularity and energy resolution, it is optimized to measure jet production rates and fragmentation functions in conjunction with the charged particle tracking in the other barrel detectors.

Figure 4.5 shows the location of ALICE electromagnetic calorimeters.

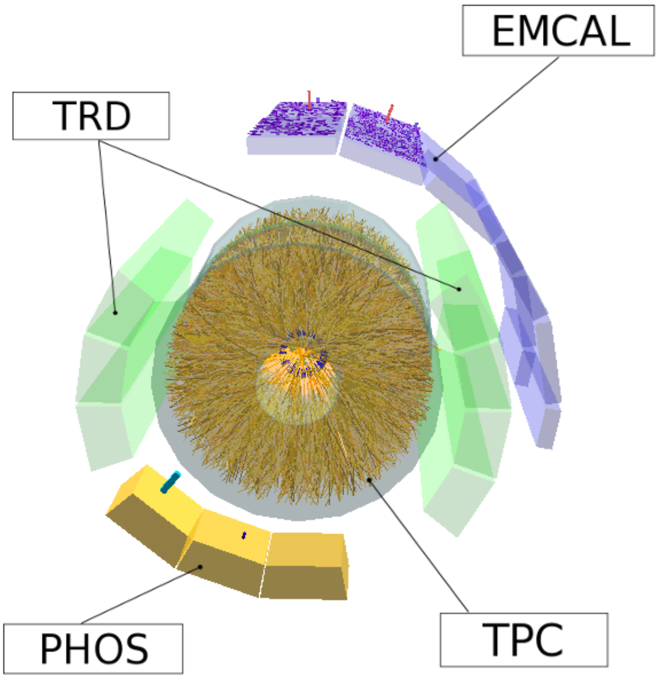

Figure 4.5 – ALICE event display of an event in a Pb-Pb run.

Photon Spectrometer (PHOS)

The PHOton Spectrometer (PHOS, [30, 6]) is a high-resolution electromagnetic spectrometer covering a limited acceptance domain at central rapidity. The main physics objectives are the test of thermal and dynamical properties of the initial phase of the collision extracted from low momentum direct photon measurements and the study of jet quenching through the measurement of high momentum π^0 and γ-jet correlations.

The high particle multiplicity in nuclear collisions requires a dense, highly segmented calorimeter with small Molière radius at a large distance from the interaction point in order to keep the cell occupancy at a manageable level of about 10–20% in central Pb-Pb collisions. A good energy and position resolution improves the signal to background ratio for meson identification, in particular at low pt where the combinatorial background is very large. The identification of photons requires high discrimination power against charged hadrons, neutrons and antineutrons. The required performance is met through a high granularity electromagnetic calorimeter, timing resolution of the individual detector cells of the order of a few ns and a charged particle detector in front of the calorimeter. Direct photons are discriminated against decay photons either through shower shape analysis at high pt or through invariant mass analysis at low pt.

PHOS is designed as a single-arm high-resolution high-granularity electromagnetic spectrometer consisting of a highly segmented electromagnetic calorimeter (PHOS) and a Charged-Particle Veto (CPV) detector. PHOS is subdivided into five independent PHOS+CPV units, called PHOS modules (three of which are present as of 2012). It is positioned on the bottom of the ALICE setup at a distance of 4.6 m from the interaction point. After its final installation it will cover approximately a quarter of a unit in pseudorapidity, $|\eta| < 0.12$, and 100° in azimuthal angle. The resulting two-photon invariant mass resolution at the π^0 peak is 3.5%. The large momentum range (0.005–80 GeV) is achieved.

The high-energy resolution and granularity is provided by using dense scintillator material (lead-tungstate, $PbWO_4$) of 20 X_0 with high photo-electron yield.

Each PHOS module is segmented into 3584 detection cells arranged in 56 rows of 64 cells. The detection cell consists of a $22 \times 22 \times 180$ mm^3 lead-tungstate crystal, $PbWO_4$ (PWO) coupled to a 5×5 mm^2 Avalanche Photo-Diode (APD) followed by a low-noise preamplifier. To increase the light yield of the PWO crystals (temperature coefficient 2% per C°), the PHOS modules are operated at a temperature of -25°C.

ElectroMagnetic CALorimeter (EMCAL)

The construction of a large ElectroMagnetic Calorimeter (EMCAL) [31] has the aim to enable ALICE to explore in detail the physics of jet quenching (interaction of energetic partons with dense matter) over the large kinematic range accessible in heavy ion collisions at the LHC [6]. The scope and basic design parameters of the calorimeter were chosen to match the physics performance requirements of the high-pt physics goals.

The EMCAL is a large Pb-scintillator sampling calorimeter with cylindrical geometry, located adjacent to the ALICE magnet coil at a radius of 4.5 meters from the beam line. It covers $|\eta| < 0.7$ and $\Delta\phi = 107°$ and is positioned approximately opposite in azimuth to the high-precision ALICE Photon-Spectrometer (PHOS) calorimeter. The size of the EMCAL is constraint by the available free space and the maximum weight which can be supported by the L3 magnet.

The choice of a large-acceptance, moderate-resolution electromagnetic calorimeter provides a cost-effective pathway into jet physics in ALICE. The EMCAL increases the electromagnetic calorimeter coverage of ALICE by nearly an order of magnitude. It provides a fast and efficient trigger (L0, L1) for hard jets, photons and electrons, allowing ALICE to exploit fully the luminosity of the LHC. The EMCAL also measures the neutral energy component of jets, enabling full jet reconstruction in all collision systems, from pp to Pb-Pb. The combination of the EMCAL, the excellent ALICE charged particle tracking capabilities, and the modest ALICE magnetic field strength, is a preferred configuration for jet reconstruction in the high-background environment of heavy ion collisions, allowing the optimization of background rejection while preserving the crucial jet-quenching signals at moderate transverse momentum. The EMCAL in ALICE in conjunction with the TPC has good jet energy resolution in Pb-Pb collisions, and excellent sensitivity to the full range of jet-quenching effects expected at the LHC. The emphasis on high pt means that the intrinsic energy resolution of the EMCAL can be modest and the detector granularity can be coarser, with moderately high occupancy. These design criteria point toward the choice of a sampling-calorimeter design, similar to those that were built for STAR and PHENIX to study high-pt phenomena in heavy ion collisions at RHIC and then in the LHC-B experiment at the LHC.

4.2.7 Muon spectrometer

The forward muon arm is primarily designed to measure the production of heavy quark resonances (J/Ψ, ψ', Υ, Υ', Υ'') with a mass resolution sufficient to separate all states. The simultaneous measurement of all the quarkonia species allows one to do a direct comparison of their production rate as a function of different parameters such as transverse momentum and collision centrality. In addition to vector mesons, the unlike-sign dimuon continuum up to masses around 10 GeV/c^2 will be measured.

Since at the LHC energies the continuum is expected to be dominated by muons from the semileptonic decay of open charm and open beauty, it will be possible to study the production of open (heavy) flavors. Heavy flavor production in the region $-2.5 < \eta < -1$ is accessible through measurement of e-μ coincidences, where the muon is detected by the muon spectrometer and the electron by the TRD.

The muon spectrometer participates in the general ALICE data taking for Pb-Pb collisions.

The muon spectrometer is located at small angles (2°– 9°, $-4 < \eta < -2.4$), gives good acceptance down to zero transverse momentum and provides a manageable background from hadron decays. It consists of :

- a composite absorber ($\approx 10\lambda_{\text{int}}$) made with layers of both high-Z and low-Z materials starting 90 cm from the vertex ;
- a large dipole magnet with a 3 Tm field integral placed outside the L3 magnet ;
- 10 planes of very thin, high- granularity, cathode strip tracking stations.

A second muon filter ($\approx 7\lambda_{\text{int}}$ of iron) at the end of the spectrometer and four planes of Resistive Plate Chambers are used for muon identification and triggering.

The spectrometer is shielded by a dense conical absorber tube, of about 60 cm outer diameter, which protects the chambers from secondary particles created in the beam pipe.

4.2.8 Forward and trigger detectors

A number of small specialized detector systems are used for triggering or to measure global event characteristics.

- Event time is measured with very good precision (< 25 ps) by the *T0 detector* – the two sets of 12 Cherenkov counters (fine mesh photomultipliers with fused silicon radiator) mounted around the beam pipe.
- Two arrays of segmented scintillator counters – the *V0 detector* – are used as minimum bias trigger and for rejection of beam-gas background.
- An array of 60 large scintillators on top of the L3 magnet – the *ALICE Cosmic Ray Detector* (ACORDE) – triggers on cosmic rays for calibration and alignment purposes as well as for cosmic ray physics.
- The *Forward Multiplicity Detector* (FMD) provides multiplicity information over a large fraction of the solid angle ($-3.4 < \eta < -1.7$ and $1.7 < \eta < 5$). Charged particles are counted in rings of silicon strip detectors located at three different positions along the beam pipe.
- The *Photon Multiplicity Detector* (PMD) measures the multiplicity and spatial distribution of photons event-by-event in the region $2.3 < \eta < 3.7$. It consists of two planes of gas proportional counters with cellular honeycomb structure, preceded by two lead converter plates of 3 radiation lengths each.
- A *Zero Degree Calorimeter* (ZDC) is located on each side in the machine tunnel, about 116 m from the interaction region. The ZDC consists of two compact calorimeters and is used to measure and trigger on the impact parameter of the collision. Each ZDC is made of tungsten (neutron calorimeters, ZN) and brass (proton calorimeters, ZP) with embedded quartz fibres. The ZDCs are designed to measure "spectator nucleons" of a collision.
- In addition, two small electromagnetic calorimeters (ZEM) are installed on one side, 7 m from the vertex, to improve the centrality selection.

4.2.9 Trigger and data acquisition

The ALICE trigger system is designed to select events having a variety of different features (e.g. selection of rare events) at rates which can be scaled down to suit physics requirements and the restrictions imposed by the bandwidth of the Data Acquisition (DAQ) system.

The *hardware* trigger in ALICE combines the input from detectors with fast trigger capability : T0, V0, ZDC, SPD, TOF, TRD, PHOS, EMCAL, Muons, ACORDE. It operates at several levels to satisfy the individual timing requirements of the different detectors, as the ALICE electronics is in general not pipelined : a pretrigger activates the TRD electronics shortly after each interaction ($< 0.9\ \mu$s) while two further levels (L0 at 1.2 μs and L1 at 6.5 μs) reduce the event rate depending on the trigger inputs. A final trigger (L2 at about 100 μs) is issued after the end of the drift time in the TPC, the slowest detector in ALICE.

The trigger includes a flexible protection against pileup and an event priority scheme which optimizes both the acceptance of rare triggers and the overall throughput of accepted events.

The *software-based* High-Level Trigger (HLT) is a farm of up to 1000 multiprocessor PCs which subject essentially complete events to a detailed online analysis. Its main task is to select or reject events and to reduce the event size by either selecting only a fraction of the data for readout (region of interest) or by compressing the complete event information.

The relatively short LHC heavy ion runs determine the main feature of the data acquisition system : very large bandwidth of 1.25 GB/s to permanent storage is required to collect a sufficient number of events. It combines a custom optical data link, used throughout the experiment, with commodity equipment (PCs and network switches) in a highly parallel and scalable architecture.

Chapitre 5

Bad channel identification for EMCAL and PHOS detectors

“ A new scientific truth does not triumph by convincing its opponents and making them see the light, but rather because its opponents eventually die, and a new generation grows up that is familiar with it. ”

Max Planck

The basic idea of data quality assurance (QA) is to have fast and simple tool to justify good and bad datasets. In the present chapter, bad channel (cell QA) and bad run (run QA) identification methods for the ALICE electromagnetic calorimeters are proposed.

5.1 Introduction

Assessment of data quality is an essential part of experimental data analysis. As defined in [32], data has quality if it satisfies the requirements of its intended use. This definition is quite applicable for data measured by detectors in high-energy physics, in particular, by calorimeters. Depending on the relative yields of a signal which is searched for and of its background, different criteria for the data quality has to be applied. In this chapter, we consider the quality assessment of data collected by electromagnetic calorimeters.

The ALICE [24] electromagnetic calorimeters, EMCAL [17] and PHOS [33], are designed to measure the energy and hit coordinates of photons and electrons. These detectors have a cellular structure and consist of *cells* (or *channels*) packed into rectangular blocks forming (super)modules. The EMCAL detector is built of 10 supermodules of 24×48 cells each, while PHOS has 3 modules of 64×56 cells. The energy and position of incoming particles are reconstructed from the amplitudes of signals in the cells measured by the front-end electronics (FEE). More details about the ALICE experiment and its detector layout are given in Chapter 4.

The size of a cell was chosen in a way that the total energy of a photon or electron is deposited in a domain formed by several adjacent cells, which is called a *cluster*. Thus, the calorimeter is intended to resolve the electromagnetic shower. A cluster with its energy and resolved position in a calorimeter represents the smallest unit which is interesting for a physical analysis.

In each collision event, the functioning of the calorimeter can be presented as a distribution of energy on a rectangular grid which covers a part of solid angle around the collision point (see Fig. 5.1). We will use an analogy of a calorimeter and its response with that of a TV screen or pixel camera with black and white colors, with energy corresponding to the level of gray color.

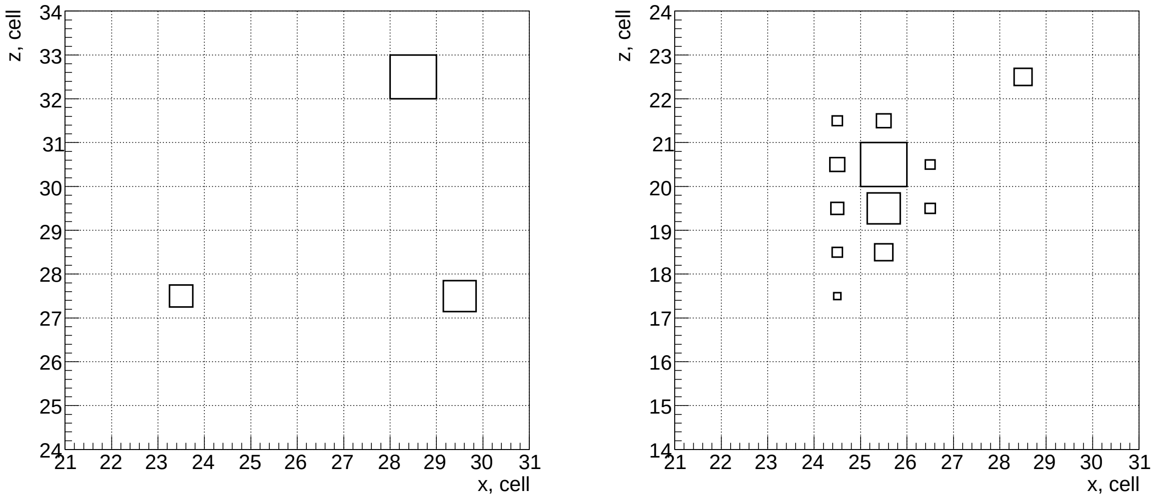

FIGURE 5.1 – Demonstration of isolated cells with deposited energy (left) and a cluster (right).

Ideally, the recorded distribution of energy would accurately match that carried by photons and electrons in the event. As a matter of fact, several problems affect the detector response, e.g. some cells may not function, others are miscalibrated. These defects can be classified into two categories :

1. those whose presence is compatible with a physical analysis, which can be corrected for at the analysis stage ;
2. those that preclude the physical analysis ; they should be identified at an early stage ; the monitoring of these defects enters the protocol of quality assurance.

For PHOS and EMCAL, the defects that enter in the second category include dead and noisy cells. Their very existence in a particle physics detector may be explained by a great complexity of each channel in comparison with a screen pixel, together with highly demanding operating conditions. While a physical signal itself is often not affected by the presence of noise in data, the level of background can be so high that the signal will not be seen. In addition, systematic uncertainties of physical quantities highly depend on the noise level. Therefore, quality assurance of channels is a necessary step for obtaining physical results.

A further aspect that affects the present consideration is that of time evolution. The collected experimental data is accumulated continuously during whole year. Thus, it is taken under slightly changing conditions. Moreover, sometimes a part of the experimental equipment may malfunction or simply be switched off if it is not ready for data taking. While doing physics analysis, one should be assured that the data analyzed is “good” in the sense that changing in time conditions of data taking does not affect measured physical quantities (up to estimated statistical and systematic error uncertainties.)

A regular way to ensure data quality is to split the datasample into several blocks and then draw for each block of data some elementary physical quantities (an example of a gauge signal for PHOS and EMCAL is the π^0 meson peak in the two-cluster invariant mass spectrum). Physical quantities should not change from block to block, and a block with too high deviation is considered as “bad" from the physical analysis point of view and should be discarded. The natural blocks of data are *runs*, which constitute data-set units recorded under same conditions, such as detector and trigger configuration, and beam conditions (beam energy, luminosity, etc.).

Lacking a test card, we make use of the particle collision signal itself, the very same we want to analyze later, for verifying the calorimeter functioning on a run-by-run basis. Since in a collision event the probability of illuminating a given cell with a particle of a given energy is almost independent of the cell location (there is no azimuth dependence and a slight dependence in pseudorapidity), on the long run each cell will be exposed to the same distribution of energy. Abnormal channels can therefore be distinguished by comparing the cell responses. In practice, basic quantities, such as mean energy or mean occupancy, do a good job for bad channel identification, and have the advantage of requiring only limited statistics.

The present chapter describes the methods developed for identification and suppression of poor-quality data for calorimeters at the level of individual cells, as well as at the level of runs. The quality of data is assessed with respect to neutral meson spectra measurements in proton-proton collisions at the LHC. However, the same algorithms are equally applicable for any other hodoscopic-type calorimeters, as well as for more precise measurements of rare signals, like direct photon spectra.

The structure of the chapter is the following. A general discussion of bad channels is given at the beginning. Then, the basic building blocks of any calorimeters of hodoscope type, cells and clusters, are introduced, and we argue that cluster-based quantities are the most relevant variables to characterize bad cells. Next, a method which allows to discriminate good and bad cells is described. Graphical presentations of the data quality per run are shown afterwards. Although the method is general enough to apply to both EMCAL and PHOS, all the examples are done on PHOS data and minimum-bias events. The datasample considered in the present chapter is LHC10c and LHC10d taken in June 2010 in *pp* collisions at 7 TeV with PHOS detector. It contains 275 million events (distributed in 157 runs) corresponding to an integrated luminosity $L = 4.4$ nb^{-1}. The average energy deposited in a cluster is $E = 0.56$ GeV (among clusters with minimum energy 0.5 GeV), the number of clusters is around 4-5 for each hundred events and the average number of cells in a cluster is between 5 and 6.

Finally, the run quality assessment is described. Relying on the behavior of basic physics observables, it can serve as a verification of a proper bad channel suppression, as well as a monitoring of the run. The architecture of the developed algorithms to identify bad channels and verify data quality, can be found in appendices.

5.2 Bad channels in calorimeters

Some cells in a calorimeter show an abnormally low response compared to others. Such malfunctioning bad cells influence the detector response incorrectly, effectively reducing the acceptance of the detector and leading to loss of signal. Other types of cell malfunctioning include, for instance, wrong cell energy spectrum. The QA analysis proposed in the chapter allows to discover such types of problematic cells. For illustration, a comparison of all cluster energy spectrum and the one excluding bad cells is shown on Fig. 5.2. The left plot shows a spectrum which distorted by bad channels, while the right plot shows a similar spectrum without bad channels. The presence of noisy channels is reflected in the irregular shape of the energy spectrum.

Let us classify possible problems which have to be pursued by the QA tasks :

- *Dead channels* are those channels which have no signals in a run. The most probable reason of a dead channel is a connection failure or a misconfigured high voltage bias, or a broken photodetector. Of course, in short runs, some channels may not have a chance to detect any signal just because of a lack of statistics. The QA treatment should take this situation into account.

  The importance of dead channels identification can be illustrated as follows. If a particle hits the calorimeter in the vicinity of a dead cell, a part of the shower which fall into this dead cell is not detected, and, as a result, the total energy deposited by the particle in the calorimeter is underestimated. Therefore, to reduce the influence of dead channels in the detected energy spectrum, all dead cells have to be marked and the clusters close to such dead channels need a special treatment.

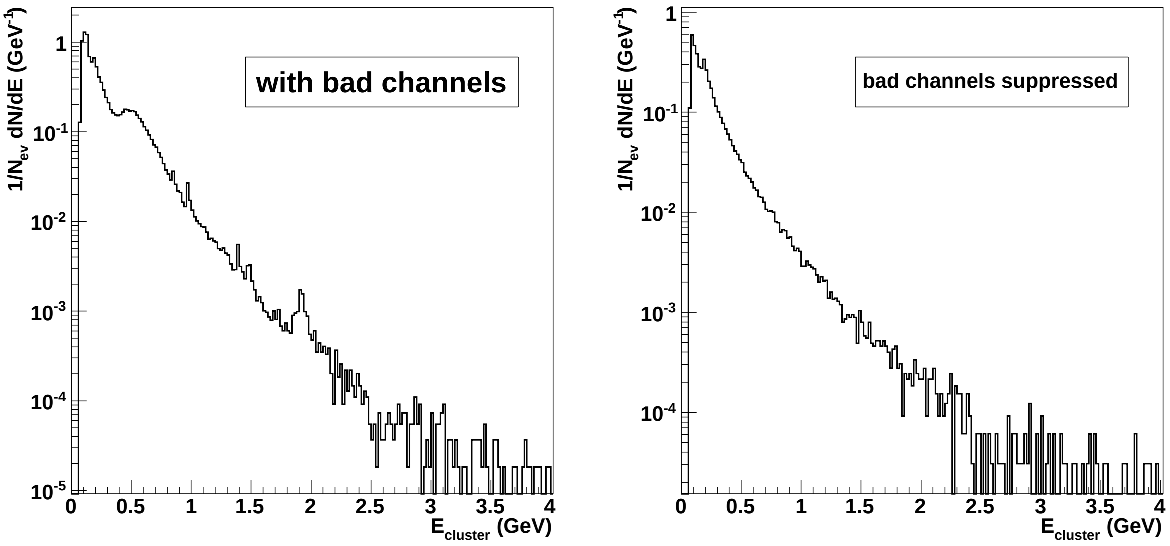

Figure 5.2 – Example of cluster energy spectrum with presence of noisy channels (left) and with noisy channels suppressed (right).

Dead channels, together with the fiducial volume around them, lead to a reduction of the detector acceptance which should be taken into account in Monte Carlo simulations performed to calculate the detection efficiency and the normalization of various spectra.

- *Noisy channels* have in common with good channels that they do have signals, but the physics quantities characterizing their data quality reveal abnormal behaviors compared to other channels. Some channels can be noisy because of an FEE failure or misconfigured high voltage bias of the photodetectors which may result, in turn, in excitation of the FEE, or in miscalibration of the channels. Noise can be intrinsic to a channel or it can be induced by a neighboring noisy channel.

  The presence of noisy channels in the datasample is usually reflected in various distortions of observed energy spectra and, in particular, in invariant mass distributions. One of the most common distortion of the spectra are false spikes which can imitate real physics peaks, but with wrong parameters, or even obscure physics signals completely, if the noise frequency is larger than the frequency of the physics events. Noisy channels especially hurt when one searches for rare signals with a very low signal-to-background ratio. As an illustration, a severe distortion can be observed in invariant mass plots of cluster pairs on Fig. 5.3, which shows the expected π^0 peak at the invariant mass of 135 MeV/c^2, highlighted by a blue line, along with the false peak at the invariant mass of 250 MeV/c^2, depicted by a red line. This example was obtained from real data and demonstrates that bad channels lead to wrong physics measurements.

The quality assessment has several stages. At first stage, we select bad channel candidates, i.e. cells which show abnormal behavior. On the second stage, we treat each candidate to understand precisely the cause of the problem. At this stage, we reveal "true" faulty cells and give them precise diagnosis.

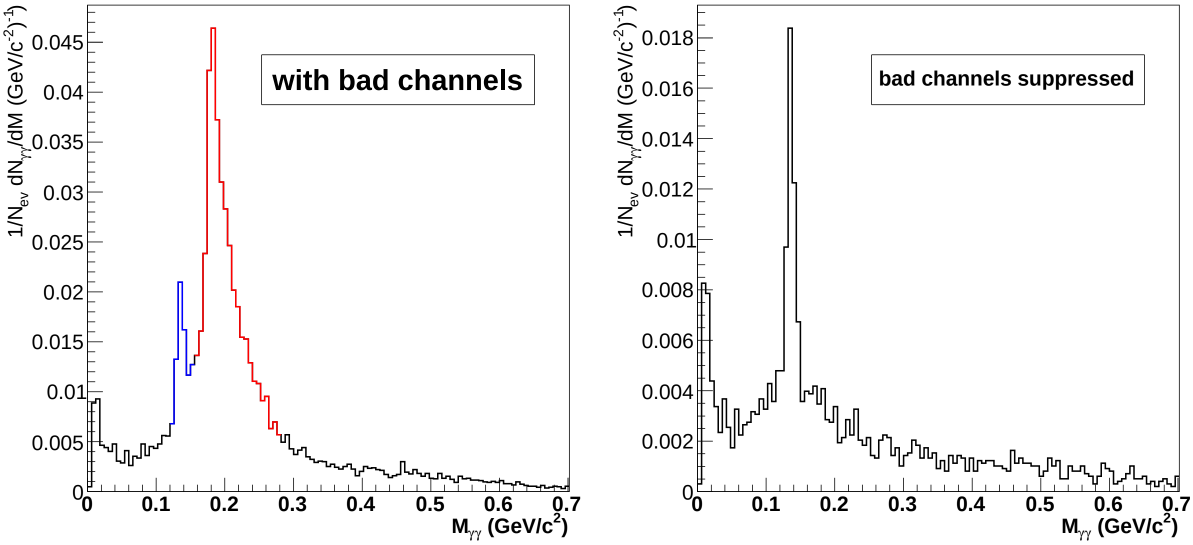

FIGURE 5.3 – Example of two-cluster invariant mass spectrum with presence of noisy channels (left) and after suppression of noisy channels (right). The scale in vertical axis is different between the plots.

The present analysis is oriented towards different users. On one hand, it is important to have a precise diagnostics of each channel and give a necessary treatment to it at the hardware level. Therefore, this analysis can be useful for hardware experts. On the other hand, the main goal is to measure physics observables. Therefore, this analysis will serve physicists. For them, it is sufficient to stop at stage 1 (selecting the candidates) and switch off the problematic cells at the level of analysis.

Let us also remark that a person doing a physical analysis tends to have a single bad channel map for a large datasample since each change of the bad channel map requires recalculation of acceptance and efficiency of the detector. In addition, division of the datasample into several subsets with uniform bad channel maps limits an accessible momentum range, which is even a stronger reason to keep a persistent bad channel map on as big datasample as possible.

One can ask an important question : to which extent do we want to clean our signal ? On one hand, we do want to suppress very noisy channels. On the other hand, each noisy channel also collects a physical signal which we do not want to lose. If we do not suppress bad channels, physics signal will not be seen. If we suppress too much, the acceptance of the detector will become too small, and we will not see physical signal either. For these reasons, a compromise must be found. It is determined by an intended use of data. In this chapter, we assume that the analysis aims at producing the π^0 spectrum and define a data quality as good if the measured π^0 spectrum is not affected by the presence of residual noisy channels.

In the following, we propose a method for identifying bad channels after each reconstruction pass of a collected data. In this way, it is possible to generate a bad channel map which evolves with time during the campaign of data taking. Although the method could be used just after the ALICE experiment started its operation, for the PHOS detector, a preselection of bad channels was done using pedestal and LED runs (see [8] for details).

5.3 Definitions

5.3.1 Cell and cluster energy

The fundamental building block in an analysis is the energy measured by a cell i in an event k, denoted as E_k^i. Note that a conversion to the cell energy from raw signal is done in several stages, in particular, using the front-end electronics (FEE).

The energy in an event is distributed over groups of adjacent cells with common sides – clusters (see Fig. 5.1). A cluster is characterized by its energy which is the sum of energies deposited in those cells which belong to the cluster.

A calorimeter cell energy becomes physically relevant when it is well above the FEE intrinsic noise. The intrinsic noise was estimated at the design level and later measured in each channel in dedicated pedestal runs. One standard deviation of the pedestal distribution in the ALICE calorimeters, expressed in energy units, is about 15 MeV for EMCAL and 2 MeV for PHOS. To be insensitive to pedestal fluctuations, a threshold on cell amplitude is set in FEE. This minimum cell energy $E_{\text{min}}^{\text{cell}}$ was set to 3 standard deviations of the pedestal distributions, that is 45 MeV and 6 MeV for EMCAL and for PHOS respectively. Taking into account the presence of this threshold, we have

$$E^i = \begin{cases} E^i, & \text{if } E^i \geq E_{\text{min}}^{\text{cell}} \\ 0, & \text{if } E^i < E_{\text{min}}^{\text{cell}}. \end{cases} \tag{5.3.1}$$

Clusters are formed from cells in a dedicated reconstruction procedure which requires that a cluster should have at least one cell with the energy greater than a so called cluster seed threshold $E_{\text{min}}^{\text{clu}}$ (see, for instance, [7]). This threshold may vary from one reconstruction pass to another and, in 2010, it was set to 100 MeV for EMCAL and 50 MeV for PHOS. One can see that single isolated noisy cells can have energies above the cell threshold $E_{\text{min}}^{\text{cell}}$ and below the cluster seed threshold $E_{\text{min}}^{\text{clu}}$.

5.3.2 Local maximum

Cell size of both calorimeters was chosen to be less than or equal to the Molière radius of the calorimeter materials. When the shower develops along the axis of a cell, the major part (80-90%) of the shower energy is deposited into one cell. Hence, in a cluster, there is a cell which carries more energy than its neighbors. This cell is called a *local maximum* (LM).

There are several reasons why there can be more than one local maximum in a cluster. For instance, this happen when two showers overlap. In the present study, several QA criteria are formulated with respect to LM cell in a cluster. The reason for this is the following. Imagine a noisy cell which would regularly give a 200 MeV response. As a consequence, all the neighboring cells, as soon as they pass the value $E^{\text{cell}}_{\text{min}}$, will show up in a cluster at a rate abnormally higher than the one of a typical cell. Considering only LM cells in clusters circumvents this problem.

5.3.3 Basic cell observables : total energy and number of events

In this analysis, four basic observables are associated with each cell :

$$N^{i\,(\text{low})}_{\text{tot}}, \qquad N^{i\,(\text{high})}_{\text{tot}}, \qquad E^{i\,(\text{low})}_{\text{tot}}, \qquad E^{i\,(\text{high})}_{\text{tot}}.$$

They are described below.

First, when a cell is LM in a cluster, it is associated to a value of the total cell energy. The accumulated cell energy E^i_{tot} for a cell i is defined as a sum of all the cell energies E^i_{cell} in a whole datasample :

$$E^i_{\text{tot}} = \sum_{k|i \text{ is LM in } k} E^i_k. \tag{5.3.2}$$

The second value is the accumulated number of events when the cell i was LM in a cluster :

$$N^i_{\text{tot}} = \sum_{k|i \text{ is LM in } k} N^i_k, \tag{5.3.3}$$

where N^i_k is 1 if the cell i is a local maximum in a cluster in event k, and 0 otherwise.

Finally, as the amount of low energy clusters is exponentially larger than the amount of high energy ones, it is useful to separate the energy range into two regions, at low energy and at high energy :

1. $E^{i\ (\text{low})}_k = E^i_k$ if 0.3 GeV $\leq E^i_k <$ 1 GeV, and 0 otherwise;
2. $E^{i\ (\text{high})}_k = E^i_k$ if $E^i_k \geq$ 1 GeV, and 0 otherwise.

The division of clusters into the two energy regions allows one to detect high energy noise which would be obscured otherwise by huge amount of low energy clusters. In addition, this splitting allows to cover a large range of energies from hundreds of MeV to hundreds of GeV, while avoiding, for memory consumption reasons, a tight binning in the whole range. In the low energy range, a detailed study of the energy spectrum for each cell is possible, owing to sufficient amount of statistics. In the high energy region, a large binning is sufficient in order to discover abnormal cell response. A good cell should show a normal (average) spectrum in the low energy range and rare signal, if any, at high energy.

The low energy threshold should be the same as the one in the anticipated physics analysis. In the present study, it was set to 300 MeV which is a natural choice in order to focus on electromagnetic showers from photons and electrons and therefore discard signal from minimum ionizing particles (MIPs), which deposit energy in the range of 230–270 MeV. The use of the two threshold values is not accidental. The lower value (0.3 GeV) allows to filter clusters with even lower energy. In a calorimeter, the lower the energy threshold, the higher the rate of intrinsic noise. Putting a threshold for the minimum cluster energy reduces the irrelevant for our task natural calorimeter noise.

Of course, the two threshold values (0.3 and 1 GeV) are adjustable. The default values are good for EMCAL detector. For PHOS, it is better to use the value 0.1 GeV for the lower threshold.

5.4 Cell quality assessment

Quality assurance of channels is a necessary step for obtaining physical results.

5.4.1 Distributions of cell observables

The QA analysis relies both on the fact that all cells are ideally identical and on the fact that they are illuminated with a comparable signal distribution. The latter fact is better realized for runs with bigger statistics. In such circumstances, the distribution of any observable among cells should have a clear peak with only small statistical fluctuations. Thus, one can make a plot with distributions of cell quantities and identify bad cells as those that stand far from the peak.

On Fig. 5.4, an example of the distribution for the average number of hits per cell and per event in one run is shown. The run was chosen to have big statistics (5 million minimum-bias events). The blue line represents the Gaussian function fitted to this distribution in the region around the non-zero maximum value. Cells which show less then 4σ deviation from the average value make up 80.5 %.

Cells with no response correspond to the bin with zero X axis value. They make up 16.5% of cells. In fact, their signals were set to zero either at the level of electronics or at the level of reconstruction. Thus, only the rest 3% of cells are real candidates to be further examined.

Let us remark that one has to keep in mind the following points :

- On Fig. 5.4, we observe that, although the Gaussian function is quite a reasonable fitting function, it doesn't explain the “shoulders” of the distribution. The cells which form the shoulder may, for instance, have incorrect calibration coefficients and, therefore, their spectra is slightly different from the spectrum of a typical cell. However, this does not mean that they are problematic. Indeed, subsequent analysis shows that such cells do not make any bias in physics observables. In this way, the 4σ criterion cuts these “shoulders” in the middle and this is not a welcome feature regarding the above explanation.
- In view of the purpose of an analysis which aims to automate the way of defining bad channels, the fitting procedure is inconvenient and is not reliable. First, fitting

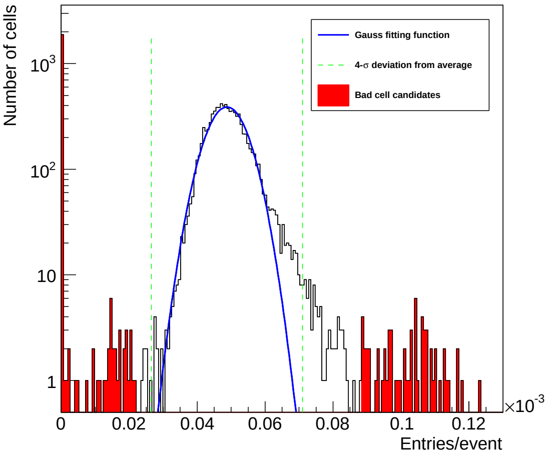

FIGURE 5.4 – Demonstration of good cells and bad and dead cell candidates on the distribution for average number of hits per cell.

depends on the correctness of a plot binning parameters. In case of a non-optimal choice, a manual work is necessary to tune the binning. Second, the fit may fail. For example, if there are two peaks instead of one in the distribution. This can happen, for instance, if one part of the detector was switched off during some time of the data taking. Below, we propose a method that avoids a fitting procedure and where no manual intervention is usually required.

5.4.2 The method of per-run analysis

The calculation of the four quantities (total deposited energy and frequency in two energy regions) for each cell introduced above forms the core of the method of searching for bad cells on a per-run basis. Let us elaborate a method which allows to find bad cells on a per run basis automatically. For each of the four cell observables, this requires a simple way to decide whether a cell is abnormal. This can be accomplished in the following way. For each run and each quantity :

1. find the average over all cells ;
2. for each cell, calculate a factor :

$$\text{factor} = \frac{[\text{value for a cell}]}{[\text{average over cells}]}; \tag{5.4.1}$$

3. claim that a cell is a bad cell candidate for the current run if its factor is outside of an allowed interval defined by two critical values. More precisely, if factor is smaller than the lower critical value, the cell is marked as dead, if the factor is greater that the upper critical value, the cell is considered to be noisy.

Let us make several comments on this algorithm.

Firstly, the algorithm is based on the calculation of averages over all cells, which can include bad cells. This can potentially bias the results, especially in case when one cell is very noisy. Thus, it is important to exclude very noisy cells from the calculation of averages over cells. This is done by an iterative procedure, namely, by repeating the calculation of average over cells and their factors (steps 1 and 2) and excluding cells that fall above the upper critical value. At each step of this iteration, the average value diminishes and after several iterations, typically between 2 and 4, becomes stable.

Second, the motivation for the consideration of the quantity called factor is that it is independent of the number of events in a datasample. In addition, it is a reduced quantity (without physical units) that makes possible the comparison between quantities of different origin (frequency and energy). Conveniently, we will use for simplicity the same critical values for all four basic cell quantities.

Let us examine the factor distributions for each of the four quantities. The four factor distributions are presented on Fig. 5.5.

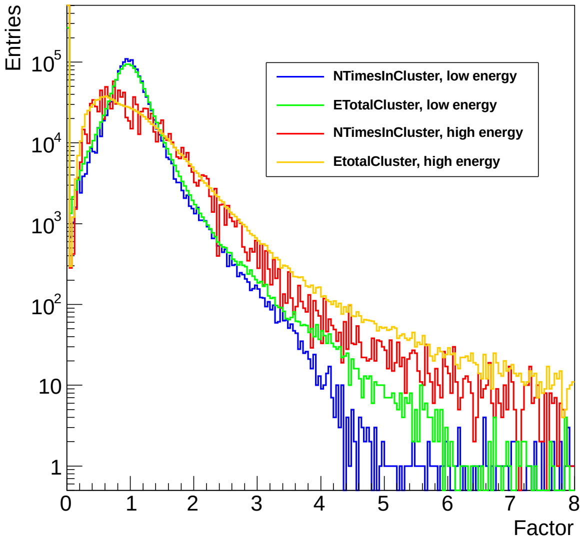

FIGURE 5.5 – Factor distributions (one entry per cell and per run) : frequency factor at low energy (blue), energy factor at low energy (green). The same for the high energy range, red and orange correspondingly.

We observe that the low and high energy range distributions slightly differ. On the contrary, for each range, the frequency and energy distributions are practically on top of each other. This means that both quantities in one energy range are interchangeable. Consequently, we pick one of them for the main analysis, while keeping the second for more detailed studies. We prefer to use frequency because it is easier to interpret and somewhat less calibration dependent.

Looking at the low energy range distributions, we notice that the bulk of entries is concentrated around 1, which shows that most of cells are good, a welcome fact ! The standard deviation is around 0.1. This is more than what would be expected if all cells were identical. As it will be shown later (see Fig. 5.28), the average number of clusters per event in PHOS is about 0.045, which turns to probability of being a local maximum in a cluster to be $4.5\%/(3 \times 64 \times 56) = 4 \cdot 10^{-6}$. With the total analyzed statistics of 275 million events, the average number of hits with a cell being a local maximum would be $1.1 \cdot 10^3$ with a deviation of about 34 which translates into 0.03 for the factor distribution. Several reasons can be put forward to explain the widening of the factor distributions :

1. Intrinsic noise fluctuations can contribute. In particular, because the intrinsic noise spectrum varies from cell to cell.
2. A cell is a complex device with its own slightly different response spectrum. This is especially true when the calibration is not yet finalized.
3. Shower fluctuations will also result in a difference in response even for one and the same cell.
4. As already mentioned, cells are located at different positions and indeed have slightly different exposure. This is especially important in the case of EMCAL due to its bigger coverage and the presence of extra material in front of it (supporting frames, TOF detector, etc.). In addition, the exposure of a cell depends on the position in pseudorapidity. Again, this is mostly relevant for EMCAL only.
5. Finally, it is likely that some cells or even whole (super)modules can be switched off in some runs, and if one considers the quantities and their distributions in several runs, their values will indeed deviate.

The factor distributions (Fig. 5.5) has irregular and asymmetric shape, and there is no evident statistical criterion to discriminate bad and good cells. Too strict criteria would lead to a significant loss of acceptance, while too loose cuts may deteriorate the quality of the datasample. By default, we choose moderate critical factor values. This appears to be enough for exclusion of most bad cells. The upper critical value is chosen by default to be 3.5. The lower critical value is 0.05 since it is only necessary to exclude dead cells.

The exact values for left and right (or lower and upper) critical numbers are not very important. Indeed, we prefer to draw bad cell map for many runs. There is a possibility that a cell fall into a bad region for some quantity and some run accidentally. This is not a problem as we rely on a statistically stable result, looking at how a cell behaves in many runs (see next section for an extensive discussion).

The high energy range distributions are wider and the right-hand side tail contains a larger number of cells than the lower energy range one. This is, at least in part, due to the much lower rate of high energy clusters and thus bigger fluctuations.

5.4.3 Graphical representations of bad channel map

We now proceed to the run to run evolution of cell observables. At this point, we already know that we mark a cell as noisy in a run and give it a red flag for the current run if its frequency factor is greater than the upper critical value 3.5. This we do twice for both the low and the high energy regions. Conversely, we spot a cell as dead and we give it a blue flag for the current run if its factor is less than 0.05. This we do only for the low energy region because of a lack of statistics at high energies.

As the QA is a multi-variable task which identifies cell quality by several complimentary criteria, we propose 6 methods of graphical presentation of the bad channel map on per-run basis. In the present section, we will show various plots useful to describe the flag evolution as a function of run number. Visualization of problematic channels is an important part of this study as it must provide quick and easy access to the quality of data for physicists doing an analysis as well as for engineers maintaining and operating the hardware of their detectors.

Visualization 1 : bad channel map in two energy regions. On Fig. 5.6, the plots show runs in chronological order versus cell absolute numbers (AbsId) for the low and high energy regions. First note that the high energy plot is in blue. This is an effect of available statistics : most cells do not have any high energy entries at all in most runs. Some isolated cells have vertical solid or partly solid blue lines. These are mostly already known problematic cells which were already switched off during the datataking or reconstruction process. We see also blue rectangular box of neighboring cells. They form regions where parts of detector were switched off or absent in data taking for some reason. The reasons could be different for this : FEE failures, lost connection, disfunctioning of electronics, etc. It is very important for a physical analysis to have information about

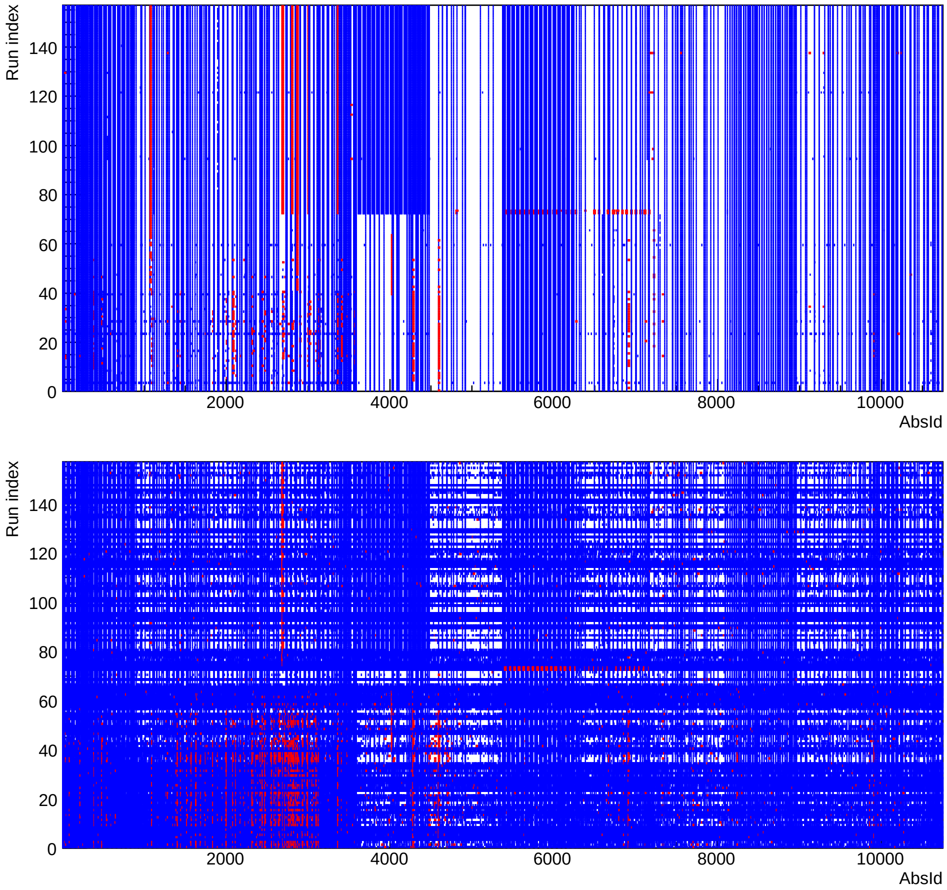

Figure 5.6 – Visualization 1 : dead/noisy channel map vs run index in the low (top) and high (bottom) energy region.

missing detector parts for correct calculation of acceptance and efficiency of the detector.

Solid or partially solid vertical red lines correspond to noisy cells. Again, one can simply exclude them from an analysis or rigorously define their problems by looking at their energy spectra or using additional parts of the QA analysis described later in this chapter. Red region of cells in the high energy plot correspond to a noisy part of the detector. They, in fact, belong to the same RCU or FEE card in a module of the detector.

Visualization 2 : combined bad channel map versus run index in chronological order. Fig. 5.7 combines (by simple addition of spots) the information from the two energy regions of Fig. 5.6 in one single plot. Note that "blue" cells from the high energy plot are not counted. The combined plot is more convenient to use for bad channel identification.

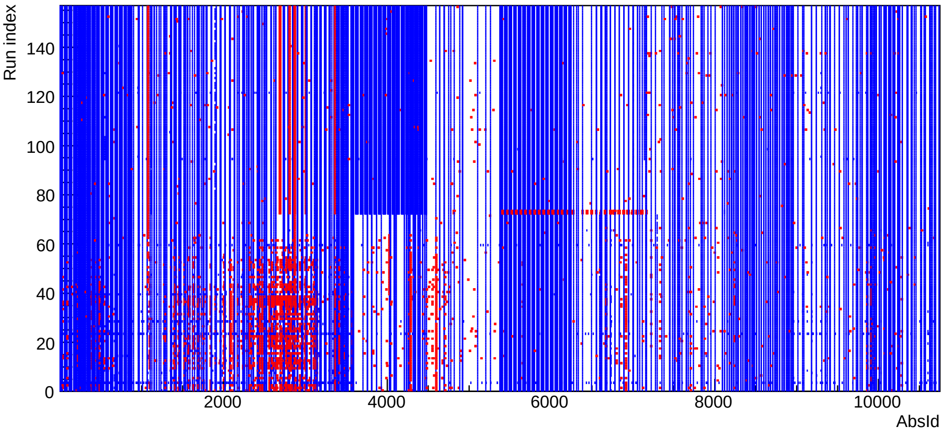

FIGURE 5.7 – Visualization 2 : combined dead/noisy channel map vs run index.

Visualization 3 : combined bad channel map versus events in chronological order. An alternative presentation of the same bad channel map as shown in Visualization 2 is also convenient. It is formed from Fig. 5.7 by changing its Y axis with the number of cumulative events, see Fig. 5.8. The number of events in a run may differ from several tens of thousand to several million, so the present plot is more representative for the percentage of time a cell was malfunctioning.

Visualization 4 : combined bad channel map, percentage of events and runs for two energy region. On Fig. 5.9 the combined information from visualizations 2 and 3 is presented in terms of percentage of runs or events in which a cell was problematic. This plot contains all useful information we can grasp in the run-by-run analysis and it is sufficient to learn all the detected problems. Therefore, it can be used solely to demonstrate the quality of a datasample. The visualization 4 is simple, compact and illustrative way to learn the quality of channels in a datasample. It may be used for a fast check of already cleaned datasample to confirm its quality.

Visualization 5 : occupancy of the detector. Fig. 5.10 demonstrates occupancy of all detector modules. We draw attention to the fact that, in this particular plot, the color flag differs from its meaning in all the other histograms. The color used here as an indication of degree of problems. Red color stands for very problematic cells, while blue is mostly statistical fluctuations. White cells are the normal cells. This plot is useful for

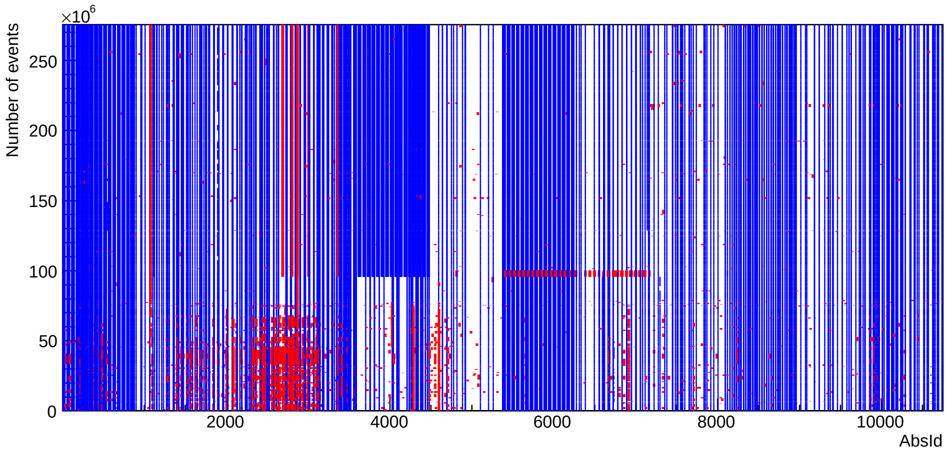

FIGURE 5.8 – Visualization 3 : combined dead/noisy channel map vs number of events.

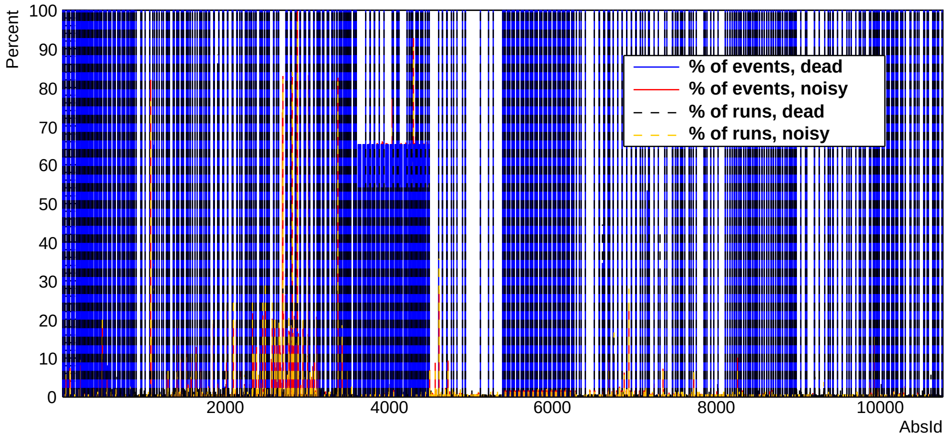

FIGURE 5.9 – Visualization 4 (main plot) : dead/noisy channel map which show percentage of each cell being problematic.

quick localization and identification of faulty regions. As an example, we clearly see the red boxes in modules 1 and 2. They stand for cells which showed up problematic in 100% and 50% of runs. The latter cells correspond to cells which were electronically switched off in the LHC10d period.

Visualization 6 : text. Finally, we can collect all the information using a text file given in the output of the analysis. In it, we can have all the relevant information. For example :

- Bad channel candidates : switched off, noisy cells. Percentage of runs and events where a cell showed abnormal behavior.
- Missing parts of the detector (dead cells in a localized part of the detector : same RCU, supermodule)
- Information obtained in the extended analysis described later in this chapter.
- other information which a user consider to be useful.

Note that, although the visualization 4 allows to grasp all the information provided by run-by-run part of the QA analysis, the visualization 6 allows also to add the information

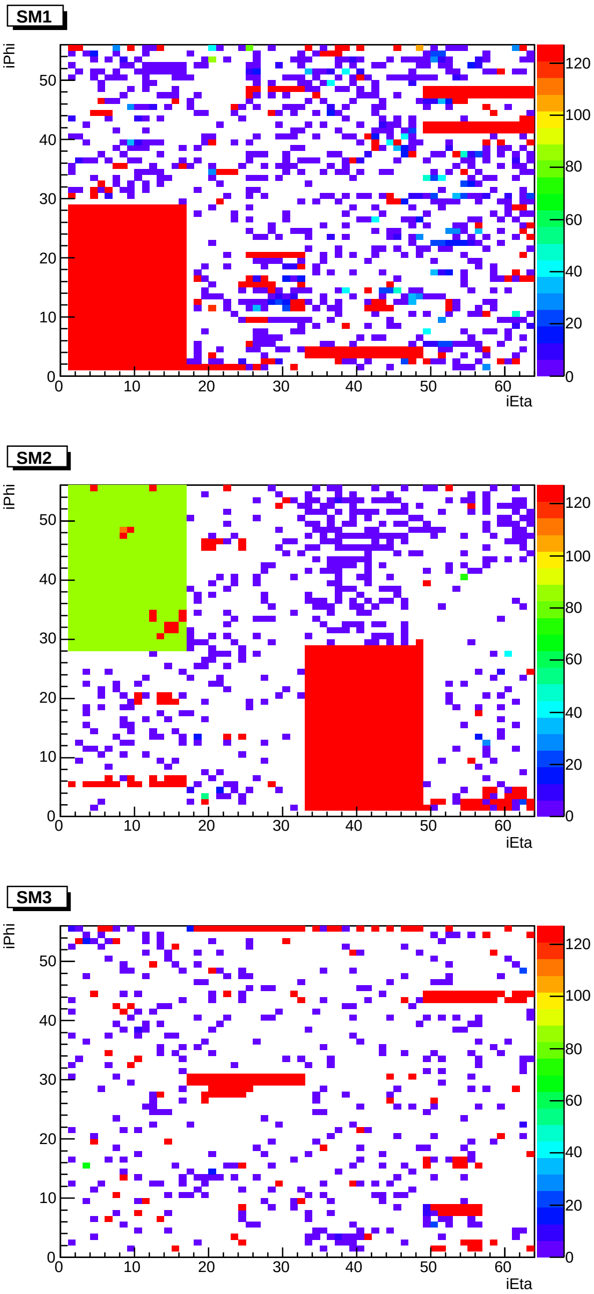

FIGURE 5.10 – Visualization 5 : detector occupancy. Color indicates degree of problem : red : very problematic, blue : mostly statistical fluctuations, white : normal.

obtained in advanced criteria, such as shape analysis (see Section 5.4.4).

Let us emphasize that cells which appeared to be noisy are *bad channel candidates*. To give them more precise diagnosis, one needs to have additional criteria. They are discussed below.

5.4.4 Shape analysis of cell energy spectra

The per-run analysis described in the former section allows one to identify most problems in a calorimeter which is usually enough for physics analysis. A person interested in improving the quality of the detector response should also use additional criteria for spotting of bad cells. These are cell energy shape and integral distributions. We describe those criteria in the present and the next sections. These criteria usually require greater amount of statistics and cannot be used on a per-run basis.

The previous analysis focused on the accumulated number of events N^i_{tot} or energy E^i_{tot} seen by the cell i. Here, we are interested in examining the shapes of cell energy spectra. The study of differential energy distribution for each cell is a natural extension, relying on the same fact that cells are exposed to similar conditions.

The typical cell energy spectrum is presented on Fig. 5.11, whereas Fig. 5.12 presents a faulty energy spectrum. The idea is that the energy spectrum of a normal cell can be well fitted by the function

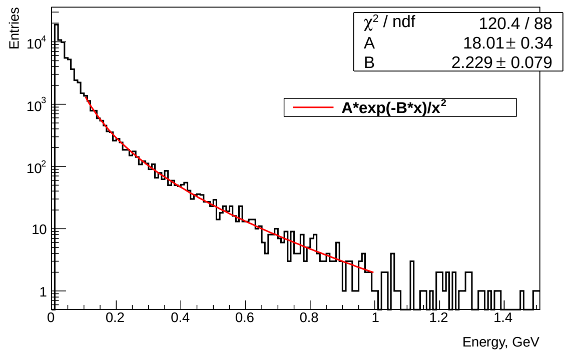

FIGURE 5.11 – Typical cell spectrum.

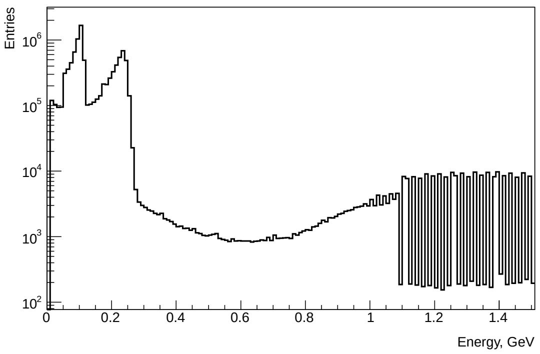

FIGURE 5.12 – Noisy cell spectrum.

$$f(x) = A\frac{e^{-Bx}}{x^2} \tag{5.4.2}$$

with positive parameters A and B. The function has no fundamental grounds. Nevertheless, it has two appealing properties. On one hand, it possesses expected decreasing exponential behavior. On the other hand, it has only two free parameters : the parameter A stands for the amplitude, while B is the slope of the spectrum in logarithmic scale.

The shape analysis is done integrally on a large datasample with many runs. This analysis would be the ultimate criterion to be applied in each run if the statistics would be at least tens of million events. Since this is never the case, for a per-run analysis, we are led back to the methods advocated before. Obviously, the shape analysis complements the per-run analyses by visualizing cell energy spectra and allowing to ensure the correctness of a decision taken with respect to a cell.

The parameters A, B, as well as χ^2/ndf of the fit serve as good observables associated with each cell. One can build distributions of these parameters among cells in the same manner as it was done on Fig. 5.4.

Fig. 5.13 shows the distribution of the amplitude A. The distribution has a tall spike in the bin $A = 0$ which corresponds to cells with an empty spectrum.

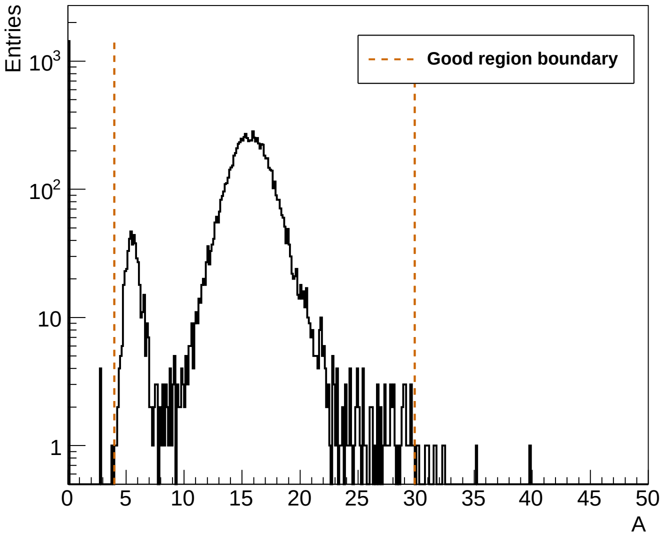

FIGURE 5.13 – Distribution of the parameter A.

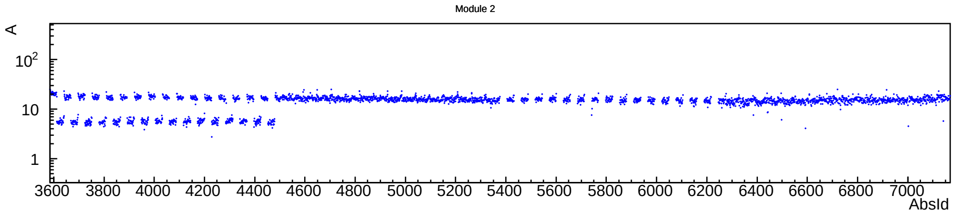

FIGURE 5.14 – Value of the parameter A versus absolute cell number.

On this plot, one clearly sees two peaks. The biggest peak contains 80.5% of the non-empty-spectrum cells. In order to understand the occurrence of the second peak, it is useful to look at Fig. 5.14 which shows the parameter A versus cell absolute number. Clearly, the second peak is formed by cells with AbsIds between 3600 and 4500. An inspection of Fig. 5.9 shows immediately that those cells were dead 60% of the runs, corresponding to runs starting from run index 70 (see Fig. 5.7). They form the big green block on Fig. 5.10, module 2.

On Fig. 5.14, half of the cells with AbsIds between 5400 and 6300 is also missing. They form the big red block on Fig. 5.10, module 2.

The distribution of the parameter B is shown on Fig. 5.15. There is only one rather narrow peak around the value 2.5 $(\mathrm{GeV}/c^2)^{-1}$.

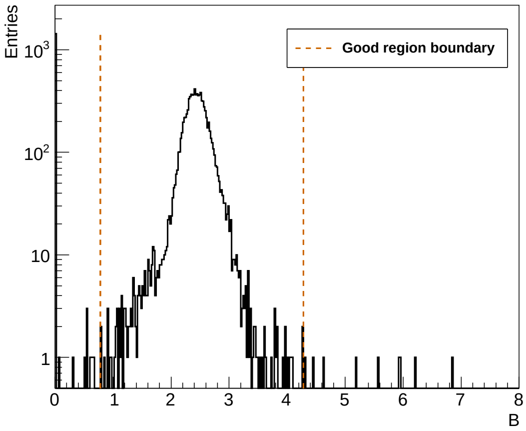

FIGURE 5.15 – Distribution of B.

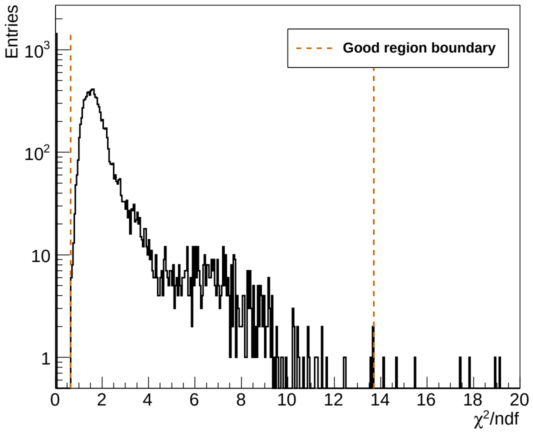

FIGURE 5.16 – Distribution of χ^2/ndf.

The χ^2/ndf distribution is shown on Fig. 5.16. Its structure is more interesting : the bulk of cells is formed around the average χ^2/ndf=1.5, while there is a shoulder between values 4.5 and 10. A dedicated QA analysis of this shoulder showed that it is associated to channels which lack in hardware a high gain signal. This worsens the energy resolution of these cells to 32 MeV instead of expected 2 MeV for PHOS. Nevertheless, these cells can be used in a physics analysis.

The shape analysis can also be used to unravel abnormal cell behaviors thus completing the identification of bad channel candidates as obtained from the run-by-run analysis. To do this, we define good regions for A, B and χ^2/ndf. They are represented by vertical orange lines, see Fig. 5.13, 5.15 and 5.16. The location of these lines is determined empirically (and usually automatically) by looking at cell behaviors located at the left or the right around a line. We see that the good region extends out to χ^2/ndf=14 which is somewhat large, but in line with the above discussion concerning the shoulder for this distribution. Inspection of the cells with higher χ^2/ndf effectively shows pathological behaviors such as spiky energy spectra which may be, in turn, responsible for false peaks as shown in Fig. 5.3.

5.4.5 Integral distribution analysis

In addition to the per-run analysis introduced earlier, we discuss here the possibility to perform a distribution analysis on a whole datasample. The idea of a distribution-based analysis was already discussed in Section 5.4.1. As previously, for each cell, a cell observable is calculated on a particular dataset and the distribution of this observable is built. Cells with considerable discrepancies from the average should be marked for further study.

In general, this type of analysis is auxiliary to what was discussed above since it usually cannot reveal new major issues in the detector. Nevertheless, this part of the QA analysis is a harmonic supplementation and natural finalization of the discussed cell QA framework. Additionally the corresponding source code gives a simple way to apply this type of analysis to new cell observables.

Let us now relist cell observables which are proposed as additional integral criteria. One can arrange them in two groups. First group is based on the histograms which are filled on per-run basis (see Section 5.3.3), namely :

1. probability of a cell in a cluster with the energy $0.3\text{GeV} < E < 1\text{GeV}$ to be a local maximum ;
2. probability of a cell in a cluster with the energy $E > 1\text{GeV}$ to be a local maximum ;
3. mean deposited energy in LM cell of a cluster with the energy $0.3\text{GeV} < E < 1\text{GeV}$;
4. mean deposited energy in LM cell of a cluster with the energy $E > 1\text{GeV}$.

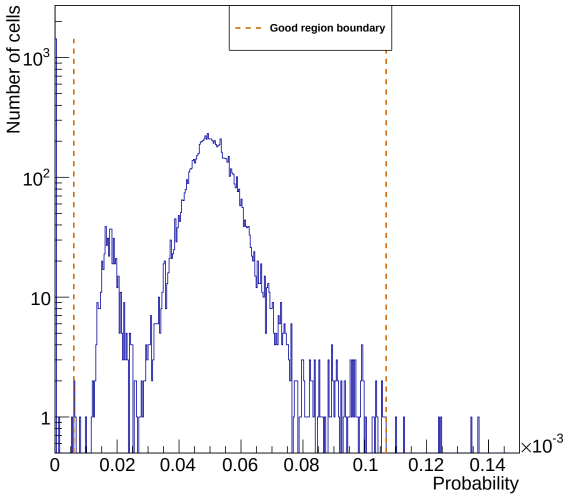

FIGURE 5.17 – Distribution of probability for a cell to be a local maximum in a cluster with energy $0.1\text{GeV} < E < 1\text{GeV}$

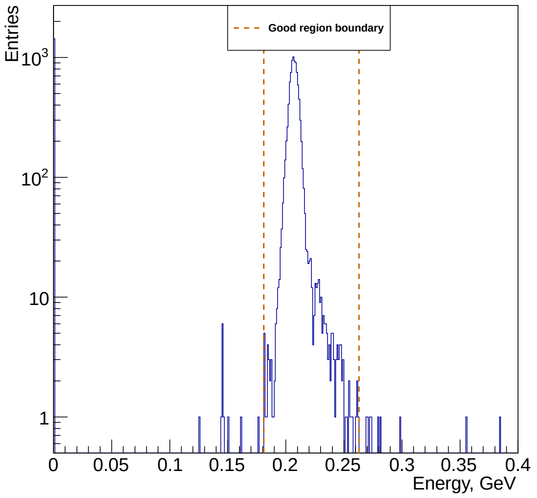

FIGURE 5.18 – Distribution of mean deposited energy in a cell in the range $0.1\text{GeV} < E < 4\text{GeV}$.

The second group of criteria is based on cell energy spectra regardless of whether a cell belongs to a cluster or not. For these criteria, the same histograms as those mentioned in Section 5.4.4 are used. Thus, the criteria in the second group are the following :

1. mean deposited cell energy in the range $0.1\text{GeV} < E < 4\text{GeV}$;
2. mean deposited cell energy in the range $4\text{GeV} < E < 400\text{GeV}$.

The limits are, of course, adjustable.

For clarity, the difference between the two groups of criteria is that in the first group cells should be local maximums in clusters, while in the second group cells are considered irrespectively of their clusters.

Both groups of criteria can be useful for finding miscalibrated cells. As these criteria are defined on the full dataset, they become more statistically significant than those defined in per-run analysis. Thus, calculated observables have small statistical fluctuations.

The distributions are demonstrated on Figs. 5.17 and 5.18. These plots also show that average probability of a cell to be a local maximum of a cluster is about $5 \cdot 10^{-5}$, while the mean deposited energy in a cell is 200 MeV.

As one can see, Fig. 5.17 looks similar to Fig. 5.13 as both plots show distributions for similar quantities. In fact, the difference expressed in the units of their X axes. In particular, the second peak on Fig. 5.17 has the same origin as on Fig. 5.13.

5.5 Run quality assessment

As was already discussed, data taking and detector conditions may evolve with time. In particular, bad channel list may be not persistent because different modules of a detector may fail and be repaired afterwards. A way to monitor this long-term evolution is to study the dependence of basic physics observables versus time, which are referred to as *trend plots*. As a run represents a unit of datasample, such trends can be shown as functions of consecutive run number or run index. They can also be shown as functions of cumulative number of events.

The following six basic observables provide a comprehensive characterization of the long-term evolution of the detector properties :

1. average cluster energy ;
2. average number of reconstructed clusters per event ;
3. average number of cells per reconstructed cluster ;
4. position of the π^0 peak ;
5. width of the π^0 peak ;
6. average number of reconstructed π^0 per event.

These observables are derived from the physics objects reconstructed in the calorimeters : clusters and π^0 mesons. For convenience, we call the criteria 1-3 as cluster averages, while the criteria 4-6 as π^0 averages. The selection criteria for the clusters and π^0 should preferably be the same as used in a physics analysis. For instance, for PHOS, only clusters consisting of 3 and more cells with the energy $E > 0.3$ GeV are selected for the trend plots.

The key point in the runs quality assessment (runs QA) is identifying runs which reveal significant deviations in the trend plots of the above-mentioned physics observables. We shall show below that the presence of bad channels is one of the source of deviations in the trend plots (especially, in cluster averages). We shall show also that not all deviations can be attributed to bad channels. There are global run conditions determined by the LHC or ALICE which can also be responsible for deviations in the trend plots. Therefore, in the next subsections, we first concentrate on effects of bad channels and then describe global run conditions. As the result of the trend plot analysis, bad runs are identified and a list of good runs for a physics analysis is created. We shall show also that some runs identified as bad can be recovered as good runs, provided the deviations are understood.

For this section, the same as previously LHC10c and LHC10d datasamples were taken (see Appendix 2 for the list of runs). For illustration purposes, the pileup events were not filtered out in the datasample, so that we could demonstrate how they appear on the trend plots. For analysis, however, it is recommended to switch off pileup events at the very beginning.

5.5.1 Cluster averages

As a first iteration of the runs QA, let us take the datasample practically "as is", without filtering out bad channels. The mean cluster energy, the mean number of clusters per event, and the mean number of cells per cluster are shown in Fig. 5.19. Cluster averages are very sensitive to cell noise in a calorimeter. Even the presence of one noisy channel may displace the average value in a particular module, which is demonstrated, for instance, in the highly deviating block seen in all three histograms at the run indices 40–60. Clearly, it appeared because of problems in module 2 (blue line). Indeed, the lines for other modules show more regular behaviors.

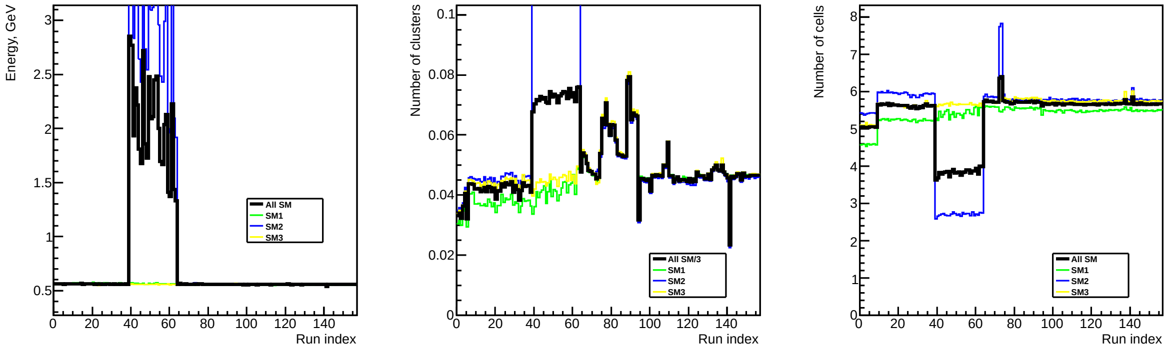

FIGURE 5.19 – Cluster averages corrected for acceptance : average cluster energy (left), average number of clusters per event (middle), average number of cells in cluster (right).

We can do acceptance correction for the cluster averages. To this end, we scale *relevant* cluster averages by the inverse number of participating cells in each module. This number is obtained directly from the datasample by counting the number of cells which have seen some signal.

The effect of the acceptance correction is shown in Fig. 5.20 for the number of reconstructed clusters. On the right histogram, after the correction, the green, blue and yellow lines become much closer to each other.

5.5.2 Influence of bad channels on cluster averages

The presence of bad channels spoils the trend plots. Let us now demonstrate how the elimination of bad channels improves the regularity of cluster averages.

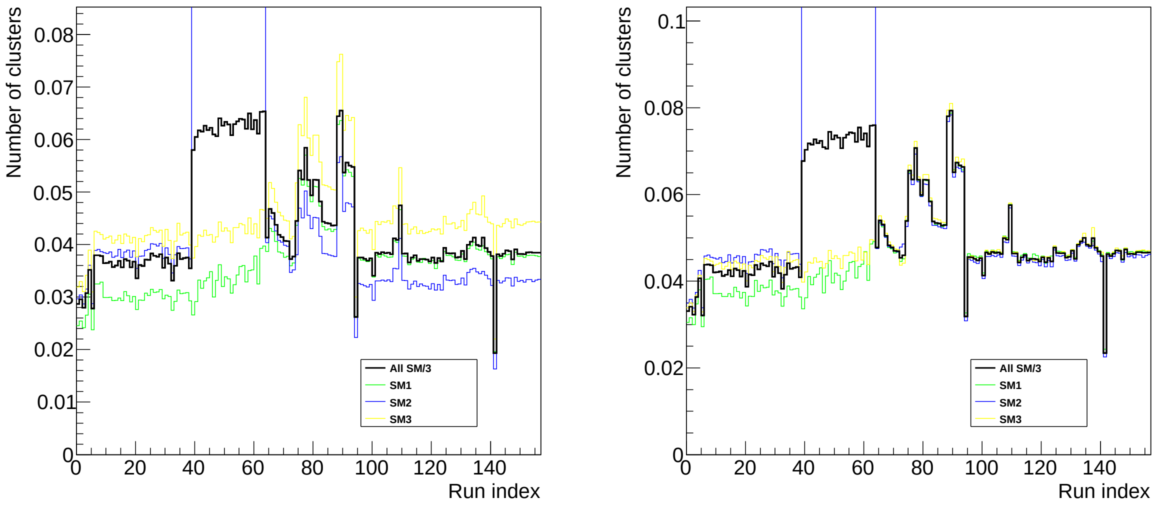

FIGURE 5.20 – Average number of clusters before (left) and after (right) acceptance correction.

To do so, we simply performed the automatic part of the cell QA analysis discussed in Section 5.4 and constructed an exhaustive bad cell map containing more suspicious cells than even necessary. Quantitatively, we suppressed bad channel candidates which appeared in more than 15% of runs. Such a rather strict criterion allows one to focus on the run quality, avoiding questions about cell quality. After that, we performed the run QA analysis again, now with the identified bad cell candidates switched off.

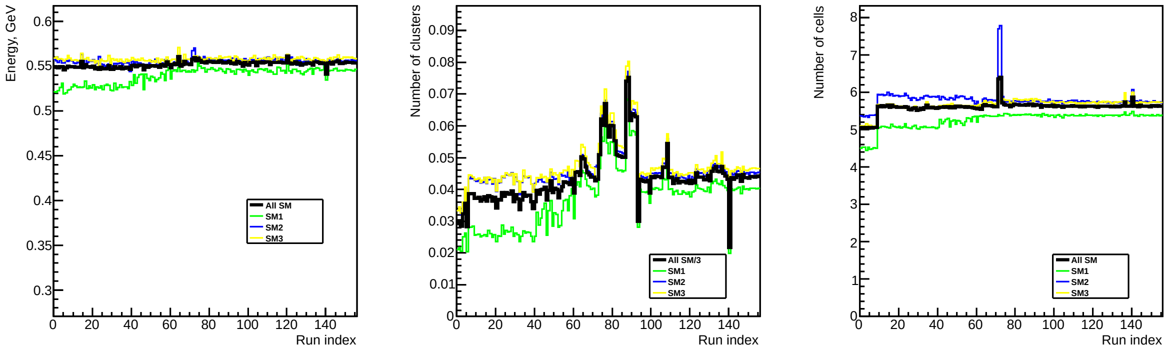

FIGURE 5.21 – Cluster averages after suppression of bad channels and correction for acceptance : average cluster energy (left), average number of clusters per event (middle), average number of cells in cluster (right).

The resulting plots with bad channels suppressed are shown in Fig. 5.21. In comparison with Fig. 5.19, the deviating block with run indices 40–60 has completely disappeared. Therefore, the runs 40–60 are recovered to be good since their deviations were caused by noisy channels.

As one can see, the structure of the left and the right plots became regular, while the structure of the middle plot is not. In contrast with the average cluster energy and the average number of cells in a cluster, the average number of clusters per event is more sensitive to external run conditions. For instance, the ugly block of runs around the run index 80 appeared due to a high pileup level in these runs (which leaded to higher number of clusters per event). Other runs, e.g. around the run indices 95 and 140, show abnormally low number of clusters and should also be disregarded.

5.5.3 π^0 averages

The reconstruction of $\pi^0 \to \gamma\gamma$ is a benchmark process for electromagnetic calorimeters as it has a large cross section and therefore is easily achievable within a limited statistics corresponding to one run. Another advantage of π^0 reconstruction in pp collisions is a clean signal with rather low signal-to-background ratio. Finally, the π^0 spectrum, unlike, for instance, inclusive cluster spectrum, is much less influenced by noise in a calorimeter. With all these advantages, the decay $\pi^0 \to \gamma\gamma$ is commonly used in QA analysis. In addition, it is very good for verifying the detector performance as well as as a gauge signal for calibration of the energy scale of calorimeters.

In principle, other gauge signals can be considered for calibration and QA purposes, like single electrons or decays $\eta \to \gamma\gamma$ or $Z^0 \to e^+e^-$. However, these processes are good for detectors with very large accumulated statistics. For the ALICE calorimeters, EMCAL and PHOS, those processes cannot be used for calibration and especially for run quality assurance because of a lack of statistics.

The π^0 meson is detected via its two-photon decay. In PHOS, the invariant mass spectrum is constructed between all cluster pairs satisfying minimum energy cut of 0.3 GeV. The invariant mass M of the pair of clusters with reconstructed 4-momenta p_1 and p_2 is given by equation

$$M^2 = (p_1 + p_2)^2 = (p_1^0 + p_2^0)^2 - (\vec{p}_1 + \vec{p}_2)^2. \tag{5.5.1}$$

The invariant mass spectrum is constructed as a function of transverse momentum $p_T = (\vec{p}_1 + \vec{p}_2)_\perp$ (where the transverse direction is taken with respect to the beam axis) and then fitted by the sum of the Crystal Ball [34] and a polynomial of the second order.

The Crystal Ball function is defined as

$$f(x; C, M, \sigma, \alpha, n) = C \begin{cases} \exp\left(-\frac{(x-M)^2}{2\sigma^2}\right), & \text{for } \frac{x-M}{\sigma} > -\alpha \\ A \cdot \left(B - \frac{x-M}{\sigma}\right)^{-n}, & \text{for } \frac{x-M}{\sigma} \leq -\alpha, \end{cases} \tag{5.5.2}$$

where

$$A = \left(\frac{n}{\alpha}\right)^n \cdot \exp\left(-\frac{\alpha^2}{2}\right), \qquad B = \frac{n}{\alpha} - \alpha, \qquad \alpha > 0. \tag{5.5.3}$$

Effectively, the Crystal Ball function is the Gaussian function with a power-law tail to the left from the peak value. The power-law tail was introduced in order to take into account the non-Gaussian shape of the π^0 peak. The power-law tail comes, for instance, from photon conversion into e^+e^- pair, when the electron (positron) gave a cluster which was misused as a cluster from a photon.

Let us remark that the parameters α and n of the Crystal Ball function are chosen to be fixed and do not vary during a fitting procedure.

The second order polynomial is written as

$$P(x; a_0, a_1, a_2) = a_0 + a_1 (x - 0.135) + a_2 (x - 0.135)^2 . \tag{5.5.4}$$

Fig. 5.22 shows an example of the two-cluster invariant mass spectrum. The π^0 meson appears as a clear peak around the expected mass 0.135 GeV/c^2. The polynomial function (blue line) as well as the fitting function itself (red line) are superimposed, illustrating the automatic fitting procedure performed in each run.

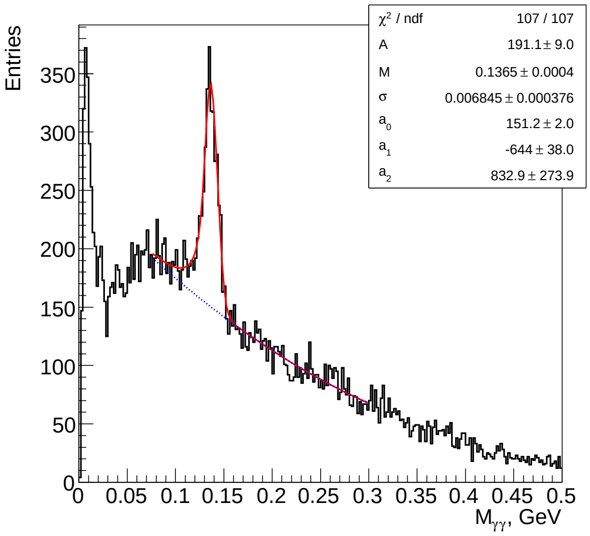

FIGURE 5.22 – Two-cluster invariant mass spectrum in a run. Each cluster energy satisfies $E \geq 0.3$ GeV. Red line : fit by the Crystal Ball with a polynomial of the second order ; blue line : the polynomial of the second order.

From the fit, the π^0 reconstruction parameters are determined. They are : the position M and the width σ of the π^0 peak as well as the average number of reconstructed π^0 per event obtained as the total area under the Crystal Ball function divided by total number of events in a run.

The position of the π^0 peak measures the overall absolute calibration of the calorimeter, while the peak width characterizes its energy resolution. Fig. 5.23 shows the reconstructed π^0 mass and width versus run index in chronological order with bad channels excluded. There is no a noticeable change in these plots before and after the bad channels exclusion, since the exclusion primarily affects the background under the π^0 peak. We observe that the second half of runs is more regular than the first half. These correspond to LHC10c (first half) and LHC10d (second half) datasamples. In LHC10d, a new channel calibration map was applied, so that, in total, the π^0 parameters become much more stable. From the plots, one can conclude that the LHC10c datasample cannot be used in an analysis together with the LHC10d datasample due to different calibration and thus different detector response.

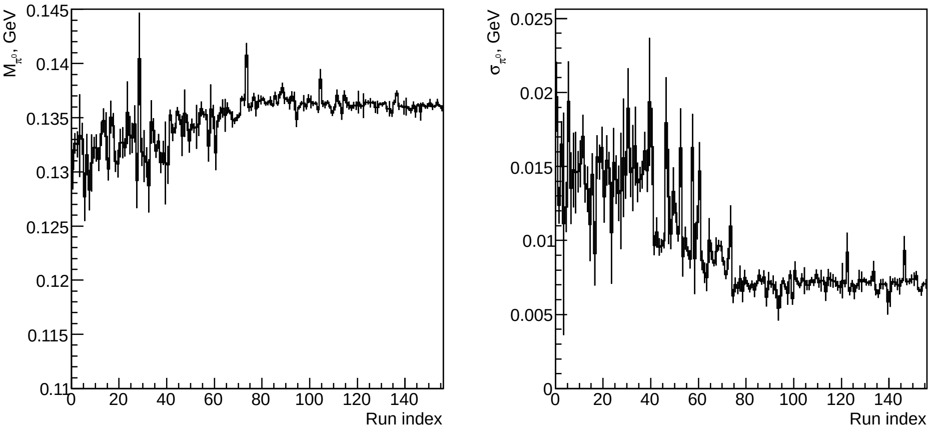

FIGURE 5.23 – π^0 mass and width versus run index ; bad channels excluded.

The average number of reconstructed π^0 per event is the last quantity required for the run QA. For the run quality validation, this quantity is the most important as it shows real physical signal which must be unaffected by changing with time experimental conditions.

The number of reconstructed π^0 for the datasample under the study is shown in Fig. 5.24. One can notice the very same deviations around run index 80, which we already observed in cluster averages, Fig. 5.21. As was already explained, these are the runs with high pileup.

In addition, starting from run index 95, the average level of the average number of π^0 per event is higher than the same level for runs with run index up to 60. This is due to the change in calibration in LHC10c and LHC10d periods.

5.5.4 Influence of global run conditions

In the previous sections, we have demonstrated that identification and suppression of bad channels improves stability of per-run observables which is reflected by a more uniform behavior of the trend plots. The residual irregularities, however, could still be observed, see for instance Fig. 5.24. The source of these irregularities may lie in hardware or software issues of the detector. Another source of problems is global run conditions of datataking which we discuss in this section.

In the context of the ALICE experiment, there are several global run conditions which affect datataking.

The most important global parameter is the beam conditions. The LHC delivers beams to the ALICE experiment which are characterized, among other parameters, by the confi-

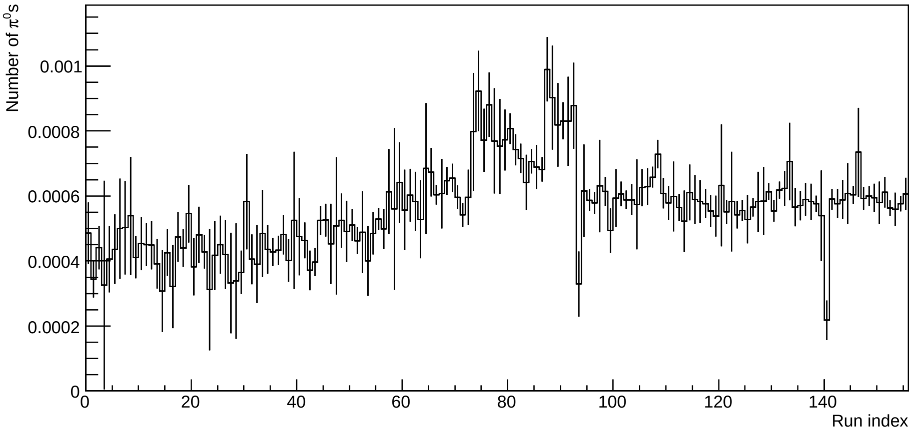

FIGURE 5.24 – Average number of π^0 per event ; bad channels excluded.

guration and time spacing of the colliding bunches called *filling scheme* [35]. Different bunch intensity and different time spacing between bunches result in different probability of pileup event (two events recorded as one due to their overlapping in the ALICE detectors).

The process of data taking of the experiment is determined by the *trigger configuration*. In the *pp* runs in 2010, the minimum bias trigger (which selects almost every *pp* collision) was used. The basic configuration of this trigger was defined by the coincidence of the signals in two beam counters BPTX, one fired chip in the Silicon Pixel Detector (SPD) and a signal in either one of the two scintillator hodoscopes V0A or V0C installed around the beam interaction point on opposite sides [36].

On Figs. 5.25, 5.26 and 5.27, the cluster averages and the π^0 averages are presented. They are obtained after removing the runs with high pileup as well as 5 other runs which deviate from general trend (see Appendix 3 for selected run list). Let us remark that, in comparison with the previous plots, the run indices has changed but still remain in chronological order.

Lastly, we see that only one irregularity remains – the step, which is now clearly seen on every plot. This step corresponds to change from LHC10c to LHC10d periods, run index 26. For instance, in the π^0 mass plot, we see a clear difference in the peak position between the two datasamples and observe that the correct position is achieved in the LHC10d period. Indeed, the step on the π^0 width plot shows that the width has changed from 15 to 8 MeV, which signifies a much better calibration. We also see the step on the average number of π^0 per event plot which was fitted by constant functions for different periods of datataking.

We have arrived at the conclusion of the run QA studies. For calibration reasons, the LHC10c period is unsuitable for physics analysis. Figs. 5.28, 5.29 and 5.30 show the final trend plots of the selected “good” runs (see Appendix 4).

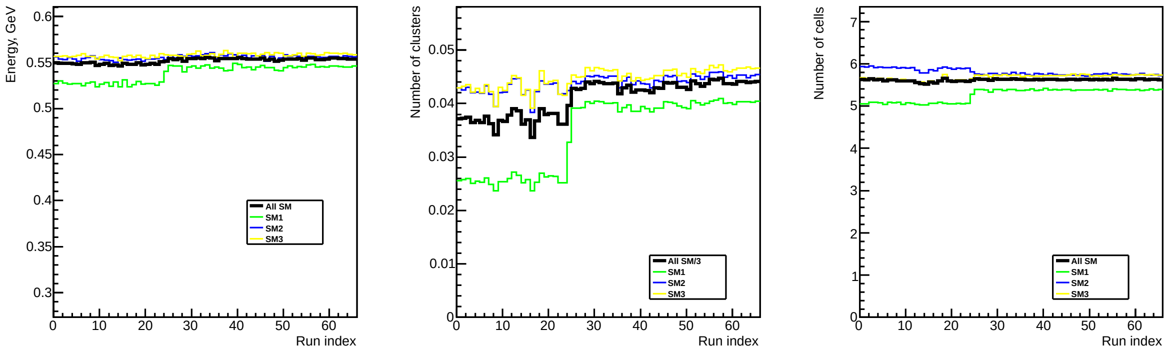

FIGURE 5.25 – Cluster averages corrected for acceptance ; bad channels excluded, no pileup runs, no bad runs.

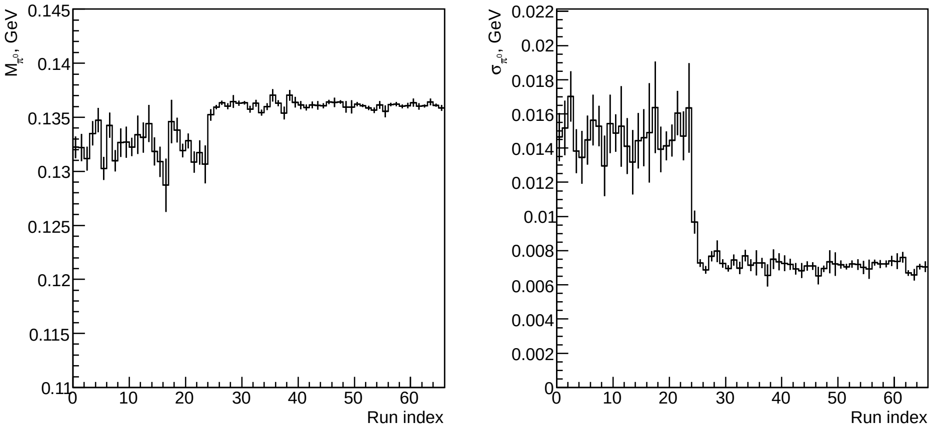

FIGURE 5.26 – π^0 mass and width ; bad channels excluded, no pileup runs, no bad runs.

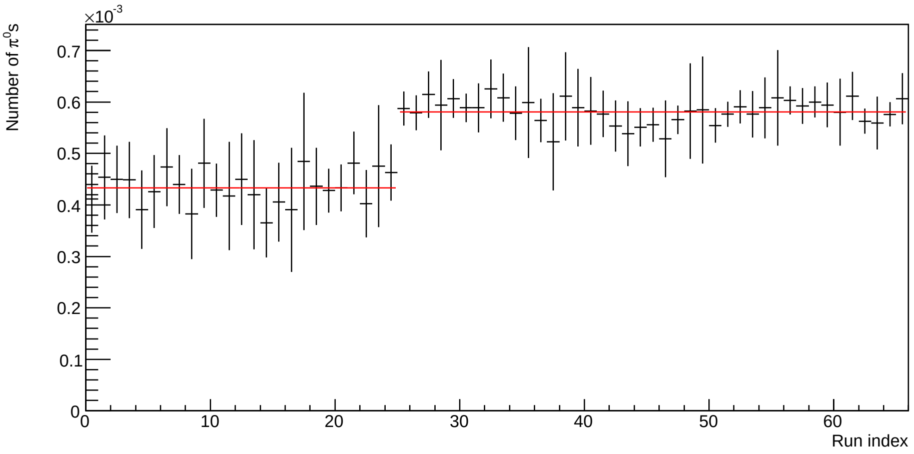

FIGURE 5.27 – Average number of π^0 per event ; bad channels excluded, no pileup runs, no bad runs. Red lines correspond to fits by a constant.

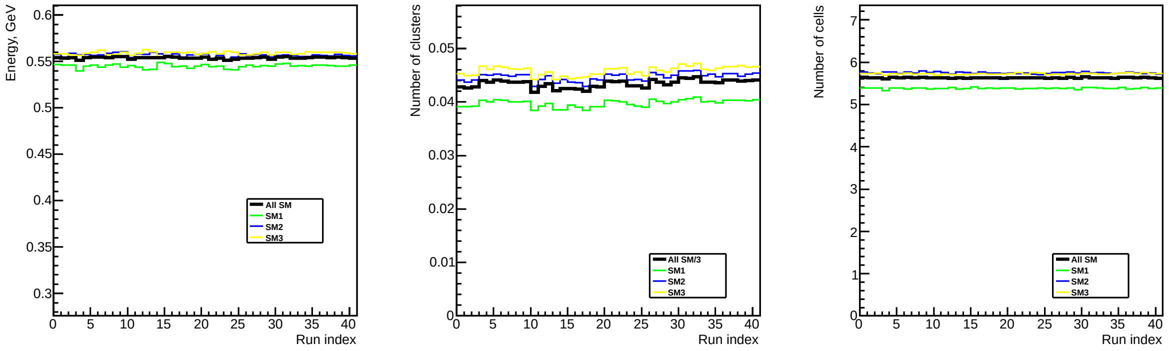

FIGURE 5.28 – Cluster averages corrected for acceptance ; good runs.

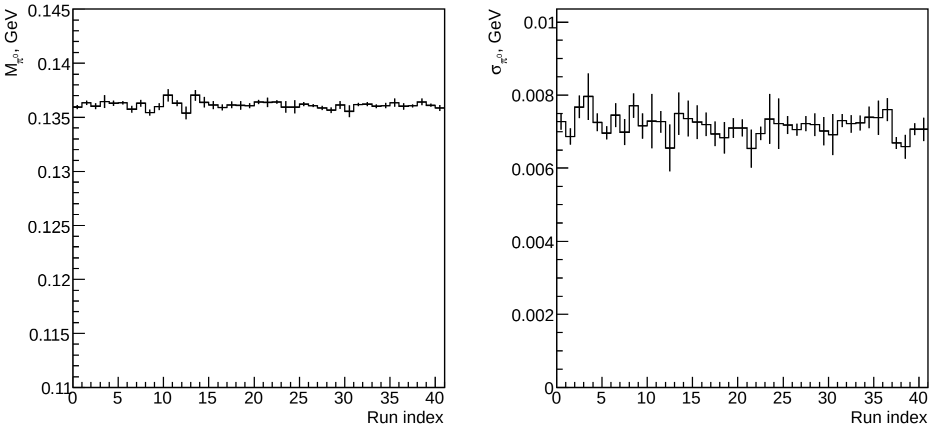

FIGURE 5.29 – π^0 mass and width ; good runs.

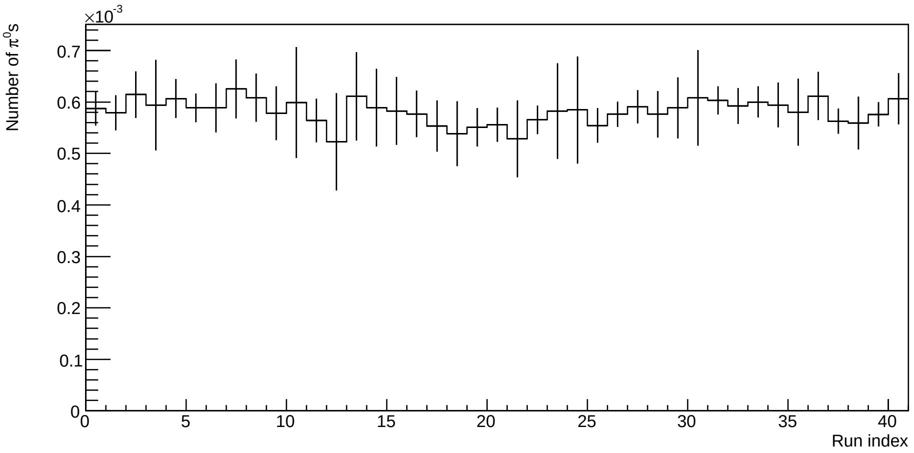

FIGURE 5.30 – Average number of π^0 per event ; good runs.

5.6 Concluding remarks

In this chapter, we have demonstrated importance of data quality assurance for a physics analysis and have shown in a few examples how bad channels can affect physics observables in the calorimeters. Several characteristic parameters were found to be adequate for identification of bad channels, which allow one to assess the quality of the channels *in each run*. We described bad channels quantitatively, i.e. with mathematical formulation, and developed per-run criteria to discriminate good and bad channels. The *full-dataset criteria* can also be applied for bad channel search.

Quality of channels and its evolution in time within the dataset is directly reflected in the quality of runs. From one hand, thorough identification and suppression of bad channels leads to uniform behavior of run observables over the whole dataset. From the other hand, any deviations in trends of run observables are indications of either unsuppressed bad channels in particular runs, hardware of software errors or changes in global run conditions.

Developed software for bad channel and bad run identification and visualization provides an easy access to the quality of data. This software package has a modular architecture which allows one to apply it to both ALICE calorimeters, EMCAL and PHOS, as well as it can also be easily ported to any experiment involving electromagnetic calorimeters. The software was implemented within the standard analysis framework of the ALICE experiment and it is a part of the official quality assurance procedures, running centrally on reconstructed data.

The approach to the data quality assessment of this study was extensively used in the analysis of EMCAL and PHOS data collected in proton-proton and lead-lead runs in 2010 and 2011. Thanks to this analysis, stability and good quality of results obtained in a data analysis was assured.

This study is published in ALICE internal analysis note [8].

5.7 Appendix 1 : how to use the QA code

This section explains how to use the QA source code which, in particular, was used to obtain the results of the present study. The source code can be found in aliroot at

`$ALICE_ROOT/PWGGA/PHOSTasks/CaloCellQA.`

It consists of two classes (AliAnalysisTaskCaloCellsQA and AliCaloCellsQA) and two macros (AddTaskCaloCellsQA.C and getCellsRunsQA.C).

The QA analysis is performed in two steps. At the first step, one applies the code on reconstructed data (i.e. on a set of runs). At this stage, the code is executed e.g. on GRID or CAF and simply fills necessary histograms. On the second step, the produced histograms are analyzed with the macro getCellsRunsQA.C. This macro builds the QA histograms, many of which were already discussed in this chapter. Additionally, the macro prints to a console sets of found bad cell candidates and other important information.

The QA source code is well documented and the reader is invited to look inside it. Here we sketch only main aspects of the two steps.

5.7.1 First step : analysis of reconstructed data

The QA analysis, as any other user-friendly analysis, can be attached to an analysis chain in a standard way :

```
gSystem->Load("libPWGGAPHOSTasks.so");
gROOT->LoadMacro("$ALICE_ROOT/PWGGA/PHOSTasks/CaloCellQA/macros/AddTaskCaloCellsQA.C");
```

and then for PHOS

```
AliAnalysisTaskCaloCellsQA *taskQA = AddTaskCaloCellsQA(4, 1);
```

where “4” is the highest module number plus one, “1” indicates that the class will be used for PHOS, while for EMCAL

```
AliAnalysisTaskCaloCellsQA *taskQA = AddTaskCaloCellsQA(10);
```

where “10” indicates the number of supermodules in EMCAL (highest supermodule number plus one). Additionally, one can customize some options :

```
// consider only minimum bias events
taskQA->SelectCollisionCandidates(AliVEvent::kMB);
// do not skip pileup events
taskQA->SetAvoidPileup(kFALSE);
// increase statistics (used for PHOS)
taskQA->GetCaloCellsQA()->SetClusterEnergyCuts(0.3, 0.1);
// more histograms, not usually necessary
taskQA->GetCaloCellsQA()->ActivateFullAnalysis();
// reject clusters containing any of these cells
Int_t badcells[] = {1, 2, 3};
taskQA->SetBadCells(badcells, 3);
```

Let us also remark that the full documentation to the macro AddTaskCaloCellsQA.C can be found inside the macro code itself.

Let us explain "the internals" of the first QA step which is implemented as two classes, AliCaloCellsQA, AliAnalysisTaskCaloCellsQA and the macro AddTaskCaloCellsQA.C.

The actual job is done by the AliCaloCellsQA class which takes as an input a run number, clusters, cells and primary vertex in each event (see AliCaloCellsQA : :Fill() method) and fills histograms as an output (see AliCaloCellsQA.h for the list of histograms). Most histograms are filled separately for each run, whereby one has, in fact, arrays of per-run histograms of same types. These are four histograms for local maximum cell criteria (and, possibly, the same four histograms, but for non-local maximum cells) as well as histograms for π^0 invariant mass spectra, distribution of the number of cells in cluster and cell amplitudes distribution. In addition, integral histograms over all runs are filled which are per-cell spectra and cell times.

AliAnalysisTaskCaloCellsQA class is a wrapper class which inherits AliAnalysisTaskSE class and steers the AliCaloCellsQA class.

The separate implementation of the AliAnalysisTaskCaloCellsQA class (which knows how to work with ALICE data format) and the AliCaloCellsQA class (which does the job) makes the code more readable and, which is more important, allows more flexibility in the usage of the QA. There are two advantages in flexibility :

1. The AliAnalysisTaskCaloCellsQA class makes certain filtering in clusters in an event, but a user may be interested in some other filtering algorithm (e.g. which removes clusters at (super)module edges or removes one-cell clusters). This can be accomplished easily by taking the AliAnalysisTaskCellsQA class source code and changing it according to particular needs. In this approach, the class AliCaloCellsQA stays without any changes.
2. In some cases it is more convenient to use the AliCaloCellsQA class directly in a user analysis. For example, one can use it several times in one and the same analysis : the first AliCaloCellsQA class instance is executed for original clusters, while the second AliCaloCellsQA class instance runs after a reclusterization algorithm.

Finally, let us remark that the purpose of the AddTaskCaloCellsQA.C macro is to give a convenient way to initialize the QA instance in an analysis.

5.7.2 Second step : analysis of produced histograms

After running the first step of the QA analysis, one has a root-file with all the necessary histograms inside.[1] Now, the actual results of the QA analysis can be produced with the macro getCellsRunsQA.C. This macro is very large, has many options and forms the most interesting part of the QA. Fortunately, most options inside the macro are already chosen in an optimal way. In many cases, as fast start it is enough to change the file name on the line :

---

[1] On the first QA step, each subjob, e.g. on GRID, will produce a separate root-file. The root-files should be merged to a single root-file. See, however, comments inside the AddTaskCaloCellsQA.C macro.

```
infile = "CellsQA.root";
```

at the beginning of the macro and execute

```
root -l getCellsRunsQA.C
```

The macro draws many histograms (which were already discussed in this chapter and which were not) and prints out to a console relevant information.

To proceed further, it is necessary to read the text at beginning of the macro, including the text inside the function getCellsRunsQA(). Each option in the macro is well documented, so that there is no need to repeat the instructions here. Let us finally remark that advanced options, usually requiring a user effort, are commented by default.

5.8 Appendix 2 : run list for the LHC10cd dataset.

Run index	Run number	Events
0	119037	1254284
1	119041	1770200
2	119047	1851163
3	119055	105531
4	119057	456321
5	119061	732769
6	119084	296622
7	119085	407531
8	119086	206522
9	119156	1747319
10	119159	1097483
11	119161	2050734
12	119163	1000603
13	119838	1058198
14	119841	247203
15	119842	1350607
16	119844	301770
17	119845	1352285
18	119846	2269943
19	119849	867376
20	119853	757632
21	119856	1070658
22	119862	2855309
23	119904	109473
24	119907	738862
25	119909	876687
26	119913	504103
27	119923	353723
28	119924	135831
29	119926	1640865
30	119935	454042
31	119941	1259548
32	119948	591769
33	119952	467957
34	119959	1048018
35	119961	3839565
36	119965	3862840
37	119969	2745428
38	119971	1721894
39	120064	186058
40	120066	785320
41	120067	1864727
42	120069	1487462
43	120072	2900648
44	120073	2469365
45	120076	1976873
46	120079	755111
47	120242	164255
48	120244	1129899
49	120503	1013659
50	120504	2524590
51	120505	3263087
52	120611	671158
53	120613	371559
54	120614	1264298
55	120616	4588847
56	120617	1277624
57	120671	369099
58	120672	835186
59	120741	113067
60	120742	354695
61	120744	549121
62	120750	817656
63	120758	634752
64	120818	315953
65	120820	131673
66	120821	1129599
67	120822	5860955
68	120823	582708
69	120824	3232618
70	120825	2795461
71	120829	3893182
72	122374	3652490
73	122375	843833
74	124187	238392
75	124355	533287
76	124358	881529
77	124360	788139
78	124362	307193
79	124367	358669
80	124371	868533
81	124374	3335550
82	124378	2833637
83	124380	2907604
84	124381	745522
85	124383	4031052
86	124385	1186086
87	124388	3820283
88	124600	1487959
89	124604	391147
90	124605	437198
91	124606	2328211
92	124607	391509
93	124608	497608
94	124751	183877
95	125083	245041
96	125085	4210761
97	125097	3642179
98	125100	204996
99	125101	2232695
100	125131	592456
101	125133	569317
102	125134	2901143
103	125139	5662167
104	125140	1867621
105	125156	196873
106	125186	1378669
107	125295	1420112
108	125296	4997009
109	125628	3229636
110	125630	2165413

TABLE 5.1 – Correspondence between run indices and run numbers for the periods LHC10c and LHC10d (part 1).

Run index	Run number	Events
111	125632	1474674
112	125633	419971
113	125842	2434538
114	125843	428620
115	125847	621164
116	125848	636756
117	125849	1114612
118	125850	2292143
119	125851	1626202
120	125855	944494
121	126004	127009
122	126007	2948725
123	126008	197232
124	126073	2392583
125	126078	4115364
126	126081	782767
127	126082	5346090
128	126086	640455
129	126087	358760
130	126088	6949457
131	126090	3876926
132	126158	7128676
133	126160	1870861
134	126162	329371
135	126167	1345896
136	126168	2175662
137	126177	1957747
138	126283	1469208
139	126284	7336322
140	126285	251344
141	126350	510869
142	126351	4040944
143	126352	2172693
144	126359	1236927
145	126403	473862
146	126404	5856200
147	126405	310521
148	126406	4054791
149	126407	4967486
150	126408	2483803
151	126409	1141258
152	126422	1962779
153	126424	7124302
154	126425	1468897
155	126432	8057274
156	126437	1862437

Events in total : 275653001

TABLE 5.2 – Correspondence between run indices and run numbers for the periods LHC10c and LHC10d (part 2).

5.9 Appendix 3 : run list for the LHC10cd dataset, pileup and bad runs excluded

Run index	Run number	Events
0	119156	1747319
1	119159	1097483
2	119161	2050734
3	119163	1000603
4	119838	1058198
5	119842	1350607
6	119845	1352285
7	119846	2269943
8	119853	757632
9	119856	1070658
10	119862	2855309
11	119907	738862
12	119909	876687
13	119913	504103
14	119926	1640865
15	119941	1259548
16	119948	591769
17	119952	467957
18	119959	1048018
19	119961	3839565
20	119965	3862840
21	119969	2745428
22	119971	1721894
23	120066	785320
24	120067	1864727
25	125085	4210761
26	125097	3642179
27	125101	2232695
28	125133	569317
29	125134	2901143
30	125139	5662167
31	125140	1867621
32	125186	1378669
33	125630	2165413
34	125632	1474674
35	125633	419971
36	125842	2434538
37	125843	428620
38	125847	621164
39	125848	636756
40	125849	1114612
41	125850	2292143
42	125851	1626202
43	125855	944494
44	126007	2948725
45	126078	4115364
46	126081	782767
47	126082	5346090
48	126086	640455
49	126087	358760
50	126090	3876926
51	126284	7336322
52	126351	4040944
53	126352	2172693
54	126359	1236927
55	126403	473862
56	126404	5856200
57	126406	4054791
58	126407	4967486
59	126408	2483803
60	126409	1141258
61	126422	1962779
62	126424	7124302
63	126425	1468897
64	126432	8057274
65	126437	1862437

Events in total : 147490555

TABLE 5.3 – Correspondence between run indices and run numbers for the periods LHC10c and LHC10d, pileup and bad runs excluded.

5.10 Appendix 4 : run list for the LHC10d dataset, good runs

Run index	Run number	Events
0	125085	4210761
1	125097	3642179
2	125101	2232695
3	125133	569317
4	125134	2901143
5	125139	5662167
6	125140	1867621
7	125186	1378669
8	125630	2165413
9	125632	1474674
10	125633	419971
11	125842	2434538
12	125843	428620
13	125847	621164
14	125848	636756
15	125849	1114612
16	125850	2292143
17	125851	1626202
18	125855	944494
19	126007	2948725
20	126078	4115364
21	126081	782767
22	126082	5346090
23	126086	640455
24	126087	358760
25	126090	3876926
26	126284	7336322
27	126351	4040944
28	126352	2172693
29	126359	1236927
30	126403	473862
31	126404	5856200
32	126406	4054791
33	126407	4967486
34	126408	2483803
35	126409	1141258
36	126422	1962779
37	126424	7124302
38	126425	1468897
39	126432	8057274
40	126437	1862437

Events in total : 108932201

TABLE 5.4 – Correspondence between run indices and run numbers for the period LHC10d, good runs which are appropriate for physics analysis.

Chapitre 6

Neutral meson measurements with the EMCAL detector

In this chapter, the inclusive spectra of π^0 and η mesons as well as their η/π^0 ratio at $\sqrt{s} = 7$ TeV are obtained through their two-photon decays with the EMCAL detector of the ALICE experiment. Correspondingly, the methodology of the measurement is described in detail, including tuning of Monte Carlo simulations to describe reality and the calculation of systematic uncertainties.
Every plot of this chapter is obtained during this thesis, unless noted otherwise in a corresponding caption.

Hadron production measurements in proton-proton collisions at the LHC energies open up a new kinematic regime for testing and validating the predictive power of quantum chromodynamics and to impose new constrains on models and their parameters. Indeed, a quantum description of hard processes is provided by the perturbative QCD (pQCD). However, in *pp* collisions, a significant fraction of hadrons is produced via soft parton interactions, and thus they cannot be well described within the framework of pQCD. Many advanced event generators have to appeal to phenomenological models, along with the pQCD predictions, in order to describe hadron production adequately. Evidently, such phenomenological models are tuned to available experimental data and have been validated using the data delivered by lower-energy colliders like RHIC, SPS and Tevatron. Extrapolation of these models to the LHC energies cannot be valid *a priori* because the increase in collision energy is very large. Even the validity of the pQCD predictions cannot be guaranteed at the LHC, since parton distribution functions and fragmentation functions are not well determined at such high energies.

Precise measurements of hadron production in *pp* collisions are crucial for a deeper understanding of QCD phenomena such as parton dynamics and hadronization. They also provide a valuable baseline for particle and jet production in heavy ion collisions, essential to the needs of the ALICE heavy ion program.

Photon detection is an essential tool in experimental studies in high energy *pp* and heavy ion physics. Decay photons, i.e. those which are produced from a particle decay, are used to measure spectra, flow, nuclear modification factors and other observables of neutral mesons decaying to photons. Direct photons, originating from a core of a collision, provide possibility to explore initial state of a collision and evolution of a fireball through the thermal emission. Separation of isolated and inclusive direct photons provides the possibility to evaluate contributions of different processes of direct photon emission. Finally, by constructing the photon–hadron and photon–jet correlations, one can study nuclear modification of parton fragmentation functions in a medium. All these topics are well developed and widely presented nowadays.

The ALICE experiment performs measurements of neutral meson production in *pp* collisions at the collision energies $\sqrt{s}$ = 0.9, 2.76, 7 and 8 TeV at mid-rapidity in a wide range of transverse momenta p_T. Conventionally, the π^0, η, $\omega(782)$, K_S^0 and other neutral mesons are detected via their photon decays in the electromagnetic calorimeters, PHOS and EMCAL. The inclusive spectra of π^0 and η production in *pp* collisions at $\sqrt{s} = 900$ GeV and 7 TeV were also measured by ALICE via identifying the conversion photons $\gamma \to e^+e^-$ produced in the material of the ALICE inner tracking system [9]. The combined results of the PHOS detector and the ALICE conversion group are published in Ref. [10].

6.1 Photon detection with the EMCAL detector

In the present chapter, we focus on the measurements of production spectra of π^0 and η mesons performed with the ALICE electromagnetic calorimeter EMCAL in *pp* collisions at $\sqrt{s} = 7$ TeV. On the way to this goal, we concentrate on the calorimeter effects related to detection of photons.[1]

The EMCAL detector is a sampling calorimeter. In contrast with PHOS channels which are just monolithic crystals with attached photodiodes, EMCAL channels have more sophisticated multi-layer structure. Due to this, in a Monte Carlo simulation, physics of a shower cascade inside a channel can be modeled rather approximately since it is not possible to account for all effects which present in the real detector. For instance, effects of transport of light through wave shifting fibers are not programmed. As a result, raw (i.e. uncorrected) energy response of the calorimeter in data and in simulation never match.

The described shortcoming can be compensated in an analysis.[2] To this end, note that in a reconstructed data only the information about clusters and cells is accessible. Respectively, the following three corrections can be applied to clusters with their energies and cells with their amplitudes :

- cluster energy non-linearity correction (both for simulation and data) ;
- cell decalibration (for simulation) ;
- cell amplitude smearing (for simulation).

While the goal of cluster energy non-linearity correction is to calibrate the *absolute energy scale in the calorimeter*, cell decalibration and cell amplitude smearing reduce the detector *energy resolution* in simulations in order to math with that in reality. These points are discussed below in Sections 6.3 and 6.5.

The methodology of extraction of raw π^0 and η yields is described in the next section. After corrections to data are applied (Chapter 5, Section 6.3) and Monte Carlo simulations are tuned and reproduce the data (Sections 6.3, 6.5 and 6.6), one can proceed to the measurement of π^0 and η production spectra. To this end, it is necessary to determine π^0 and η^0 reconstruction efficiencies (Section 6.7). Finally, systematic uncertainties must be estimated (Section 6.8.1).

Let us emphasize that *all plots of this chapter are obtained during the present studies, unless noted otherwise in the corresponding captions.*

In this chapter, several types of Monte Carlo simulations were used. They are :

- single photon simulation, where photons have only certain discrete energies ;
- single π^0 and η simulations, where mesons have realistic momentum distributions ;
- single π^0 and η simulations, where mesons have flat (uniform) momentum distributions ;
- single π^0 simulation, where pions have only certain discrete transverse momenta ;
- single π^0 simulation without the ALICE magnetic field, where pions have realistic momentum distribution.

---

[1] Although the shower shape and the energy response from an electron (positron) is very similar to that of a photon, the methodology of detection of electrons (positrons) has several key differences. Indeed, trajectories of electrons (positrons) are bent by the magnetic field in the ALICE machine. Thus, they hit the calorimeter under some angle, giving a cluster of a different (more elongated) shape, which is especially important at small energies. In addition, electron (positron) detection requires a coordinated work between the EMCAL detector and other detectors (e.g. the TPC or the TRD) as the corresponding cluster in the EMCAL should be matched with a track reconstructed from the signals left in other detectors.

[2] Ideally, the corrections described in Sections 6.3–6.5 should be applied centrally during a data reconstruction. This is especially efficient in the case of cell decalibration and/or cell amplitude smearing since this requires a recalculation of cluster's center and other cluster parameters.

6.2 π^0 and η meson reconstruction and raw yield extraction

Neutral pions and η mesons are reconstructed as excess yields, visible as peaks at their respective rest masses 0.135 GeV/c^2 and 0.548 GeV/c^2 respectively, above the background in the two-photon invariant mass spectrum. Invariant mass spectra demonstrating the π^0 and η meson peaks in some selected p_T slices are shown in Fig. 6.1. Photons are detected in the EMCAL detector as clusters which are characterized by particular energies and positions in the ALICE global coordinate system.

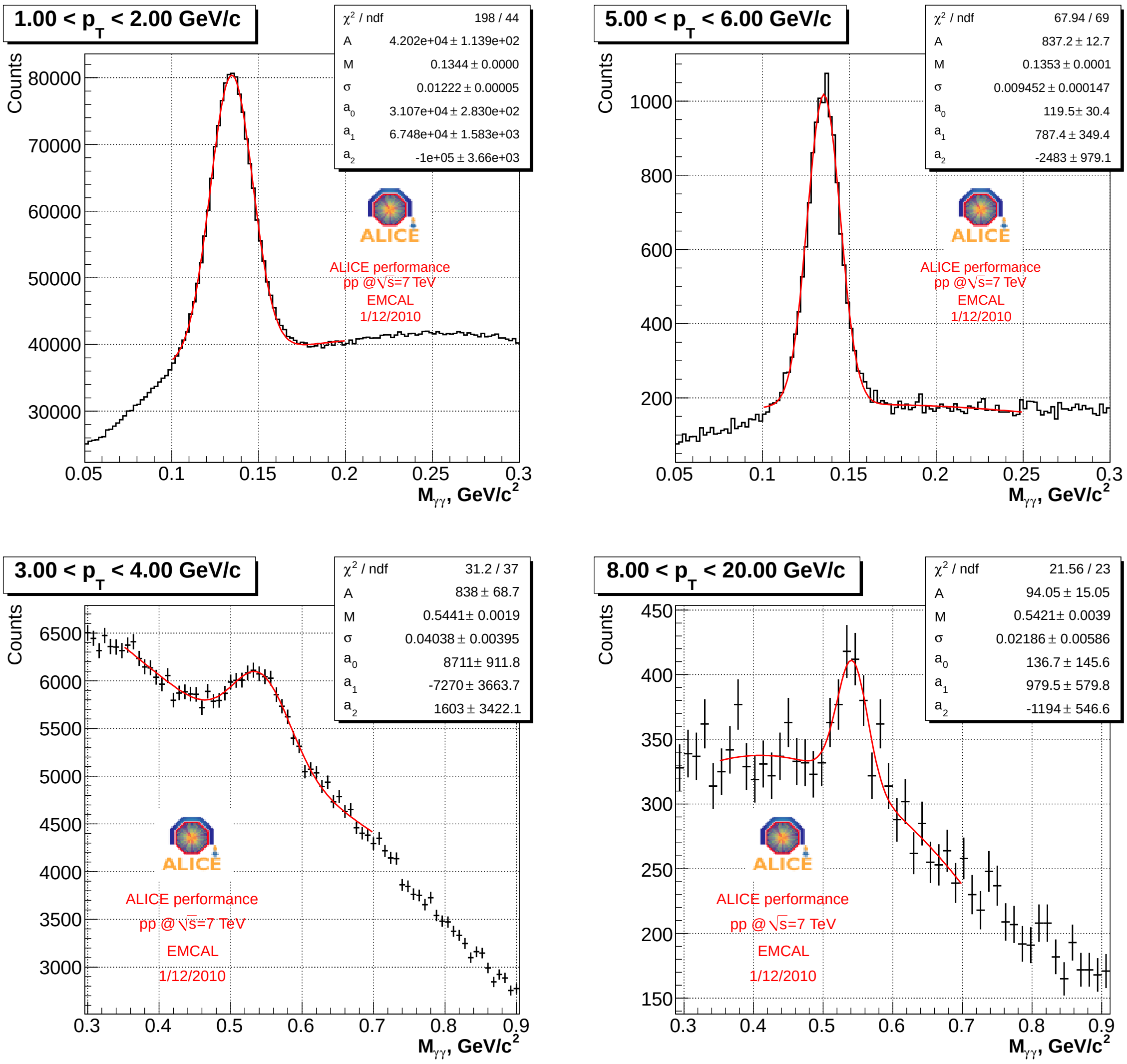

FIGURE 6.1 – Two-cluster invariant mass p_T slices demonstrating the π^0 meson (top) and the η meson (bottom) peaks. Red lines show fits with a Gaussian function and a polynomial of second order.

We start from a description of run and cluster selection conditions which were used throughout this chapter. After that, we proceed to the two-cluster invariant mass analysis. In principle, the procedure of extraction of masses, widths and raw yields from the π^0 and η peaks is identical to the one discussed in Section 5.5.3. In this section, however, the data was already corrected with an energy non-linearity correction, which is addressed later in Section 6.3.

6.2.1 Run Selection

The proton-proton datasample at $\sqrt{s} = 7$ TeV used in this chapter was collected by ALICE in 2010 with the minimum bias trigger [36]. An offline event selection based on time and amplitude signals of the V0 and the SPD detectors was applied to reject noise and beam-induced background. Pileup events were identified by imposing a criterion based on multiple primary vertices reconstructed with the SPD detector and were removed from further analysis. Moreover, the quality assurance framework of Chapter 5 was applied to identify EMCAL bad channels and select a set of good runs applicable for the measurement.

The *pp* datasample at $\sqrt{s} = 7$ TeV collected by the EMCAL in 2010 corresponds to 450 million events of the integrated luminosity $L_{\text{int}} = 6.7$ nb^{-1}. By applying the above cuts, only about 190 million events left, however. At this statistics, the EMCAL is capable to measure the π^0 and η mesons in the momentum region up to 20 GeV/c.

The list of run numbers taken for the analysis is given in Table 6.9. In total, 100 runs were selected. Figure 6.2 shows the data quality of all the runs. As one can see, cluster and π^0 averages are uniform, the detector calibration is also very stable. Some runs show larger deviations, but a close inspection shows that this is related to runs with small statistics.

6.2.2 Cluster selection

The EMCAL bad channel map which was taken during these studies contains 45 bad channels, which were either miscalibrated or switched off at the level of reconstruction, or they were noisy and switched off in the current analysis. The map is presented in Fig. 6.3. It is uniform and have no issues with missing EMCAL parts (e.g. missing RCUs).

To maximize the pion and η reconstruction efficiency, relatively loose cuts on clusters were used. The following clusters were removed during the analysis :

- clusters containing a bad channel ;
- clusters with a local maximum cell being an immediate neighbor to a bad channel or a supermodule edge.

The cluster energy was required to be above the 0.5 GeV threshold, $E_{\text{clus}} \geq 0.5$ GeV. (However, during the non-linearity studies of Section 6.3.3, this cut was set to 0.3 GeV to avoid the π^0 detection threshold effects.)

Neither particle identification criteria nor energy asymmetry cuts of cluster pairs were applied in the analysis in order to minimize the impact of cuts on measured spectra.

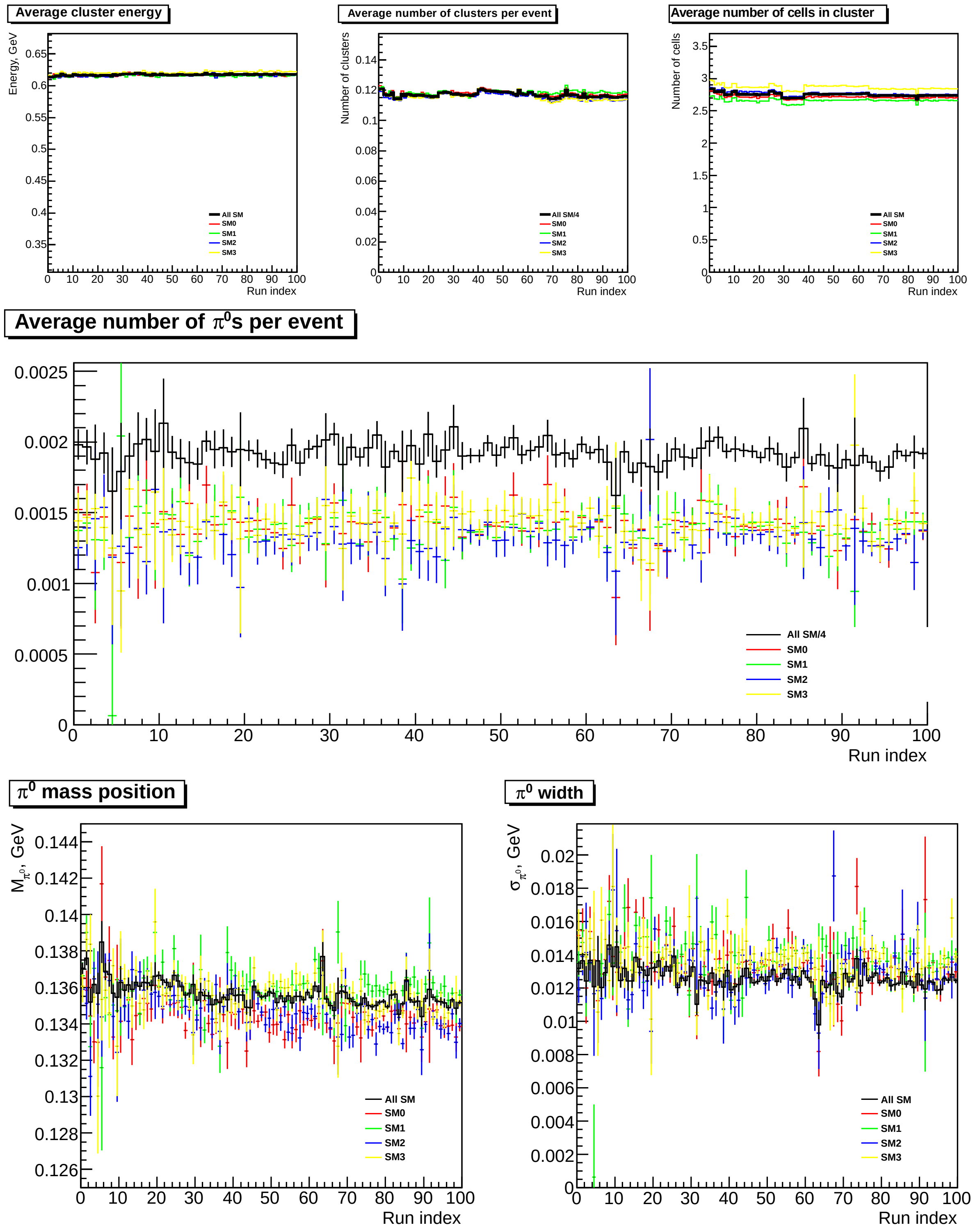

FIGURE 6.2 – Cluster averages (top), average number of π^0 per event (middle) and π^0 mass and width (bottom) of the runs selected for these studies.

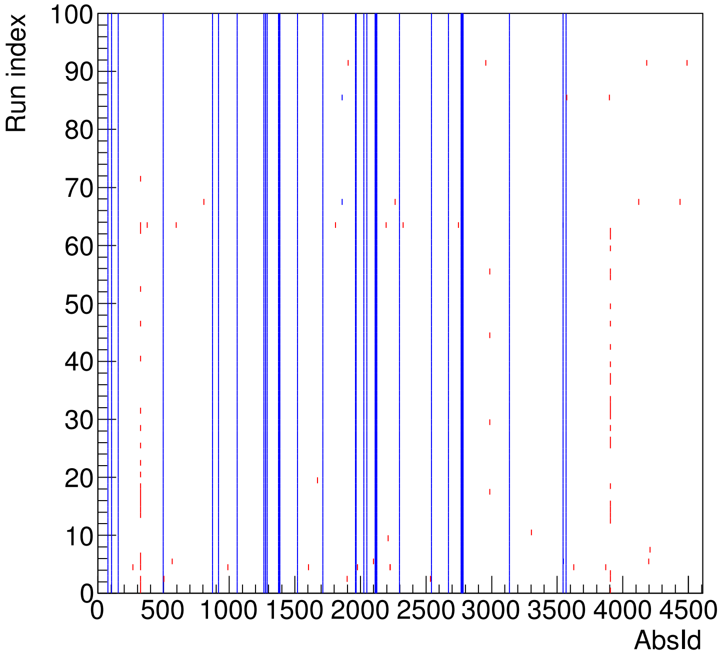

FIGURE 6.3 – Dead/noisy channel map for EMCAL.

6.2.3 Raw yield extraction and mixed events technique

The reconstruction of the π^0 and η mesons through their two-photon decays is performed by the two-cluster invariant mass analysis. The two-cluster invariant mass is given by

$$M_{12}^2 = (E_1 + E_2)^2 - (\vec{p}_1 + \vec{p}_2)^2, \tag{6.2.1}$$

where $E_{1,2}$ are the cluster energies, while $\vec{p}_{1,2}$ are the reconstructed three-momenta of the two photons. The latters are calculated from the knowledge of cluster energies and positions as well as the knowledge of the primary vertex position, since the π^0 and η mesons to not have time to displace from the primary collision point before decaying.

The invariant mass spectra are constructed from all cluster pairs in the EMCAL, where each cluster have passed the cluster selection criteria. The corresponding invariant mass distribution $N(M_{12}, p_T)$ is then filled with fine bins of 1–2 MeV width in mass and 100 MeV width in transverse momentum and then grouped according to available statistics. After that, the invariant mass p_T slices are fitted with a Gaussian function and a polynomial of the second or the third order. Alternatively for the π^0 meson, the Crystal Ball function (5.5.2) with fixed parameters α and n and a polynomial of the second or the third order can be used, as it is better reproduces the "tail" to the left from the pion peak, see Fig. 6.4.

Finally, the background (i.e. the polynomial of the fit) is subtracted and the resultant histogram ("the signal") is refitted in order to estimate the mass m and width σ more precisely. Then, the π^0 or η raw yield is obtained by summing all the bins of the

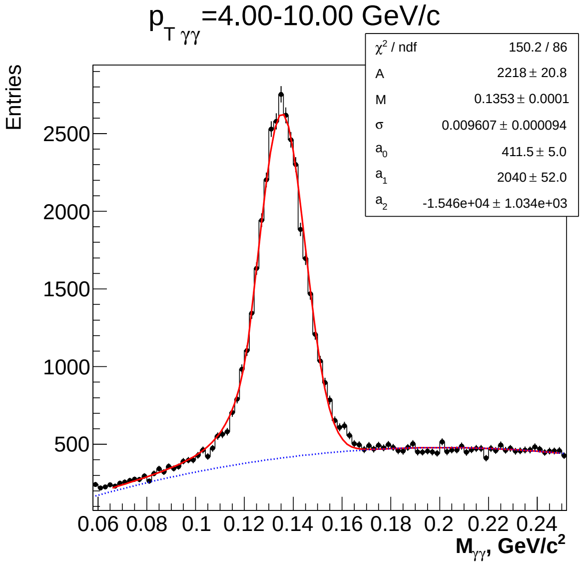

Figure 6.4 – Invariant mass spectrum of cluster pairs with transverse momentum 4–10 GeV/c with the π^0 meson peak fitted with the Crystal Ball function and a polynomial of the second order (red line). The polynomial of the second order is shown with the blue dashed line.

resultant histogram under the region $m \pm 3\sigma$. While performing the above steps, the statistical/fitting errors are accurately propagated.

It turns out, however, that *the above procedure can be significantly improved*. To this end, the powerful *event mixing technique* is used. The idea is the following. The considerable (if not major) part of the background under the π^0 and η peaks are formed by uncorrelated cluster pairs. If so, for such a background, in principle, there is no importance that the two clusters were taken in one and the same event. On the other hand, one knows for sure that it is not possible to form the π^0 or η meson peak if one takes clusters from different events. As a result, the background may be considerably "weakened" if one forms a bin-by-bin "real/mixed" ratio, there "real" stands for a conventional invariant mass slice, whereas "mixed" corresponds to a similar slice of the two-cluster invariant mass, but filled for all clusters from different events.

The last point is illustrated for the η meson on Fig. 6.5. Here, the left "real" plot was fitted with a Gaussian function and a polynomial of the second order. Obviously, for such a combinatorial background, the polynomial of the second order is not enough. At the same time, the right plot demonstrates the ratio of the left plot to the mixed events invariant mass. Clearly, the η peak is enhanced while the background is much more regular and is now well approximated by the polynomial.

Let us note also that for the ALICE experiment which focuses on heavy ion physics, the mixed events technique is indispensable for many detector subsystems. Indeed, in heavy ion collisions, the particle multiplicities are so high that a searched signal may be very weak in comparison with a huge combinatorial background of clusters or tracks.

As one can see, the background on Fig. 6.5 (right) is not constant. This is due to a remained correlated background which may, for example, be produced from the photon

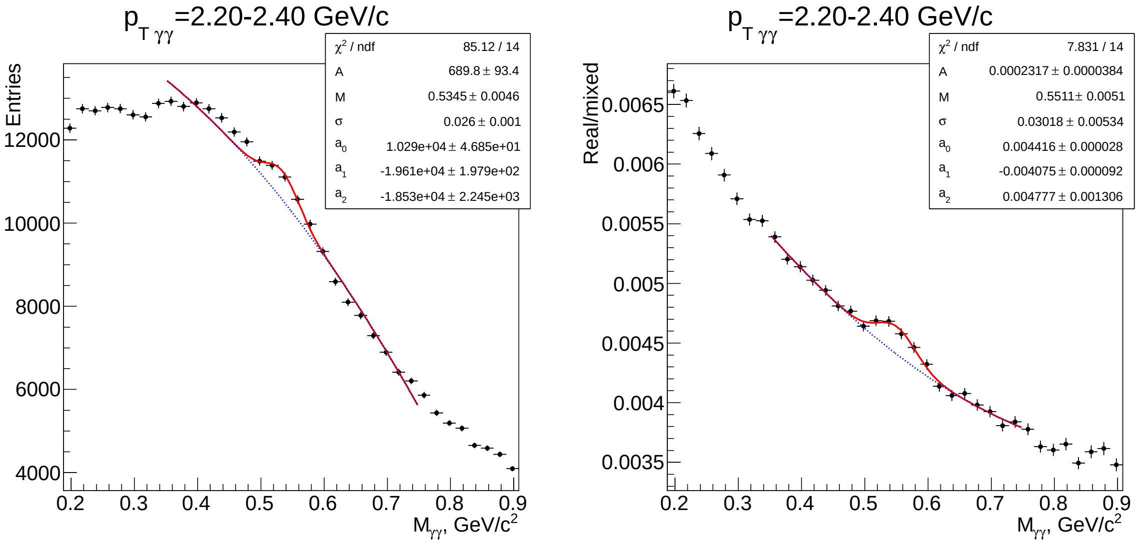

FIGURE 6.5 – The demonstration of the event mixing technique : invariant mass plot (left) versus real/mixed ratio (right) which is obtained by division of the left plot by the mixed events combinatorial background. In both cases, the fitting functions are a Gaussian function and a polynomial of the second order.

conversion into the e^+e^- pair. Another comment is that for the ratio real/mixed to be of good quality, it it important to fill the mixed events histogram from as many events as possible. To this end, we formed mixed pairs by taking all clusters from the current event and all the clusters from previous 100 events.

Lastly, to obtain the π^0 or η raw yield, the resulting mixed events histogram is multiplied by the fit of the real/mixed plot and then subtracted from the real distribution. The resultant difference is a pure signal which is, as earlier, refitted with a Gaussian or a Crystal Ball function, so that the raw yield is calculated by bin counting within three standard deviations around the mean value of the fit. Again, the statistical/fitting errors are accurately propagated.

Results

The π^0 and η invariant mass slices together with their fits are shown in Appendices 6.10 and 6.11. The reconstructed π^0 and η masses and widths as functions of the transverse momentum p_T are shown later in this chapter in Figs. 6.20 and 6.22, where comparisons with Monte Carlo simulations are also given. The η mass does not show any particular p_T behavior and is close to its PDG value, which confirms the quality of the non-linearity correction calculated from symmetric π^0 decays (see Section 6.3.3).

Also, on Fig. 6.6 we demonstrate signal-to-background ratios for the π^0 and η mesons, which are obtained as the extracted raw yields (the sum of bins in the "signal" histogram in three standard deviations from the peak) over the extracted backgrounds (the sum of bins in the "real" – "signal" histogram in three standard deviations from the peak). Note that the η signal-to-background ratio is very small, so that the mixed events technique

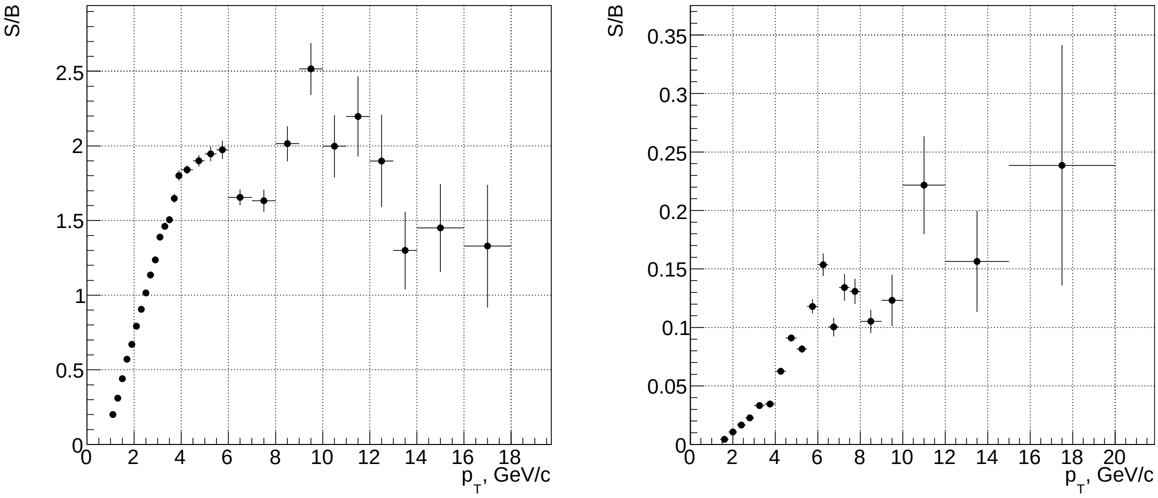

FIGURE 6.6 – Signal to background ratios for the π^0 meson (left) and for the η meson (right).

turned out to be very useful here indeed.

Finally, the extracted raw π^0 and η yields are shown in Fig. 6.7. They will be used later for the production spectra calculation.

6.2.4 Cluster merging in the EMCAL detector

In subsequent sections, we will see an irregular behavior of the π^0 mass and width for the transverse momenta from approximately 5–6 GeV/c. This effect is inherent to the EMCAL detector only and turns out to be a consequence of a big physical size of the EMCAL channel : at high π^0 energies, the angle between its two decay photons becomes so small that this results in only one cluster detected in the calorimeter instead of two. This effect is referred to as *cluster merging.* As a consequence, the pion is not detected. Thus, a rise of transverse momentum leads to a progressive worsening of the EMCAL π^0 reconstruction efficiency until it vanishes when even highly asymmetric π^0 decays (i.e. one high-energy photon and one low-energy photon with large angle between them) cannot be reconstructed since the energy of the low-energy cluster becomes smaller than the minimum cluster energy threshold.

Due to the cluster merging, the accessible p_T region for the π^0 meson is about 7–9 GeV/c.

The cluster merging is dealt by a cluster separation algorithm, the idea of which is to find the two (or more) cluster local maxima and then separate them in some way. This process is usually referred to as *cluster unfolding.* In the present studies, this algorithm is used for the π^0 production spectrum measurement in order to prolongate the accessible p_T region to well above 9 GeV/c. With the cluster unfolding, we are able to reconstruct the π^0 mesons with transverse momenta up to 20 GeV/c.

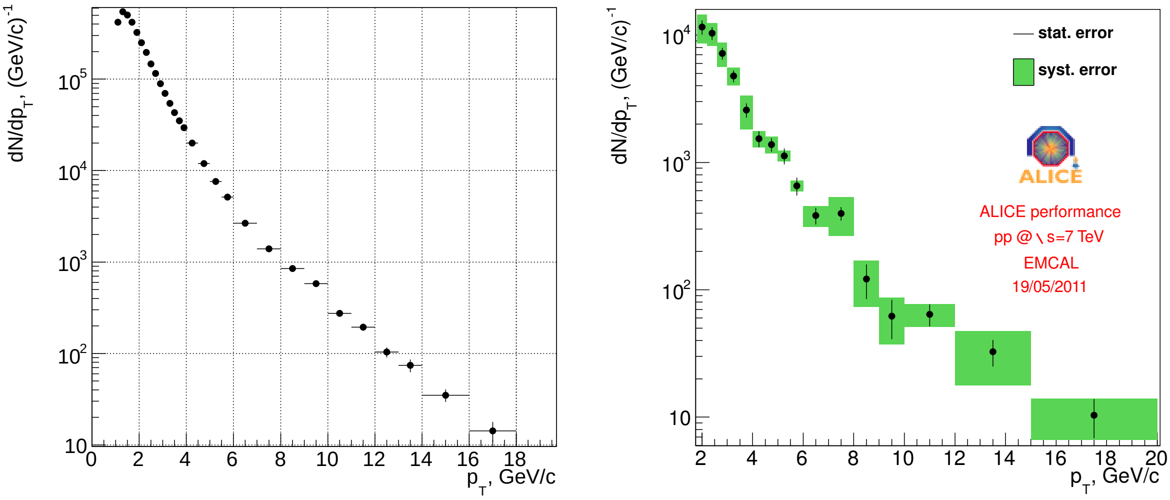

FIGURE 6.7 – Number of reconstructed π^0 (left) and η (right) mesons as a function of transverse momentum. The right plot is shown with systematic uncertainties.

Unfortunately, the implementation of this algorithm is not completed. In particular, its parameters were optimized for Monte Carlo simulations and do not describe the data with the same quality. In addition, the π^0 meson mass above 5–6 GeV/c rises with momentum. These issues could in principle be compensated by an application of an energy non-linearity correction to unfolded clusters (see the next section). In its current state, however, one has to deal with the non-linear energy behavior above 5–6 GeV/c as well as with a different behavior of the algorithm in data and simulation.

Lastly, let us remark that cluster merging is not a problem for the η meson, since this effect begins at very high η transverse momenta. Indeed, the η meson reconstruction efficiency (Fig. 6.24, right) is still rising at 30 GeV/c, but where is no statistics at such momenta in any case.

6.3 Cluster energy non-linearity correction

It is well known that raw energy response of a photon (or electron, or any other particle) hitting the calorimeter is underestimated. This is true both in real data as well as in Monte Carlo simulations. Indeed, not all released photon energy (through an electromagnetic shower cascade) is detected by the electronics. In addition, the photon may already lost some energy on its way from a birth point by interacting with the material inside the ALICE machine. The latter is especially important for the EMCAL detector since the material budget in front of it is about 0.8–1.1 of photon radiation wavelengths. In particular, the probability of photon conversion into e^+e^- pair (which is the dominant process for photons with energies above 1 MeV) is at least $1 - e^{-0.8} = 55\%$, and there is a chance that the leptons yield two clusters instead of one or even one of the leptons is not detected at all, see Fig. 6.8.

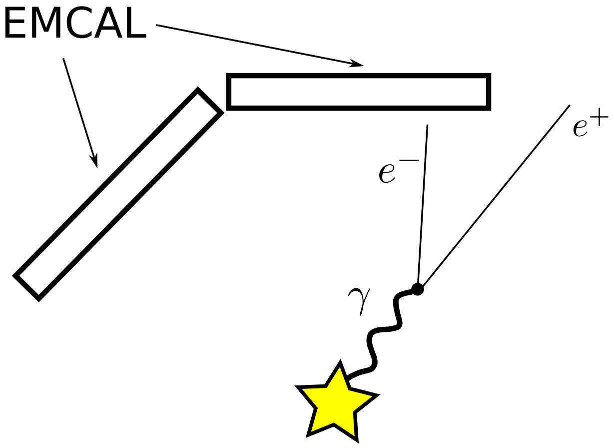

FIGURE 6.8 – Photon energy leakage due to its conversion to e^+e^- pair.

The energy leakage in the detector response can be compensated by a multiplication of raw (uncorrected) cluster energy by an energy-dependent factor,

$$E_{\text{clus}}^{\text{true}} = \frac{E_{\text{clus}}^{\text{rec}}}{f(E_{\text{clus}}^{\text{rec}})}, \tag{6.3.1}$$

where $E_{\text{clus}}^{\text{rec}}$ is the raw reconstructed cluster energy, whereas $E_{\text{clus}}^{\text{true}}$ is the corrected (true) energy of incoming particle. The function $f(E)$ is *cluster energy non-linearity correction.* Thereby, it corrects for the energy scale in the response of the calorimeter. This function generally differs for photons and electrons, at least due to the material budget and the magnetic field effects. Moreover, it differs for the case when the magnetic field is absent. Finally, for EMCAL, it differs between data and Monte Carlo simulations, which follows from the discussion of Section 6.1.

In what follows, the non-linearity correction is considered *for photons* under normal conditions of the ALICE experiment operation (e.g. with the 0.5T magnetic field).

6.3.1 Non-linearity for simulations : single photon simulation

The non-linearity correction corrects measured photon energy. Consequently, for simulations, it can be determined from a *single photon simulation*, where only photons of definitive discrete energies are generated in the primary collision vertex (“Test Beam” in a simulation). In any other aspect, such a simulation is taken under exactly the same conditions as are used in other simulations with particles of interest (real ALICE geometry, same as in data reconstruction parameters, same as in data cluster filtering conditions, *etc.*).

In a more detail, the method proposed is following. One generates a bunch of events with a single proton originating from the primary vertex. The generated proton may have only a discrete set of energies. It is propagated then in the ALICE medium to the EMCAL detector. At the same time, for the non-linearity calculation, we select only events with exactly one cluster detected in the EMCAL. This reduces bias due to photon conversion to e^+e^- pair. Knowing the shape of the energy response of the EMCAL and the corresponding true energy of the photon, one can determine the non-linearity correction.

In what follows, we used three single photon simulations with 2 million events in each. Photons were generated within the EMCAL acceptance, but in a somewhat wider rapidity range in order to avoid edge effects : $|\eta| < 0.75$ and $80° < \varphi < 120°$. The generated photon energies were :

1. from 200 MeV to 2.2 GeV with a step 50 MeV ;
2. from 200 MeV to 5.2 GeV with a step 500 MeV ;
3. from 200 MeV to 29.2 GeV with a step 1 GeV.

In total, 71 points of fixed photon energy were generated. Let us also remark that in the low-energy region more events were generated. This allows one to keep a good precision of results at low energy.

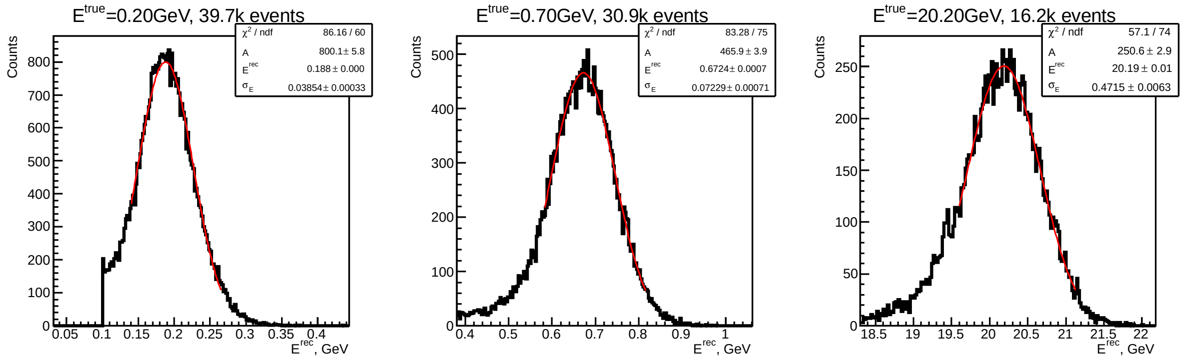

FIGURE 6.9 – Typical energy response of the EMCAL (cluster spectrum) in the single photon simulation for three fixed photon energies. Red curves represent Gaussian fits.

Fig. 6.9 shows examples of typical energy response of the EMCAL (which is just the cluster spectrum) for three fixed photon energies. As one can see, the peaks are not symmetric with tails to the left from the peaks which in agreement with the statement about the energy leakage. The fitting of the peaks with Gaussian functions in asymmetric energy regions allows one to extract the detector non-linearity :

$$f(E^{\text{rec}}_{\text{clus}}) = \frac{E^{\text{rec}}_{\text{clus}}}{E^{\text{true}}_{\text{clus}}} \qquad \text{[single photon simulation]}, \tag{6.3.2}$$

as it follows from the definition (6.3.1). In this equation, one should take the mean value of the Gaussian fit as $E^{\text{rec}}_{\text{clus}}$, while $E^{\text{true}}_{\text{clus}}$ is the initial energy of the generated photon. The result is shown on Fig. 6.10, where the red line represents the sought non-linear correction

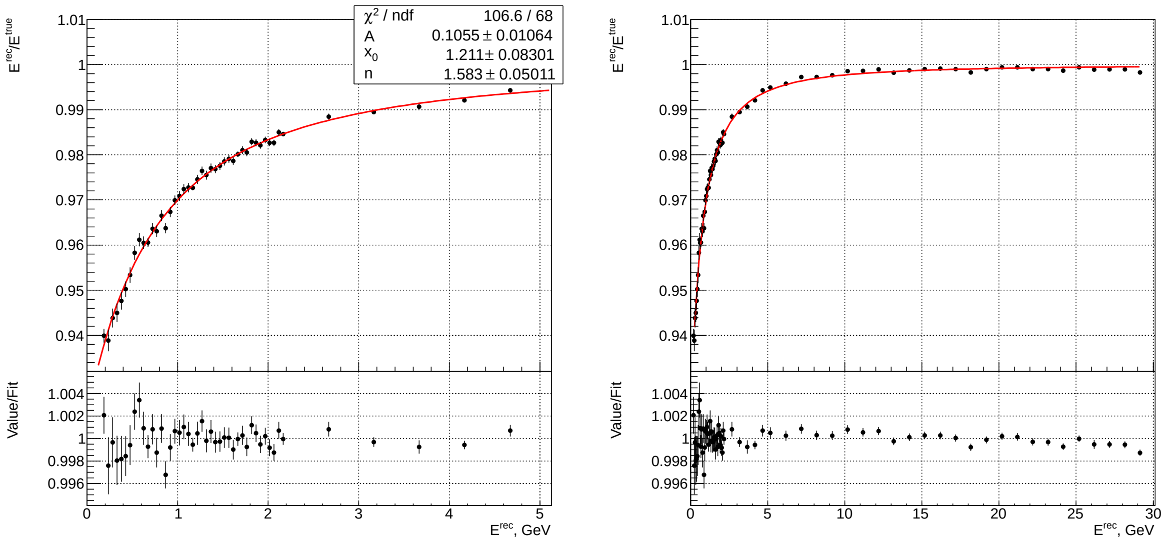

FIGURE 6.10 – Non-linear correction as a function of the reconstructed energy drawn up to 5 GeV (left) and up to 30 GeV (right).

function. It turns out that the points are very well fitted [3] with a three-parameter function

$$f(x) = 1 - \frac{A}{(x+x_0)^n}, \tag{6.3.3}$$

with positive parameters A, x_0 and n. (The parameter x_0 must be positive because otherwise this function will have a non-physical pole at a positive value of $x = |x_0|$.)

To be on a safe side, let us also quote the fit qualities of cluster spectra for each fixed photon energy, see Fig. 6.11 (left). In addition, the single photon simulation allows one to estimate the expected relative energy resolution for the EMCAL in simulation, see Fig. 6.11 (right).

Finally, let us point out that the non-linearity disappears (tends to unity) at high energies.

6.3.2 Non-linearity for real data : Test Beam experiment

Ideally, the non-linear behavior of the energy response of an electromagnetic calorimeter should be measured in a dedicated *Test Beam experiment*, where the detector module fragment is exposed to beams of photons or electrons of known energies. Repeating the steps described in the previous section, one can thus determine the detector non-linearity correction.

The case of the EMCAL detector is special. As was already pointed out, the material budget in front of the EMCAL is very high, 0.8–1.1 of radiation wavelengths, which

---

[3] Note that the tiny fluctuations below 1 GeV on the bottom plots of Fig. 6.10 are purely statistical.

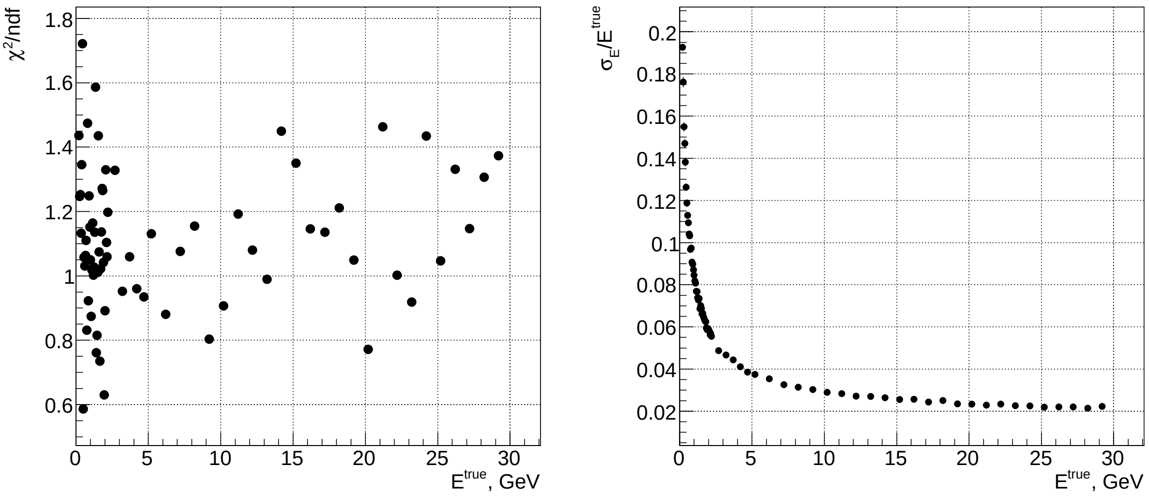

FIGURE 6.11 – Fit quality of cluster spectra versus true photon energies (left) and relative energy resolution of the EMCAL in simulation.

results in a very high probability (at least 55%) for a photon to be converted into e^+e^- pair, giving a huge influence on the energy non-linearity response of the EMCAL. For a high-energy photons or for photons which convert close to the detector surface, this is not that important since both leptons would hit the surface close to each other and would produce only a single cluster. For a low-energy photons or photons which converted far from the EMCAL surface, however, the angle between the electron and the positron (the trajectories of those are also bent by the magnetic field) is large enough to result in two clusters detected in the calorimeter, if the leptons would hit the calorimeter at all. The situation is even worse for the data collected starting from 2011, when all ten EMCAL supermodules were installed. Indeed, only some of the ten supermodules have the TRD detector in front, the material budget of which is very high. Consequently, the non-uniform material budget in front of the EMCAL results in the dependence of the energy non-linearity with supermodule number.

In the EMCAL Test Beam experiment [37], electrons traveled to the EMCAL supermodule fragment through the air, without a magnetic field. Taking into account the above reasonings, one can conclude that particle energy loss under these conditions is quite different from what is found inside the ALICE machine, and one has to search for other ways to account for the non-linear energy response of the EMCAL.

Lastly, in principle, it is possible to use the Test Beam non-linearity in conjunction with a determined Monte Carlo non-linearity from a single photon or electron simulation in the air without the ALICE medium. Indeed, whatever the recipe of determination of the non-linearity is, the goal is to have a particle (e.g. π^0 or η) mass behavior from real data to be reproduced by simulations. This complicates things, however, since it gives incorrect absolute energy scale. The latter, moreover, would be supermodule-dependent (not uniform among cells positions), thus at least reducing the total detector energy resolution.

6.3.3 Non-linearity for real data : symmetric π^0 decays

In the present section, we propose a method which can be used for measuring the non-linearity correction for the EMCAL using the collected data itself.

To this end, consider the process $\pi^0 \to \gamma\gamma$, where the π^0 meson decays into two photons which yield two clusters with energies $E_1^{\rm rec}$ and $E_2^{\rm rec}$ in the calorimeter. In addition, the reconstructed angle $\theta_{12}^{\rm rec}$ between the photons is restored from the coordinates of the two clusters and the primary vertex. When, the invariant mass of the two clusters is given by

$$M_{12}^2 = 2E_1^{\rm rec}E_2^{\rm rec}\left(1-\cos\theta_{12}^{\rm rec}\right). \tag{6.3.4}$$

Now, let us consider only *symmetric* π^0 *decays*, where the two clusters have same energies, $E_1^{\rm rec} = E_2^{\rm rec} = E^{\rm rec}$ (which corresponds to equal energies of the two photons and to a half of the π^0 energy), and make a distribution of the two-cluster invariant mass M_{12} as a function of $E^{\rm rec}$. A clear π^0 meson peak would be visible, the position $M_{\pi^0}^{\rm rec}$ of which can be extracted from a fitting procedure. When, in average, as it follows from Eqs. (6.3.1) and 6.3.4,

$$M_{\pi^0}^{\rm rec} = E^{\rm rec}\sqrt{2\left(1-\cos\theta_{12}^{\rm rec}\right)} = f(E^{\rm rec})M_{\pi^0}^{\rm true} \times \frac{\sqrt{2\left(1-\cos\theta_{12}^{\rm rec}\right)}}{\sqrt{2\left(1-\cos\theta_{12}^{\rm true}\right)}}, \tag{6.3.5}$$

where $M_{\pi^0}^{\rm true} = 0.135$ GeV is the known π^0 meson mass, $\theta_{12}^{\rm true}$ is a true angle between the two photons.

In contrast with energy reconstruction, the angle reconstruction does not have a “non-linearity”, i.e. there is no a systematical effect of its under- or overestimation. This already follows from the fact that, while the angle for symmetric π^0 decays is fixed by the kinematics at a particular energy $E^{\rm rec}$, the original π^0 meson direction is distributed uniformly in all directions. This leads to a uniform (but correlated between each other) distribution of the positions of the two clusters in the calorimeter and thus, in average, gives no bias in the angle measurement. In principle, this statement requires a separate research with a single π^0 simulation, which is not given here. See the next section, though.

As a result of the above, one concludes that, in average, $\theta_{12}^{\rm rec} = \theta_{12}^{\rm true}$, yielding

$$f(E^{\rm rec}) = \frac{M_{\pi^0}^{\rm rec}}{M_{\pi^0}^{\rm true}} \qquad \text{[symmetric } \pi^0 \text{ decays]}. \tag{6.3.6}$$

In practice, it is not possible to consider clusters of exactly equal energies. To overcome this problem, one introduces the *energy asymmetry* between the two clusters,

$$A = \frac{E_1^{\rm rec} - E_2^{\rm rec}}{E_1^{\rm rec} + E_2^{\rm rec}}, \tag{6.3.7}$$

and performs the above procedure for clusters with energy asymmetry $A < A_0$, where $A_0 \ll 1$ being a fixed value, while taking the half π^0 energy $E^{\rm rec}$ to be

$$E^{\rm rec} = \frac{1}{2}\left(E_1^{\rm rec} + E_1^{\rm rec}\right). \tag{6.3.8}$$

In what follows, the cluster energy cut is $E_{\rm clus} \geq 0.5$, while the asymmetry cut is $A < 0.1$. Note also that the procedure above must be performed on a good calorimeter data.

Fig. 6.12 shows examples of two-cluster invariant mass slices in three π^0 energy regions. The peaks were fitted with Gaussian function and a polynomial of the 3rd order (red lines). Blue lines show the polynomial behaviors. The final result for the extracted non-linearity in real data is presented on Fig. 6.13 (left), while the fit qualities of the invariant mass slices are shown on Fig. 6.13 (right). As one can see, the non-linearity for real data (blue line) is considerably stronger than that for a simulation (red line). We took the fitting function in the form (6.3.3), as it was suggested by the single photon simulations. Clearly, this function describes the data very well. Still, two comments are relevant here.

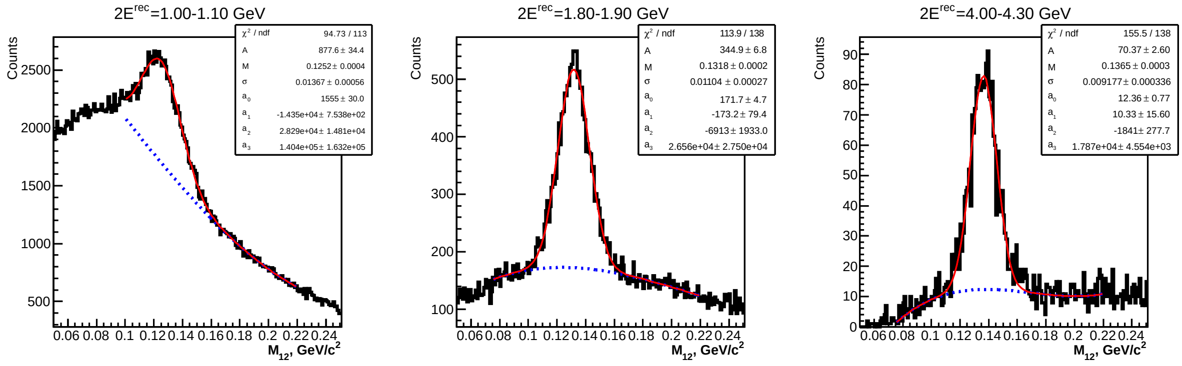

FIGURE 6.12 – Examples of two-cluster invariant mass slices in three energy regions. Red lines correspond to signal+background fits. Blue lines show the backgrounds.

First, there are two points around 0.5 GeV which are lower that the fit by 0.5%. This can be explained by the fact that, at very low energies, it is difficult to extract the π^0 peak reliably since it merges with the background in favor of smaller invariant mass values, see Fig. 6.12 (left). This effect can be verified more accurately, provided more data would be present so that one can consider energies below 0.5 GeV and can distinguish the π^0 peak from the combinatorial background to the left of it.

Second, the two points above 2.5 GeV (i.e. for the π^0 energy above 5 GeV) are higher

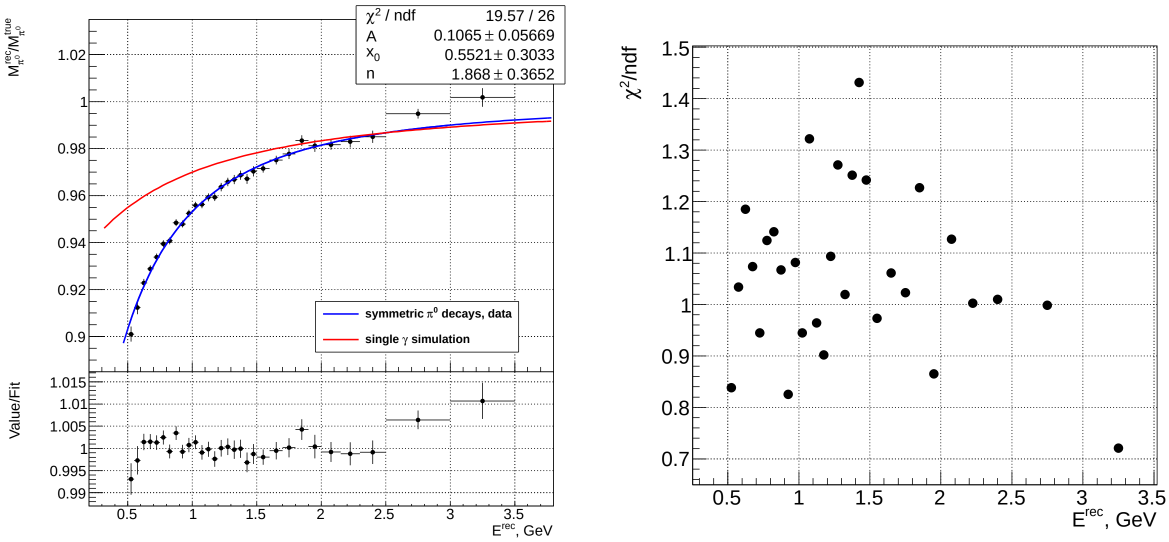

FIGURE 6.13 – Non-linear correction obtained from real data through symmetric π^0 decays (left) and fit quality of the energy slices (right). Blue line represents a fit with function (6.3.3). Red line is the non-linearity obtained from the single photon simulation, Section 6.3.1.

than the non-linearity correction. This effect is known and is due to the merging of the two photon clusters for the π^0 mesons of energies above 5 GeV. Surely, this effect is absent in the single photon simulation as on Fig. 6.10, but do present in the single π^0 meson simulation as on Fig. 6.14 (see below). It was discussed in more detail in Section 6.2.4. Of course, the two points above 2.5 GeV should not be used for fitting and the non-linearity correction extraction.

Finally, let us emphasize that the method of symmetric π^0 decays is reliable and indeed gives correct results. This statement can be verified in a single π^0 simulation with realistic momentum distribution. The Monte Carlo result is shown on Fig. 6.14, where the blue line corresponds to the extracted non-linearity, whereas the red line is the non-linearity extracted previously from the single photon simulation.[4] As one can see, the non-linearities go in parallel and differ only by an irrelevant constant factor.

6.3.4 Non-linearity for real data : asymmetric π^0 decays

There is yet another method of calculation of the non-linearity for real data which gives a powerful cross-check for the method of symmetric π^0 decays.

---

[4] The small fluctuation of points is due to limited statistics of the generated π^0 simulation. Also, on Fig. 6.14, a rise of the π^0 mass starts at 3 GeV, whereas on Fig. 6.13 (left) this happens at 2.5 GeV. This is due to the fact that the simulation was taken without any cell decalibration, so that the energy resolution in simulation is better and thus clusters are smaller and their merging begins later than in data. In addition, the cluster unfolding algorithm works better in simulation.

Note also that the decalibration does not affect the non-linearity, see Section 6.5.

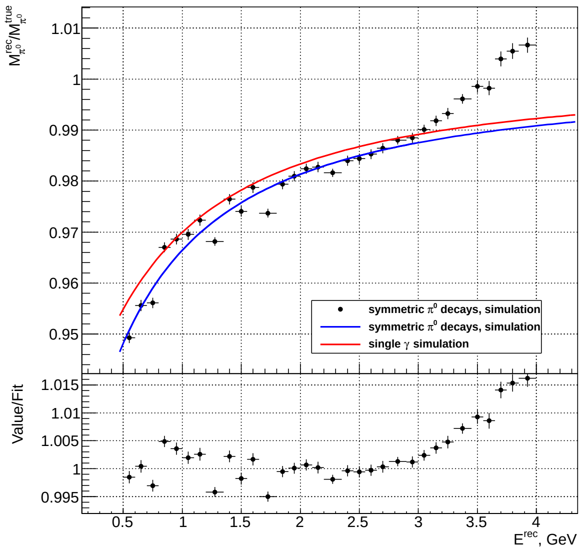

FIGURE 6.14 – Comparison between the non-linearity extracted from single photon simulation and from π^0 simulation with realistic momentum distribution.

We start from Eq. (6.3.4) and consider *asymmetric* π^0 *decays*, where one photon cluster has a high energy. For definiteness, let it be E_2^{rec}. As we already know, the non-linearity is close to unity at high energies, and we can substitute $E_2^{\text{rec}} \approx E_2^{\text{true}}$. Then, one has

$$M_{12}^2 = 2E_1^{\text{rec}} E_2^{\text{true}} \left(1 - \cos\theta_{12}^{\text{true}}\right), \tag{6.3.9}$$

which gives

$$f(E^{\text{rec}}) = \frac{(M_{\pi^0}^{\text{rec}})^2}{(M_{\pi^0}^{\text{true}})^2} \qquad \text{[asymmetric } \pi^0 \text{ decays]}, \tag{6.3.10}$$

where $E^{\text{rec}} = E_1^{\text{rec}}$.

Let us remark that practically, when filling histograms of slices of invariant mass squared, one sums other high-energy clusters, considering the slices as functions of the energy E^{rec} of a lower-energy cluster. In our analysis, we took high-energy clusters in the region 3–5 GeV. Fig. 6.15 shows examples of slices at three energies of a lower-energy cluster.

As was already pointed out, the method of asymmetric π^0 decays is very useful as a cross-check for the method of symmetric π^0 decays, as it is very sensitive to the angle resolution and thus allows one to verify the assumption $\theta_{12}^{\text{rec}} = \theta_{12}^{\text{true}}$. Moreover, this method can be used in order to check the shape of the non-linearity at energies below 0.5 GeV. In addition, it is insensitive to cluster merging effect, as the angle between the two photons is large.

The method also has two disadvantages. First, the approximation $E_2^{\text{rec}} \approx E_2^{\text{true}}$ is not quite correct since the non-linearity is a relatively slow function of energy. Thus, for a

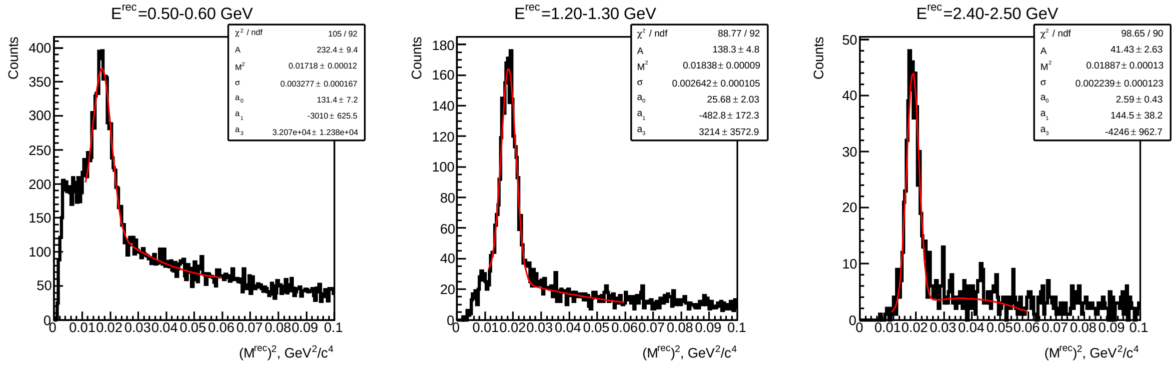

FIGURE 6.15 – Examples of slices of two-cluster invariant mass squared, zero-order approximation.

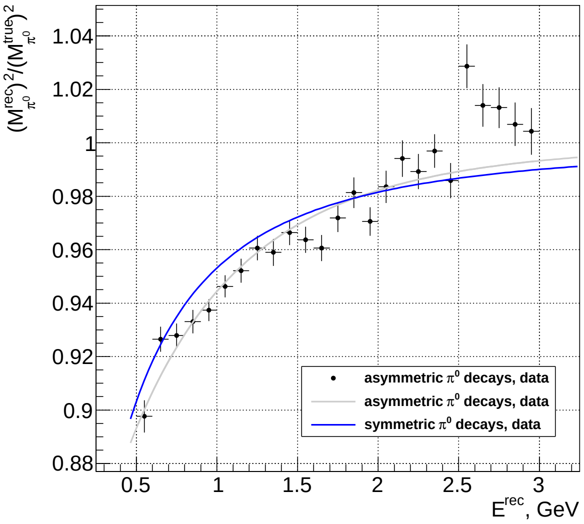

FIGURE 6.16 – Non-linear correction extracted from asymmetric π^0 decays (zero-order approximation) and its comparison with that obtained from symmetric π^0 decays.

better non-linearity, an iterative procedure should be performed : after the extraction of the zero-order non-linearity, the analysis should be repeated with the energy E_2^{rec} of the high-energy cluster being corrected with the zero-order non-linearity, and so on. Second, this method, at least on its zero-order iteration, may require more statistics than the method of symmetric π^0 decays since with the minimum-bias trigger there are not many high-energy clusters. This can be especially harmful if both clusters are taken in one and the same supermodule, which is necessary sometimes and is the case in current studies.

A lack of statistics is reflected on Fig. 6.16, where some points do fluctuate. As one can see, the zero-order approximation already gives very good coincidence between the two methods. Further iterations should improve this result.

6.4 Reconstruction of $\omega(782)$ and K_S^0 mesons

Other neutral mesons can be reconstructed using an invariant mass analysis similar to what was discussed in Section 6.2, and their visibility as peaks is a question of available statistics and data quality. On Fig. 6.17, the reconstructed mesons $\omega(782) \to \pi^0\gamma \to 3\gamma$ and $K_S^0 \to \pi^0\pi^0 \to 4\gamma$ in the EMCAL detector are shown.

The details of $\omega(782)$ and K_S^0 meson studies are not presented here. Let us only remark that the observation of these mesons on a limited statistics of 2010 was not possible until a good energy non-linearity correction as well as cluster unfolding was applied. In particular, the peaks visibility demonstrated a correct choice of the non-linearity which was a considerable progress in understanding of the EMCAL detector response.

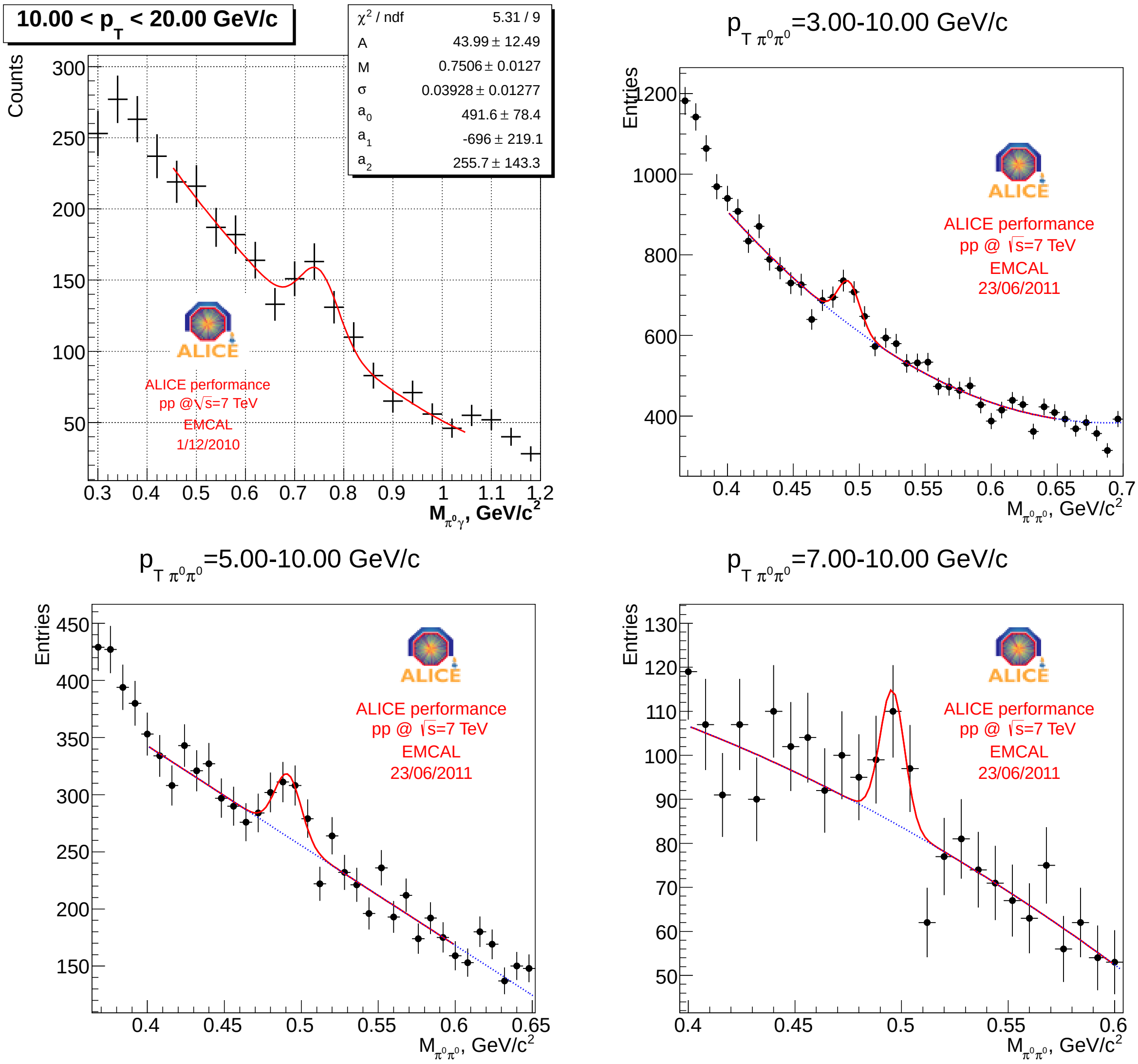

FIGURE 6.17 – Neutral mesons $\omega(782)$ (top left) and K_S^0 (top right and bottom) reconstructed in the EMCAL through their photon decays. Data corresponds to 450 and 382 million minimum-bias events respectively.

Note also that in the studies of $K^0_S \to \pi^0\pi^0$, the masses of the π^0 candidates (reconstructed from two clusters in the EMCAL) were scaled to the PDG value of 134.9 MeV. Without this, the K^0_S peak was not observable.

6.5 Cells decalibration and amplitude smearing in simulation

The energy non-linearity discussed in the previous section corrects the absolute energy scale in data as well as in simulation, ideally making the two scales to coincide. It cannot, however, account for the difference in energy resolution between data and simulation. In fact, by default, the energy resolution in simulation is better than in data. To account for this, cell decalibration and/or cell smearing methods can be used.

The relative energy resolution σ_E/E of a calorimeter comprises three contributions : a noise term a/E, a stochastic term $b/\sqrt{E}$ and a sampling term c :

$$\frac{\sigma_E}{E} = \sqrt{\left(\frac{a}{E}\right)^2 + \frac{b^2}{E} + c^2}. \tag{6.5.1}$$

The noise term a is defined by the intrinsic noise of the front-end electronics, and thus it is a property of the readout rather than of the calorimeter itself. The stochastic term b comes from a finite statistics of photoelectrons detected by a photodetector. The sampling term c results from the energy loss in a passive material of the calorimeter and from a residual miscalibration.

Cell decalibration is a simple method of reducing energy resolution in a simulation in order to account for a *residual miscalibration* of the EMCAL channels in reality. According to this method, to each cell of the detector, a permanent decalibration coefficient k is applied, so that the energy response in a cell in each event would be kA and not A. The decalibration coefficient k varies from cell to cell and is calculated with a Gaussian probability function

$$\rho_{\text{dec}}(k) = \frac{1}{\sqrt{2\pi\sigma_{\text{dec}}}} e^{-(k-1)^2/2\sigma_{\text{dec}}}, \tag{6.5.2}$$

where always $k > 0$. The constant dispersion σ_{dec} reflects the desired degree of decalibration : 0.01 for 1% decalibration, 0.05 for 5% decalibration, *etc.* As it was mentioned above, miscalibration contributes to the sampling term c of the energy resolution.

Cell smearing accounts for an *intrinsic energy irresolution* of the calorimeter. In contrast to the cell decalibration, cell smearing modifies cells amplitudes in a probabilistic manner : in each event, for each cell with a nonzero signal, the cell amplitude A

is replaced by an amplitude $A' \geq 0$, where the probability of such the new amplitude is

$$\rho_{\mathrm{sm}}(A') = \frac{1}{\sqrt{2\pi\sigma_{\mathrm{sm}}}} e^{-(A'-A)^2/2\sigma_{\mathrm{sm}}}. \tag{6.5.3}$$

Here, the smearing dispersion σ_{sm} is a function of the original cell amplitude, $\sigma_{\mathrm{sm}}(A) = \alpha\sqrt{A}$ with a constant α. For the EMCAL detector, the latter is believed to be $\alpha = 0.07$ [37], so that

$$\sigma_{\mathrm{sm}}(A) = 0.07\sqrt{A}. \tag{6.5.4}$$

As the smearing dispersion σ_{sm} depends on the original cell amplitude, this ultimately changes the total shape of the EMCAL resolution curve in simulation.

Evidently, after cell smearing and further cell decalibration, all cluster energies, positions and other parameters must be recalculated.

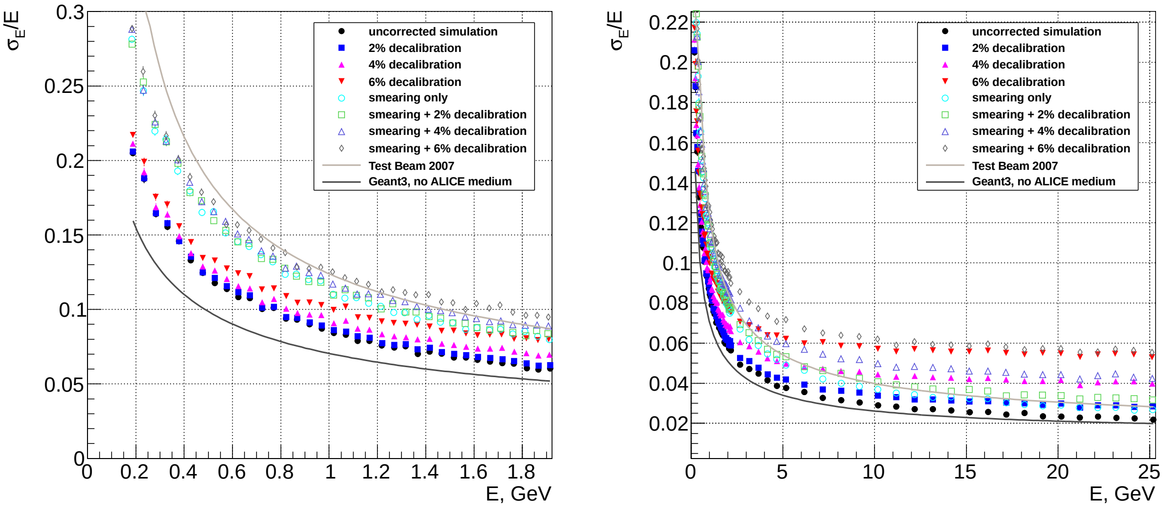

FIGURE 6.18 – Relative energy resolution for different decalibrations, with or without smearing with dispersion of Eq. (6.5.4) in the single photon simulation : up to 2 GeV (left) and up to 25 GeV (right).

By changing cell smearing and decalibration parameters, σ_{dec} and α, one can achieve a match between Monte Carlo simulations and reality. Fig. 6.18 shows dependence of the relative energy resolution obtained from the single photon simulation discussed in Section 6.3.1 on decalibration and smearing parameters. Here, the smearing was taken to be as in Eq. (6.5.4). As one can see, the relative energy resolution of the calorimeter decreases with energy.

Finally, it is worth saying that the non-linearity correction is not affected by the cell calibration. Indeed, the decalibration widens the energy response at each particular energy, but it does not shift the energy scale. On the contrary, cell smearing does influence on the non-linearity. This is due to the amplitude dependence in the smearing dispersion

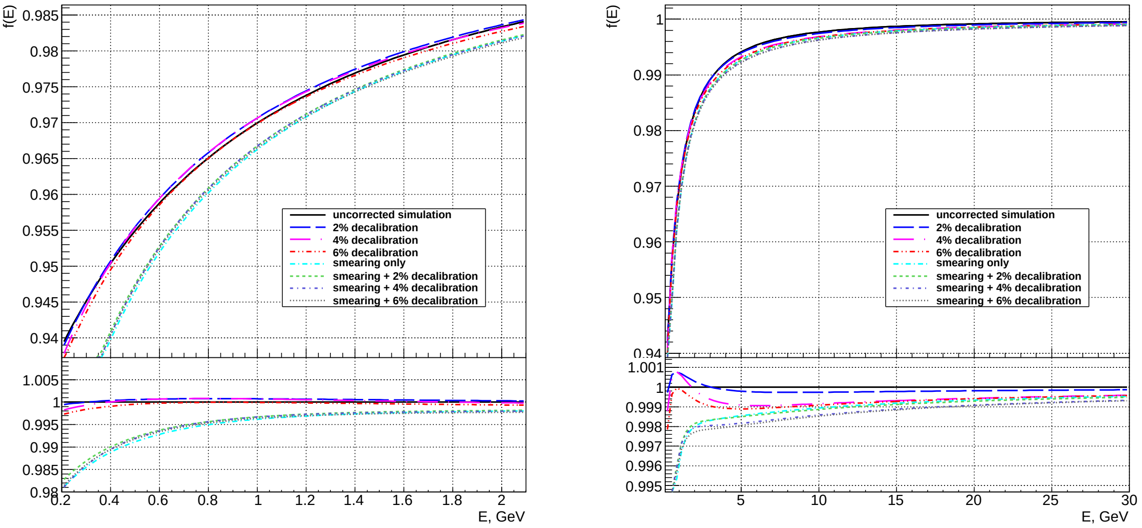

FIGURE 6.19 – Comparison of the non-linearity corrections obtained with different decalibrations and with or without smearing with dispersion of Eq. (6.5.4) in the single photon simulation : up to 2 GeV (left) and up to 30 GeV (right). Bottom plots show ratios with respect to the non-linearity of the uncorrected simulation.

$\sigma_{\mathrm{sm}}(A)$, where smaller A values are more favorable, leading to a stronger non-linearity. These points are illustrated on Fig. 6.19, where the two groups of the non-linearities corresponding to $\alpha = 0$ and $\alpha = 0.07$ are clearly visible. Needless to say that the tiny difference inside each group is within the uncertainties of the non-linearities extraction.

6.6 Comparing data and simulation : mass and width of the π^0 meson

So far, it was shown how to correct energy scale of the calorimeter in data and in Monte Carlo simulations as well as how to reduce the calorimeter energy resolution in simulations in order to match with that in data. Now one comes to a very important point. At this stage, it is possible to determine the expectations of future systematic uncertainties in energy and momentum measurement of the π^0 meson. Let us emphasize that, as we are also interested in the η meson measurement, the concerns given below must be repeated for the η meson as well.

First note that the spectrum of the π^0 meson is measured (through its two-photon decay) as a function of its reconstructed transverse momentum p_T^{rec} (which is obtained from a knowledge of reconstructed energies of the two photons and reconstructed angle between them), whereas the final result must be presented as a function of its genuine transverse momentum p_T^{true}. Reasonably, one expects that $p_T^{\mathrm{rec}} = p_T^{\mathrm{true}}$, but this is not valid automatically. Indeed, if the energies are reconstructed incorrectly (in average over many events), for instance, they are underestimated, the reconstructed transverse momentum would be underestimated as well, $p_T^{\text{rec}} < p_T^{\text{true}}$.

For this not to happen, the energy non-linearity correction is applied which serves exactly as a way to calibrate the response of the detector in a measurement of photon energy. Nevertheless, a verification of the equality $p_T^{\text{rec}} = p_T^{\text{true}}$ is still necessary, at least for an estimation of the systematic error of the transverse momentum reconstruction. This task can be accomplished by looking at the behavior of the *reconstructed* π^0 *meson mass as a function of its reconstructed transverse momentum* since the earlier is proportional to the latter.

One should also pay attention to the following circumstance : the above is valid provided angle reconstruction between the two photons do not give an additional bias. This topic was already discussed in Section 6.3.3. In principle, this statement requires a separate verification with, for instance, a single π^0 simulation.

Thus, the relative difference $(M_{\pi^0}^{\text{rec}} - M_{\pi^0}^{\text{true}})/M_{\pi^0}^{\text{true}}$ is propagated to the uncertainty $\Delta p_T^{\text{true}}/p_T^{\text{true}}$ of the transverse momentum measurement and often gives one of the main contributions to the total uncertainty of the π^0 spectrum measurement. This is one of the two reasons why it is important to apply the non-linearity correction for the photon energy reconstruction. We will return to this point in Section 6.8.1.

The second reason was already discussed in Section 6.1 : the application of corresponding non-linearities both in data as well as in simulations leads to a matching in the energy scales of the two. Since the measured π^0 production spectrum is obtained as a ratio of the raw π^0 yield, taken from data, and the π^0 reconstruction efficiency, calculated in simulation, the difference in the energy scales of the two is another significant uncertainty of the measurement. As to the π^0 meson mass, the coincidence of the two energy scales means that the reconstructed masses in data/simulation as functions of transverse momentum must exhibit a close coincidence.

Another important quantity for us here is the *reconstructed* π^0 *meson width as a function of its transverse momentum* defined as the dispersion of the Gaussian fit around the π^0 peak of the two-cluster invariant mass slices. By its nature, the π^0 width is directly affected by the energy resolution of the calorimeter. At the same time, it is almost insensitive to a change of the energy scale, i.e. to the application of an energy non-linearity correction. Consequently, the π^0 width is to be used for determination of decalibration and smearing parameters in simulation which give a match with real data.

The matching of reconstructed π^0 widths in data/simulation is an important element which additionally confirms that the simulation produces adequate results. In practice, this is a way to calculate the systematic error of the π^0 reconstruction efficiency (Section 6.7). The latter, apparently, depends on simulation conditions.

Let us proceed to illustrations of the above ideas. To this end, we took a *single* π^0 *simulation*, there the momentum of the generated meson was distributed realistically (as in data). The procedure of the corresponding two-cluster invariant mass analysis was done as usual (Section 6.2), but with the cluster unfolding algorithm being used (Section 6.2.4). Without it, it is not possible to see the π^0 peak above 7–9 GeV/c on the selected statistics of 190 and even of 450 million events.

On Fig. 6.20, reconstructed π^0 masses (left plots) and widths (right plots) are shown

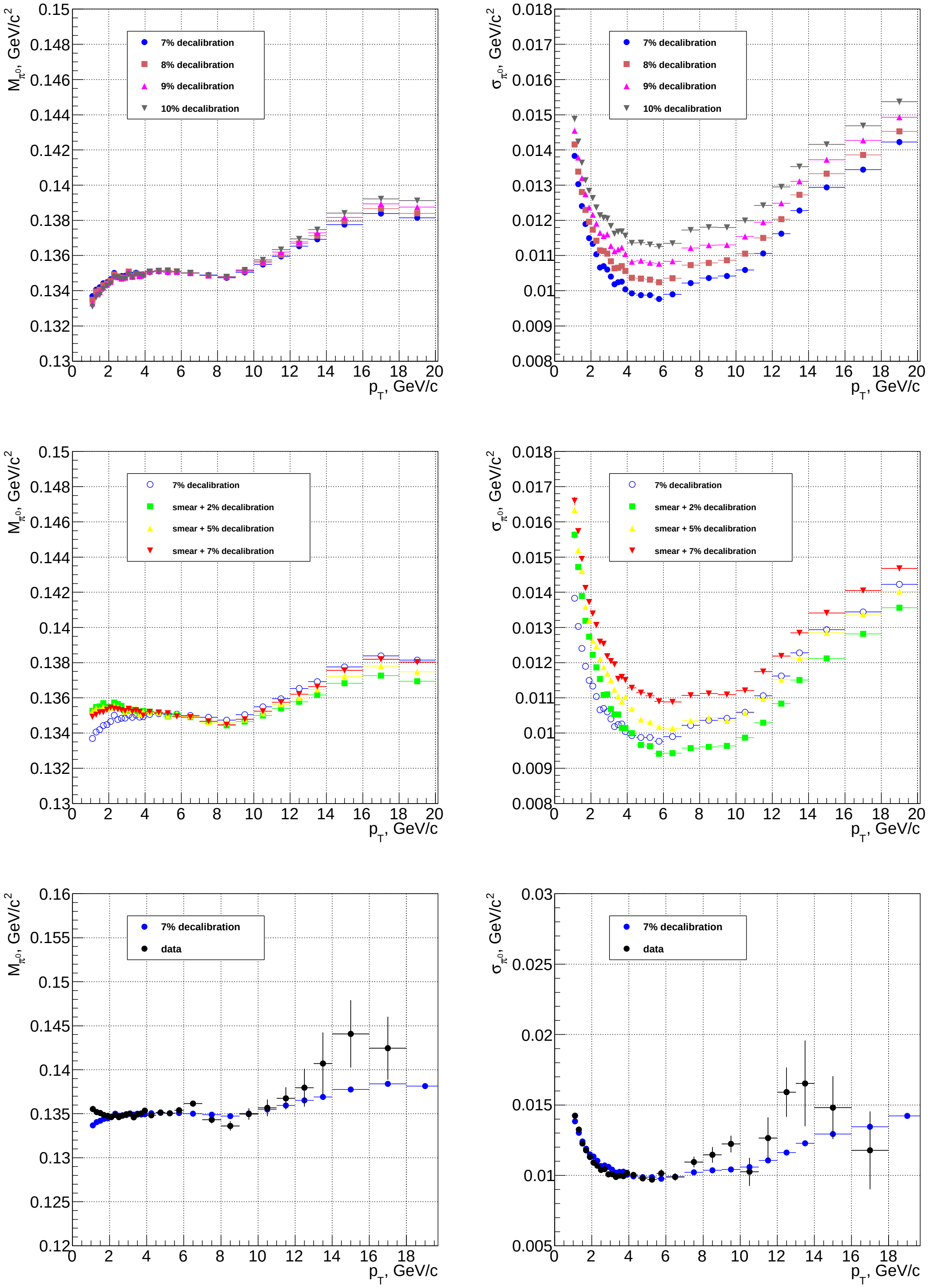

FIGURE 6.20 – Reconstructed π^0 meson masses (left) and widths (right) in simulations and data. On these plots, legacy Monte Carlo non-linearity corrections were applied. Smearing-related points correspond to the smearing dispersion of Eq. (6.5.4). Data corresponds to 190 million minimum-bias events.

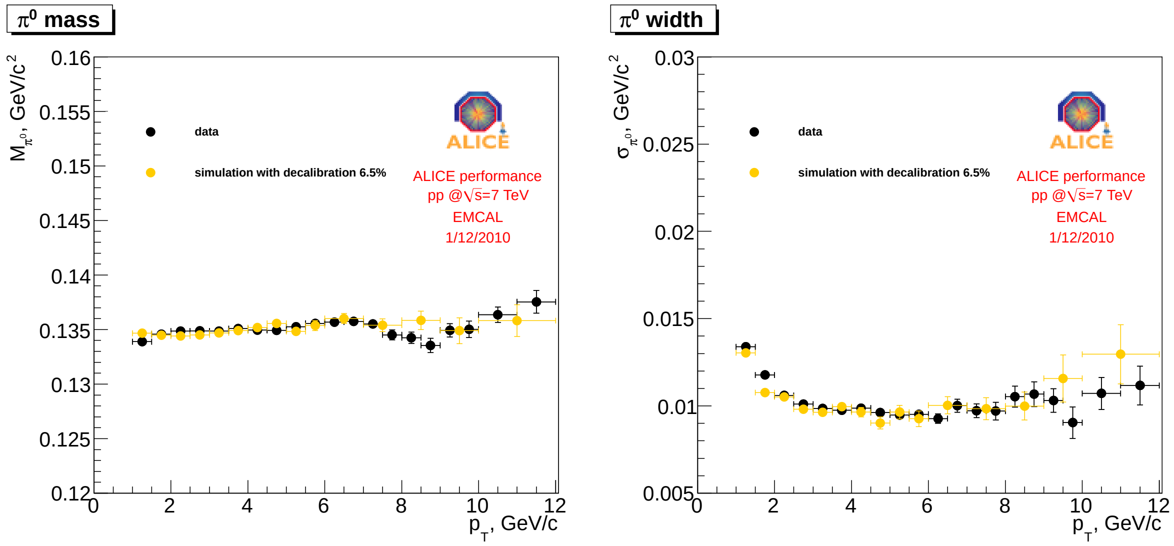

FIGURE 6.21 – Comparison of reconstructed π^0 meson masses (left) and widths (right) in data and in simulation. Data corresponds to 450 million minimum-bias events.

as functions of reconstructed transverse momentum p_T.[5] The plots at the top show how the π^0 mass and width are affected by a change in decalibration, without any cell smearing applied. The middle plots show the same, but with the smearing applied with the dispersion taken as in Eq. (6.5.4). In addition, as a reference for comparison, empty blue points correspond to the blue points from the two top plots.

As was discussed earlier, the reconstructed masses are not affected by a change of calibration, but the change to the situation with smearing changes their low-momentum behaviors. The π^0 widths show clear dependence on decalibration/smearing parameters, where cell smearing changes the shape of the widths as functions of transverse momentum. Moreover, the π^0 widths have a rather strong decrease between 1 and 3 GeV associated to the improvement of the energy resolution. Again, the rise of masses and widths at large momenta corresponds to cluster merging in the detector and its following unfolding with the algorithm which was not corrected for that rise.

Finally, the bottom plots show a comparison between data and Monte Carlo, where a rather good coincidence was achieved at the decalibration of 7% and without cell smearing. There is a small difference of about 2 MeV in the low-momentum region. This is due to an old (outdated) non-linearity of the form

$$f(E) = \left(1 + a\, e^{-b\,E}\right)^{-1}, \qquad a = 0.1389, \quad b = 1.046, \tag{6.6.1}$$

---

[5] Generally, the “flat” region 2–6 GeV/c of reconstructed π^0 mass is found at values which differ from 135 MeV, even with energy non-linearity correction applied. In simulation, this value is usually of about 137 MeV, while in data it depends on the average calibration coefficient of the detector. It is easy, however, to rescale the masses (and widths) by a constant thus compensating the mass shifts and putting the absolute energy scale to its right place.

which is steeper at low energies, being applied in the simulation. Of course, better results can be achieved with correct or at least function-matching non-linearities, see e.g. Fig. 6.21.

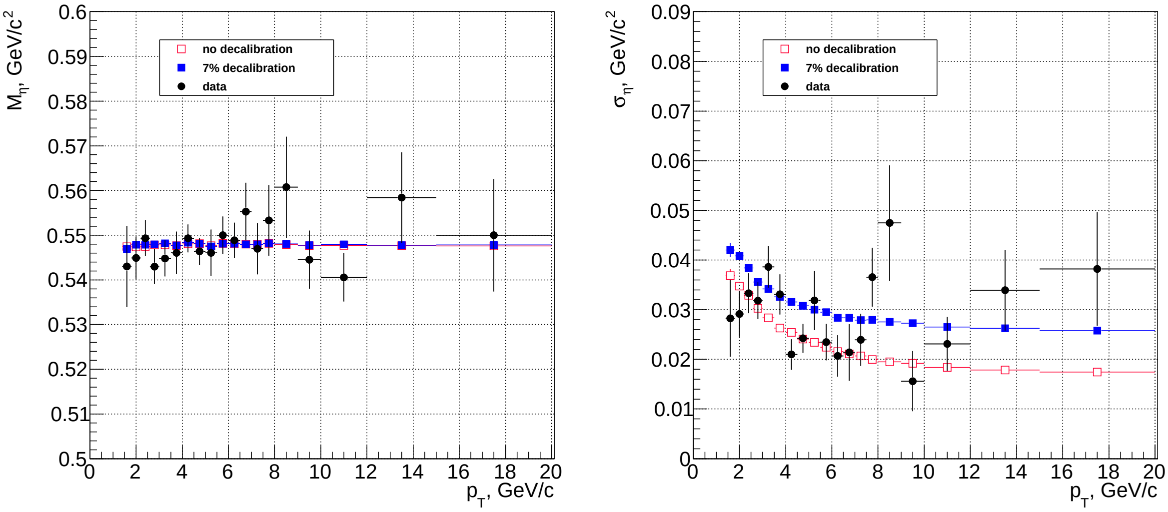

FIGURE 6.22 – Reconstructed η meson masses (left) and widths (right) in simulations and data. Data corresponds to 190 million minimum-bias events.

Lastly, on the bottom plots, the region 2–6 GeV/c exhibits a regular (flat) π^0 mass behavior. However, for data points, one can also observe an irregular wavy behavior in the momentum region 6–10 GeV/c. This is due to a change of proportion between merged-and-unfolded clusters and normal clusters. Finally, the important difference of masses in data/simulation points above 12 GeV/c is seen, which must be accounted for while calculating systematic uncertainties.

In conclusion, let us show the η meson mass and width comparison with simulations, see Fig. 6.22. As one can see, the stability of the reconstructed η mass gives clear evidence about good energy linearity of the EMCAL response. In addition, on this plot, there was no need to scale the η masses to their PDG values : this happened automatically. The η meson widths on data, though being consistent with the simulations, do not show a clear behavior. This is a consequence of high statistical fluctuations due to a limited datasample of 190 million minimum-bias events.

6.7 π^0 and η reconstruction efficiency

A measurement of a particle production spectrum with an experimental device is connected, in fact, with counting of number of particles ΔN^{rec} which were detected (reconstructed) in some region of interest $\Delta\Gamma$ of the particle's parameter space Γ. In order to obtain the final result, however, this information needs to be supplemented by the information on how the number ΔN^{rec} is related to the number of particles N^{prod} which were actually produced. It is natural to assume that these numbers are proportional to each other. Indeed, if twice as much particles were produced, then twice as much particles are counted.[6] The coefficient of proportionality,

$$\varepsilon(\Gamma,\,\Delta\Gamma) = \frac{\Delta N^{\text{rec}}}{N^{\text{prod}}}, \tag{6.7.1}$$

considered as a function of the parameter space Γ and the region of interest $\Delta\Gamma$, is called the particle's *reconstruction efficiency.*[7] Knowing this function as well as the counted number of particles ΔN^{rec}, one then can deduce the number of produced particles N^{prod}. The efficiency ε can be calculated from its very definition (6.7.1) in a Monte Carlo simulation which is tuned to reproduce the detector response.

In the case of π^0 and η meson production measurement, their parameter space Γ consists of three variables : the transverse momentum p_T, the pseudorapidity η and the azimuth angle φ. In what follows, we consider the efficiencies to be calculated in full EMCAL acceptance, taking thus the region of interest of the parameter space to be

$$\Delta\Gamma: \quad \Delta p_T; \quad |\eta| \le 0.7,\, \Delta\eta = 1.4; \quad 80^\circ \le \varphi \le 120^\circ,\, \Delta\varphi = 40^\circ, \tag{6.7.2}$$

ultimately leaving only one parameter p_T on which the efficiency depends, $\varepsilon = \varepsilon(p_T,\,\Delta p_T)$.

Below, a mathematical background on the efficiency is given, where, for illustrations, we consider the pion as a measured particle. After that, the π^0 and η reconstruction efficiencies are calculated from single π^0 and η simulations respectively.

6.7.1 Mathematical background

Let us consider a convenient mathematical limit $\Delta p_T \to 0$. Respectively, we substitute

$$\begin{aligned} &\Delta p_T \to dp_T, \\ &\Delta N^{\text{rec}}(p_T, \Delta p_T) \to n^{\text{rec}}(p_T) dp_T. \end{aligned} \tag{6.7.3}$$

---

[6] This is true provided the experimental device distinguishes particles with the same effectiveness under doubled particle multiplicity. In the case of the electromagnetic calorimeter EMCAL, this translates into the requirement that a chance of two particles to hit one region of the detector and yield one cluster instead of two is very low. This is true indeed in *pp* collisions, where an average number of clusters per event is small (see e.g. middle plot on Fig. 6.2). In heavy-ion runs, however, this is not the case, since total particle multiplicity can be very high. Nevertheless, this is not a problem as this only requires to include the collision centrality class (which is an equivalent to multiplicity) into the parameter space Γ. Below, we focus on *pp* collisions, where no dependence on multiplicity is present.

[7] Note that in what follows we do not make a difference between the detector efficiency and the detector acceptance as the latter is included in the earlier.

As was already pointed out, the measured raw spectrum of particles $n^{\mathrm{rec}}(p_T^{\mathrm{rec}})$ and the unknown production spectrum $N^{\mathrm{prod}}(p_T^{\mathrm{true}})$ are proportional to each other. Then, it is a well known mathematical fact that they should be related by a linear integral equation,

$$n^{\mathrm{rec}}(p_T^{\mathrm{rec}}) = \int_0^{\infty} G(p_T^{\mathrm{rec}},\, p_T^{\mathrm{true}})\, N^{\mathrm{prod}}(p_T^{\mathrm{true}})\, dp_T^{\mathrm{true}}. \tag{6.7.4}$$

The kernel $G(p_T^{\mathrm{rec}}, p_T^{\mathrm{true}})$ of this equation is referred to as the detector response function. It takes into account particle loss in the ALICE medium, the detector acceptance, reconstruction efficiency, the detector energy resolution as well as correlation between the reconstructed transverse momentum p_T^{rec} and the genuine transverse momentum p_T^{true}. Due to the latter, the kernel $G(p_T^{\mathrm{rec}}, p_T^{\mathrm{true}})$ also depends on the shape of the production spectrum $N^{\mathrm{prod}}(p_T^{\mathrm{true}})$. This fact is demonstrated below.

The equation (6.7.4) is called Fredholm equation of the first kind. The problem of its solving was addressed in Ref. [38]. The following main conclusions were made :

- it is not possible to obtain exact numerical solution because of singularities of the function G ;
- numerical solution requires a regularization of G.

Therefore, Eq. (6.7.4) can be solved approximately under different simplifying assumptions of the kernel G, which are discussed in the present section.

1. The simplest way to approximate Eq. (6.7.4) is to assume that the detector has an ideal response :

$$G(p_T^{\mathrm{rec}}, p_T^{\mathrm{true}}) = g(p_T^{\mathrm{true}})\delta(p_T^{\mathrm{true}} - p_T^{\mathrm{rec}}). \tag{6.7.5}$$

In this case Eq. (6.7.4) reads

$$g(p_T^{\mathrm{rec}}) = \frac{n^{\mathrm{rec}}(p_T^{\mathrm{rec}})}{N^{\mathrm{prod}}(p_T^{\mathrm{rec}})} \tag{6.7.6}$$

with $p_T^{\mathrm{true}} = p_T^{\mathrm{rec}}$, thus giving just a simple proportionality between the density of reconstructed number of particles and the produced number of particles. Note also that there is a point to point correspondence between the produced number of particles at particular momentum and the reconstructed particle density at the very same momentum. Due to this, the efficiency function $g(p_T)$ is independent of the shape of the particle production spectrum $N^{\mathrm{prod}}(p_T)$.

2. As a second approximation to the EMCAL detector, it is better to consider an ideal response, but with a shift between the two transverse momenta (see also Fig. 6.23) :

$$G(p_T^{\mathrm{rec}}, p_T^{\mathrm{true}}) = g(p_T^{\mathrm{true}})\delta(p_T^{\mathrm{true}} - p_T^{\mathrm{rec}} - \Delta(p_T^{\mathrm{rec}})), \tag{6.7.7}$$

which gives a relation $p_T^{\mathrm{true}} = p_T^{\mathrm{rec}} + \Delta(p_T^{\mathrm{rec}})$, where $\Delta(p_T^{\mathrm{rec}})$ is the shift between the genuine and the reconstructed momenta as a function of reconstructed momentum. Therefore, Eq. (6.7.4) gives

$$g(p_T^{\mathrm{true}}) = \frac{n^{\mathrm{rec}}(p_T^{\mathrm{rec}} - \Delta)}{N^{\mathrm{prod}}(p_T^{\mathrm{true}})}, \tag{6.7.8}$$

where $\Delta(p_T^{\mathrm{rec}})$ must be considered as a function of p_T^{true}.

In contrast with the previous situation, although there is a point to point correspondence between the produced number of particles and the reconstructed particle density, the efficiency function $g(p_T)$ does depend on particle production $N^{\mathrm{prod}}(p_T)$ shape. Indeed, the shift Δ between the two momenta is a function of this shape. Thus, to correctly obtain the efficiency $g(p_T)$ from a simulation, one has to consider a π^0 simulation with a realistic pion spectrum.

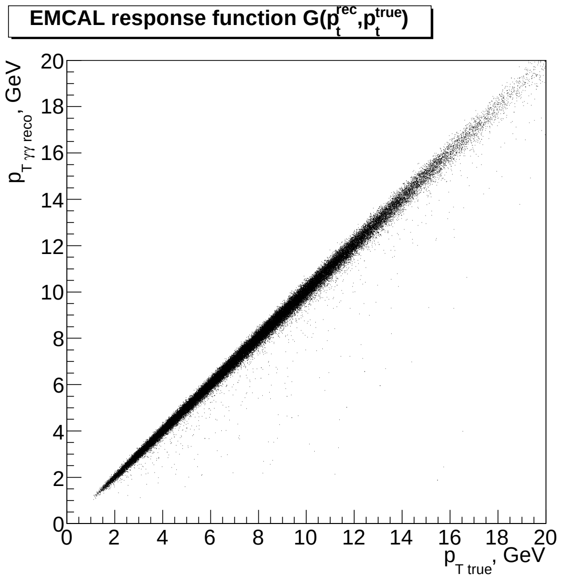

FIGURE 6.23 – Correlation function $G(p_T^{\mathrm{rec}}, p_T^{\mathrm{true}})$ between the generated and the reconstructed transverse momentum obtained in a single π^0 simulation, where the pion can have only certain discrete set of transverse momenta.

3. One can find the kernel G of Eq. (6.7.4) by taking a π^0 simulation with non-realistic spectrum

$$N^{\mathrm{prod}}(p_T) = n_0\, \delta(p_T - p_0). \tag{6.7.9}$$

Obviously, in this case

$$G(p_T^{\mathrm{rec}},\, p_0) = \frac{n^{\mathrm{rec}}(p_T^{\mathrm{rec}})}{n_0}. \tag{6.7.10}$$

Although the corresponding solution is not exact, it still can be considered as a good approximation since the genuine function G shape is indeed a narrow stripe around $p_T^{\mathrm{true}} = p_T^{\mathrm{rec}} + \Delta(p_T^{\mathrm{rec}})$, where Δ is a small momentum-dependent shift, see Fig. 6.23. On this figure, a corresponding histogram was filled for pairs of clusters the invariant mass of those was close to the π^0 mass, since it is not possible to do a π^0 identification in that case.

4. The equation (6.7.4) can be solved numerically in a Monte Carlo simulation if one returns from the infinitesimal transverse momentum dp_T back to a finite momentum region Δp_T. To this end, let us return to the equation (6.7.1).

To calculate the reconstruction efficiency (6.7.1), it is sufficient to take a single π^0 simulation with (already estimated) pion spectrum as in real data, calculate the pion raw yield and divide it by the corresponding produced yield. When, as the taken π^0 production spectrum coincides with that in data, the relation (6.7.1) between the reconstructed and the generated spectrum can be propagated to real data *with the very same efficiency*.

Note that the efficiency should be obtained using an already tuned Monte Carlo simulation, where the detector response reproduces that in reality, as was already discussed before.

Let us emphasize that this approach requires a realistic shape of the π^0 spectrum. Its knowledge can be obtained from an iterative procedure : as a zero approximation, one takes a flat p_T spectrum, calculates the zero-order efficiency and the next-order production spectrum. Then, this process is repeated, if necessary, several times.

6.7.2 The efficiencies for the EMCAL

In this section, we present the π^0 and η reconstruction efficiencies for the EMCAL detector. For this, simulations of single π^0 and single η, there the mesons have realistic (estimated from the data) momentum spectra, were taken.

The problem with these simulations is that the meson spectra are steeply falling with transverse momentum. As a result, high fluctuations of efficiencies would happen at high p_T due to a lack of statistics. To overcome this issue, the mesons were generated in several blocks of events, where in each block the spectra are steeply falling, but start at different transverse momenta $p_T^{\min}$. In the analysis, it was then possible to merge all the blocks for which $p_T^{\min} \ll p_T$, where p_T is a transverse momentum of interest.

For the π^0 analysis, we simulated about 22.8 million events with $p_T^{\min}$ starting from 0.5 GeV/c up to 30 GeV/c and with the step 1 GeV. The same parameters and number of events were taken for the η meson simulation.

Fig. 6.24 demonstrates the reconstruction efficiencies and their comparison for simulations with different detector decalibrations. In addition, although the EMCAL detector covers only 40° in the azimuth angle, by a popular demand the efficiencies were scaled to the full azimuth angle with a factor 360°/40°.

The π^0 reconstruction efficiency has a clear peak near 8–9 GeV/c with further decreasing due to the cluster merging effect. Since the angle between the two photons for the η meson is much larger, the η efficiency continues to rise even at 30 GeV/c. The diminishing of the η efficiency should start at approximately (8–9 GeV/c) $\cdot\, m_\eta/m_{\pi^0} =$ 32–37 GeV/c.

One can also observe how the efficiencies are affected by the detector decalibration. This information allows one to calculate the systematic error due to uncertainty of the detector decalibration, see Section 6.8.1. Clearly, the η meson reconstruction efficiency is almost not affected by the detector calibration.

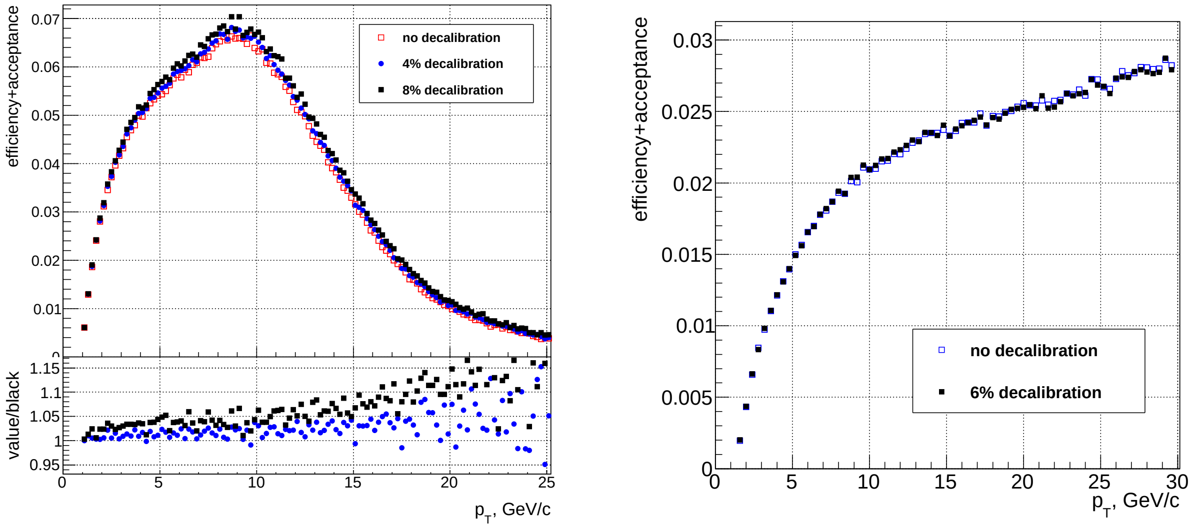

FIGURE 6.24 – Comparison of π^0 (left) and η (right) reconstruction efficiencies obtained with different decalibrations. The efficiencies are scaled by a factor 360°/40°. Statistical errors are not shown for clarity.

6.8 π^0 and η production spectra

In this section, the π^0 and η production spectra are presented with statistical errors only. The possible sources of systematic uncertainties will be discussed shortly.

The mesons production spectra are obtained using the formula (6.7.1), where the raw yields and the efficiencies are shown on Figs. 6.7 and 6.24, respectively. However, the following widely accepted normalization is used here :

$$E\frac{d^3N}{dp^3} \equiv \frac{1}{2\pi p_T}\frac{1}{N_{pp}} \cdot \frac{d^2N}{dp_T dy} = \frac{1}{2\pi p_T}\frac{1}{N_{pp}} \cdot \frac{\Delta N^{\text{rec}}}{\varepsilon \Delta p_T}, \tag{6.8.1}$$

where $N_{pp} \approx 190 \cdot 10^6$ is the number of analyzed events. Let us remark that in this way the production spectra are *not scaled* by the $\pi^0 \to \gamma\gamma$ and $\eta \to \gamma\gamma$ branching ratios.

On Figs. 6.25 and 6.26, the production yields of the π^0 and the η mesons are shown. [8] As expected, the spectra are steeply falling functions of the transverse momentum, decreasing by more than 5 orders of magnitude in the range 2–20 GeV. These spectra were compared with those obtained by the PHOS calorimeter. A good coincidence was observed.

---

[8] These spectra, however, were additionally corrected by a factor 1.1 in order to account for the material budget errors in simulations, see Section 6.8.2 and Fig. 6.28 (right).

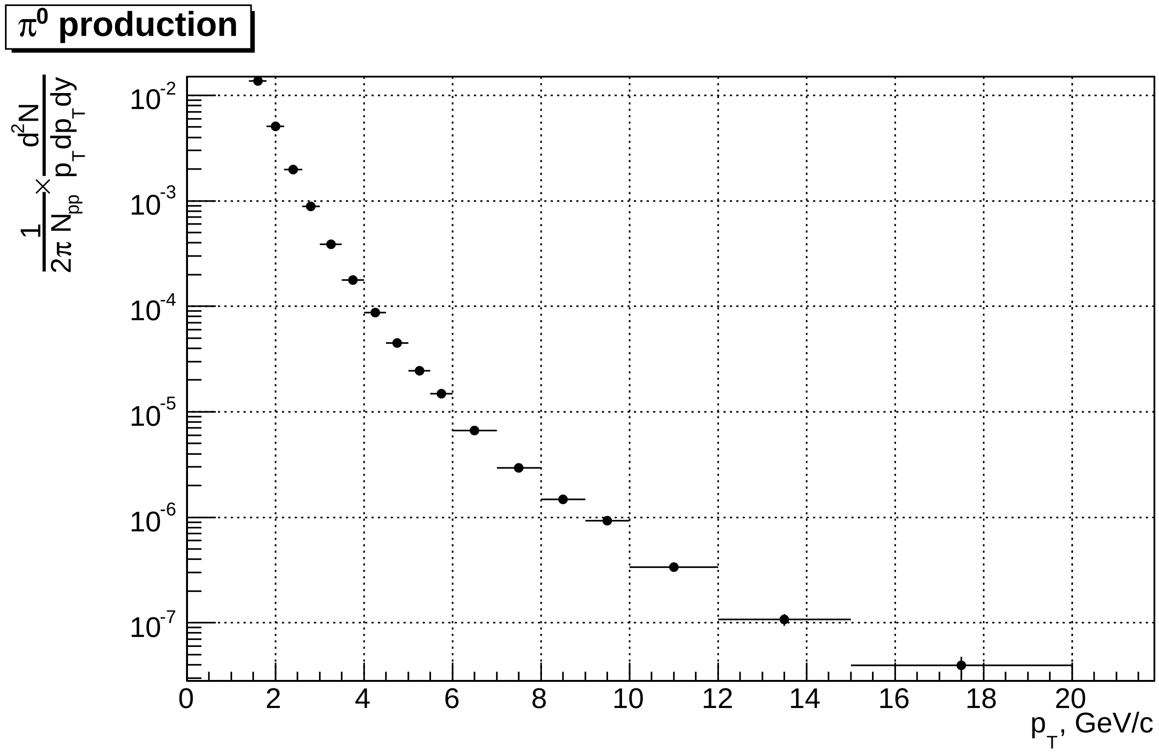

FIGURE 6.25 – π^0 meson production yield, Eq. (6.8.1).

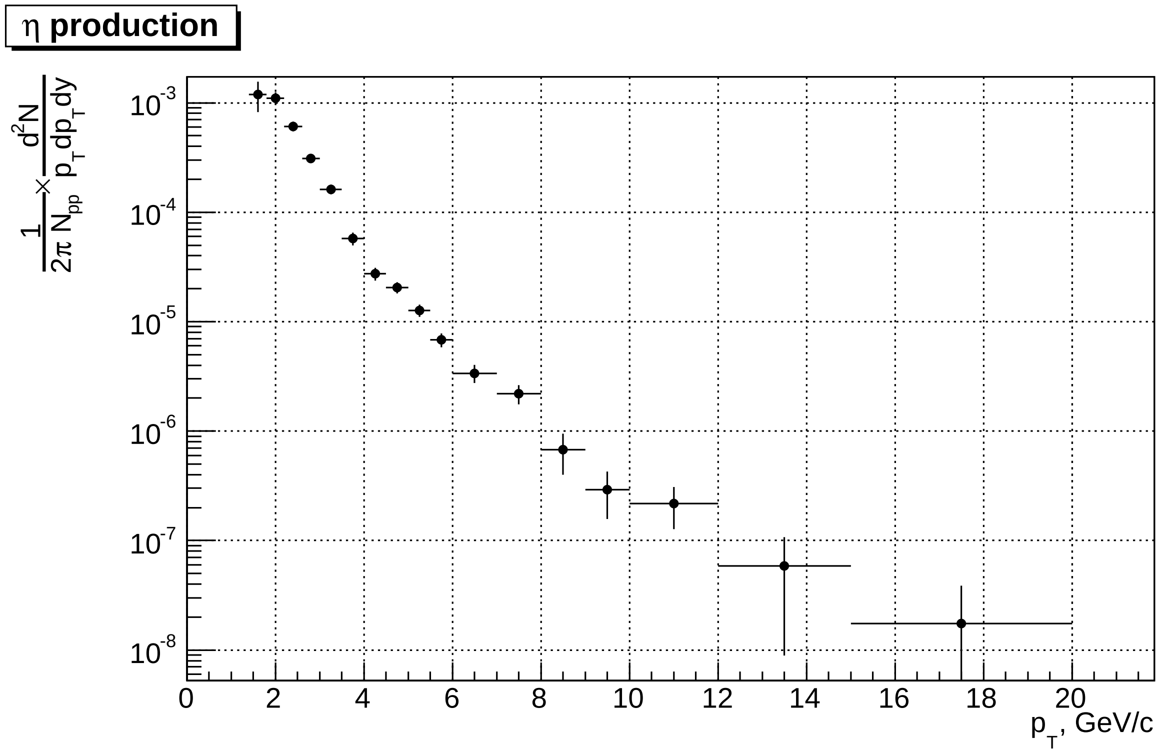

FIGURE 6.26 – η meson production yield, Eq. (6.8.1).

6.8.1 Systematic uncertainties

To obtain final π^0 and η production spectra, various systematic uncertainties must be taken into account. As it follows from Eq. (6.8.1), they are formed by uncertainties of the raw yield extraction (in the numerator) and uncertainties of the efficiency calculation (in the denominator). Their estimation is performed by a respective change of a quality, the uncertainty of which one wants to estimate, and further comparison of old and new results.

Typical uncertainties and their values for the π^0 meson are shown in Fig. 6.1. The classification of the uncertainties is the following.

uncertainty	p_T = 1–1.5 GeV/c	p_T > 1.5 GeV/c
raw yield extraction	2%	2%
absolute energy scale, decalibration	5%	5%
energy non-linearity	17%	< 2%
finite knowledge of EMCAL position	2%	< 2%
material budget	3%	3%

Table 6.1 – Typical systematic uncertainties for the production spectrum of the π^0 meson at $\sqrt{s} = 7$ TeV.

1. For real data, there is an *uncertainty of raw yield extraction.* It comes from the fact that it is not possible to separate signal from background without errors. Indeed, let us look, for instance, at Fig. 6.4, where the signal is separated from the background by fitting the invariant mass plot with some function. The result, of course, depends on the fitting function as well as on fitting region. Consequently, the finite accuracy in the invariant mass fitting must be taken into account by attributing an error to the fitting procedure. The latter can be obtained by fitting the histogram with different functions (e.g. Gaussian/Crystal Ball function plus polynomial of the second or the third order in our case) as well as with different parameters like fitting region.

The raw yield extraction uncertainty is the first principal uncertainty of our measurement. In our studies, this uncertainty was estimated with the above procedure for both the π^0 and the η raw yields in all invariant mass p_T slices. Fig. 6.27 shows an illustration of the calculation of the raw yields extraction uncertainties.

2. The *second class* of uncertainties is attributed to the π^0 *and η reconstruction efficiencies calculation.* They emerge due to the fact that simulations do not reproduce the data absolutely correctly. Thus, the efficiencies were calculated for a detector, which does not exist in reality. Here is the list of uncertainties :

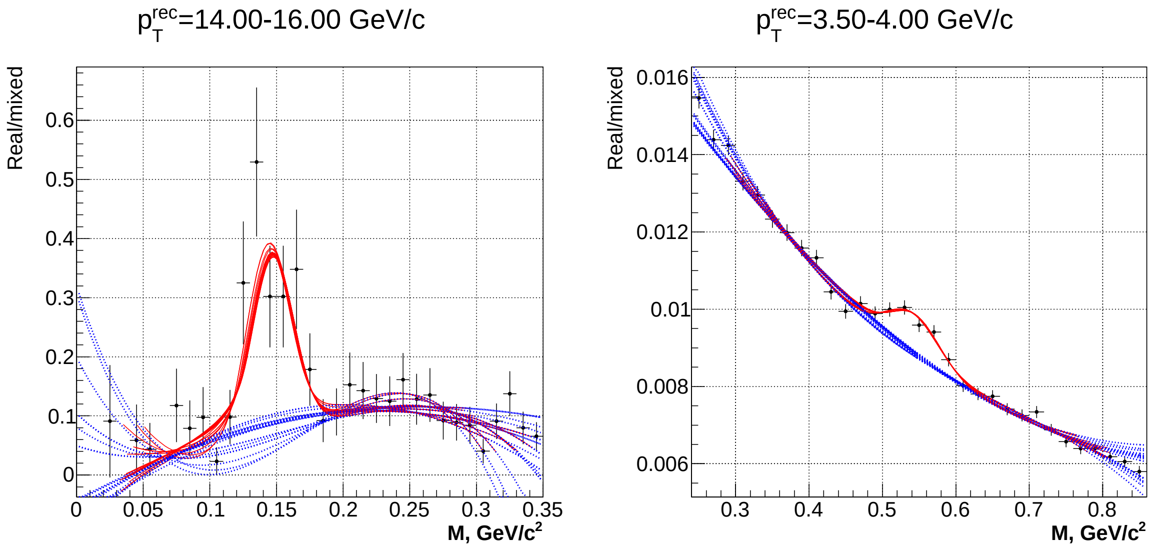

FIGURE 6.27 – Visualization of calculation of the raw yield extraction uncertainty for π^0 meson (left) and η meson (right).

- Uncertainty due to a not quite correct bad channel map. Indeed, imagine that in the real detector there is another bad channel which was not taken into account in simulations. This uncertainty is small, however. To account for it, the efficiencies must be recalculated with more bad channels added to the EMCAL bad channel map.
- Uncertainty in the π^0 and η yields due to the off-vertex production, which is also small, see [39].
- Uncertainty due to finite knowledge of position of the EMCAL in the ALICE machine. It can be estimated by displacing the EMCAL in simulation and recalculating the efficiencies.
- Uncertainties related to the cuts applied. In our case there is only one such uncertainty – the cluster energy cut $E_{\text{clus}} \geq 0.5$ GeV. To account for it, one needs to change this cut a little to a bigger and smaller value and recalculate the efficiencies. Naturally, this uncertainty gives a big contribution only for the π^0 transverse momenta close to 1 GeV/c, i.e. near the two-cluster energy cut itself. The η meson efficiency is almost unaffected since we are considering it for transverse momenta $p_T \geq 1.4$ GeV/c.
- Uncertainty due to the difference in the absolute energy scales in data and in simulation. For instance, as it follows from Fig. 6.20 (bottom left), the mass behavior in data and in simulation differs at $p_T > 6$ GeV/c. The simplest way to correct for it is to consider two simulations with different non-linearity corrections, so that the π^0 meson mass on data lies in the region within the masses in those two simulations. The calculated efficiencies must be compared to each other in order to extract the uncertainty.
- Uncertainty of the cluster unfolding procedure. Indeed, the algorithm works differently in data in comparison with simulations. It is accounted for by changing the

unfolding parameters in a simulation and recalculating the efficiencies. As expected, this uncertainty is the second principal uncertainty, but solely for the π^0 efficiency and at transverse momenta starting from 6 GeV/c, since only in this case the cluster unfolding is applied.

- Uncertainty due to the difference in the ALICE medium in reality and in simulation. In fact, this is an uncertainty of material budget in front of the EMCAL which is related to photon loss due to photon conversions into e^+e^- pairs. This uncertainty is a major EMCAL issue and is considered separately in Section 6.8.2.

3. Finally, as was discussed in Sections 6.6 and 6.7, there is a difference between the reconstructed transverse momentum p_T^{rec} and the genuine particle momentum p_T^{true}. This leads to an *uncertainty of the absolute energy scale* of the EMCAL detector : the calculated difference between p_T^{true} and p_T^{rec} must be taken into account by correcting the production spectra, which are derived as functions of the reconstructed transverse momentum. This uncertainty is the third principal uncertainty of our measurement.

6.8.2 Material budget in front of the EMCAL

The uncertainty of material budget in front of the EMCAL can be estimated in the following way.

The material budget leads to a photon loss due to photon conversion into e^+e^- pairs which are then separated from each other by the ALICE magnetic field. At the same time, if the magnetic field is absent, the conversion leptons would not be separated that much and may hit the EMCAL surface close to each other, still producing only one cluster. As a consequence, the reconstruction efficiency in the absence of the magnetic field should be greater than that under normal ALICE operation conditions. Consequently, the comparison of the π^0 meson production spectra obtained in the ALICE magnetic field on/off cases allows one to estimate the difference in the material budget in data and in Monte Carlo simulation and then estimate the uncertainty under consideration. Needless to say that the ultimate π^0 meson production spectrum does not depend on experimental conditions.

Now, if Monte Carlo simulations are capable to reproduce data correctly, then the ratios of raw π^0 yields (*normalized to one event*) in simulations with the magnetic field on and off would coincide with the very same ratios, but on the data. [9] We calculated those ratios using a dedicated ALICE datasample, where the magnetic field was absent, as well as using a π^0 simulation without the magnetic field. The result is shown on Fig. 6.28 (left). As one can see, the ratios for data/simulation do not coincide. Thereby, this is a direct indication that simulation conditions considerably differ from those in data.

---

[9] Indeed, as it follows from Eq. (6.7.1),

$$\left.\frac{\Delta N^{\text{rec}}_{\text{Bon}}}{\Delta N^{\text{rec}}_{\text{Boff}}}\right|_{\text{data}} = \frac{\varepsilon_{\text{Bon}}}{\varepsilon_{\text{Boff}}} \equiv \left.\frac{\Delta N^{\text{rec}}_{\text{Bon}}}{\Delta N^{\text{rec}}_{\text{Boff}}}\right|_{\text{simulation}} \tag{6.8.2}$$

(Bon and Boff subscripts correspond to the ALICE magnetic field on and off, respectively) since the π^0 production N^{prod} is the same in all cases, while the efficiencies in simulation are expected to coincide with the efficiencies in reality.

Further analysis shows that this difference turns out to be due to a difference in data/simulation material budgets in front of the EMCAL. In particular, smaller material budget in simulations leads to less photon conversions and to an overestimated efficiency in a π^0 simulation with the ALICE magnetic field.

The material budget problem of the EMCAL can be (temporary) circumvented. To this end, let us assume that there is no difference in photon loss between data and simulation in the absence of the ALICE magnetic field, i.e. *simulations without the ALICE magnetic field correctly reproduce reality without the magnetic field.* This assumption can be argued in the following way.

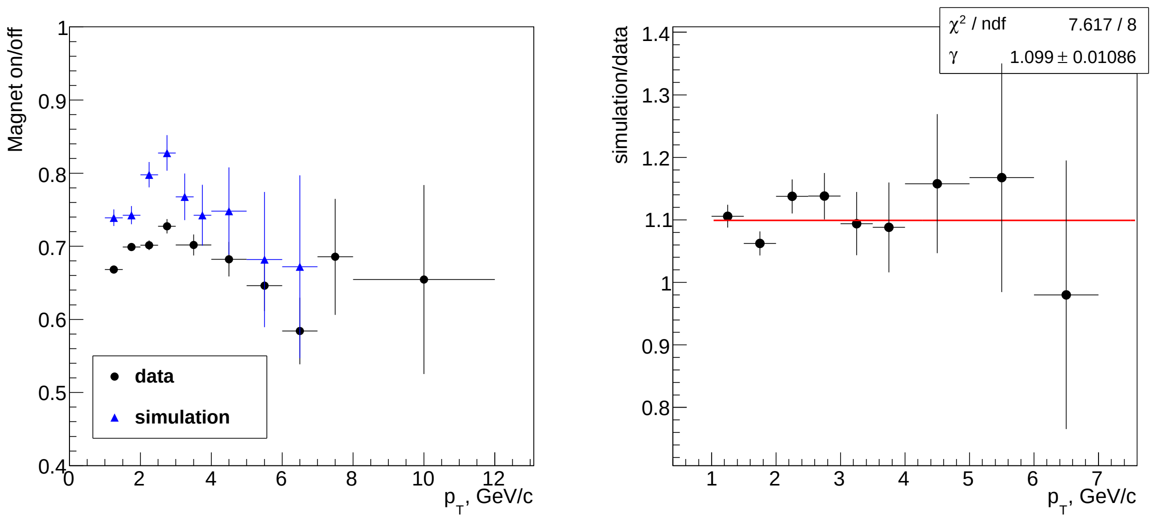

FIGURE 6.28 – Left : ratios of π^0 raw yields with the ALICE magnetic field on and off. Right : the γ-factor (ratio of ratios).

Consider a situation without the magnetic field. If a photon converts not too far from the EMCAL surface, the e^+e^- pair would be detected as one cluster, thus not leading to the photon loss. The maximum distance at which the loss shows up can be deduced from a simulation, where a thick (of order of one radiation wavelength) iron plate is placed at various distances from the EMCAL. As it was verified [39], the photon loss starts inside the ALICE inner tracking system (thanks to a big physical size of the EMCAL channel), i.e. within the TPC. It turns out, however, that photon conversions inside the ALICE inner tracking system are described correctly both in data and in simulation, since the material budget inside the TPC is very well studied and is known with a good precision.

In this way, using the above assumption and Eq. (6.7.1), one has :

$$N^{\mathrm{prod}}_{\mathrm{event}} = \frac{\Delta N^{\mathrm{rec}}_{\mathrm{Bon}}}{\varepsilon^{\mathrm{correct}}_{\mathrm{Bon}}} = \gamma \times \frac{\Delta N^{\mathrm{rec}}_{\mathrm{Bon}}}{\varepsilon^{\mathrm{invalid}}_{\mathrm{Bon}}} \equiv \frac{\Delta N^{\mathrm{rec}}_{\mathrm{Boff}}}{\varepsilon^{\mathrm{correct}}_{\mathrm{Boff}}}, \tag{6.8.3}$$

where the definitions are clear from their indices, while all the raw yields as well as the π^0 production spectrum $N^{\mathrm{prod}}_{\mathrm{event}}$ were normalized to one event. A factor γ was introduced in order to compensate the incorrect reconstruction efficiency $\varepsilon_{\text{Bon}}^{\text{invalid}}$. In principle, it depends on p_T. It can be easily found from the above equation :

$$\gamma = \frac{\Delta N_{\text{Boff}}^{\text{rec}}}{\varepsilon_{\text{Boff}}^{\text{correct}}} \times \left(\frac{\Delta N_{\text{Bon}}^{\text{rec}}}{\varepsilon_{\text{Bon}}^{\text{invalid}}} \right)^{-1} = \left. \frac{\Delta N_{\text{on}}^{\text{rec}}}{\Delta N_{\text{off}}^{\text{rec}}} \right|_{\text{simulation}} \times \left(\left. \frac{\Delta N_{\text{on}}^{\text{rec}}}{\Delta N_{\text{off}}^{\text{rec}}} \right|_{\text{data}} \right)^{-1} . \tag{6.8.4}$$

Thus, the γ-factor is just a point-by-point ratio [simulation]/[data] of blue/black points shown on Fig. 6.28 (left).

The γ-factor as a function of transverse momentum is shown on Fig. 6.28 (right). At this point, we assume that it does not depend on the transverse momentum, which is consistent with the right plot within statistical errors. Of course, this assumption can also be verified in a simulation. In any case, the p_T-dependence of the γ-factor is expected only at low transverse momenta.

On Fig. 6.28 (right), the red line shows a fit of all the points with a constant. The constant factor appears to be $\gamma = 1.1 \pm 0.01$. This means that, in order to obtain the final π^0 and η production spectra, one has to correct them with this factor, which was already done on Figs. 6.25 and 6.26. In addition, the systematic uncertainty of $0.01/1.1 \approx 1\%$ must be attributed to the production spectra.

Finally, let us emphasize that the proposed method, which is expressed by Eq. (6.8.4), has an additional strong advantage : as the ratio in Eq. (6.8.4) is constructed from the ratios obtained separately for data and for simulations, the calculated γ-factor is free of many uncertainties inherent to the difference between data and simulation.

6.8.3 η to π^0 ratio

The ratio of the η and the π^0 production spectra is the first measurement which is feasible to do with the EMCAL calorimeter. There is a good reason for that : in the ratio, many of systematic uncertainties of the production spectra totally cancel or partially cancel. These uncertainties are :

1. Uncertainties which affect absolute energy scale in simulation : energy non-linearity, residual miscalibration and cell smearing.

   In data, however, due to finite p_T bin width, the change of p_T resolution would also affect the extracted raw yields. Still, if η and π^0 "signals" (invariant mass slices with background subtracted) have similar shapes, the yields are also affected equally and thus cancel in the η/π^0 ratio. The approximate proportionality of the π^0 and η signals is supported *a posteriori*, since the η/π^0 ratio is approximately constant, at least for $p_T > 3$ GeV/c (see Fig. 6.29).
2. Uncertainty due to material budget, which was thoroughly discussed in Section 6.8.2, is mainly determined by the probability of one of the two photons to convert. [10] Since

---

[10] There is also a possibility of simultaneous conversion of both photons and the possibility of photon recovery, if the resulting electron/positron carries almost all energy of an initial photon, but this effect is a second order correction.

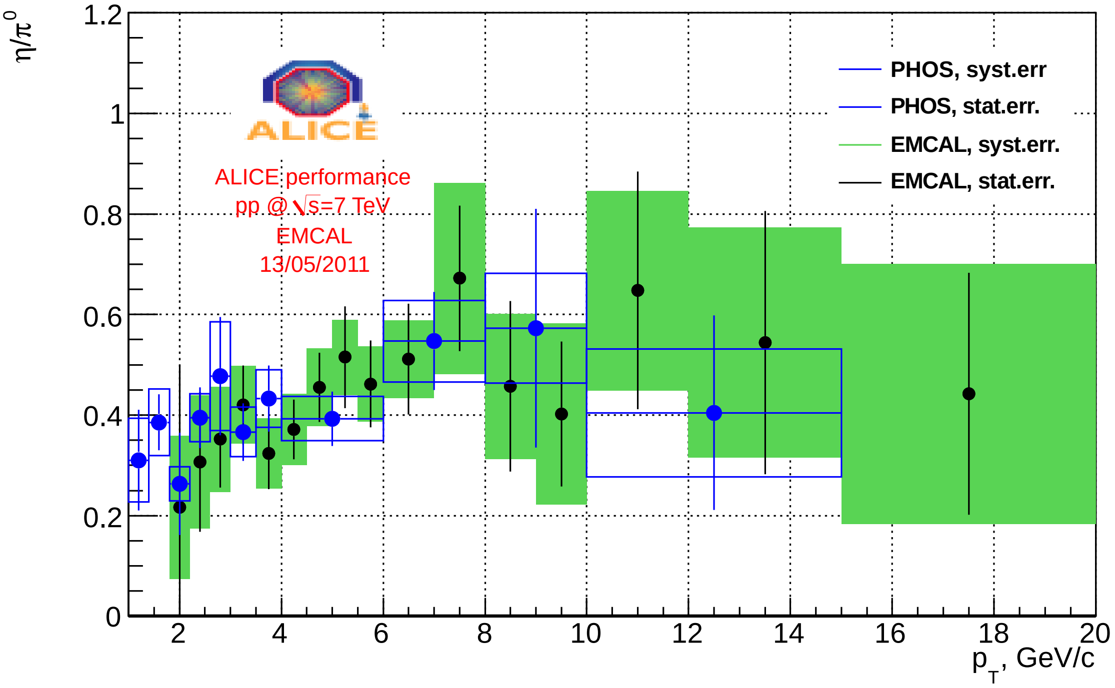

FIGURE 6.29 – First measurement of the η/π^0 ratio with the EMCAL detector, obtained in this thesis.

this probability at the same p_T value is the same for the π^0 photons as well as for the η photons, the effect of conversion cancels in the ratio.

3. Uncertainty due to finite knowledge of position of the EMCAL in the ALICE machine is the same for both mesons.
4. Off-vertex production and its uncertainty is also the same for both mesons.

On Fig. 6.29, the final result of these studies for the η/π^0 ratio as a function of p_T is shown. It incorporates all relevant statistical and systematic uncertainties. The ratio is found around 0.4 and is approximately constant, starting from $p_T > 3$ GeV/c, which is in accordance with the result previously obtained by the PHENIX experiment.

6.8.4 Comparison with pQCD and world experimental data

The π^0 and η production spectra can be compared with the Next-to-Leading Order (NLO) pQCD calculations using different set of parameters.

In the NLO calculations, the factorization, renormalization and fragmentation scales are chosen to have the same value given by the parameter μ. As it was shown in Ref. [40], the NLO calculations at $\mu = 1p_T$ describe the measured π^0 data well, whereas at $\sqrt{s} = 7$ TeV the higher scale $\mu = 2p_T$ and a different set of fragmentation functions is required for a description of the low energy data. In any case, at $\sqrt{s} = 7$ TeV, the NLO pQCD calculations show harder slope compared to the experimental data. Moreover, different fragmentation functions (FFs) and different parton distribution functions (PDFs) give similar results : pQCD predicts harder slopes, and variation of PDFs and FFs does not change the shape, resulting mainly in the variation of the absolute cross section.

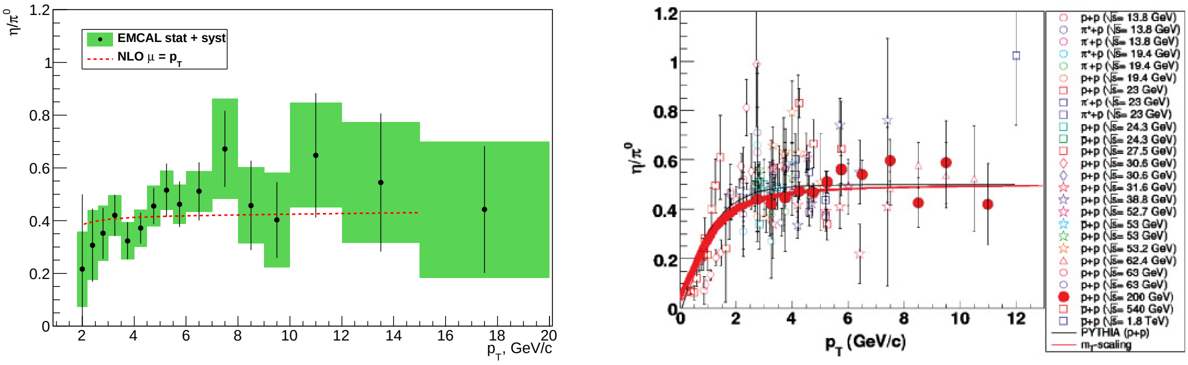

FIGURE 6.30 – Left : η/π^0 ratio measured with the ALICE EMCAL in *pp* collisions at $\sqrt{s} = 7$ TeV compared to the NLO pQCD calculations. Right : η/π^0 ratio measured in hadron-hadron collisions at different center-of-mass energies. The plot is taken from [41]. The black line is the prediction of PYTHIA in *pp* collisions at $\sqrt{s} = 200$ GeV. The red shaded area indicates the empirical m_T-scaling prescription.

A similar trend is observed for the η meson, although the discrepancy is less significant due to larger error bars and smaller transverse momentum reach.

However, the ratio η/π^0, as discussed earlier, has the advantage of simplified systematic uncertainties. This is also the case for the NLO pQCD calculation, where, in particular, the influence of the PDF is reduced. As shown on Fig. 6.30 (left), the calculations of NLO pQCD are consistent with the experimental data measured with the ALICE EMCAL detector at $\sqrt{s} = 7$ TeV.

The world experimental data of the ratio in hadron–hadron collisions show a rapid increase with p_T and flattening out above $p_T = 3$ GeV/c at values of about 0.40–0.50, see Fig. 6.30 (right). No difference is observed for different colliding systems and for different center of mass energies. The world experimental data were compared to the two phenomenological curves with PYTHIA 6.131 [42] based on the Lund fragmentation model [43, 44] and an empirical m_T-scaling prescription which gives an asymptotic value of the ratio. More details on the formalisms as well as on world experimental data can be found in Ref. [41].

6.9 Appendix 1 : list of runs

Run index	Run number	Events	Run index	Run number	Events	Run index	Run number	Events
0	115393	1109490	34	119853	686269	68	125847	671618
1	115401	841735	35	119856	1255907	69	125848	732600
2	116102	182058	36	119859	344534	70	125849	1704082
3	116288	602596	37	119862	4161618	71	125851	1383740
4	116402	114934	38	119904	257125	72	125855	2753948
5	116403	111666	39	119907	1100050	73	126004	620222
6	116562	436557	40	119909	858347	74	126008	1038700
7	116571	227687	41	119913	473455	75	126073	2138555
8	116574	595401	42	119917	910240	76	126078	4861416
9	116643	171379	43	119935	734107	77	126081	1524801
10	116645	162000	44	119952	508004	78	126082	5391692
11	117048	971924	45	119959	1359984	79	126088	6412605
12	117050	721982	46	119961	4675194	80	126090	7060546
13	117052	514696	47	119965	5912828	81	126097	1512212
14	117053	884503	48	119969	3832505	82	126168	1848651
15	117054	2222414	49	119971	1936407	83	126283	1140142
16	117059	731254	50	120067	2069201	84	126284	6694468
17	117063	758542	51	120069	1693417	85	126285	282347
18	117065	1099453	52	120072	2845729	86	126351	4324513
19	117077	192882	53	120073	2310166	87	126352	1914128
20	117099	2349898	54	120076	2191048	88	126359	1169135
21	117109	1341298	55	120079	1047918	89	126403	444884
22	117112	2663785	56	120244	1656335	90	126404	2658102
23	117116	2121563	57	120503	1261751	91	126405	120782
24	117220	1440465	58	120504	2957886	92	126406	3822861
25	117222	975667	59	120505	4099031	93	126407	5123984
26	119159	1479498	60	120616	5618540	94	126408	2174376
27	119161	3008017	61	120617	1403371	95	126409	1626075
28	119163	1724466	62	120671	711050	96	126422	4103591
29	119841	352307	63	120741	121300	97	126424	6484988
30	119842	1982518	64	125630	2042969	98	126425	927517
31	119844	298351	65	125842	2127947	99	126432	7777500
32	119845	1397683	66	125843	417100			
33	119846	2616286	67	125844	176595			

Table 6.2 – List of runs used in the analysis, LHC10bcde datasample, 190607664 events in total.

6.10 Appendix 2 : reconstructed π^0 meson slices

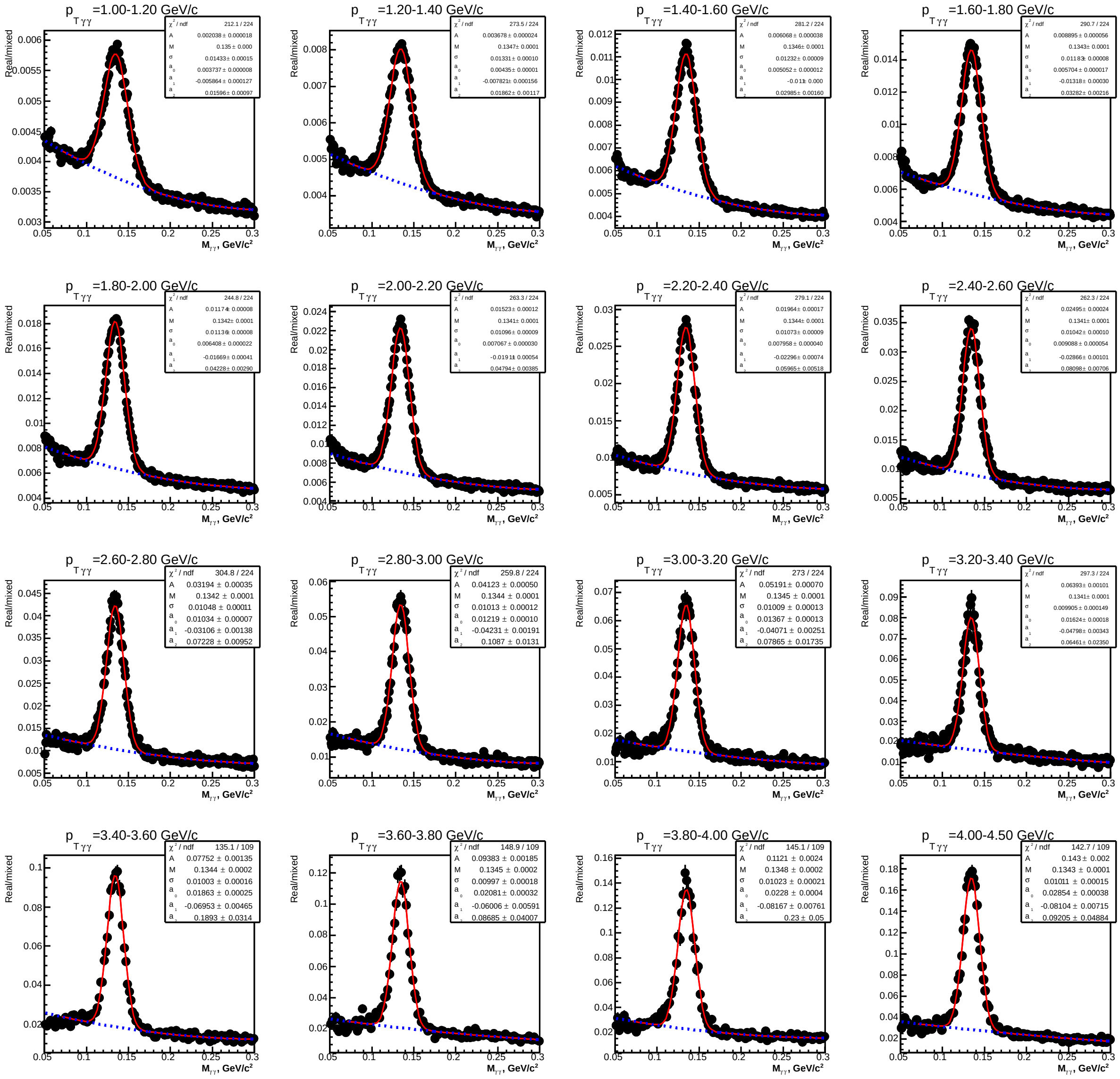

FIGURE 6.31 – π^0 meson real/mixed ratios, part I. Fits are made with a Gaussian function plus a polynomial of the second order.

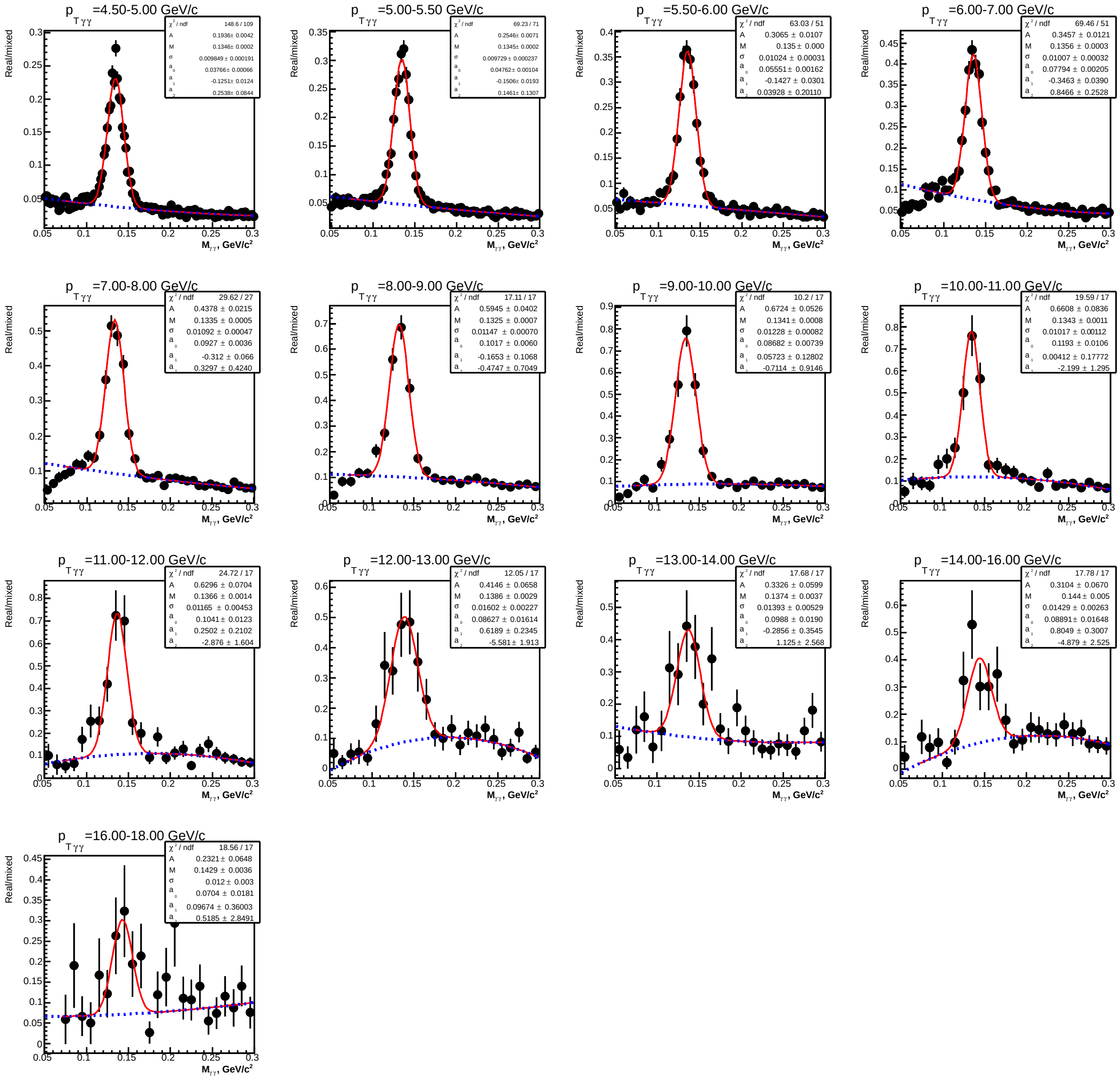

FIGURE 6.32 – π^0 meson real/mixed ratios, part II. Fits are made with a Gaussian function plus a polynomial of the second order.

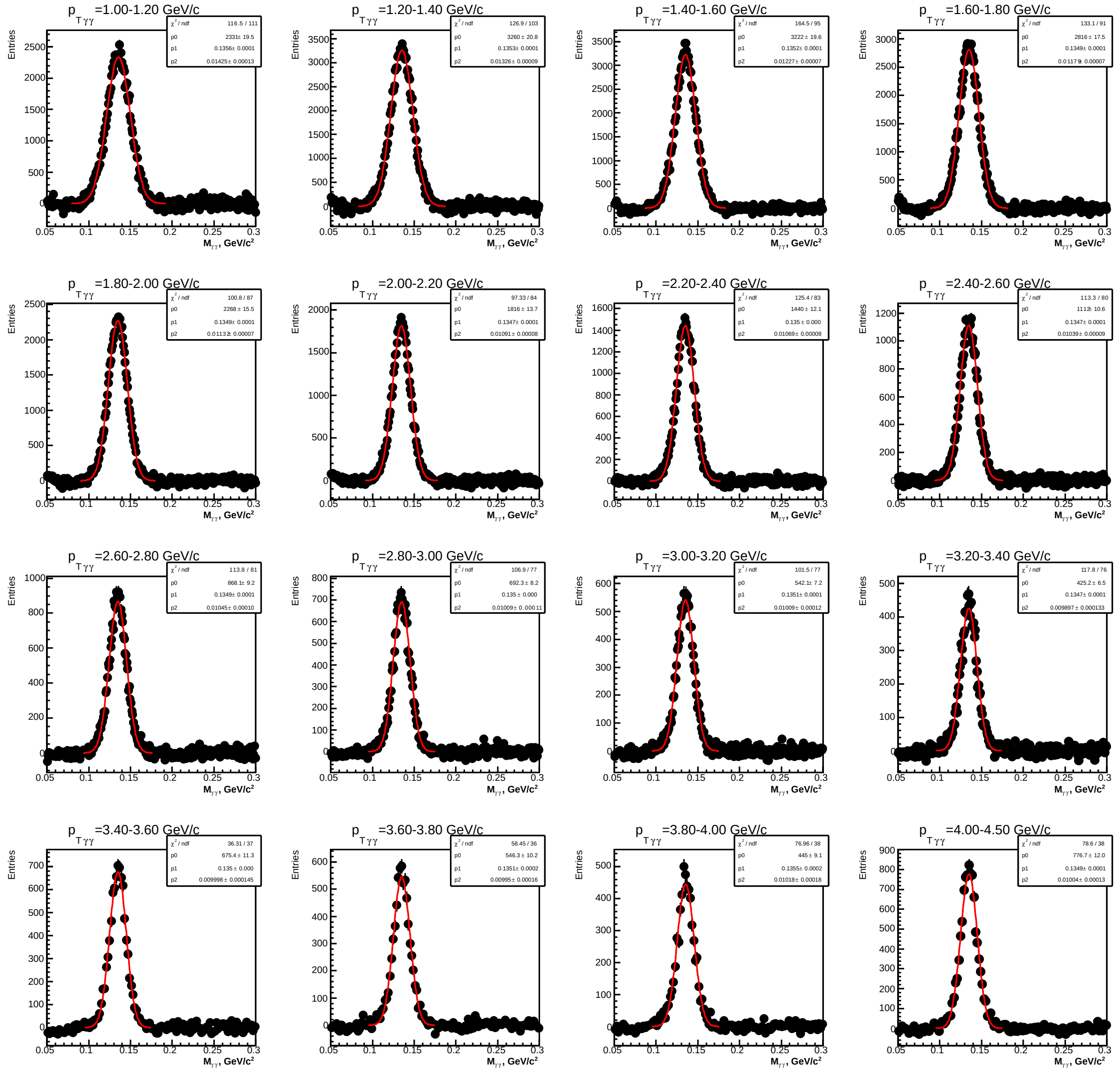

FIGURE 6.33 – Extracted π^0 meson signals, part I. Fits are made with a Gaussian function.

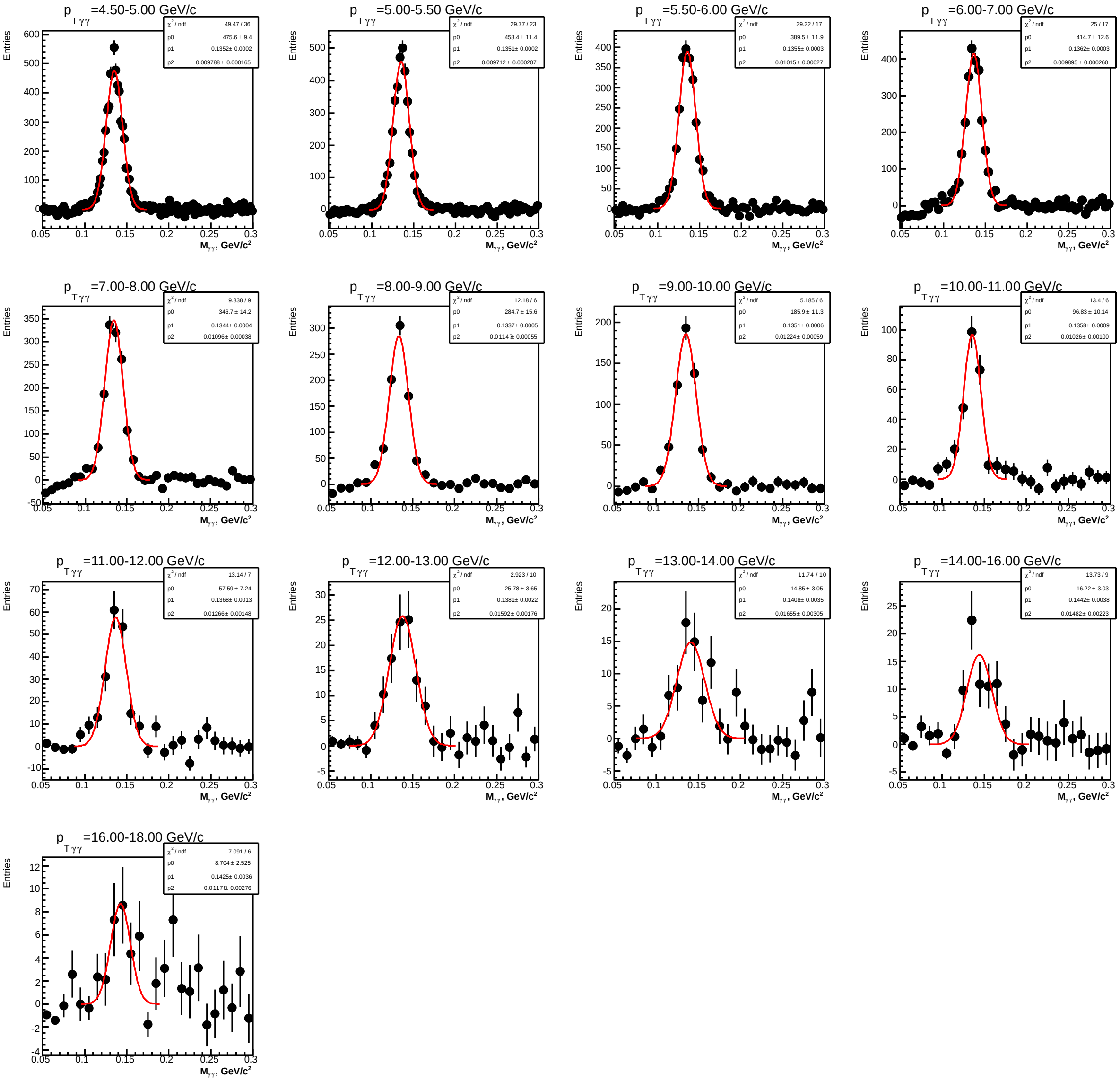

FIGURE 6.34 – Extracted π^0 meson signals, part II. Fits are made with a Gaussian function.

6.11 Appendix 3 : reconstructed η meson slices

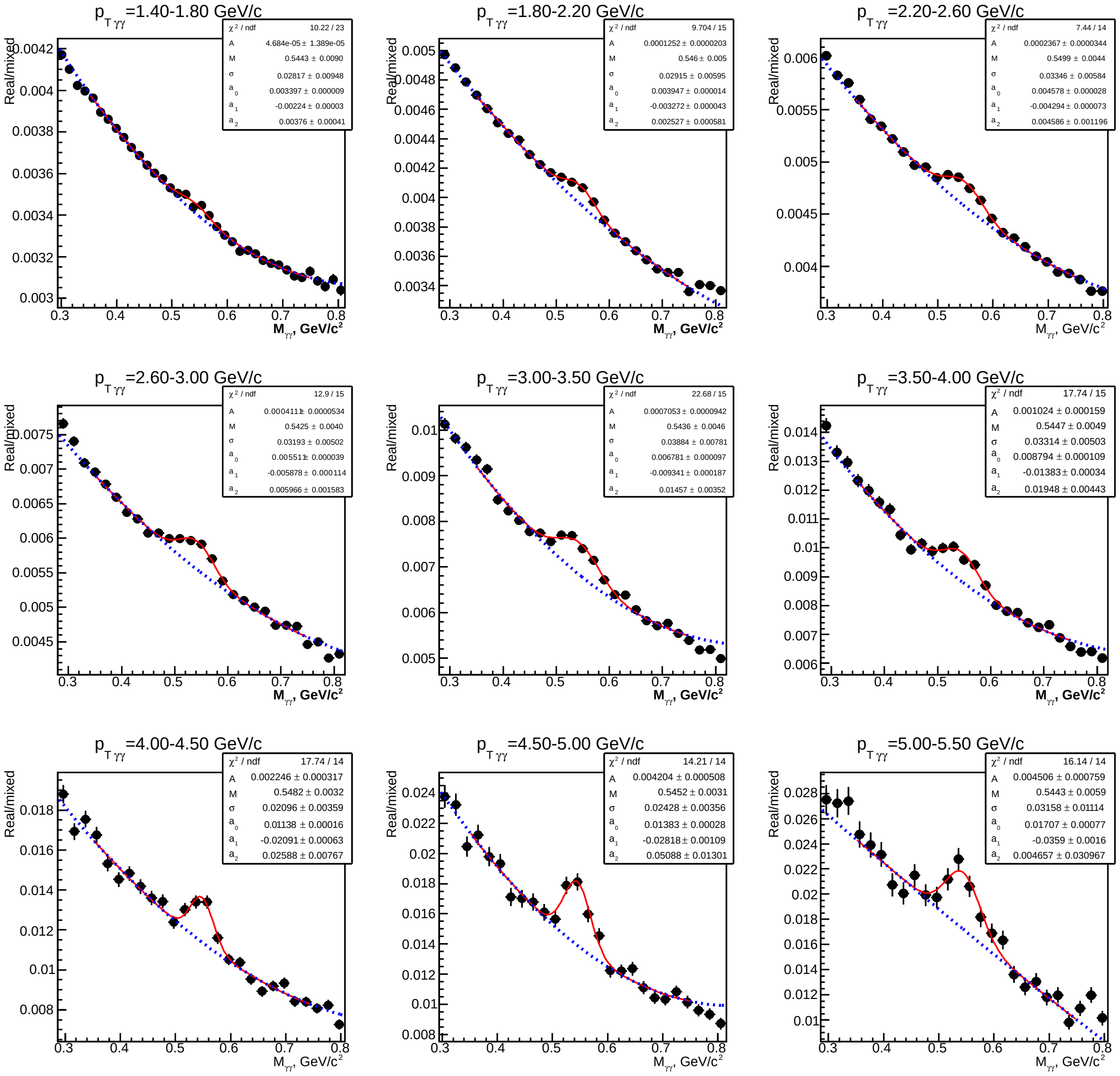

FIGURE 6.35 – η meson real/mixed ratios, part I. Fits are made with a Gaussian function plus a polynomial of the second order.

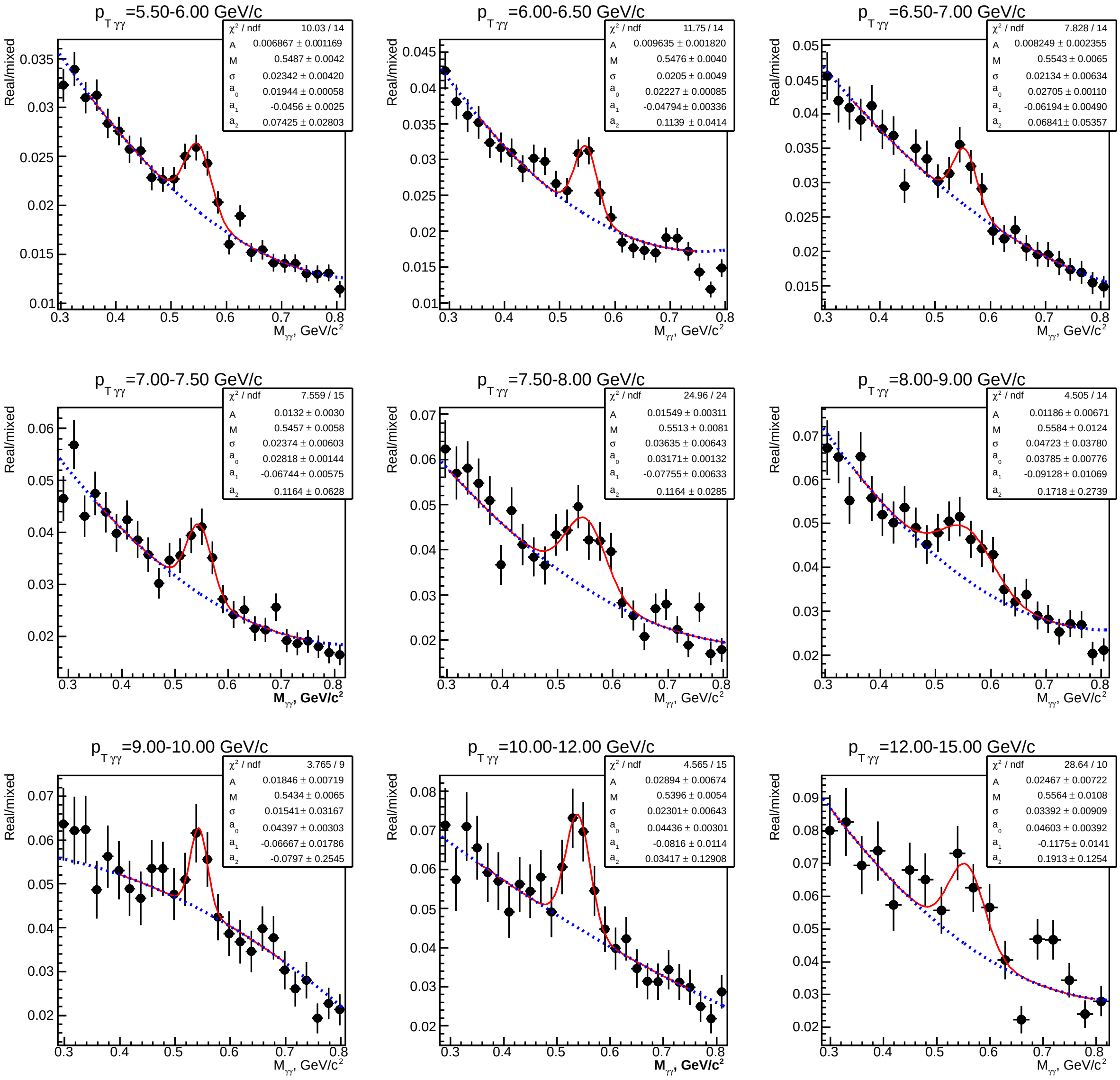

FIGURE 6.36 – η meson real/mixed ratios, part II. Fits are made with a Gaussian function plus a polynomial of the second order.

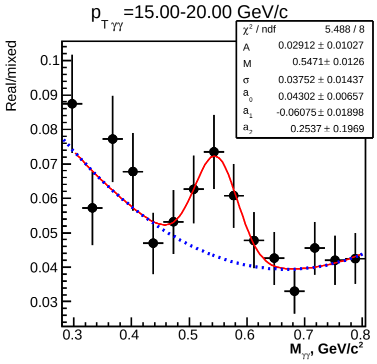

FIGURE 6.37 – η meson real/mixed ratios, part III. Fits are made with a Gaussian function plus a polynomial of the second order.

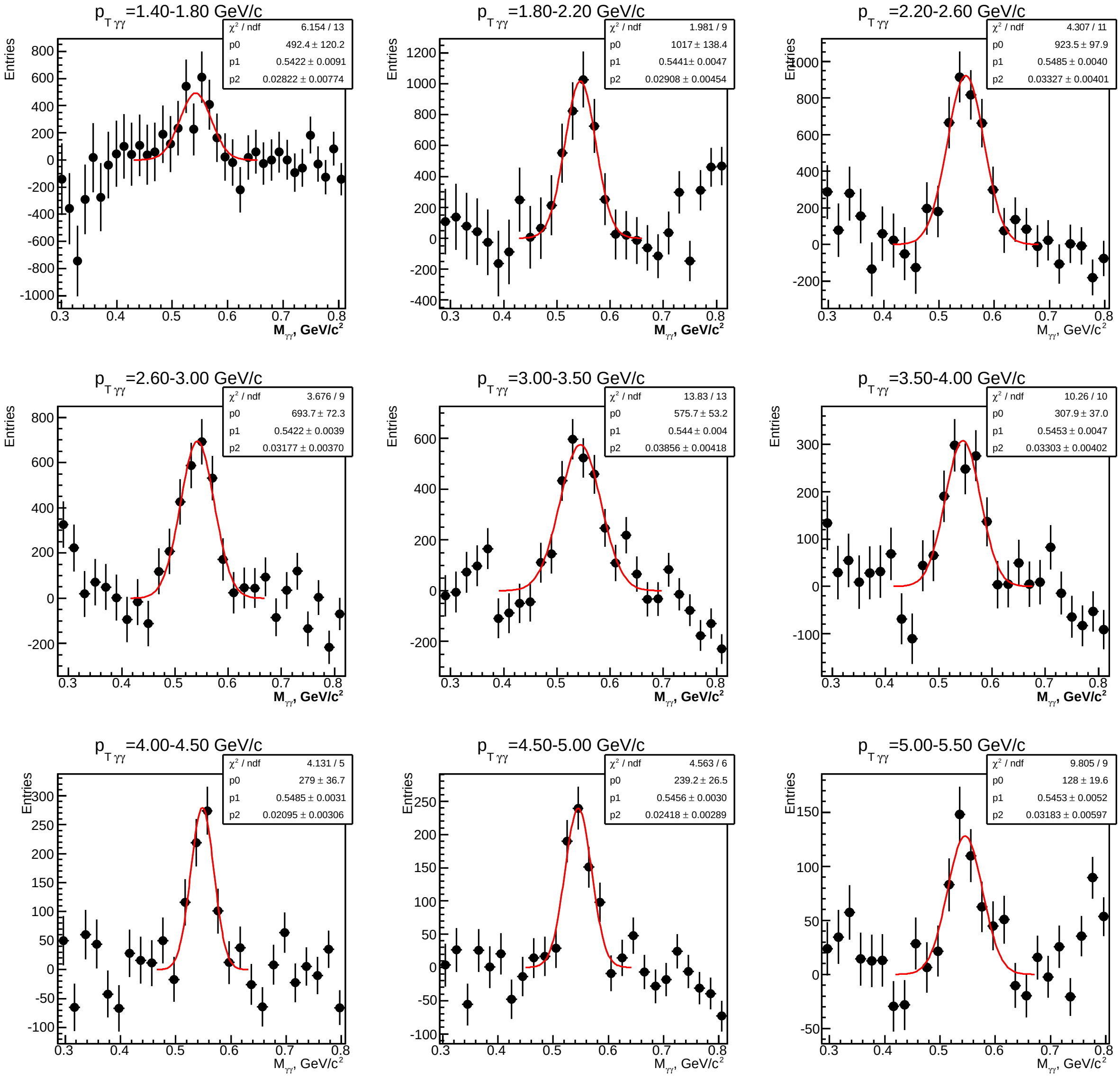

FIGURE 6.38 – Extracted η meson signals, part I. Fits are made with a Gaussian function.

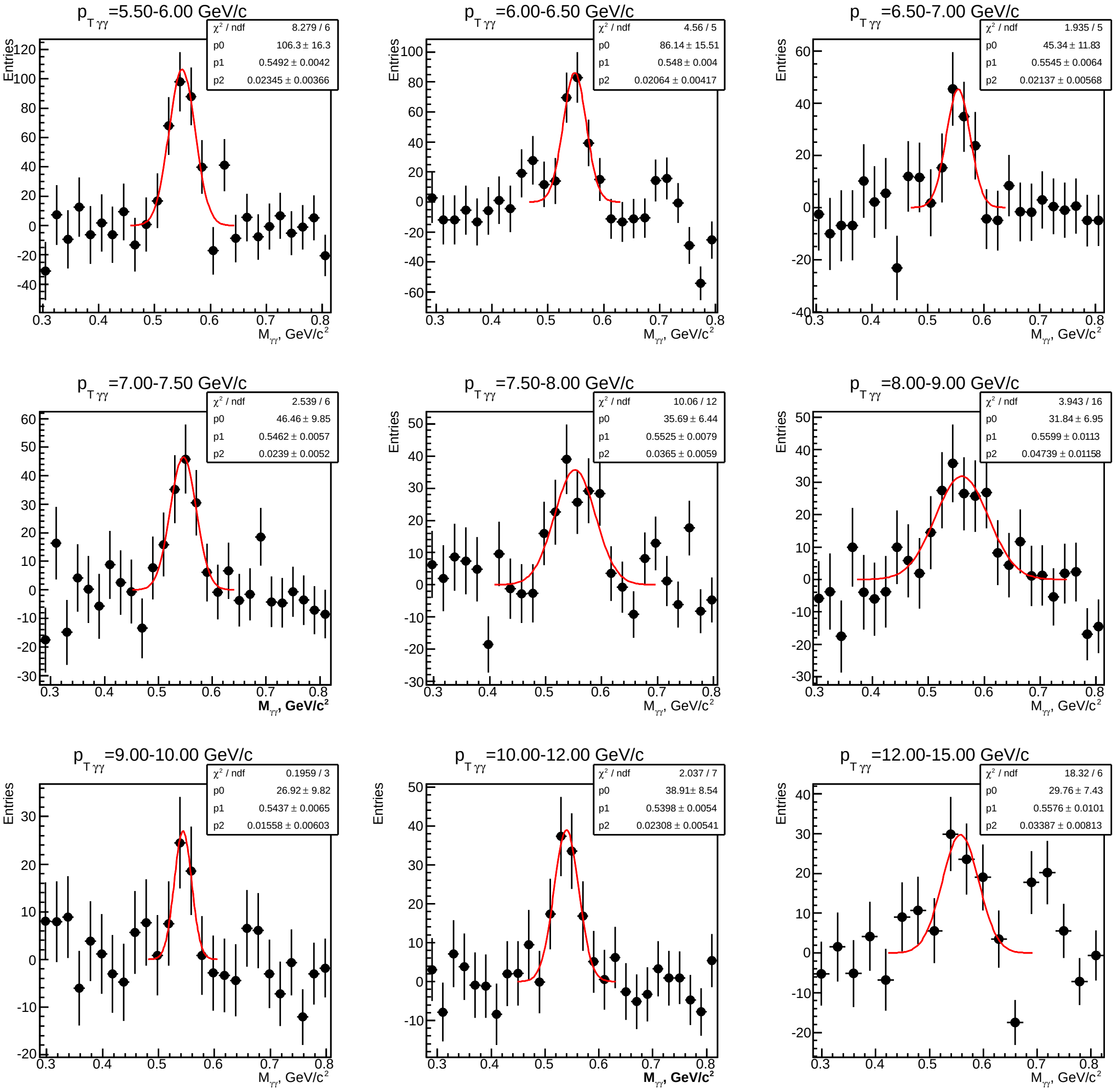

FIGURE 6.39 – Extracted η meson signals, part II. Fits are made with a Gaussian function.

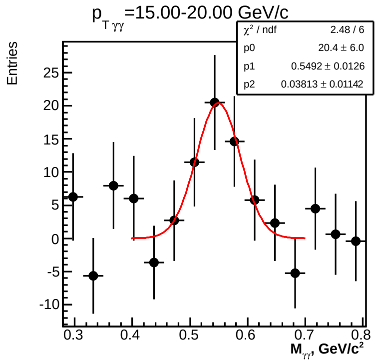

FIGURE 6.40 – Extracted η meson signals, part III. Fits are made with a Gaussian function.

Chapitre 7

Soft hadron spectra in zero momentum limit

We perform systematic studies of the zero momentum limit of identified hadron spectra ($\pi^{\pm}$, $K^{\pm}$, (anti)protons) taken from several hadron and lepton experiments at the collision energies from tenth of GeV up to the TeV scale of the LHC. To test the color coherence predictions, we fit the spectra with different functions and extrapolate the fits to zero momentum. At the end of this chapter, we discuss the obtained results.

7.1 Soft particle production and theoretical predictions

In the present chapter, we focus on verification of the universality of inclusive hadron production spectra at low momentum. Namely, we test the following theoretical predictions as discussed earlier :

1. The limit
$$I_0 = \lim_{p\to 0} E\frac{d^3N}{dp^3} \tag{7.1.1}$$
is independent of the collision energy $\sqrt{s}$.
2. The ratio of pp and e^+e^- limits is
$$\frac{I_0^{pp}}{I_0^{ee}} = \frac{C_A}{C_F} = \frac{9}{4}. \tag{7.1.2}$$

We try to give some systematics to our analysis for some of the available experimental data for identified hadron spectra ($\pi^\pm$, $K^\pm$, $p\bar{p}$). This phenomenology will be discussed in Section 7.3. The main difficulty will be to perform fits of the spectra and extrapolate them to zero momentum point. This question is addressed in Section 7.2. The extrapolation can be made using *different fitting functions*. Still, we will compare the results for different experiments obtained with for *one and the same fitting function*.

Fig. 7.1 shows charged pion invariant density, Ed^3N/dp^3 as a function of the particle momenta p, at different collision energies ranging from DORIS energy at $\sqrt{s} = 10$ GeV to LEP energy at $\sqrt{s} = 91$ GeV. We want to see the tendency of converging of all the spectra in the limit $p \to 0$. First, the multiplication by E helps to limit the range of variation to one order in magnitude. Second, the linear scale on the left plot helps

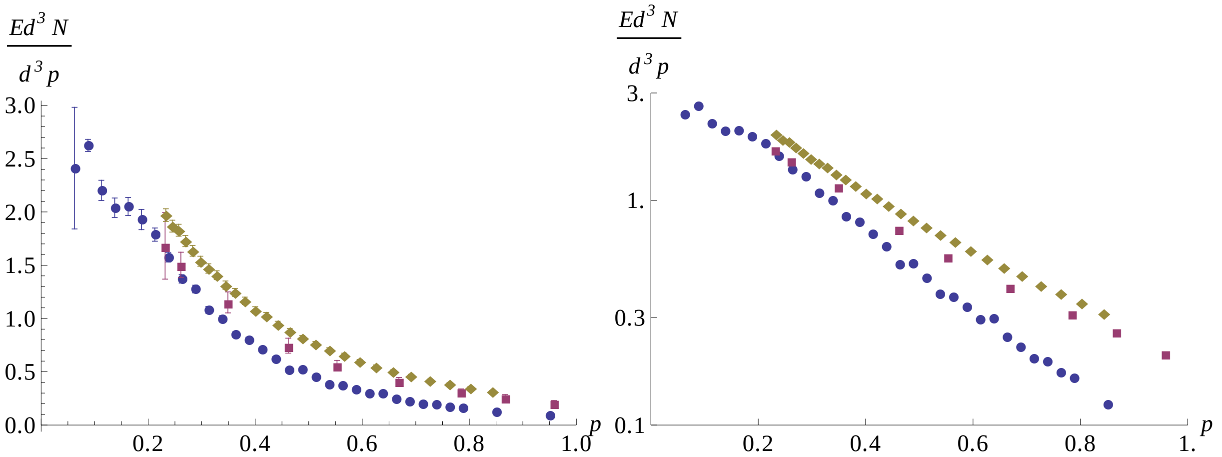

FIGURE 7.1 – Inclusive particle density of identified charged pions $\frac{1}{2}(\pi^+ + \pi^-)$ in e^+e^- collisions : linear scale (left) and log scale (right). Data are from ARGUS (10 GeV), TOPAZ (58 GeV) and OPAL (91 GeV), blue, dark red and brown points, respectively.

questioning how the limit is reached (e.g. linearly or quadratically) and to see that it may not be a straightforward task to perform a proper extrapolation to $p = 0$. In the left plot, the joining between LEP and lower energy data is difficult to decide, although a decrease of the ratio between LEP/OPAL (full diamonds) and ARGUS (full circles) can be anticipated, and confirmed when looking at the log scale plot on the right. Also regarding the question of extrapolation to $p = 0$, let us mention that identified spectra may help to better disentangle possible hadron mass effects.

In analogy with e^+e^- process, the same quantity can be investigated for the collisions of two protons. The results for two measurements are displayed on Fig. 7.2. Looking closely at the log-plot, we anticipate that the result depends on the way data will be extrapolated. Drawing a straight line would lead to the conclusion of an increase of the $p_T \to 0$ limit with energy, while if some leveling off is assumed, the energy independence of this limit cannot be excluded.

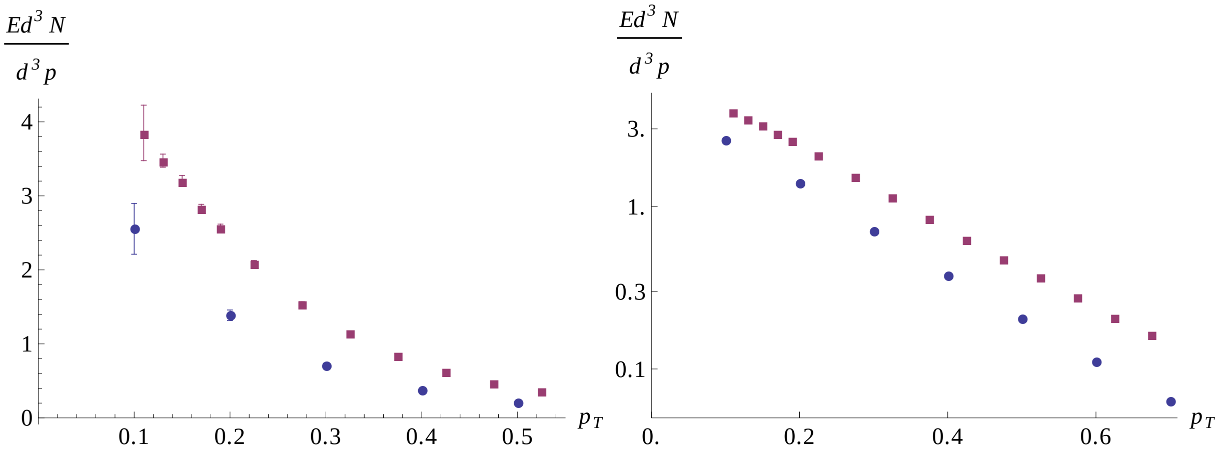

FIGURE 7.2 – Inclusive particle density of identified charged pions $\frac{1}{2}(\pi^+ + \pi^-)$ in *pp* collisions : linear scale (left) and log scale (right). Data are from BS (23 GeV) and ALICE (900 GeV), blue and dark red points, respectively.

Results for the zero-momentum limits of particle densities (7.1.1) in *pp* collisions were derived in [11] and are shown in Fig. 7.3. Examining the plot, we get a general impression of points horizontally lining up with deviations at random around the average value. However, looking at the first three points given by the ISR experiment, we could remark rather a tendency to increase, and only the consideration of all available energies speaks in favor of the independence on collision energy of the zero momentum limit. The rather impressive results displayed in Fig. 7.3, speaking in favor of an explanation of low momentum production driven by color coherence, was the trigger to further investigations, in particular, extending the study to encompass the LHC energies, as carried out in the present chapter.

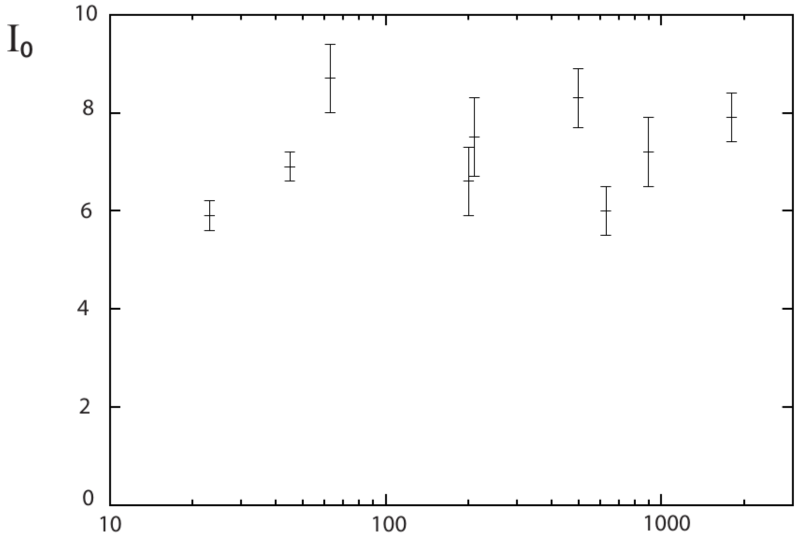

FIGURE 7.3 – Zero momentum limit I_0 of invariant densities of charged particles $[(h^+ + h^-)/2]$ in pp collisions as a function of center-of-mass energy $\sqrt{s}$ [11].

7.2 Extrapolation of the spectra to zero momentum

Let us discuss different ways of fitting and extrapolating experimental data. The goal of the study is to pinpoint the differences between various models (fitting functions) and the best available experimental data and then, in Section 7.3, use some of the relevant fits to extract the quantities of interest.

7.2.1 General strategy

The basic observable is $E\frac{d^3N}{dp^3}$ which is measured in case of e^+e^- as a function of total particle momentum p and in the case of pp collisions as a function of transverse particle momentum p_T and rapidity y, at $y = 0$. Thus, depending on the case, we will either need a fitting function $f(p)$ or $f(p_T, y = 0)$, simply denoted as $f(p_T)$.

However, the invariant particle density $E\frac{d^3N}{dp^3}$ is not the value which was measured directly in the experiment. Usually the measured quantity is either the production spectrum $\frac{dN}{dp}$ or the differential cross section $\frac{d\sigma}{dp}$, which can be transformed into the production spectrum by dividing by the inelastic cross section. To avoid the difficulty of recalculating errors, we fit directly the quantity which was measured experimentally and then perform the necessary mathematical operations to obtain the desired form $E\frac{d^3N}{dp^3}$.

The fitting procedure of the spectra may be performed with different functions. Moreover, in practice, different experiments used different fitting functions for their data. For instance, the invariant particle density for ISR data at $y = 0$ were fitted with

$$E\frac{d^3\sigma}{dp^3} = A\,e^{-\frac{p_T}{T}+Bp_T^2} \tag{7.2.1}$$

(with parameters A, B and T), while PHENIX and ALICE collaborations used the parametrization (again of their data at $y = 0$)

$$E\frac{d^3\sigma}{dp^3} = \frac{A}{\left(1 + \frac{m_T}{nT}\right)^n}, \qquad m_T = \sqrt{m^2 + p_T^2} \tag{7.2.2}$$

(with parameters A, T and n), where m is the mass of particle under consideration. In particular, the extrapolation to the zero momentum point in Ref. [11] was based on different fits from different experiments.

In the present study, we stick to the following strategy. We fit the spectrum of each experiment with one and the same function, extrapolate it to the zero momentum point and extract values for I_0. Such a uniform treatment of the spectra is natural for our studies as we want to test the dependences of some characteristics of hadron spectra with respect to the collision energy.

7.2.2 Considered fitting functions

Several universal parameterizations of the spectra suit for our task.

It was observed in the 1950s that secondary soft particles in cosmic rays have limited transverse momentum ~ 0.5 GeV (over the huge range of primary cosmic particle energies, which can reach $\sim 10^{11}$ GeV) independent of the primary collision energy [45, 46]. Cocconi, Koester and Perkins [47] then proposed the empirical formula for the transverse momentum spectrum of meson production :

$$\frac{d\sigma}{d(p_T^2)} = Ae^{-6p_T}, \tag{7.2.3}$$

where p_T is the transverse momentum in GeV/c. Further analysis [48, 49, 50] led to the interpretation that soft hadron production is “thermal” with a Boltzmann statistical spectrum (7.2.3) and $T = 1/6 = 0.167$ GeV/c representing the “temperature” at which soft hadrons are produced. In thermal scenarios (see e.g. [51, 52]) of pp collisions, it is more natural to represent the invariant cross-section as a function of rapidity y and transverse mass $m_T = \sqrt{m^2 + p_T^2}$, where m is the considered hadron mass.

A natural extension of the thermal model is to change the Boltzmann exponent in Eq. (7.2.3) into Fermi-Dirac or Bose-Einstein expression,

$$e^{-p_T/T} \longrightarrow \frac{1}{e^{p_T/T} \pm 1}. \tag{7.2.4}$$

As was pointed out earlier, hadron production can in general be categorized into two different regimes depending on particle momentum. The first one is that of soft multiparticle production, dominant at low momentum ($p \lesssim 1-2$ GeV) and the second regime is that of hard-scattering particle production, evident at high momentum ($p \gtrsim 2$ GeV), with no strict boundary between the two regimes. Thus, it is well-known that hadron spectra in *pp* collisions can be well fitted in the whole momentum region by a single function which has only three parameters : A, T, n. This is the so-called Tsallis function [53], also referred to as the Levy function [54, 55] :

$$f(p_T) = \frac{A}{\left(1 + \frac{m_T}{nT}\right)^n}, \qquad m_T = \sqrt{m^2 + p_T^2}. \tag{7.2.5}$$

The parameters T and n characterize, respectively, the low- and high-p_T region of the spectra. Constantino Tsallis derived the formula named after him by postulating a generalized form for the entropy of a thermalized system in which long-range correlations are present. By doing so, he introduced, along with the temperature T, a second "non-extensibility" parameter q, which is related to n as

$$n = \frac{1}{q-1}. \tag{7.2.6}$$

When $q \to 1$ ($n \to \infty$), the formula (7.2.5) is reduced to ordinary Boltzmann expression :

$$\lim_{n\to\infty} \frac{1}{\left(1 + \frac{m_T}{nT}\right)^n} = e^{-\frac{m_T}{T}}. \tag{7.2.7}$$

To make contact with functions used in [11], we will also consider a "Tsallis_p" function obtained by setting the mass $m = 0$, i.e. replacing m_T by p_T in $f(p_T)$, or E by p in $f(p)$. The conventional Tsallis form of (7.2.5) will be named just the Tsallis function.

Finally, we will use also the fitting function

$$f(p) = \frac{I_0}{\left(1 + \frac{p^2}{n\, I_1^2}\right)^n} \tag{7.2.8}$$

inspired by the low momentum dependence expected within the MLLA framework. The reason for the choice of this function is as follows. We start from the limiting form (2.2)

$$f(p_T, y) = \frac{A}{p_T^2} \tag{7.2.9}$$

and incorporate the absence of small-p_T radiation in the form of a leveling-off at small p_T,

$$\frac{A}{p_T^2} \longrightarrow \frac{A}{p_T^2 + Q_0^2}. \tag{7.2.10}$$

The power n can be considered as a way to restore the power law behavior at high p_T inspired by the Tsallis function.

To sum-up we give the list of the various fitting functions used with their names in Table 7.1.

TABLE 7.1 – Fitting functions. For Tsallis and Tsallis_p, there is also a limiting form obtained when $n \to \infty$, respectively named Boltzmann and exponential.

Function	$f(p_T)$	$f(p)$
Tsallis_p	$\frac{A}{(1+p_T/(nT))^n}$	$\frac{A}{(1+p/(nT))^n}$
Tsallis	$\frac{A}{(1+m_T/(nT))^n}$	$\frac{A}{(1+E/(nT))^n}$
Coherent	$\frac{I_0}{(1+p_T^2/(nI_1^2))^n}$	$\frac{I_0}{(1+p^2/(nI_1^2))^n}$
ISR	$A\exp\left(-\frac{p_T}{T}+B\,p_T^2\right)$	$A\exp\left(-\frac{p}{T}+B\,p^2\right)$
Bose-Einstein	$\frac{A}{\exp(m_T/T)-1}$	$\frac{A}{\exp(E/T)-1}$

7.2.3 Comparison of fitting functions

To choose the fitting functions which will be exploited for extracting the I_0 value, we compare them on a few data sets and will then apply the selected functions to a collection of available spectra. For this, we selected pion and proton data in e^+e^- and pp collisions. The criteria to select these data samples were to have the most precise data from the point of view of error bars and number of points. This way, we choose OPAL data for e^+e^- collisions with $\sqrt{s} = 91.2$ GeV and ALICE data for pp collisions with $\sqrt{s} = 900$ GeV. To give an idea about the quality of the selected data, we cite some characteristics in Table 7.2.

Table 7.2 – OPAL and ALICE data characteristics. p stands both for protons and antiprotons.

Experiment	process	number of points	stat	syst
OPAL	$e^+e^- \to \pi^\pm + X$	27 points $\leq$ 1 GeV	$< 1\%$	$\sim 3\%$
OPAL	$e^+e^- \to p + X$	27 points 0.4-1.4 GeV	$\sim 5\%$	$\sim 5\%$
ALICE	$pp \to \pi^\pm + X$	21 points $\leq$ 1 GeV	$< 1\%$	$\sim 3\%$
ALICE	$pp \to p + X$	17 points 0.35-1.4 GeV	$\sim 3\%$	$\sim 4\%$

Methodology of fitting of $e^+e^- \to \pi^\pm + X$

To explain various tests we performed in order to decide which functional forms are adequate for the extrapolation, let us start with charged pion production as measured by OPAL, fitted with the Tsallis_p function from Table 7.1. Let us note that here $A = I_0$, which is directly the extrapolated quantity of interest.

Note that OPAL data is given in $\frac{dN}{dp} = \frac{1}{\sigma}\frac{d\sigma}{dp}$ format. Thus, the actual fitting is performed with the function

$$h(p) = \frac{4\pi p^2}{\sqrt{m_\pi^2 + p^2}} f(p). \tag{7.2.11}$$

For the fitting procedure, the method of least squares is used.

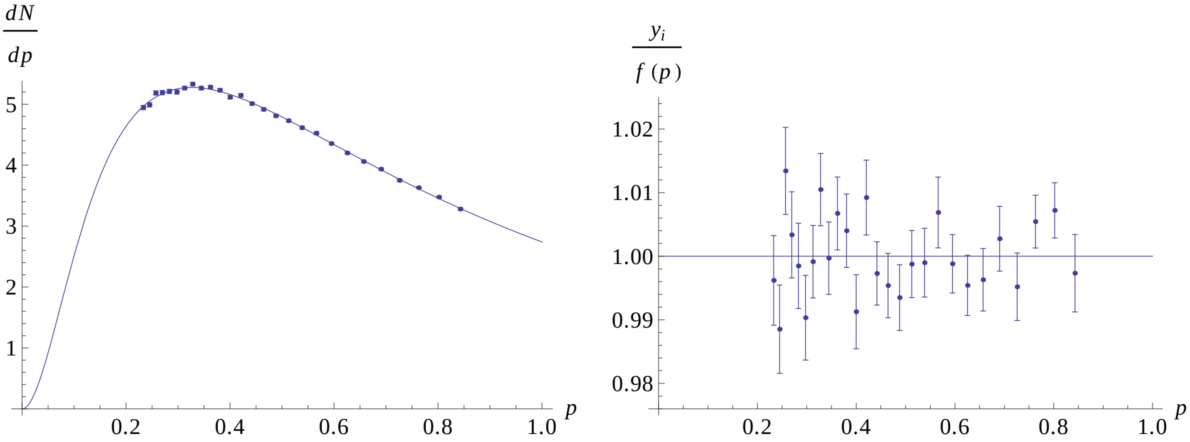

Figure 7.4 – Left : OPAL data with the fit ; right : data/fit ratios.

On Fig. 7.4 (left), the points with their statistical errors are shown together with the fitted function. As one can see, this fitting function provides a good description of the data in this range of momentum. To further investigate the quality of the fit, we form the ratio $y_i/h(p_i)$ which is also shown on Fig. 7.4 (right). The point-to-point fluctuations appear to be comparable with statistical errors, while the systematical errors are three times larger. Thus, in what follows we ignore the systematical errors during the fitting procedure and consider them later when calculating the errors of the fitting parameters.

The extrapolated value for the I_0 quantity for the Tsallis_p function is 5.6±0.1 GeV^{-2}

as given by the fitting routine. The resulting χ^2/ndf value being 1.25, confirms the quality of the fit. This value also shows that OPAL statistical errors practically saturates the point-to-point standard errors, confirming the necessity to put systematic errors aside for the fitting.

Let us also show confidence level intervals for the fitted function, Fig. 7.5. Here and below 95% is chosen for the confidence level. For the quantity dN/dp (left) they are much less visible than for the quantity Ed^3N/dp^3 (right) which is of interest for us. This is a reminder of the inherent difficulty of the extrapolation procedure.

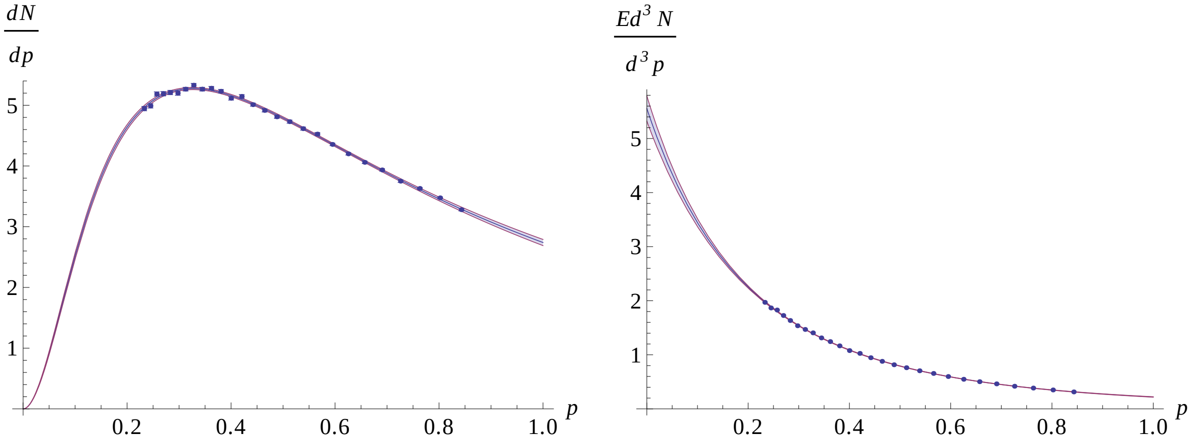

FIGURE 7.5 – OPAL data with confidence-level bands.

Various other fits of $e^+e^- \to \pi^\pm + X$

Let us now show a less satisfying example using the exponential function, i.e. the Tsallis_p function in the particular case when $n \to \infty$. On Fig. 7.6 (left) one can see that the fitting function is completely out compared to points and the general tendency is not well-reproduced. We remark, however, that counting also the systematic errors would improve the situation. Still, the tendency of this fitting function differs from the one of the data.

It turns out that for the OPAL data, the Tsallis function as well as the Bose-Einstein function of Table 7.1 both give a satisfactory description, the former being as good as the Tsallis_p, whereas the latter is slightly off, but with one free parameter less.

Regarding the question of extrapolation, the comparison of the exponential function with the Bose-Einstein function illustrates a lack of data at low momentum. The comparison is shown on Fig. 7.7. The two functions have different behaviors in the vicinity of $p = 0$: the exponential form is linear in p, while the Bose-Einstein function is quadratic in p. However we see that the fitted function that does not change its concavity at low p has a limit at $p = 0$ that turns out to be smaller than that of the function whose curvature sign changes. This somewhat paradoxical feature is due to the fact that there is no data at small enough p in the region where the existence of a change of concavity could be felt, if not observed. If the momentum scale for this change is in some way connected to the hadron mass, we may expect some indications with produced protons instead of pions.

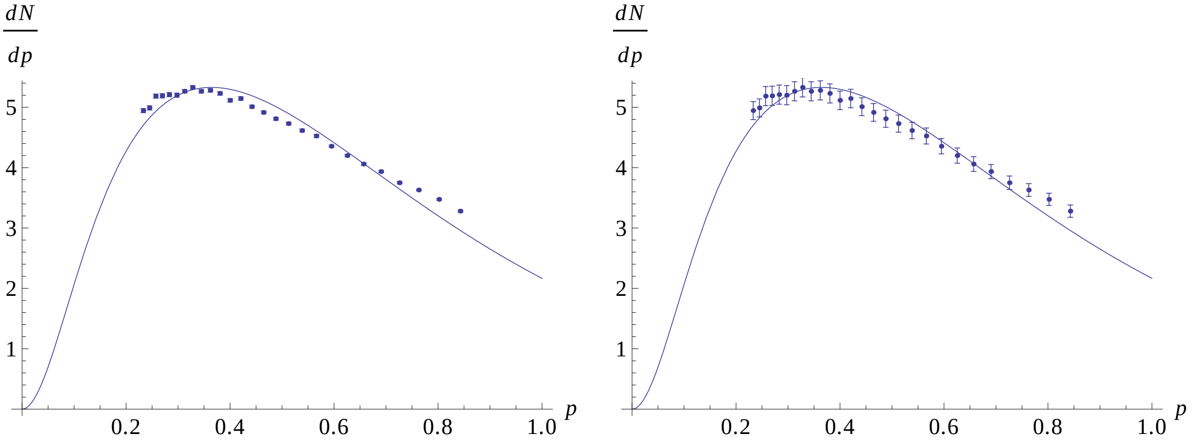

FIGURE 7.6 – OPAL data without (left) and with systematical errors (right) fitted by the Boltzmann function.

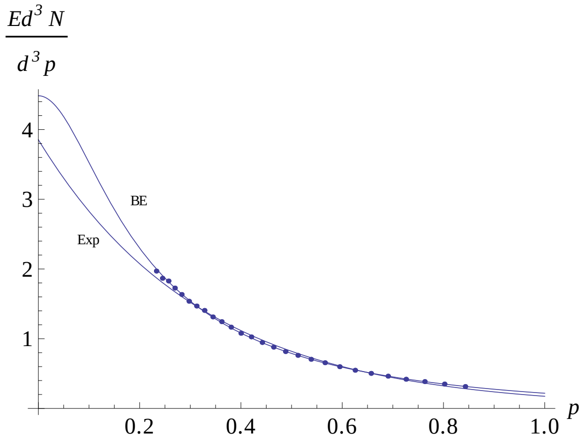

FIGURE 7.7 – Comparison of two fitting functions and their extrapolations to $p = 0$: exponential form and Bose-Einstein form.

The quality of the fit for the coherent function (from Table 7.1) is shown on Fig. 7.8.

Fits of $e^+e^- \to p + X$

We now consider the proton production data in e^+e^- collisions aiming, in particular, at investigation of possible mass effects in the spectra and the fits. The Tsallis_p function again does a good job, see Fig. 7.9 (left). The parameter n of the fit ($n = 3.4$) is comparable to that obtained for pions ($n = 3.8$), but the momentum scale $T = 0.36$ GeV is larger since it is $T = 0.30$ GeV for pions.

The Bose-Einstein function is less satisfying than it was for the pions. This conclusion would be less clear if the full error bars were to be considered. However, consideration of residuals for both the Tsallis_p function and the Bose-Einstein one (Fig. 7.10) shows that, first, the scale of fluctuations is smaller for Tsallis_p, and second, that part of the trend is missed by the Bose-Einstein function. The Tsallis function also showed similar

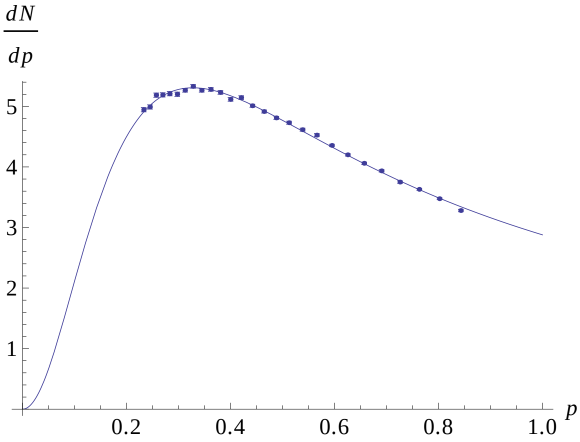

FIGURE 7.8 – OPAL data fitted by the coherent function.

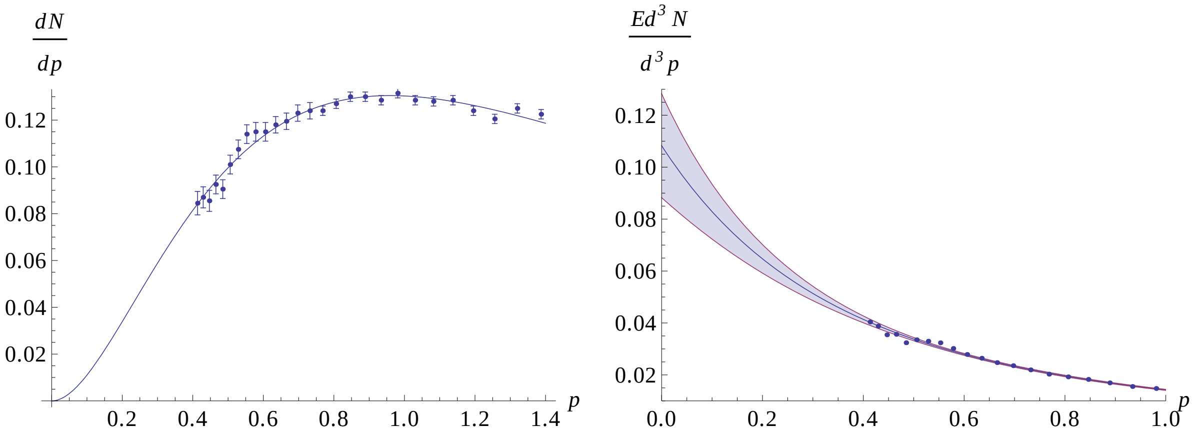

FIGURE 7.9 – OPAL (anti)proton data fitted with the Tsallis_p function (left) and confidence level bands (right).

difficulties.

The coherent function works pretty well, as can be seen on Fig. 7.11 (left). The power n is close to 1, as for pions. The momentum scale $I_1 = 0.53$ GeV is greater than it was for pions ($I_1 = 0.29$ GeV). The quality of the fit is comparable with that obtained with Tsallis_p as was checked by looking at residuals (not shown) and at the average quadratic deviation.

Again we observe by comparing Tsallis_p with the coherent function that the linear versus quadratic behavior at small p cannot be disentangled. The inflexion point for the coherent function is located around $p = 300$ MeV, where is no data. Only locations of inflexion points around 500 MeV, as obtained when fitting either with Bose-Einstein or Tsallis functions, could be rejected from the data and lead to the conclusion that the momentum scale for this location set by the proton mass in these functions is too high, while lower scale such as I_1 in the coherent function is not excluded.

The good description of e^+e^- data generally obtained with the coherent function prompted us to use it systematically in Sect. 7.3.

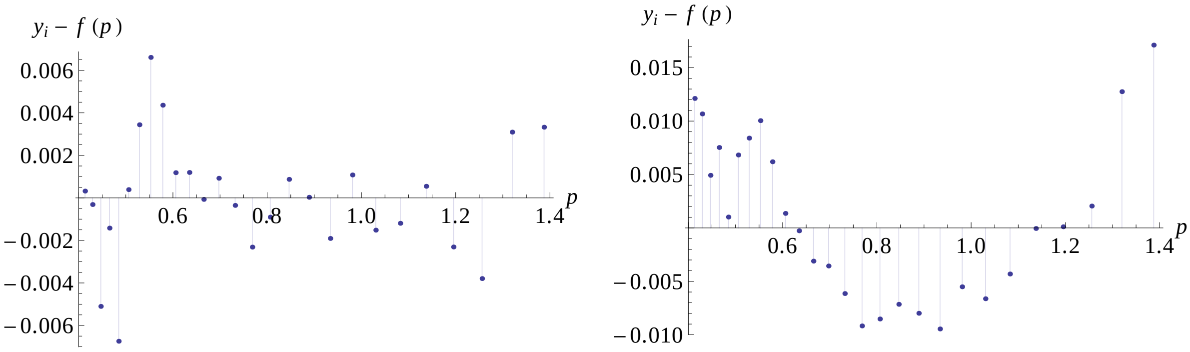

FIGURE 7.10 – OPAL (anti)proton data residuals with the Tsallis_p function (left) and the Bose-Einstein function (right).

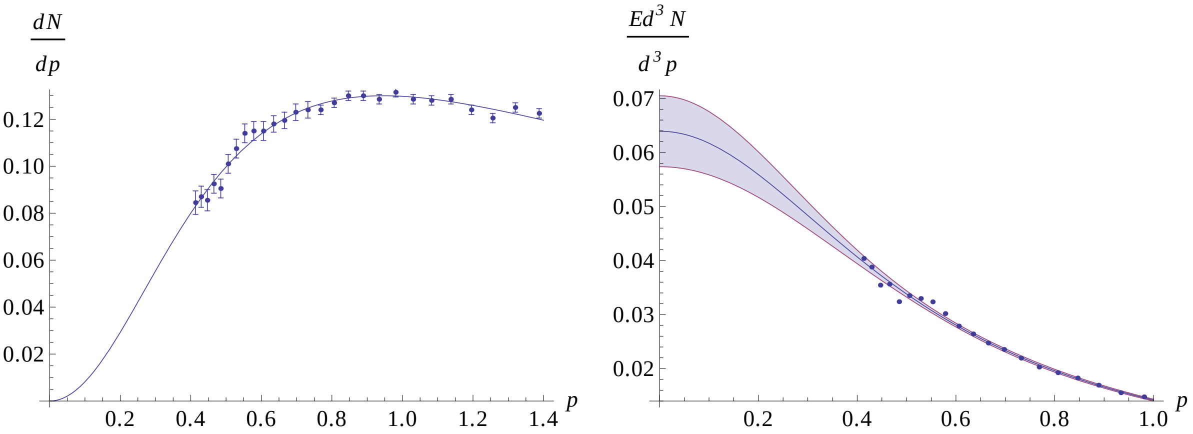

FIGURE 7.11 – OPAL (anti)proton data fitted with the coherent function (left) and confidence level bands (right).

Fits for pp collisions

Let us now consider charged pion data of the ALICE experiment.

Starting again with the Tsallis_p function, we observe first that the fit and the extrapolated limit I_0 only slightly depend on the chosen maximum fitting momentum p_T, at least in the range between 0.5 and 1.0 GeV. We therefore decided to stick to 1 GeV for pions.

The power n is large, at variance with what was observed with e^+e^- collisions, in line with the well-known exponential behavior of p_T spectra at small p_T. However, as can be seen on Fig. 7.12 (left), the quality of the fit is not good when we look at it in more detail. Concerning this aspect, we observed a much better behavior with the Tsallis function, as is visible on Fig. 7.12 (right).

The description of the ALICE data with both the ISR and the Bose-Einstein functions was not also very satisfactory.

The coherent function could provide a good description when limiting the range of p_T to $p_T \leq 0.5$ GeV. For larger values, a systematic deviation is unavoidable, but since this does not affect strongly the extracted parameter, we again refrained from adapting the

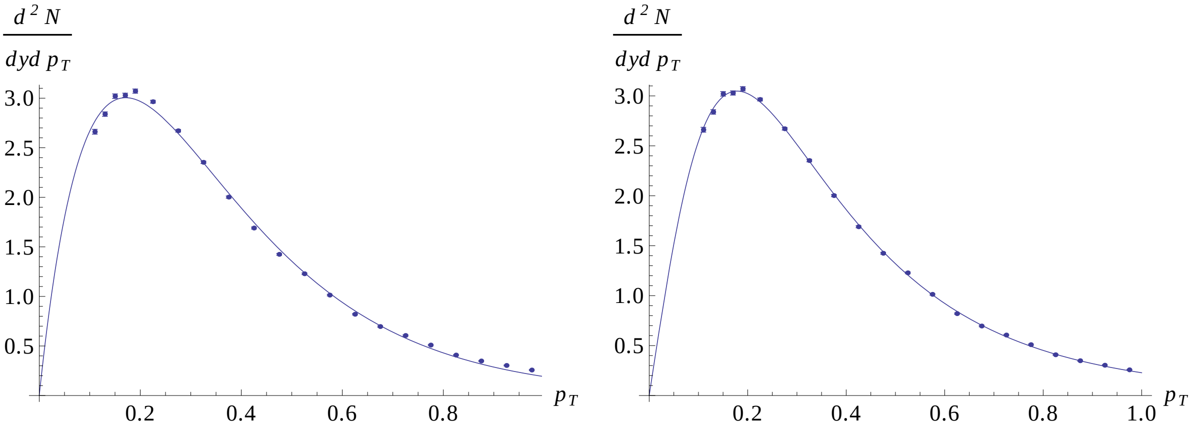

FIGURE 7.12 – ALICE pion data fitted with the Tsallis_p function (left) and the Tsallis function (right).

p_T range and continued to use 1 GeV as the upper bound of the fitting range.

The result of this fit is shown on Fig.7.13 (left). The power n is close to 2, while the scale parameter $I_1 \approx 0.22$ GeV is somewhat smaller than that obtained in e^+e^- collisions. On Fig. 7.13 (right), a comparison of the invariant spectra for Tsallis_p and the coherent function is shown. As it can be seen, contrary to the situation in e^+e^- collisions, the inflexion point of the coherent function stands at a location where the first data-points sit, with the consequence that we get systematically higher I_0 for functions where the small p_T behaviors are linear than for those where it is quadratic.

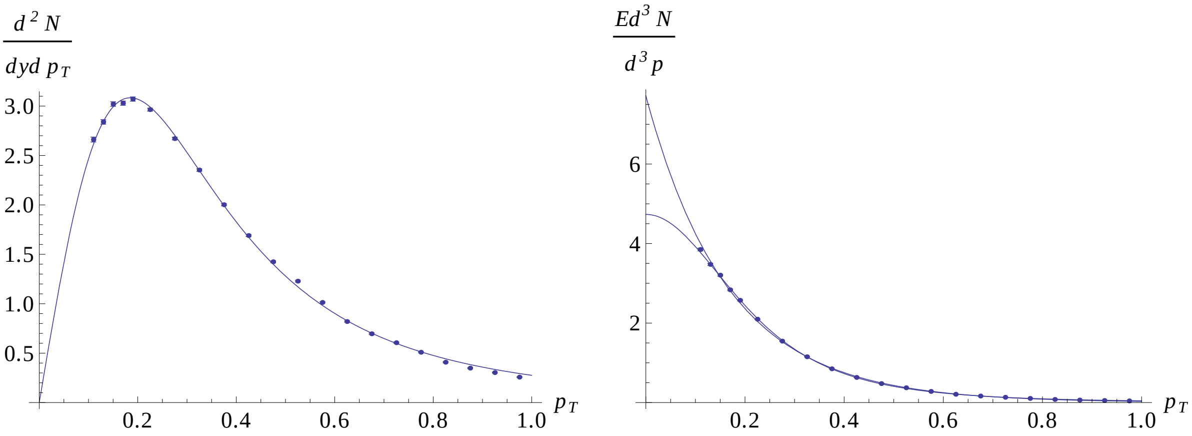

FIGURE 7.13 – ALICE pion data fitted with the coherent function (left) ; comparison between Tsallis_p and coherent function for the invariant particle production (right).

7.3 Results and discussion

In this section, we present the results obtained for the limit I_0. We report it systematically for the two fitting functions identified previously, namely, the Tsallis and the coherent function (see Table 7.1), sometimes quoting values obtained with other fits. We perform our study for identified charged pions, kaons and protons, both in e^+e^- and pp collisions.

7.3.1 e^+e^- collisions

The results for different fitting functions can be seen on Fig. 7.14. Some values are also quoted in Table 7.3. Considering several extrapolation functions has the advantage of giving a comprehensive view of the evolution of extracted I_0 values. Although the magnitude of the extrapolation varies between 3 and 6 GeV^{-2} and depends on fitting function, the general tendency for each particular fitting function is more clear. Looking at Fig. 7.14, one may conclude that the soft momentum limit for the invariant distribution of particles is quite the same for all experiments, although the errors are large. Thus, the energy independence of the zero momentum limit seems to be compatible with experimental results in e^+e^- collisions.

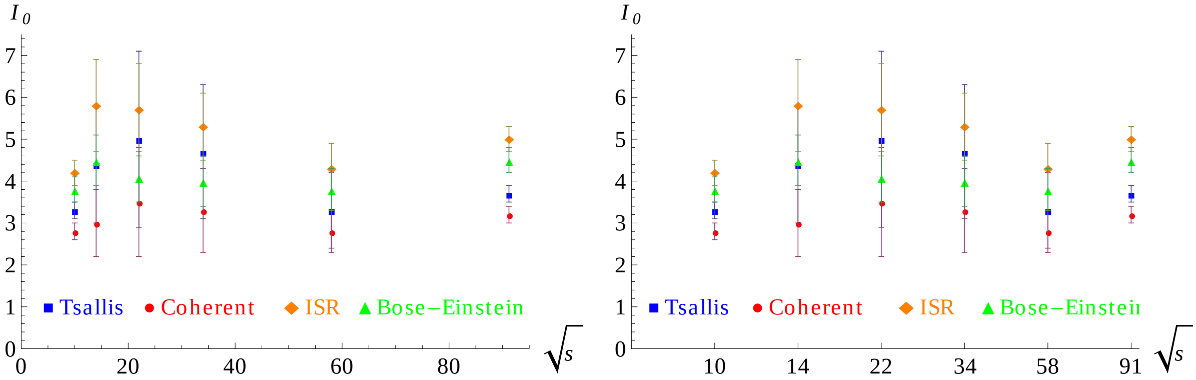

FIGURE 7.14 – Zero momentum limit I_0 of the extrapolated invariant distribution of charged pions $\frac{1}{2}(\pi^+ + \pi^-)$ in e^+e^- collisions. Plots differ by the scale in the X axis.

Table 7.3 also contains information about the quality of the fit. It is either given by an estimate of the χ^2/ndf, when statistical errors are known (ARGUS and OPAL), dividing the quadratic error by the number of degrees of freedom and by the average statistical error squared, or given by the percentage of the total variance that is explained by the fit, i.e.

$$R^2 = \frac{\sum_i (f(p_i) - \bar{y})^2}{\sum_i (y_i - \bar{y})^2}. \tag{7.3.1}$$

Both quantities are above all interesting for comparing different functions for the same data set. Their absolute values are more difficult to interpret. The quantity R^2 lacks a

Table 7.3 – I_0 values for pion production in e^+e^- collisions for different fitting functions.

Experiment ($\sqrt{s}$)	fit	I_0^{ee}, GeV^{-2}	ndf	χ^2/ndf	R^2
ARGUS (10 GeV)	Tsallis	3.1 ± 0.2	29	1.9	98%
	Coherent	2.8 ± 0.2		1.4	99%
	ISR	4.2 ± 0.3		3.0	97%
	B-E	3.8 ± 0.3	30	4.4	96%
TOPAZ (58 GeV)	Tsallis	3.3 ± 0.9	6	-	99.6%
	Coherent	2.8 ± 0.5		-	99.6%
	ISR	4.3 ± 0.6		-	99.4%
	B-E	3.8 ± 0.5	7	-	99.4%
OPAL (91 GeV)	Tsallis	3.7 ± 0.2	24	1.3	99.8%
	Coherent	3.2 ± 0.2		1.9	99.7%
	ISR	5.0 ± 0.3		1.4	99.7%
	B-E	4.5 ± 0.3	25	2.4	99.6%

reference to data precision, but that is this very fact which makes it possible to compute it for any data.

We performed a detailed study on all quoted functions, including the four functions given in Table 7.1, in order to test the capabilities of each functions to cope with the considered data. Our study concluded that there is no fitting function that stands out as being universally correct, in line with the conclusions drawn from the previous section. In e^+e^- collisions, among the best χ^2/ndf values for all three types of mesons were obtained with the coherent fit, as is also indicated in Table 7.3.

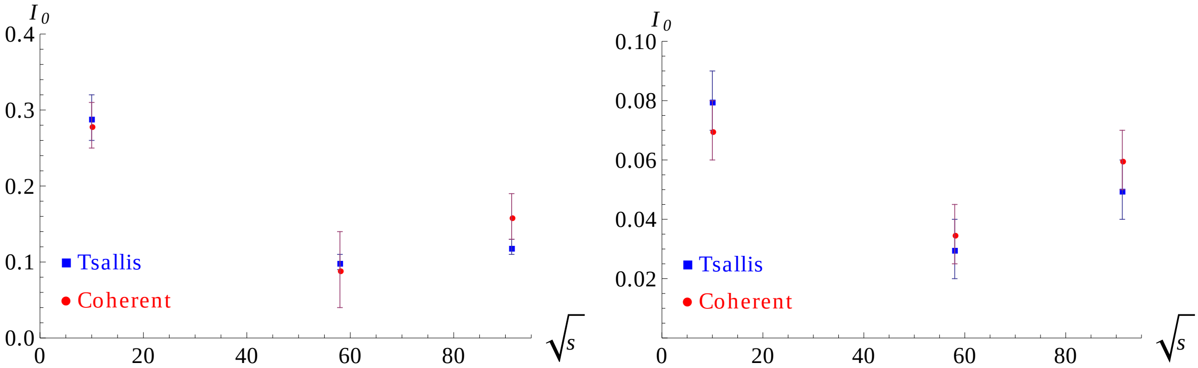

Figure 7.15 – Zero momentum limit I_0 of extrapolated invariant distributions for charged kaons (left) and (anti)protons (right) in e^+e^- collisions.

On Fig. 7.15, the results for charged kaons and protons for the Tsallis and the coherent fits for three data sets spanning the range of e^+e^- collision energies are given. Corresponding numbers are quoted in Tables 7.4 and 7.5. We also tested other fitting functions as well and observed that the tendency obtained here is also reproduced with the same spread in magnitude. In the case of kaons, the I_0 value is in between 0.1 and 0.3 GeV^{-2}, whereas for protons the value is placed in between 0.04 and 0.08 GeV^{-2}. Obviously, in the case of kaons and protons, the conclusion about collision energy independence is more difficult to draw since the values show rather large fluctuations. This is partly explained by bigger uncertainties of the experimental points and smaller number of available points per collision energy.

These data *per se* are only marginally amenable to the phenomenology we want to explore, and the only conclusion we can hope to reach is that there is no evidence for a strong energy dependence of the limits $I^{ee}_{0\,K}$ and $I^{ee}_{0\,p}$.

TABLE 7.4 – I_0 values in GeV^{-2} for the Tsallis function for pions, kaons and protons in e^+e^- collisions.

Experiment	$\sqrt{s}$, GeV	$I^{ee}_{0\,\pi}$	$I^{ee}_{0\,K}$	$I^{ee}_{0\,p}$
ARGUS	10	3.1 ± 0.2	0.29 ± 0.03	0.08 ± 0.01
TASSO	14	4.4 ± 1.4	0.22 ± 0.03	0.03 ± 0.01
TASSO	22	5.0 ± 2.1	0.15 ± 0.02	0.03 ± 0.01
TASSO	34	4.7 ± 1.6	0.16 ± 0.02	0.03 ± 0.01
TOPAZ	58	3.3 ± 0.9	0.10 ± 0.01	0.03 ± 0.01
OPAL	91.2	3.7 ± 0.2	0.12 ± 0.01	0.05 ± 0.01

TABLE 7.5 – I_0 values in GeV^{-2} for the coherent function for pions, kaons and protons in e^+e^- collisions.

Experiment	$\sqrt{s}$, GeV	$I^{ee}_{0\,\pi}$	$I^{ee}_{0\,K}$	$I^{ee}_{0\,p}$
ARGUS	10	2.8 ± 0.2	0.28 ± 0.01	0.07 ± 0.01
TASSO	14	3.0 ± 0.8	0.24 ± 0.08	0.03 ± 0.01
TASSO	22	3.5 ± 1.3	0.13 ± 0.03	0.06 ± 0.02
TASSO	34	3.3 ± 1.0	0.15 ± 0.03	0.03 ± 0.01
TOPAZ	58	2.8 ± 0.5	0.09 ± 0.05	0.03 ± 0.01
OPAL	91.2	3.2 ± 0.2	0.16 ± 0.03	0.06 ± 0.01

7.3.2 pp collisions

The results obtained with pp collisions are shown in Figs. 7.16 and 7.17. It is worth noting that ISR points (23, 45, 63 GeV) show a small increase, also observed in [11], which becomes milder for charged kaons. For protons, however, this tendency is no more visible. However, looking at the PHENIX experiment point which was measured at almost the same energy as ISR (62.4 GeV), we do not see this increase any more. This fact can probably be explained by the general uncertainty of normalization of experimental data. The extrapolation point of the ALICE data at 900 GeV gives an increased value compared to that from PHENIX data at 200 GeV, which is reproduced by all extrapolation functions. However, the ALICE point gives the same value as ISR point at 63 GeV, so that it is difficult to claim a significant increase, at variance with the expectation of color coherence. A more conservative conclusion is that the zero momentum limit do not show any significant variation in the whole explored energy range.

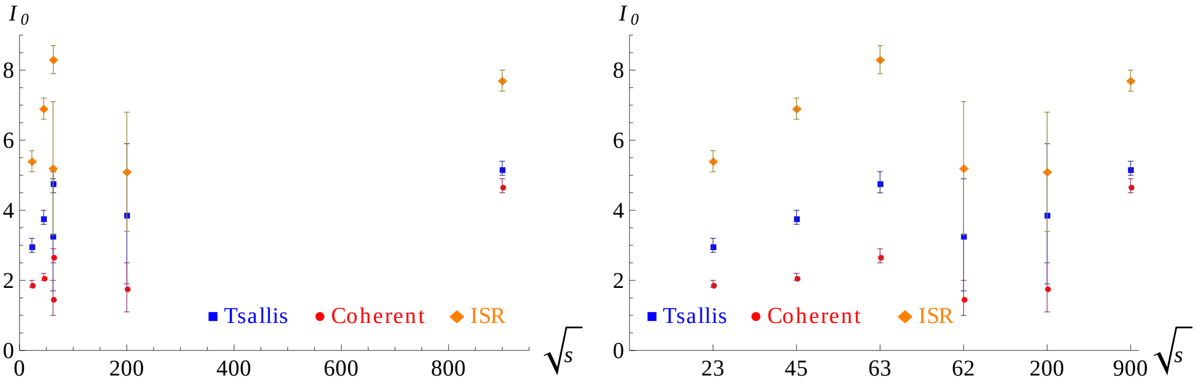

FIGURE 7.16 – Zero momentum limit I_0^{pp} of invariant distribution of charged pions in pp collisions.

For pp data, only the Tsallis fit showed good results for all three types of particles. For charged kaons and protons, the zero momentum limit shows the tendency of being independent on the collision energy, except of the PHENIX point at 62.4 GeV, the extrapolation of which gives smaller value. As a summary we conclude that the extracted zero momentum limit of the invariant distributions of charged protons and kaons speaks in favor of the $\sqrt{s}$ independence, but uncertainties are large.

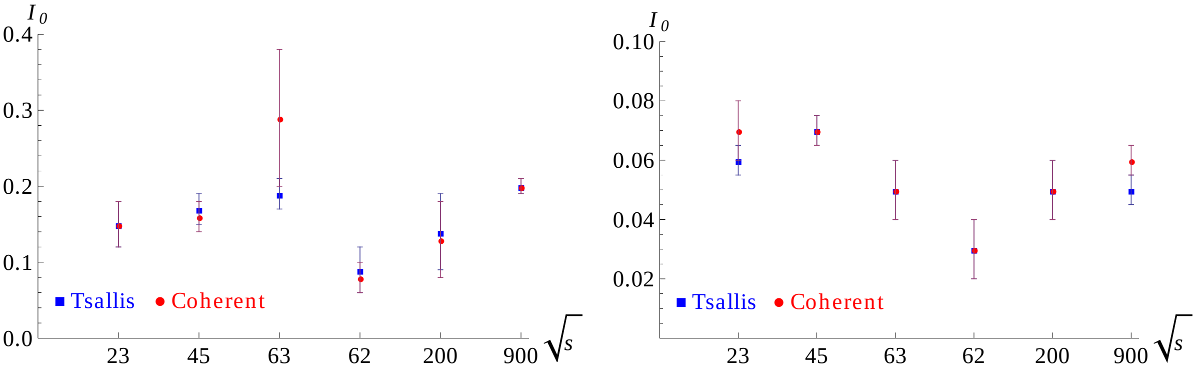

FIGURE 7.17 – Zero momentum limit I_0 of the invariant distribution of charged kaons and (anti)protons in pp collisions.

7.3.3 Comparison between e^+e^- and pp

Having observed that the zero momentum limits of the invariant distributions of pions are consistent with the prediction of the collision energy independence, it is meaningful to extract an average $I_{0\,\pi}$. One has :

$$\begin{aligned} &I_{0\,\pi}^{ee} = 3.5 \pm 0.2, \quad &&I_{0\,\pi}^{pp} = 4.1 \pm 0.2 \qquad &&\text{[Tsallis fit]}, \\ &I_{0\,\pi}^{ee} = 3.0 \pm 0.2, \quad &&I_{0\,\pi}^{pp} = 3.2 \pm 0.2 \qquad &&\text{[coherent function fit]}. \end{aligned} \tag{7.3.2}$$

From these results, ratios I_0^{pp}/I_0^{ee} are estimated as

$$\frac{I_{0\,\pi}^{pp}}{I_{0\,\pi}^{ee}} = 1.1 \pm 0.1 \quad \text{[Tsallis]}, \qquad \frac{I_{0\,\pi}^{pp}}{I_{0\,\pi}^{ee}} = 1.1 \pm 0.1 \quad \text{[coherent]}. \tag{7.3.3}$$

Based on the observed χ^2/ndf values which tended in favor the coherent function for e^+e^- collisions and the Tsallis function for pp ones, the ratio may better estimated by using the Tsallis fit for $I_{0\,\pi}^{pp}$ and the coherent result for $I_{0\,\pi}^{ee}$. This pushes the ratio a little up :

$$\frac{I_{0\,\pi}^{pp}}{I_{0\,\pi}^{ee}} = 1.4 \pm 0.1. \tag{7.3.4}$$

We conclude with a remark that a strong statement about the discussed universality cannot be made from extrapolations of inclusive hadron spectra to zero momentum. In the next chapter, we continue on this topic by considering ratios of the spectra. In contrast with hadron spectra themselves which are steeply falling functions of momentum, their ratios turn our to be linear functions in a wide range of momentum. This fact results in definitive statement about the universality, see the next chapter.

Chapitre 8

Ratios of charged particle spectra and tests of the universality

In this chapter, the universality of soft hadron spectra — the independence of the collision energy — is addressed in a new way : we consider the ratios of the spectra of different collision energies. The ratios exhibit linear behavior with the momentum, starting from approximately 0.6 GeV/c. The extrapolation to zero momentum gives unity. With this new approach, we are able to conclude that, indeed, the universality takes place. In particular, it takes place in the case of the LHC energies.

8.1 Overview

In Chapter 7, we tried to systematically extract the quantity

$$I_0 = \lim_{p \to 0} E \frac{d^3n}{dp^3} \tag{8.1.1}$$

for the production spectra of different hadrons in e^+e^- and pp experiments. The insufficient number of data points at low momentum combined with steeply falling shapes of the spectra resulted in ambiguity in choice of a fitting function (for an illustration, see Fig. 8.1). Consequently, the extrapolation to the zero momentum point does not give us a possibility to make a conclusion. Indeed, the expected universality (i.e. independence of the collision energy $\sqrt{s}$) of the values I_0^{ee} and I_0^{pp} in e^+e^- and pp collisions respectively was verified with large uncertainties caused by extrapolation of the fitting functions to zero momentum. In addition, the value for the ratio I_0^{pp}/I_0^{ee} turned out to be highly dependent on fitting functions. Moreover, by taking different fitting functions in e^+e^- and in pp collisions, one can highly vary the value of this ratio.

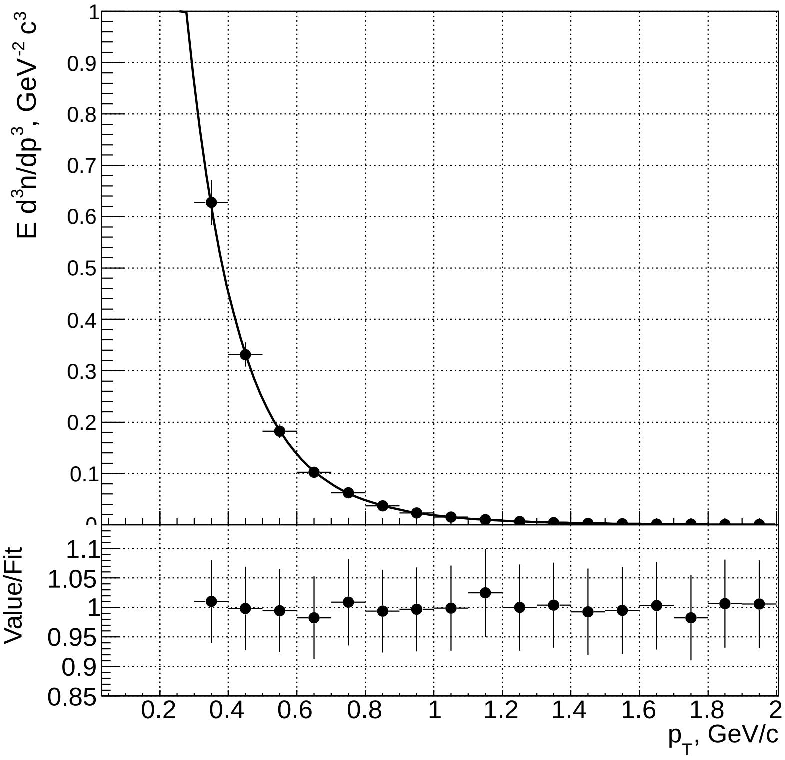

FIGURE 8.1 – The PHENIX experiment $\frac{1}{2}(\pi^+ + \pi^-)$ spectrum, pp collisions at $\sqrt{s}$ = 200 GeV [56]. Data points are fitted with Tsallis function. Steeply falling shape of the spectrum leaves ambiguity for the extrapolation to the zero momentum.

In this chapter, for the verification of the universality of soft hadron spectra, we elaborate a different approach. To this end, instead of fitting the spectra themselves, we calculate the spectra ratios measured by the same experiment at different collision energies $\sqrt{s}$. As will become clear soon, such an approach has a huge advantage : *whereas the spectra themselves are steeply falling, their ratios change slowly with momentum and exhibit linear behavior in a wide range*. Thus, the ratios of the spectra can be easily and reliably fitted and extrapolated to the zero momentum. The universality takes place if the quantity [1]

$$R(p) = \frac{E\frac{d^3n}{dp^3}(\sqrt{s_1}, p)}{E\frac{d^3n}{dp^3}(\sqrt{s_2}, p)} \tag{8.1.2}$$

equals to unity at zero momentum :

$$\lim_{p\to 0} R(p) = 1. \tag{8.1.3}$$

Let us also remark that making ratios of soft hadron spectra of one and the same experiment has two additional important advantages :

- the spectra of one experiment are given with same binning parameters over the momentum, so that their ratios can be built as point-by-point ratios;
- several systematic errors and uncertainties of an original measurement cancel (e.g. systematic error of total cross-section measurement).

In practice, the latter, however, means that, for publicly available data, we can exclude only the error of total cross-section measurement, which is usually of about 10%.

8.2 Ratios of the spectra

For what follows, we took the data for *inclusive charged particle spectra* for the following experiments :

- UA1 experiment, $p\bar{p}$ at $\sqrt{s} = 200$, 500 and 900 GeV [57];
- CDF experiment, $p\bar{p}$ at $\sqrt{s} = 630$ and 1800 GeV [58];
- CMS experiment, pp at $\sqrt{s} = 900$ GeV and 7 TeV [59];
- CMS experiment, pp at $\sqrt{s} = 900$ GeV and 7 TeV, older papers [60, 61]; corresponding values will be marked with “prev.” suffix;
- ALICE experiment, $\sqrt{s} = 900$ GeV, 2.76 TeV and 7 TeV [62, 63].

The UA1 and the CDF data points are given in $Ed^3\sigma/dp^3$ format. Before making the ratios, we scaled them by a factor $1/\sigma_{\text{inel}}$,

$$E\frac{d^3n}{dp^3} = \frac{1}{\sigma_{\text{inel}}} \times E\frac{d^3\sigma}{dp^3}, \tag{8.2.1}$$

---

[1] By the momentum p here we mean, in fact, the transverse momentum p_T. As long as the rapidity region is finite, the limit of zero momentum coincides with the limit of zero transverse momentum.

where total inelastic cross-sections are given in Table 8.1.

Table 8.1 – Total cross-sections for the UA1 and the CDF experiments.

Exp	$\sqrt{s}$ [GeV]	σ_{tot} [mb]	σ_{inel} [mb]
UA1	200	52	43 ± 4
UA1	500	62	49 ± 2
CDF	630	63	50 ± 2
UA1	900	68	53 ± 4
CDF	1800	74	57 ± 3

The ratios, with their systematic and statistical errors added in quadrature, are drawn in Figs. 8.2–8.5, separately for each experiment. The overall plot, with error bars being omitted for clearness, is shown in Fig. 8.6.

As one can see, all the ratios, surprisingly, exhibit *linear behavior* with momentum, starting from approximately 0.6 GeV/c. On the figures, we additionally fitted the ratios with linear functions in the region 0.6–2.5 GeV/c. The tendency of the points below 0.6 GeV/c differ from the linear behavior above 0.6 GeV/c and do not go to unity. At the same time, the linear behavior of the points above 0.6 GeV/c does extrapolate well to unity at zero momentum, which is clearly visible from the fits. Table 8.2 summarizes the fitting parameters of the linear fits

$$R(p_T) = R_0 + Bp_T. \tag{8.2.2}$$

Table 8.2 – Parameters of linear fits $R(p_T) = R_0 + Bp_T$.

Exp	$\sqrt{s_1}$ [GeV]	$\sqrt{s_2}$ [GeV]	$\sqrt{s_1}/\sqrt{s_2}$	ratio at zero momentum, R_0	slope, B [GeV^{-1}]
UA1	900	500	1.8	1.19 ± 0.08	0.18 ± 0.05
UA1	500	200	2.5	0.96 ± 0.09	0.44 ± 0.07
ALICE	7000	2760	2.54	0.94 ± 0.06	0.24 ± 0.05
CDF	1800	630	2.86	1.24 ± 0.08	0.40 ± 0.08
ALICE	2760	900	3.07	1.15 ± 0.08	0.40 ± 0.06
UA1	900	200	4.5	0.99 ± 0.11	0.96 ± 0.09
CMS	7000	900	7.78	0.96 ± 0.20	0.97 ± 0.17
CMS, prev.	7000	900	7.78	1.03 ± 0.11	1.01 ± 0.09
ALICE	7000	900	7.78	0.93 ± 0.09	0.91 ± 0.07

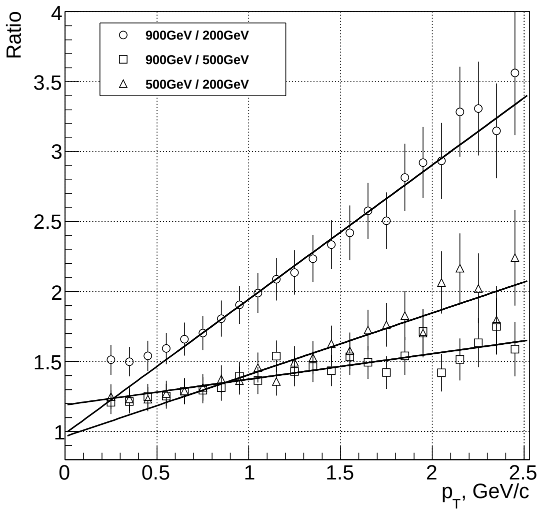

FIGURE 8.2 – The UA1 ratios.

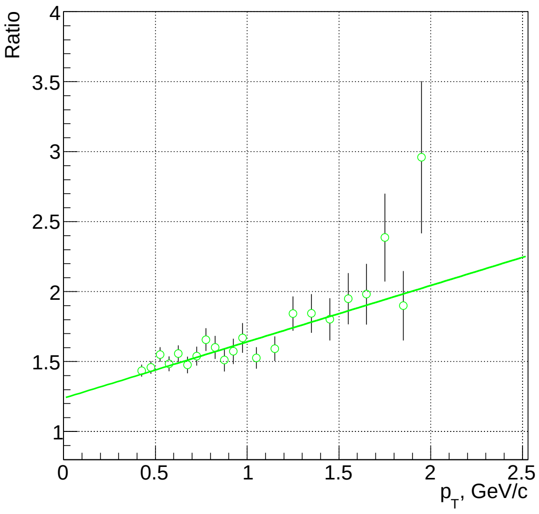

FIGURE 8.3 – The CDF ratios.

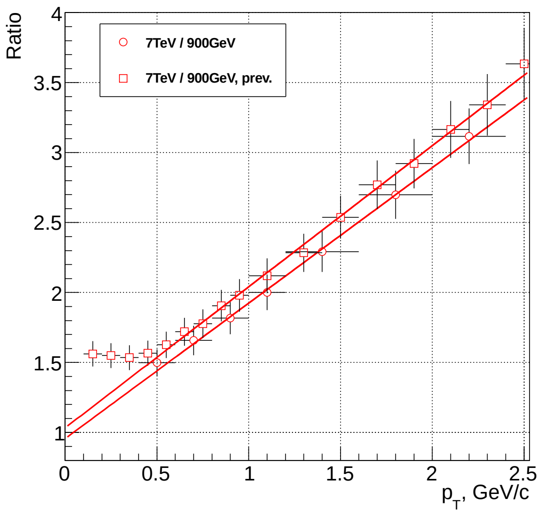

FIGURE 8.4 – The CMS ratios.

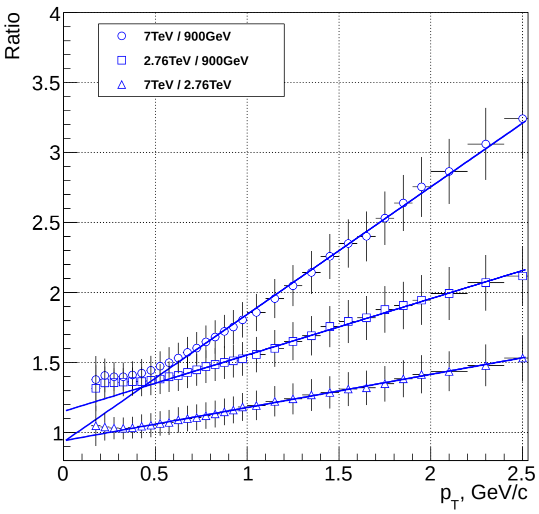

FIGURE 8.5 – The ALICE ratios.

We see from the table that the values of the R_0 parameter, which is nothing else than the extrapolated value at zero momentum, are indeed very close to unity. The average error is about 10%. The biggest deviations from unity present in the ratios with small slopes B wich correspond to small ratios $\sqrt{s_1}/\sqrt{s_2}$. Thus, one can conclude that, indeed, to the extent of experimental uncertainties, the universal behavior of the considered spectra – the independence of the collision energy $\sqrt{s}$ – takes place, provided one considers data points above the 0.6 GeV/c threshold. In particular, one concludes that *the universality is valid at the LHC energies.* Moreover, it is suggested from the table that the slopes of the linear fits depend on ratios of collision energies $\sqrt{s_1}/\sqrt{s_2}$ and do not depend on the collision energies themselves. The only exception for this rule is seen for the (unofficial) $\sqrt{s} = 2.76$ TeV data of the ALICE experiment.

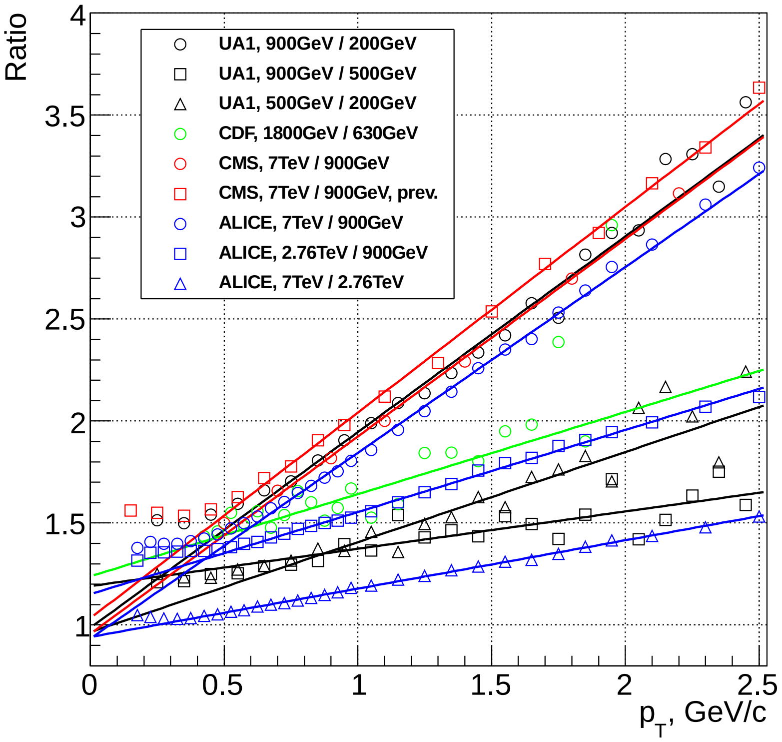

FIGURE 8.6 – Combined plot of the spectra ratios with all data points and linear fits. Error bars are omitted.

The breaking tendency below the threshold is not surprising. The coherence phenomenon of QCD was deduced in the approximation of zero masses of all participating partons. If quarks were massless, so as the pions, the universality would extend to the zero momentum. Due to the nonzero quark masses, this is not the case.

Thereby, one can definitely state that the color coherence and/or the LPHD principle are broken at very low momentum. The behavior in the region below 0.6 GeV/c is not predicted from the theory.

8.3 Discussion of the linear behavior

The linear tendency of the spectra ratios in the coherent region of momenta is surprising and is not understood. The simplicity of the ratios may suggest that this behavior can be deduced theoretically. To this end, it is useful to see how the ratios and the linear fits behave with momentum at larger momenta. The Figs. 8.7–8.10 show further evolution of the fits and the data points. While deviations between the data points and the fits are noticeable, they are not large.

Let us show how the linearity in the ratios can be understood "phenomenologically". In the ALICE and the CMS experiments, the spectra are fitted with the Tsallis function,

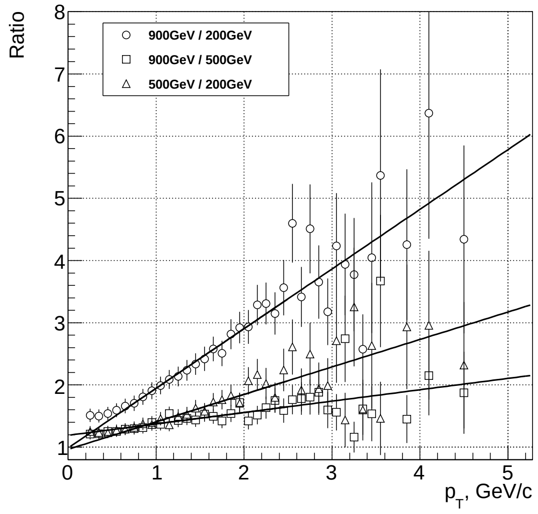

FIGURE 8.7 – The UA1 ratios in wider momentum region.

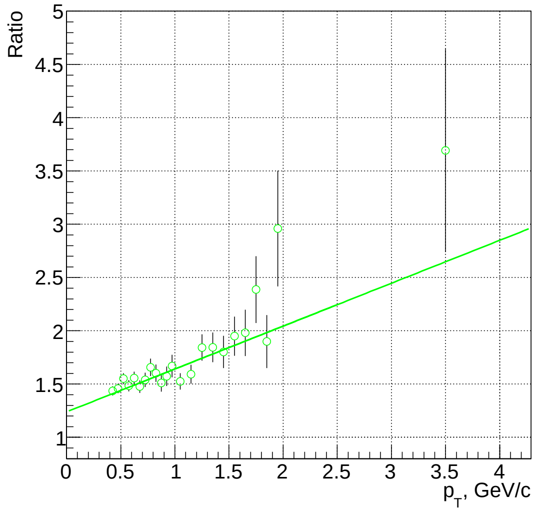

FIGURE 8.8 – The CDF ratios in wider momentum region.

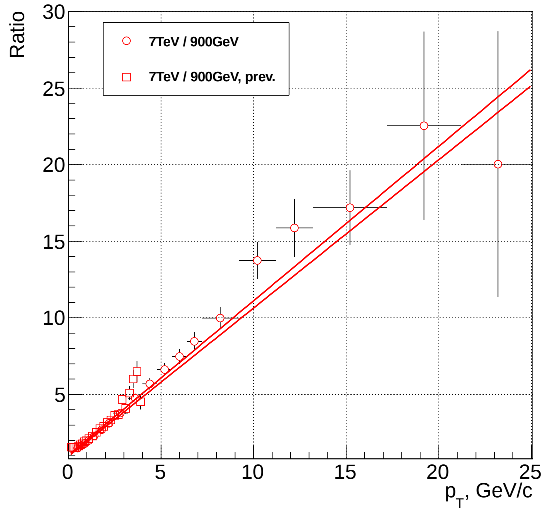

FIGURE 8.9 – The CMS ratios in wider momentum region.

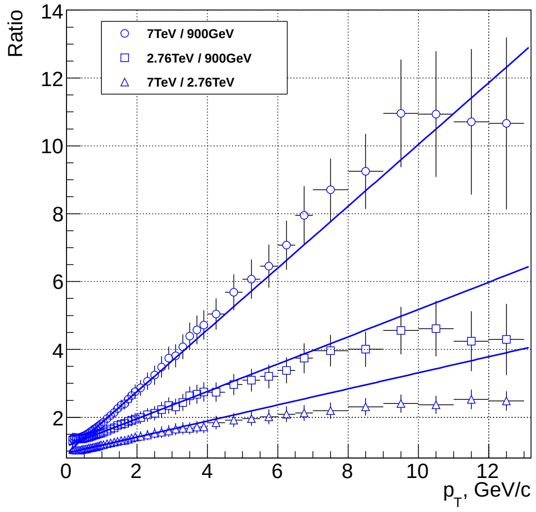

FIGURE 8.10 – The ALICE ratios in wider momentum region.

which we, for further convenience, write as

$$f(p_T) = \frac{C}{\left[1 + p_T/(nT)\right]^n}, \tag{8.3.1}$$

neglecting any mass parameters in this formula. This function has three free parameters : C, T and n. The parameter T is usually interpreted as "temperature", since the limit $n \to \infty$ corresponds to the Boltzmann statistical distribution $Ce^{-p_T/T}$.

Let us take, for instance, the values of fitting parameters for the inclusive charged particle spectra of the CMS experiment [60, 61] :

$$\begin{aligned} &900 \text{ GeV}: && T = 0.13 \pm 0.01; && n = 7.7 \pm 0.2, \\ &7 \text{ TeV}: && T = 0.145 \pm 0.005; && n = 6.6 \pm 0.2. \end{aligned}$$

This gives $\frac{\Delta T}{T} \approx 0.1$, $\frac{\Delta n}{n} \approx 0.2$, i.e. the parameters T and n are slow functions of the center of mass energy $\sqrt{s}$, and their variations are small : $\frac{\Delta T}{T} \ll 1$, $\frac{\Delta n}{n} \ll 1$. This allows one to expand the ratio $R(p_T)$ into Taylor series with respect to $\frac{\Delta T}{T}$ and $\frac{\Delta n}{n}$ [2]. One has, up to the second order :

$$R(p_T) = \frac{f_7(p_T)}{f_{900}(p_T)} = 1 + p_T\left(\frac{1}{T_{900}} - \frac{1}{T_7}\right) + \frac{p_T^2}{2}\left[\left(\frac{1}{T_{900}} - \frac{1}{T_7}\right)^2 + \left(\frac{1}{n_7 T_7^2} - \frac{1}{n_{900} T_{900}^2}\right)\right], \quad (8.3.2)$$

where the index “7” denotes the corresponding 7 TeV values, while the index “900” denotes the corresponding 900 GeV values. Additionally, we omitted the difference between C_7 and C_{900} since their ratio is close to unity.

Let us calculate the region where the expansion (8.3.2) is valid. For this, the second term of the series must be much smaller than the first term, as well as the first term must be much smaller than 1. One has :

$$p_T \ll \left(\frac{1}{T_{900}} - \frac{1}{T_7}\right)^{-1} \approx \frac{T^2}{\Delta T}, \qquad \frac{\Delta T}{T} \ll 1, \qquad \frac{\Delta n}{n} \ll 1. \quad (8.3.3)$$

which approximately gives $p_T < 1.5$ GeV/c. Note that experimentally the linear region is even wider.

In this way, the linearity of the ratios is related to slow evolution of the parameters of the spectra with respect to the collision energy $\sqrt{s}$.

Note also that, as a by-product, a linear fit of a ratio of two spectra allows one to determine the value ΔT with a better precision compared to the value which can be extracted as the difference of the temperatures of the Tsallis fits themselves.

---

[2] Strictly speaking, according to Eq. (8.3.1), the expansion of the numerator and the denominator in Taylor series is possible, provided that $p_T/(nT) \ll 1$, which is true in our particular case only at larger values of n. Still, knowing that the ratio should be linear with momentum, we proceed with the Taylor expansion.

Conclusion

The aim of this study was to find and measure observables appropriate for the ALICE experiment in order to verify the color coherence phenomenon of QCD. The following two topics were elaborated : inclusive momentum distribution of particles in a jet and universality of hadron production in the limiting case of zero momentum.

The measurement of inclusive momentum distribution of particles in a jet is a long-term project requiring several years of the LHC operation needed to collect necessary statistics. Meanwhile, the author of this study was involved in analysis of data collected with the ALICE electromagnetic calorimeters, EMCAL and PHOS.

The experimental part of this study was mainly devoted to neutral meson measurements through their photon decays — the most feasible and adequate topic for the EMCAL detector in the beginning of the LHC operation. The following mesons and their decay modes were considered : $\pi^0 \to \gamma\gamma$, $\eta \to \gamma\gamma$, $\omega(782) \to \pi^0\gamma \to 3\gamma$, $K_S^0 \to \pi^0\pi^0 \to 4\gamma$. During the studies, several important topics related to EMCAL were resolved.

First, the energy non-linearity correction of the EMCAL response was found both for Monte Carlo simulations (from a single photon simulation) as well as for real data (from symmetric $\pi^0 \to \gamma\gamma$ decays). It is the energy non-linearity correction which allowed us to see the $\omega(782)$ and K_S^0 peaks with the limited statistics $L_{\text{int}} = 6.7\ \text{nb}^{-1}$ of the ALICE experiment in 2010. The data/simulation non-linearity corrections, being supplemented with an appropriate decalibration of the EMCAL detector in simulations, allowed us to attain a good matching between the data and Monte Carlo simulations.

Second, the data quality assurance framework was developed for both electromagnetic calorimeters and is now a part of the official ALICE analysis train. This work was published as an ALICE analysis note [8]. Thanks to it, good runs appropriate for the π^0 and η meson measurements were selected, while the EMCAL acceptance was correctly accounted for.

Although the above-mentioned preparatory work is mainly technical, it is an essential pre-requisite for physics analysis since without it no physics results could be obtained.

Third, all steps necessary for the π^0 as well as for the η meson measurements were performed. This includes extraction of raw yields, calculation of production yields and calculation of relevant systematic errors. The measured neutral meson spectra, being interesting by themselves, give a baseline for heavy ion measurements to which the ALICE experiment is dedicated.

Fourth, the η/π^0 ratio of the two production spectra was measured. Let us remark that this measurement is simpler than separate measurements of the π^0 and η spectra since several important (for the case of EMCAL) uncertainties cancel in the ratio. These include : uncertainty of the detector position inside the ALICE machine, uncertainty of material budget in front of the EMCAL, uncertainty in decalibration parameters of the Monte Carlo simulations. These three factors turned out to be hot topics inside the EMCAL community. Thus, the η/π^0 ratio was, in fact, the first physical measurement which was done with the EMCAL detector.

Lastly, it is worth mentioning that, due to these studies for the EMCAL, a high level of friendly competition was constantly maintained between the two calorimeters.

As a nearest perspective, the results of neutral meson measurements with the EMCAL detector should be finalized and published. This will demonstrate that all the detector-related issues are resolved or under control, i.e. the detector response is well understood and it is known how to work it in other physics analyses related to photons and electrons. Most importantly, this will guarantee good detector performance in future.

Separately from the studies discussed above, we performed a phenomenological verification of the expected universality (independence of the collision energy $\sqrt{s}$) of hadron spectra in the limiting case of zero hadron momentum. To this end, we applied two independent approaches to this topic.

In the first approach, we took measured inclusive spectra for $\pi^\pm$, $K^\pm$ and (anti)protons for several pp ($p\bar{p}$) and e^+e^- experiments in a wide range of collision energies, performed a fitting procedure for each spectrum and extracted the extrapolated values of the invariant hadron yields at the limit of zero momentum. Although the results are consistent with the theoretical predictions, their large systematic uncertainties do not allow to make a firm statement about the spectra universality. This was mainly caused by the absence of data at very low momentum and thus unavoidable uncertainties in the extrapolations to zero momentum.

As the second approach, we considered ratios of inclusive spectra of charged particles in pp collisions. In contrast with hadron spectra themselves, the ratios of the spectra of different collision energies $\sqrt{s}$ are slow functions of momentum. Surprisingly, they turned out to be linear functions in a wide range of momentum $0.6\,\mathrm{GeV/c} < p_T < 2.5\,\mathrm{GeV/c}$. This fact allowed us to make extrapolations of the ratios to zero momentum safely and reliably. At a result, the extrapolations yielded unity with a good precision which permitted us to conclude that, at least in pp collisions, the universality does take place, within systematic errors of about 10%.

As for the hadron spectra themselves, the found linearity turned out to be related to slow parameter evolution with $\sqrt{s}$ of the fitting functions. In addition, we were able to observe “mass effects” at momentum $p_T < 0.6$ GeV/c, i.e. breaking of the linear tendency due to nonzero quark masses. The latter suggests that, in practice, instead of considering the extrapolation of the fits of hadron spectra to zero momentum, it is more appropriate to consider the ratios of those fits taken in a region of momentum starting from about 0.6 GeV/c and linearly extrapolate the ratios to zero momentum point. Moreover, the discovered “mass effects” should be studied with inclusive spectra of identified pions, kaons and protons. This work is, however, a subject of a separate research.

The approach of ratios of spectra is simple, efficient and promising. In respect to the perspectives, it is very tempting to consider the corresponding theoretical predictions for the ratios of two gluon-jets or two quark-jets at different energies $\sqrt{s}$ within the MLLA framework.

Bibliography

[1] D. J. Gross and F. Wilczek, Phys. Rev. Lett. **30**, 1343 (1973).

[2] Y. L. Dokshitzer, V. A. Khoze, A. H. Mueller and S. I. Troian, *"Basics of perturbative QCD"*, Gif-sur-Yvette, France : Ed. Frontieres (1991) 274 p.

[3] V. A. Khoze and W. Ochs, Int. J. Mod. Phys. A **12**, 2949 (1997) [hep-ph/9701421] ; V. A. Khoze, W. Ochs and J. Wosiek, In *Shifman, M. (ed.) : At the frontier of particle physics, vol. 2*, 1101-1194 [hep-ph/0009298].

[4] Y. I. Azimov, Y. L. Dokshitzer, V. A. Khoze and S. I. Troyan, Z. Phys. C **27**, 65 (1985).

[5] D. Acosta *et al.* [CDF Collaboration], Phys. Rev. D **68**, 012003 (2003).

[6] F. Carminati *et al.*, *"ALICE : physics performance report"*, volume I, J. Phys. G **30** 1517 (2004).

[7] ALICE Collaboration, B. Alessandro *et al.*, J. Phys. G32, 1295 (2006).

[8] O. Driga, T. Gousset, Y. Kharlov, D. Peressounko, B. Polichtchouk, *"Data quality assessment for the ALICE PHOS detector"*, ALICE internal note ALICE-INT-2012-006 (2012).

[9] K. Koch [ALICE Collaboration], Nucl. Phys. A, **855**, 281 (2011)

[10] B. Abelev *et al.* [ALICE Collaboration], arXiv :1205.5724 [hep-ex].

[11] W. Ochs, V. A. Khoze and M. G. Ryskin, Eur. Phys. J. C **68**, 141 (2010) [arXiv :1003.2127 [hep-ph]].

[12] W. Ochs, V. A. Khoze and M. G. Ryskin, arXiv :1011.5649 [hep-ph].

[13] W. Ochs, Acta Phys. Polon. B **41**, 2839 (2010) [arXiv :1011.2422 [hep-ph]].

[14] O. Driga, *"Inclusive production of π^0 meson in pp collisions at 7 TeV in the EMCAL detector"*, not published.

[15] O. Driga, *"Analysis of η to π^0 ratio in pp collisions at 7 TeV measured with the ALICE EMCAL"*, not published.

[16] G. Conesa, H. Delagrange, J. Diaz, M. Ippolitov, Y. Kharlov, D. Peresunko and Y. Schutz, Nucl. Instrum. Meth. A **537**, 363 (2005).

[17] U. Abeysekara *et al.* [ALICE EMCal Collaboration], *"ALICE EMCal Physics Performance Report"*, [arXiv :1008.0413 [hep-ex]].

[18] A. E. Chudakov, Izv. Akad. Nauk SSSR, ser. fiz. **19**, 650 (1955).

[19] Y. I. Azimov, Y. L. Dokshitzer, V. A. Khoze and S. I. Troyan, Z. Phys. C **31**, 213 (1986).

[20] O. S. Bruning, (Ed.), P. Collier, (Ed.), P. Lebrun, (Ed.), S. Myers, (Ed.), R. Ostojic, (Ed.), J. Poole, (Ed.) and P. Proudlock, (Ed.), *"LHC Design Report. 1. The LHC Main Ring"*, CERN-2004-003-V-1.

[21] O. Buning, (Ed.), P. Collier, (Ed.), P. Lebrun, (Ed.), S. Myers, (Ed.), R. Ostojic, (Ed.), J. Poole, (Ed.) and P. Proudlock, (Ed.), *"LHC Design Report. 2. The LHC infrastructure and general services"*, CERN-2004-003-V-2.

[22] M. Benedikt, (Ed.), P. Collier, (Ed.), V. Mertens, (Ed.), J. Poole, (Ed.) and K. Schindl, (Ed.), *"LHC Design Report. 3. The LHC injector chain"*, CERN-2004-003-V-3.

[23] G. Aad *et al.* [ATLAS Collaboration], Phys. Lett. B [arXiv :1207.7214 [hep-ex]] ; S. Chatrchyan *et al.* [CMS Collaboration], Phys. Lett. B [arXiv :1207.7235 [hep-ex]].

[24] K. Aamodt *et al.* [ALICE Collaboration], *"The ALICE experiment at the CERN LHC"*, JINST **3**, S08002 (2008).

[25] [ALICE collaboration], *"ALICE time projection chamber : Technical Design Report"*, CERN-LHCC-2000-001, http ://cdsweb.cern.ch/record/451098.

[26] [ALICE collaboration], *"ALICE transition-radiation detector : Technical Design Report"*, CERN-LHCC-2001-021, http ://cdsweb.cern.ch/record/519145.

[27] [ALICE collaboration], *"ALICE : a transition radiation detector for electron identification within the ALICE central detector - an addendum to the Technical Proposal"*, CERN-LHCC-99-013, http ://cdsweb.cern.ch/record/401988.

[28] [ALICE collaboration], *"ALICE Time-Of-Flight system (TOF) : Technical Design Report"*, CERN-LHCC-2000-012, http ://cdsweb.cern.ch/record/430132 ; *"ALICE Time-Of Flight system (TOF) : addendum to the technical design report"*, CERN-LHCC-2002-016, http ://cdsweb.cern.ch/record/545834.

[29] [ALICE collaboration], *"ALICE high-momentum particle identification : Technical Design Report"*, CERN-LHCC-98-019, http ://cdsweb.cern.ch/record/381431.

[30] [ALICE collaboration], *"Technical design report of the photon spectrometer"*, CERN-LHCC-99-004, http ://cdsweb.cern.ch/record/381432.

[31] [ALICE collaboration], *"ALICE electromagnetic calorimeter : addendum to the ALICE technical proposal"*, CERN-LHCC-2006-014, http ://cdsweb.cern.ch/record/932676.

[32] J. Olson, *"Data Quality : The Accuracy Dimension"*, Morgan Kaufmann Publishers, ISBN : 978-1-55860-891-7 (2003).

[33] G. Dellacasa *et al.* [ALICE Collaboration], *"ALICE technical design report of the photon spectrometer (PHOS)"*, CERN-LHCC-99-04.

[34] M. J. Oreglia, Ph.D. Thesis, SLAC-R-236, Appendix D (1980).

[35] L. Evans, (ed.), P. Bryant, (ed.), *"LHC Machine"*, JINST **3**, S08001 (2008).

[36] K. Aamodt *et al.* [ALICE Collaboration], Eur. Phys. J. C **68**, 345 (2010) [arXiv :1004.3514 [hep-ex]].

[37] J. Allen *et al.* [ALICE EMCal Collaboration], Nucl. Instrum. Meth. A **615**, 6 (2010) [arXiv :0912.2005 [physics.ins-det]].

[38] D. Aleksandrov *et al.* [ALICE PHOS Collaboration], NIM, A **620**, 526 (2010)

[39] Y. Kharlov, D. Peressounko, B. Polichtchouk, *"Neutral pion and η meson production in proton-proton collisions at $\sqrt{s} = 0.9$ TeV and $\sqrt{s} = 7$ TeV"*, ALICE internal note (2010).

[40] B. Abelev *et al.* [ALICE Collaboration], arXiv :1205.5724 [hep-ex].

[41] S. S. Adler *et al.* [PHENIX Collaboration], Phys. Rev. C **75**, 024909 (2007) [nucl-ex/0611006].

[42] T. Sjostrand, P. Eden, C. Friberg, L. Lonnblad, G. Miu, S. Mrenna and E. Norrbin, Comput. Phys. Commun. **135**, 238 (2001) [hep-ph/0010017].

[43] B. Andersson, G. Gustafson, G. Ingelman and T. Sjostrand, Phys. Rept. **97**, 31 (1983).

[44] B. Andersson, Camb. Monogr. Part. Phys. Nucl. Phys. Cosmol. **7**, 1 (1997).

[45] J. Nishimura, Soryushiron Kenkyu **12**, 24 (1956).

[46] G. Cocconi, Phys. Rev. **111**, 1699 (1958).

[47] G. Cocconi, L. J. Koester and D. H. Perkins, LRL Report No. UCRL-10022, 167 (1961), unpublished.

[48] J. Orear, Phys. Rev. Lett. **12**, 112 (1964).

[49] R. Hagedorn, pp. 13–46 (1995), invited talk at NATO Advanced Study Workshop on Hot Hadronic Matter : Theory and Experiment, Divonne-les-Bains, France, 27 Jun – 1 Jul 1994.

[50] J. Erwin, W. Ko, R. L. Lander, D. E. Pellett and P. M. Yager, Phys. Rev. Lett. **27**, 1534 (1971).

[51] R. Hagedorn, Nucl. Phys. **B24**, 93 (1970).

[52] S. Barshay and Y. A. Chao, Phys. Lett. **B38**, 229 (1972).

[53] C. Tsallis, J. Statist. Phys. **52**, 479 (1988).

[54] J. Adams *et al.* [STAR Collaboration], Phys. Lett. **B637**, 161 (2006), ISSN 0370-2693.

[55] G. Wilk and Z. Wlodarczyk, Phys. Rev. Lett. **84**, 2770 (2000).

[56] A. Adare *et al.* [PHENIX Collaboration], Phys. Rev. C **83**, 064903 (2011) [arXiv :1102.0753 [nucl-ex]].

[57] C. Albajar *et al.* [UA1 Collaboration], Nucl. Phys. B **335**, 261 (1990).

[58] F. Abe *et al.* [CDF Collaboration], Phys. Rev. Lett. **61**, 1819 (1988).

[59] S. Chatrchyan *et al.* [CMS Collaboration], JHEP **1108**, 086 (2011) [arXiv :1104.3547 [hep-ex]].

[60] V. Khachatryan *et al.* [CMS Collaboration], JHEP **1002**, 041 (2010) [arXiv :1002.0621 [hep-ex]].

[61] V. Khachatryan *et al.* [CMS Collaboration], Phys. Rev. Lett. **105**, 022002 (2010) [arXiv :1005.3299 [hep-ex]].

[62] K. Aamodt *et al.* [ALICE Collaboration], Phys. Lett. B **693**, 53 (2010) [arXiv :1007.0719 [hep-ex]].

[63] K. Aamodt *et al.* [ALICE Collaboration], unpublished.

Analyse des données des calorimètres d'ALICE et étude de la production des hadrons de basse impulsion dans les collisions de grande énergie

L'expérience ALICE auprès du LHC est dédiée à l'étude des multiples facettes de l'interaction forte. La théorie microscopique de cette dernière, QCD, et sa manifestation dans la production de particules peuvent être explorées en étudiant les observables de jets. La maîtrise de sa calorimétrie est centrale à l'étude de la physique des jets avec ALICE. C'est l'un des sujets abordés dans ce travail. Plus précisément, une des premières tâches est de vérifier la qualité des données disponibles. A cet effet, l'assurance de la qualité (AQ) des données pour les calorimètres électromagnétiques d'ALICE, PHOS et EMCAL, a été développée. Sur cette base, la mesure des pions neutres, π^0 et η via leur désintégration en deux photons a été réalisée. Le succès dans la compréhension de la dynamique des particules de basse énergie à l'intérieur des jets s'appuie sur des calculs de la QCD perturbative, laquelle a déjà été testée expérimentalement avec un niveau d'accord impressionnant. La théorie prédit que le spectre des particules à l'intérieur des jets est indépendante de l'énergie de la collision dans la limite d'impulsion nulle ($p \to 0$). Afin de tester cette prédiction, une étude systématique des données expérimentales provenant des collisionneurs de hadrons et de leptons aux énergies de collision de quelques dizaines de GeV jusqu'à l'échelle du TeV au LHC a été réalisée.

Mots-clés : cohérence de couleur, spectres des hadrons, calorimétrie, calorimètres, l'assurance de la qualité des données, les mesures de mésons neutres,Hump-Backed Plateau, expériences ALICE.

Analysis of the ALICE calorimeter data and soft hadron production in high energy collisions

The ALICE experiment at LHC is dedicated to the study of many facets of the strong interaction. The microscopic theory of the latter, QCD, and its manifestation in particle production can be thoroughly explored by studying jet observables. Central to the study of jet physics with ALICE is the mastering of its calorimetry. This is one of the topics addressed in this work namely carrying out one of the first tasks which is to verify the quality of available data. For this purpose the Quality Assurance (QA) framework for ALICE electromagnetic calorimeters, PHOS and EMCAL, was developed. On this base, the measurement of neutral pions, π^0 and η, via their two photon decays was performed. The success in understanding dynamics of soft particles inside jets relies on calculations of perturbative QCD, impressive accuracy of which has already been tested experimentally. The theory predicts that the inclusive particle spectrum inside jets is independent of a collision energy in the limiting case of zero momentum ($p \to 0$). In order to test this prediction, a systematic study of world experimental data from hadron and lepton colliders at the collision energies from tens of GeV up to the TeV scale at the LHC has been performed.

Keywords : color coherence, soft hadron spectra, calorimetry, calorimeters, data quality assurance, neutral meson measurements, Hump-Backed Plateau, ALICE experiment.